

# Parameter Estimation with GNSS-Reflectometry and GNSS Synthetic Aperture Techniques

THÈSE N° 8350 (2018)

PRÉSENTÉE LE 23 FÉVRIER 2018

À LA FACULTÉ DES SCIENCES ET TECHNIQUES DE L'INGÉNIEUR  
LABORATOIRE D'ÉLECTRONIQUE ET TRAITEMENT DU SIGNAL  
PROGRAMME DOCTORAL EN MICROSYSTÈMES ET MICROÉLECTRONIQUE

ÉCOLE POLYTECHNIQUE FÉDÉRALE DE LAUSANNE

POUR L'OBTENTION DU GRADE DE DOCTEUR ÈS SCIENCES

PAR

Miguel Angel RIBOT SANFELIX

acceptée sur proposition du jury:

Prof. H. Shea, président du jury  
Prof. P.-A. Farine, Dr C. Botteron, directeurs de thèse  
Dr A. Jovanovic, rapporteur  
Dr P. Closas, rapporteur  
Dr J. Skaloud, rapporteur



ÉCOLE POLYTECHNIQUE  
FÉDÉRALE DE LAUSANNE

Suisse  
2018



“The thing that doesn’t fit  
is the thing that is most interesting:  
that part that doesn’t go according to  
what you expected.”

— Richard Feynman

“An investment in knowledge  
pays the best interest.”

— Benjamin Franklin

*In memory of s’abuelo Miquel,*

*and to my family*



# Acknowledgements

This thesis would not have been possible without the help, support, guidance, and encouragement of several people. Firstly, I shall express my most sincere gratitude to my thesis director Prof. Pierre-André Farine for giving me the opportunity to conduct the research described in this thesis as a member of the ESPLAB, for his support, and for providing the best possible working environment during these past years.

I am especially thankful to my thesis co-director, Dr Cyril Botteron, for his guidance, support, insightful review of all my work, and particularly for trusting me with the freedom to explore my ideas. He was always available

I would also like to express my gratitude to the rest of the thesis jury committee, Dr Jan Skaloud, Dr Pau Closas, Dr Aleksandar Jovanovic and Prof. Herbert Shea for accepting to review my dissertation and evaluate this work.

I had the pleasure of advising Joaquín's Cabeza's MSc thesis, and since then, two years ago, he has worked with me on the synthetic aperture antenna. I really appreciate all the hard work that he has put into this project. I enjoyed every moment of working with him. I would like also to thank Ferràn Valdés, the handy engineer who designed and built our (low-cost) mechanical rotating arm, and Dr Bartomeu Alorda, who supervised him while doing so. I also thank Florian Degardins for his early contribution to the synthetic aperture antenna project during his MSc thesis.

My most sincere gratitude goes also to Dr Pau Closas for granting me with a little of his statistical signal processing wisdom/magic in our collaborations during these last two years. Many of the discussion we had will turned into fruitful research ideas.

I would like to extend my gratitude to my colleagues in the GNSS group: Dr Vincenzo Capuano, Dr Paul Blunt and Dr Jérôme Leclère. Their drive, deep GNSS knowledge, and meticulousness have been a model for me. I learned a great deal from our many discussions. Moreover, I thank Prof. Thomas Pany for kindly providing us with their data recordings collected with IFEN's rotating antenna, and LISIC-ULCO group, especially to Dr Serge Reboul and Dr Jean-Christophe Kucwaj, for our early collaborations on GNSS-R work.

I am grateful for the financial support from the Swiss National Science Foundation who supported this work under grants Grant No. 200020-134766 and 200020-153052.

I thank my colleagues and friend at the ESPLAB. It has been a privilege to share this time with you: Milad, Saeed, Vasili, Patrick, Christian, Aleksandar, Marko, Urs, Mohssen, Sara, Pradyumna and Mitko. Special thanks to Vincenzo who has been my office mate during most of my PhD. We compensated those weekends in the office with some amazing experiences. Thanks also to Christelle and Abbas, who have made my life in Neuchâtel much nicer and exciting. My appreciation goes to Mrs. Joëlle Banjac for all the administrative

## Acknowledgements

---

help and support she gave me during my PhD. She was beyond helpful from the very first day until the last.

My special thanks go to Carlos and Laura for their friendship and for all the great people that I have met in Lausanne because of them. Their support during this years made things much easier, interesting and enjoyable. I would also like to thank Manel for his long-term friendship, for all the beers and discussions that we shared, and for letting me stay in his place as if it was my own home. I also thank all my friends back in Mallorca, who, no matter the distance, have been be my side during the good and the bad times. I hope I can always live to be the friend you deserve.

I especially thank my beloved Anna, because of her love and support during these past years I have become a better person. Life will always be brighter by your side.

Per acabar, agraeixo el seu suport a la meva mare, al meu pare, a la meva germana i a la resta de la meva família. Vos estim molt. Gràcies per haver cregut en mi.

*Neuchâtel, 31 October 2017*

M.A. Ribot Sanfèlix

# Abstract

Aside from intentional interference, multipath is the most significant error source for Global Navigation Satellite Systems (GNSS) receivers in many operational scenarios. In this thesis, we study the multipath estimation from two different perspectives: to retrieve useful information from it using GNSS-Reflectometry (GNSS-R) techniques; and to mitigate its effects or to estimate its direction-of-arrival (DOA) as well as the line-of-sight (LOS) signal's using synthetic aperture (SA) processing.

The first part of the thesis focuses on precision bounds for GNSS-R techniques for ground-based receivers, in scenarios where a single antenna simultaneously receives the LOS signal and a specular reflection. First, we derive the Cramér-Rao bound (CRB) of the receiver's height and the reflection coefficient, with the latter depending on the surface's electrical properties. More specifically, we propose a CRB derivation applicable to GNSS-R techniques that make use of the phase information and long observation times, such as the interference pattern technique (IPT). The derivation is based on the parameter transformation of the Fisher information matrix. We study the dependence of the computed CRB on the scenario and the receiver bandwidth. The CRB results for the simulated scenarios are consistent with the precision reported for many GNSS-R techniques used in these scenarios. The proposed CRB is meant to benchmark and compare new and existing techniques.

Besides the derived CRB, we propose an algorithm to obtain the maximum-likelihood (ML) estimator of the parameters of interest with the IPT: the segmented ML estimator (SML). The SML transforms a complex multivariate optimization problem into multiple simpler ones by dividing the parameter search space taking advantage of the cost function's particular structure. The SML is validated with simulated signal and asymptotically cross-validates the CRB results.

The second part of the thesis is devoted to the study of the SA processing of GNSS signals. The goal is to estimate the DOA of the signals received, and mitigate errors in the navigation solution caused by interfering signals, such as multipath. We start by deriving the CRB for the SA context, as a function of the antenna trajectory. This CRB considers the effect of the antenna complex gain, and we show in simulations that it is possible to achieve meaningful DOA estimation only by changing the antenna's orientation. We continue by proposing a development framework built upon a signal tracking architecture integrating SA processing. Before any SA processing, it is necessary to estimate and compensate any carrier phase contribution not related to the antenna motion. To do so, we propose two new sequential techniques based on the extended Kalman filter (EKF). Also, we develop an open-loop version of the proposed SA tracking architecture, more robust than its closed-loop counterpart. Finally, we validate the proposed architecture and SA-based techniques with synthetic GPS signals at first, and then with real signals, recorded using an antenna mounted on a mechanical rotating arm. The obtained results validate the implemented techniques and show how the proposed SA architecture can ultimately mitigate the position bias error observed in environments with severe multipath interference.

**Key words:** Global Navigation Satellite System (GNSS), GNSS-Reflectometry, Galileo,

## Abstract

---

GPS, Multipath, Parameter Estimation, Interference Pattern Technique (IPT), Coherent reflection, Cramér-Rao Bound (CRB), Synthetic Aperture Processing, Spatial Filtering, Direction-of-Arrival (DOA), Adaptive Beamforming, SA Tracking Architecture, Open-Loop Tracking, Extended Kalman Filter (EKF), Maximum-Likelihood (ML), Segmented Maximum Likelihood (SML), Rotating Antenna



# Résumé

Pour beaucoup d'applications, l'une des principales sources d'erreur pour les récepteurs de systèmes de positionnement par satellites (GNSS), à côté des interférences intentionnelles, provient des trajets multiples dus aux réflexions. Dans cette thèse, nous étudions l'estimation des multi-trajets sous deux perspectives différentes : pour estimer l'information utile qu'il peut apporter sur la physique de la réflexion (GNSS-R) ; et pour atténuer son effet ou pour estimer sa direction d'arrivée (ainsi que celle du trajet direct) en utilisant le traitement de l'ouverture synthétique (SA) appliqué à une antenne mobile.

La première partie de la thèse porte sur les limites de précision pour les techniques GNSS-R pour les récepteurs au sol, dans des scénarios où une seule antenne reçoit simultanément le signal direct (LOS) et une réflexion spéculaire. Dans un premier temps, nous dérivons la limite de Cramér-Rao (CRB) pour la hauteur du récepteur et le coefficient de réflexion, ce dernier dépendant des propriétés électriques de la surface. Plus précisément, nous proposons une dérivation de cette limite CRB applicable aux techniques GNSS-R qui utilisent l'information de phase et des temps d'observation longs, comme avec la technique du modèle d'interférence (IPT). La dérivation est basée sur une transformation des paramètres de la matrice d'information de Fisher. Nous étudions la dépendance de la limite CRB sur le scénario considéré et la bande passante du récepteur. Les résultats obtenus sont cohérents avec la précision rapportée pour de nombreuses techniques GNSS-R utilisées dans les scénarios considérés. Le CRB proposé est conçu pour évaluer et comparer les techniques nouvelles et existantes.

En addition, nous proposons un algorithme pour obtenir l'estimateur de maximum de vraisemblance (ML) des paramètres d'intérêt avec l'IPT : l'estimateur ML segmenté (SML). Le SML transforme un problème complexe d'optimisation multivariée en plusieurs problèmes plus simples en divisant l'espace de recherche en tirant parti de la structure particulière de la fonction de coût. Le SML est validé avec un signal simulé et est efficace, atteignant asymptotiquement la limite CRB.

La deuxième partie de la thèse est consacrée à l'étude du traitement de SA pour des signaux GNSS. Le but est d'estimer la direction d'arrivée (DOA) des signaux reçus, et d'atténuer les erreurs dans la solution de navigation provoquées par des signaux interférents, tels que les trajets multiples. Nous commençons par dériver la limite CRB pour le contexte SA, en fonction de la trajectoire de l'antenne mobile. Ce CRB considère l'effet du gain complexe de l'antenne, et nous montrons en simulations qu'il est possible d'obtenir une bonne estimation de l'angle d'arrivée uniquement en changeant l'orientation de l'antenne. Nous continuons en proposant une architecture de récepteur GNSS intégrant le traitement SA. Avant tout traitement SA, il est nécessaire d'estimer et de compenser toute contribution de la phase porteuse non liée au mouvement de l'antenne. Pour ce faire, nous proposons deux nouvelles techniques séquentielles basées sur le filtrage de Kalman étendu (EKF). En outre, nous développons une version en boucle ouverte de l'architecture de suivi SA proposée, plus robuste que sa contrepartie en boucle fermée. Enfin, nous validons l'architecture proposée dans un premier temps avec des signaux GPS synthétiques, puis avec des signaux réels, enregistrés à l'aide d'une antenne montée sur un bras rotatif mécanique. Les résultats obtenus

## Abstract

---

valident les techniques mises en œuvre et montrent comment l'architecture SA proposée peut en fin de compte atténuer l'erreur sur la position observée dans des environnements présentant de graves perturbations liées aux trajets multiples.

**Mots clefs :** Global Navigation Satellite System (GNSS), GNSS-Reflectometry, Galileo, GPS, Multipath, Parameter Estimation, Interference Pattern Technique (IPT), Coherent reflection, Cramér-Rao Bound (CRB), Synthetic Aperture Processing, Spatial Filtering, Direction-of-Arrival (DOA), Adaptive Beamforming, SA Tracking Architecture, Open-Loop Tracking, Extended Kalman Filter (EKF), Maximum-Likelihood (ML), Segmented Maximum Likelihood (SML), Rotating Antenna

# Contents

Acknowledgements	i
Abstract (English/Français)	iii
List of figures	ix
List of tables	xii
Notation	xv
Acronyms	xvi
<b>1 Introduction</b>	<b>1</b>
1.1 Background and Motivation	1
1.2 Contributions	3
1.3 Thesis Outline	5
<b>2 GNSS-Reflectometry and Synthetic Aperture Processing: An Overview</b>	<b>7</b>
2.1 GNSS Concept	7
2.2 GPS and Galileo Signals	10
2.2.1 GPS Signals	12
2.2.2 Galileo Signals	14
2.3 GNSS Receiver Architecture	17
2.3.1 The RF Front End	18
2.3.2 Acquisition	19
2.3.3 Tracking	20
2.3.4 Open-Loop Tracking	21
2.4 GNSS-Reflectometry	23
2.4.1 Model for Scattered and Reflected GNSS Signals	25
2.4.2 The Interference Pattern Technique (IPT)	26
2.5 Spatial Filtering of GNSS Signals	28
2.5.1 Synthetic Aperture Processing	30
2.5.2 Delay-and-Sum and Beamscan Algorithms	32
2.5.3 Adaptive DOA Estimation: MPDR-Capon and MUSIC	33
2.6 Estimation Precision: The Cramér-Rao Bound	34
<b>3 Parameter Estimation in GNSS-Reflectometry Scenarios with Coherent Reflection</b>	<b>37</b>
3.1 Signal Model and Scenario Assumptions	38
3.1.1 Signal Model for the LOS Signal with Coherent Multipath	39
3.2 CRB Derivation for GNSS-R Coherent Reflection Scenarios	40
3.2.1 Definition and General Case for $M$ Propagation Paths	41

## Contents

---

3.2.2	Two Propagation Path Case for a Ground-Based Static Receiver . . .	43
3.2.3	Introducing Phase Coherence Using FIM's Parameter Transformation	45
3.3	Analysis of the CRB for Short Observation Intervals . . . . .	46
3.3.1	CRB when $\Delta\rho > \rho_{chip}$ . . . . .	47
3.3.2	CRB when $\Delta\rho < \rho_{chip}$ : Interference Case . . . . .	51
3.4	Derivation of the CRB for Long Observation Intervals: $\text{CRB}(\Psi_{long})$ . . . . .	52
3.5	Analysis of the CRB for Long Observation Times . . . . .	54
3.5.1	$\text{CRB}(\Psi_{long})$ vs. $\Delta\theta$ . . . . .	55
3.5.2	Effects of the Signal Modulation on the $\text{CRB}(\Psi_{long})$ . . . . .	57
3.6	The Segmented ML Algorithm . . . . .	59
3.6.1	Signal Model at the Output of the Prompt Correlator . . . . .	59
3.6.2	SML Description . . . . .	61
3.7	Chapter Conclusion . . . . .	67
<b>4</b>	<b>Spatial Filtering of GNSS Signals with Synthetic Aperture Processing</b>	<b>69</b>
4.1	Signal Model for Synthetic Aperture Processing . . . . .	70
4.1.1	Antenna Pattern and Polarization Mismatch Effects . . . . .	73
4.2	Estimation Bounds: CRB Derivation . . . . .	75
4.2.1	CRB Evaluation . . . . .	77
4.2.2	CRB Comparison to Maximum Likelihood Estimator . . . . .	82
4.3	A Tracking Architecture for SA Processing with Uniform Circular Motion . .	84
4.3.1	Receiver Baseband Processing Prior to SA . . . . .	87
4.3.2	Practical Challenges of SA Processing . . . . .	90
4.3.3	Open-Loop Tracking with SA Processing . . . . .	92
4.3.4	Closed-Loop Tracking: Estimation the Reference Carrier Frequency . .	96
4.4	Results with Simulated Signal . . . . .	101
4.4.1	SA Closed-Loop Tracking: Direction-of-Arrival Estimation (I) . . . . .	102
4.4.2	Reference Frequency Estimation Methods Comparison (I) . . . . .	105
4.4.3	Corrected Code-Delays with SA Closed-Loop Tracking . . . . .	108
4.4.4	ACF Correction with SA Open-Loop Tracking (I) . . . . .	110
4.5	Experimental Results with Real Signals Recorded with a Rotating Arm . . .	113
4.5.1	SA Closed-Loop Tracking: Direction-of-Arrival Estimation (II) . . . . .	116
4.5.2	Reference Frequency Estimation Methods Comparison (II) . . . . .	120
4.5.3	SA Spatial Filtering Effect on the Navigation Solution . . . . .	126
4.5.4	ACF Correction with SA Open-Loop Tracking (II) . . . . .	127
4.6	Chapter Conclusion . . . . .	131
<b>5</b>	<b>Conclusions</b>	<b>133</b>
5.1	Thesis Achievements . . . . .	133
5.2	Directions for Future Research . . . . .	135
<b>A</b>	<b>Transformation Matrices and CRB Expressions for Short Observation Times</b>	<b>139</b>
<b>B</b>	<b>Zavorotny–Larson Model for the Surface Reflection Coefficient <math>\Gamma</math></b>	<b>143</b>
	<b>Bibliography</b>	<b>161</b>
	<b>Curriculum Vitae</b>	<b>163</b>

# List of Figures

2.1	GNSS positioning concept. The pseudoranges $\rho_i$ are computed as the product of the signals' estimated TOA $\hat{\tau}_i$ , times the propagation speed $c$ . . . . .	8
2.2	Overview of current and planned GNSS signals: spectrum and modulations. Updated in 2011. [1] . . . . .	9
2.3	Comparison of the different GNSS orbits (Credit: Cmglee, Ceo. Licensed under CC BY 3.0). . . . .	10
2.4	Main components of the GPS L1 C/A signal [2]. The signals are not to scale .	11
2.5	(Top) Normalized autocorrelation function of the transmitted GNSS signals considered (real part). The $x$ -axis showing the delay $\tau$ is normalized to $T_c = (1.023 \times 10^6)^{-1}$ s. (Bottom) PSD of the signals. See Table 2.1 for more details. . . . .	13
2.6	One period of the CBOC sub-carriers functions for (a) E1-B and (b) E1-C [3].	16
2.7	One period of the two sub-carriers functions, i.e., $sc_{E5-S}(t)$ and $sc_{E5-P}(t)$ , involved in E5 signal's AltBOC modulation [3]. . . . .	17
2.8	GNSS receiver main functional blocks. HW: Implementation with specific hardware. SW: Software implementation running on general purpose hardware.	18
2.9	Typical RF front end topology for GNSS receivers [4] . . . . .	19
2.10	Example of the CAF for a clearly detectable GPS L1 C/A signal (BPSK modulation) over one code period. . . . .	20
2.11	Generalized open-loop tracking architecture (adapted from [5]) . . . . .	22
2.12	Sketch of the IPT for ground-based scenarios [6]. The total measured power $P$ varies the evolution of the observed satellite elevation angle $\theta$ . $\phi_0$ is the phase of the LOS signal, and $\Delta\rho$ is the propagation path difference between the LOS and the reflected signal. . . . .	27
2.13	Definition of the elevation ( $\theta$ ) and azimuth ( $\phi$ ) angles in the selected frame of reference, and Cartesian projection of the steering vector $\mathbf{k}(\psi)$ . . . . .	28
2.14	Synthetic aperture concept: single antenna moving along the trajectory in the selected frame of reference. $\hat{\mathbf{r}}_\varphi(t)$ represents the unit vector in the direction of the satellite. . . . .	30
2.15	Example of DOA map computed with the Beamscan algorithm for a uniform circular aperture of 100 elements and a normalized radius of $4.72\lambda$ . The magnitude is has been normalized and, therefore, represented in arbitrary units (a.u.). . . . .	33
3.1	Scenario geometry depicting the propagation paths of the LOS (blue) and the specular reflection (red) signals. The values $\theta = 30^\circ$ and $h = 2$ m were used in this case as an example. . . . .	39
3.2	$\sqrt{\text{CRB}(h)}$ as a function of the front end's bandwidth for the different GNSS signals considered. Computed from the inverse of Eq. (3.30). Vertical dashed lines represent the $B_{Tx}/2$ (one-sided bandwidth) for each signals. . . . .	48

## List of Figures

---

3.3	$\sqrt{\text{CRB}(h)}$ as a function of $\Delta\rho$ computed by numerical evaluation of Eq. (3.30)'s inverse. $B_{fe}$ is the bandwidth of the receiver's front end assumed for each signal, set to match the signal bandwidth, i.e., $B_{Tx}/2$ (see Table 2.1). The two vertical lines represent the chip lengths: 293.25 m, of the GPS L1 CA and Galileo E1 BC signals; and 29.32 m, of the GPS L5 and Galileo E5 signals. The CRB values for the flat regions can be computed using (3.32) . . . . .	50
3.4	$\sqrt{\text{CRB}(h)}$ for different $ \Gamma ^2$ and $\Delta\rho$ values. Computed by numerical evaluation of Eq. (3.30). Red lines are used to represent the level curves, each one labeled with its corresponding value of $\sqrt{\text{CRB}(h)}$ (in m). $B_{fe}$ represents the assumed front end's one-sided 3-dB bandwidth. . . . .	52
3.5	Leica GNSS AR25 antenna's gain as a function of the angle to the boresight for RHCP and LHCP at L1 carrier frequency . . . . .	55
3.6	$\sqrt{\text{CRB}(h)}$ for different $\Delta\theta$ 's (vertical axis), starting from an initial elevation of $10^\circ$ , and true receiver heights $h$ (horizontal axis). Computed by numerically evaluating the inverse of Eq. (3.47). Black lines represent the level curves for the values labeled on top of them. . . . .	56
3.7	$\sqrt{\text{CRB}}$ for different $\Delta\theta$ starting from an initial $\theta_0 = 10^\circ$ . Computed by numerically evaluating the inverse of Eq. (3.47). . . . .	57
3.8	Accumulated area within the first Fresnel zone for $h = 3$ m with the variation of $\theta$ . Right axis shows the displacement of the specular reflection point from its initial location when $\theta = 10^\circ$ . . . . .	58
3.9	Mean value of the magnitude of DFT( $J_{\text{SML}}(h)$ ) for $\Delta\theta_1 = [10^\circ, 13^\circ]$ , with $d_h(\Delta\theta_1) = 0.47$ m, and $\Delta\theta_2 = [20^\circ, 23^\circ]$ , with $d_h(\Delta\theta_2) = 0.26$ m; and two surfaces: "Dry Surface" (DS): $\epsilon_{\text{DS}} = 4 - j1.14$ , and "Sea Water" (SW): $\epsilon_{\text{SW}} = 20 - j45.69$ . . . . .	63
3.10	(Top) Example of $J_{\text{SML}}(h)$ evaluated for $h = [0, 7]$ m. (Bottom) Magnified version around the global minimum of $J_{\text{SML}}(h)$ (dashed green rectangle). Dashed-red and dashed-blue lines are used for the subspaces' bounds computed by the SML. . . . .	65
3.11	RMSE of the MLE computed using the SML compared with the $\sqrt{\text{CRB}}$ for the joint estimation of $\beta$ for different elevation spans $\Delta\rho$ starting at $\theta_0 = 15^\circ$ . . . . .	66
4.1	Additional propagation path $\Delta\rho(t)$ within the defined frame of reference . . . . .	71
4.2	Construction of the transmitter and receiver spherical basis vectors to compute polarization mismatch coefficient ([7] - "Polarized Fields" entry). . . . .	73
4.3	Polarization mismatch coefficient as a function of the signal's DOA for the RHCP signal - RHCP receiving antenna case. Antenna boresight tilted $45^\circ$ with respect to the vertical ( $z$ ) axis. (a) Power losses due to the mismatch. (b) Induced carrier frequency shift. . . . .	73
4.4	CRB Scenario I geometry: Antenna mounted on a rotating arm . . . . .	78
4.5	$\sqrt{\text{CRB}}$ of $\theta$ (a), and $\phi$ (b) in Scenario I, for different true values of $\theta$ and normalized trajectory radius $r$ . Blue contours represent level curves. . . . .	80
4.6	$\sqrt{\text{CRB}}$ of $\theta$ (a), and $\phi$ (b) in Scenario II, for different true values of $\theta$ and antenna boresight elevations $\theta_{ant}$ . Red contours represent level curves. Axes are exchanged from (a) to (b) for clarity. . . . .	81
4.7	CRB vs MLE's standard deviation for CRB Scenario I -(a), (b)-, and CRB Scenario II -(c), (d)-. . . . .	84
4.8	Proposed tracking architecture (single channel) supporting SA processing. Newly introduced blocks specific to SA are depicted with gray background. . . . .	85

4.9	SA tracking architecture (single channel) in a closed-loop scheme. This architecture implements an auxiliary tracking channel to generate “beamformed” code delay estimates. Blocks depicted with gray background are specific to SA processing. . . . .	86
4.10	Comparison of the reference carrier frequency estimation methods described in [8]. . . . .	91
4.11	Proposed SA open-loop beamforming scheme flow diagram . . . . .	92
4.12	Beamformed CAFs for 3 different cases using Delay-and-sum . . . . .	95
4.13	Simulation test bench diagram . . . . .	101
4.14	Skyplot for the scenario simulated using the Spirent GSS8800 simulating the a receiver located at the position: 46° 59' 52.73" N, 6° 56' 44.83" E; at time 14h41 UTC+1 on 28/11/2016. . . . .	102
4.15	Radius effect on the DOA map when using the Beamscan algorithm (PRN 3) . . . . .	103
4.16	DOA maps computed using adaptive algorithms (PRN 3) . . . . .	103
4.17	Multipath effect on DOA estimation for PRN 23. Synthetic signal. The DOAs for the two peaks in the 3 subfigures are the same, but it has been represented only once on (a). Red font is used for the multipath DOA estimates. . . . .	104
4.18	Elevation estimation using Beamscan algorithm during 80 s, for different coherent multipath power values, defined with respect to the LOS signal power, i.e., from -3 dB to -9 dB of attenuation. . . . .	105
4.19	Estimated reference Doppler for (a) PRN 22, and (b) PRN 23. Synthetic signal. For each method, the beginning of the line marks the first estimation. . . . .	106
4.20	DOA map for PRN 23 with reference frequency compensated using EKF1 method. Synthetic signal. . . . .	107
4.21	DOA map peak’s projections in azimuth (top) and elevation (bottom) for PRN 23, using different reference frequency compensation methods. Synthetic signal. . . . .	107
4.22	Code delay error over time for the tracking of PRN 23’s signal in the presence of multipath from $t = 70$ s. . . . .	108
4.23	Navigation Solution Comparison in Simulated Scenario. ENU coordinates with respect to the true position. . . . .	109
4.24	DOA map computed with Open-Loop version of the Beamscan algorithm for PRN 23 in the presence of coherent multipath with an additional delay of 0.15 chips. Doppler rate of $-0.26 \text{ Hz}^2$ . Synthetic signal. . . . .	110
4.25	Accumulated and Beamformed CAFs, respectively, for the static receiver and for the SA Open-Loop receiver. Coherent multipath component with additional delay of 0.5 chips. Synthetic signal. . . . .	111
4.26	Normalized ACF over time, obtained from the accumulated CAF and the beamformed CAF, respectively, for the static receiver and the SA tracking architecture. . . . .	112
4.27	Average ACFs over 6 s in the presence of coherent multipath. Synthetic Signal. . . . .	113
4.28	Experimental setup for the antenna mounted on the rotating arm . . . . .	114
4.29	Skyplot for the two data collection sites considered when the signal recording took place. . . . .	114
4.30	Experimental sites where the rotating arm was deployed for the recording of real GPS L1 signal. . . . .	115
4.31	DOA estimation for PRN 7 with measurements from Microcity Rooftop Scenario. The DOAs for the peaks in the 3 subfigures are the same, but it has been represented only once on (a). . . . .	117
4.32	DOA map computed using Beamscan for PRN 23 in MC 3rd Floor Terrace Scenario. . . . .	119

## List of Figures

---

4.33	DOA map computed using Beamscan for PRN 19 in MC 3rd Floor Terrace Scenario. . . . .	119
4.34	Single specular reflection hypothesis to explain the main secondary peak in the DOA map for PRN 19. . . . .	120
4.35	DOA map computed using MPDR-Capon for PRN 19 in MC 3rd Floor Terrace Scenario. . . . .	121
4.36	DOA map computed using Beamscan for PRN 17 in MC 3rd Floor Terrace Scenario. . . . .	121
4.37	Estimated reference carrier frequency for the MC Rooftop scenario. For each method, the beginning of the line marks the first estimation. . . . .	122
4.38	DOA maps computed for the MC Rooftop scenario, starting at the instant $t = 52$ s. (a) PRN 23 and linear interpolation; (b) PRN 23 and EKF1; (c) PRN 7 and linear interpolation; and (d) PRN 7 with EKF2. . . . .	123
4.39	DOA map peak's projections in azimuth (top) and elevation (bottom) for PRN 23 for the signal recorded at the MC Rooftop site, starting at $t_1 = 62$ s, using different reference carrier estimation methods. . . . .	124
4.40	DOA map peak's projections in azimuth (top) and elevation (bottom) for PRN 23 for the signal recorded at the MC Rooftop site, starting at $t_2 = 52$ s, using different reference carrier estimation methods. . . . .	124
4.41	Elevation error for PRN 23, using the Beamscan algorithm, for the different reference carrier estimation methods. MC Rooftop site. . . . .	125
4.42	Elevation error for PRN 7, using the Beamscan algorithm, for the different reference carrier estimation methods. MC Rooftop site. . . . .	125
4.43	Estimated antenna rotation speed using PRN 23 and PRN 7 signals in the MC Rooftop scenario. . . . .	126
4.44	Estimated reference carrier for PRN 19 for the MC 3rd Floor Terrace scenario. Magnified view from $t = 26.7$ s to $t = 33.2$ s. . . . .	126
4.45	Error comparison over time: static receiver versus rotating antenna with SA tracking architecture. . . . .	128
4.46	2D navigation solutions using the static antenna signal versus the rotating antenna signal with the proposed SA tracking architecture at the MC 3rd Floor Terrace site. The yellow push pins represent the average positions. . . . .	129
4.47	Beamformed CAFs at $t = 3$ s. MC 3rd Floor Terrace scenario. . . . .	130
4.48	Normalized ACF over time, obtained from the beamformed CAF. MC 3rd Floor Terrace scenario. . . . .	130
4.49	Average ACFs over 6 s for signals recorded in MC 3rd Floor Terrace Scenario. . . . .	131



# List of Tables

2.1	GNSS signal characteristics considered [3, 9, 10]. $f_c$ is the signal's carrier frequency; $f_{chip}$ the modulation's primary code chip rate; and $B_{Tx}$ the considered transmitted signal bandwidth. $B_{Tx}$ has been selected to be equal to the receiver's reference bandwidth, defined in the corresponding Interface Control Documents for each signal. The specs for GPS signals correspond to the Block III satellite vehicles. . . . .	12
4.1	Tuning parameters selected in the system noise description for the the EKF1 case. . . . .	99
4.2	Tuning parameters selected in the system noise description for the the EKF2 case. . . . .	100
4.3	Tracking channel settings for reference carrier frequency estimation methods comparison. $d$ is the Early-Late correlator spacing. $B_{(D/P/F)LL}$ represent the filter bandwidth. . . . .	106
4.4	Experimental sites selected where the rotating antenna was deployed to record GPS L1 signal. . . . .	116
4.5	RMSE of the LOS signal elevation estimate ( $\hat{\theta}$ ) for PRNs 23 and 7, obtained using the Beamscan DOA estimaton algorithm after removing the reference carrier frequency with the different methods considered. MC Rooftop site. . .	125
4.6	Code and carrier tracking settings used in the receiver at the MC 3rd Floor Terrace Scenario when comparing navigation solutions. Main and Auxiliary tracking channels (bold) are part of the SA tracking architecture processing the signal from the rotating antenna. . . . .	127
4.7	RMSE and standard deviation comparison between the navigation solutions.	127



# Notation

Bold-face, lower-case letters refer to column vectors and bold-face, capital letters refer to matrices.

$f(x) _{x=u}$	Function $f(x)$ evaluated at $x = u$
$ x $	Absolute value of scalar $x$
$\ \mathbf{x}\ $	$\ell^2$ -norm of vector $\mathbf{x}$ , defined as $(\mathbf{x}^H \mathbf{x})^{\frac{1}{2}}$
$[\mathbf{X}]_{rc}$	Element of the matrix $\mathbf{X}$ located in row $r$ and column $c$
$\text{Tr}\{\mathbf{X}\}$	Trace of $n \times n$ square matrix $\mathbf{X}$ . $\text{Tr}\{\mathbf{X}\} = \sum_{i=1}^n [\mathbf{X}]_{ii}$
$\det(\mathbf{X})$	Determinant of matrix $\mathbf{X}$
$\text{diag}\{\mathbf{x}\}$	Diagonal matrix whose diagonal entries are defined by $\mathbf{x}$
$(\cdot)^*$	Complex conjugate
$(\cdot)^T$	Matrix or vector transpose
$(\cdot)^H$	Matrix or vector conjugate transpose
$\mathbf{I}_n$	Identity matrix. Subscript $n$ indicates the dimension
$\odot$	Schur-Hadamard (elementwise) product of two matrices
$\otimes$	Kronecker product of two matrices. If $\mathbf{A}$ is $m \times n$ , then
	$\mathbf{A} \otimes \mathbf{B} = \begin{pmatrix} [\mathbf{A}]_{11} \mathbf{B} & \cdots & [\mathbf{A}]_{1n} \mathbf{B} \\ \vdots & & \vdots \\ [\mathbf{A}]_{m1} \mathbf{B} & \cdots & [\mathbf{A}]_{mn} \mathbf{B} \end{pmatrix}.$
$(\mathcal{C}) \mathcal{N}(\boldsymbol{\mu}, \boldsymbol{\Sigma})$	Multivariate (complex) Gaussian distribution of mean $\boldsymbol{\mu}$ and covariance matrix $\boldsymbol{\Sigma}$
$\mathbb{E}\{\cdot\}$	Statistical expectation
$\Re\{\cdot\}, \Im\{\cdot\}$	Real and imaginary parts, respectively
$\delta(t)$	Dirac delta function
$\frac{\partial f(\mathbf{x})}{\partial x_i}$	Partial derivative of function $f(\mathbf{x})$ with respect to variable $x_i$
$\frac{\partial f(\mathbf{x})}{\partial \mathbf{x}}$	Partial derivative of function $f(\mathbf{x})$ with respect to vector $\mathbf{x}$
$\frac{\partial^2 f(\mathbf{x})}{\partial \mathbf{x}^2}$	Hessian matrix of function $f(\mathbf{x})$
$f'(x_0), f''(x_0)$	First and second order derivatives of $f(x)$ evaluated at $x_0$
$\mathcal{F}\{\cdot\}, \mathcal{F}^{-1}\{\cdot\}$	Discrete Fourier Transform (DFT) and its inverse



# Acronyms

<b>ACF</b>	Autocorrelation Function
<b>ADC</b>	Analog-to-Digital Converter
<b>AltBOC</b>	Alternative Binary Offset Carrier
<b>BOC</b>	Binary Offset Carrier
<b>BPSK</b>	Binary Phase-Shift Keying
<b>CBOC</b>	Composite Binary Offset Carrier
<b>CDMA</b>	Code Division Multiple Access
<b>CRB</b>	Cramér-Rao Bound
<b>CS</b>	Commercial Service
<b>CWGN</b>	Complex White Gaussian Noise
<b>DFT</b>	Discrete Fourier Transform
<b>DLL</b>	Delay-Locked Loop
<b>DOA</b>	Direction Of Arrival
<b>DSSS</b>	Direct Sequence Spread Spectrum
<b>EKF</b>	Extended Kalman Filter
<b>FIM</b>	Fisher Information Matrix
<b>FLL</b>	Frequency-Locked Loop
<b>GLONASS</b>	Globalnaya Navigatsionnaya Sputnikovaya Sistema
<b>GNSS</b>	Global Navigation Satellite System(s)
<b>GNSS-MR</b>	GNSS Multipath Reflectometry
<b>GNSS-R</b>	GNSS-Reflectometry
<b>GO</b>	Geometric Optics
<b>GPS</b>	Global Positioning System
<b>I</b>	In-phase
<b>IF</b>	Intermediate Frequency
<b>IMU</b>	Inertial Measurement Unit
<b>IPT</b>	Interference Pattern Technique
<b>KA</b>	Kirchhoff Approximation
<b>LHCP</b>	Left-Hand Circular Polarization
<b>LNA</b>	Low-Noise Amplifier
<b>LO</b>	Local Oscillator
<b>LOS</b>	Line-Of-Sight
<b>MEO</b>	Medium Earth Orbit
<b>MLE</b>	Maximum Likelihood Estimator
<b>MSE</b>	Mean Square Error
<b>MUSIC</b>	MUltiple SIgnal Classification (algorithm)
<b>NAVIC</b>	Navigation with Indian Constellation
<b>NCO</b>	Numerically Controlled Oscillator
<b>OCXO</b>	Oven-Controlled Crystal Oscillator
<b>OS</b>	Open Service
<b>PDF</b>	Probability Density Function

## Acronyms

---

<b>PLL</b>	Phase-Locked Loop
<b>PRN</b>	Pseudo-Random Noise
<b>PRS</b>	Public Regulated Service
<b>PSD</b>	Power Spectral Density
<b>PSK</b>	Phase-Shift Keying
<b>PVT</b>	Position, Velocity and Timing
<b>Q</b>	Quadrature
<b>QPSK</b>	Quadrature Phase-Shift Keying
<b>QZSS</b>	Quasi-Zenith Satellite System
<b>RF</b>	Radio Frequency
<b>RHCP</b>	Right-Hand Circular Polarization
<b>RMSE</b>	Root-Mean-Square Error
<b>SA</b>	Synthetic Aperture
<b>SAR</b>	Search And Rescue
<b>SDR</b>	Software-Defined Radio
<b>SML</b>	Segmented Maximum-Likelihood
<b>SNR</b>	Signal-to-Noise Ratio
<b>SoL</b>	Safety-of-Life
<b>TOA</b>	Time-Of-Arrival
<b>UAV</b>	Unmanned Air Vehicles
<b>UCA</b>	Uniform Circular Array
<b>UTC</b>	Coordinated Universal Time
<b>Z-L</b>	Zavorotny-Larson (model)
<b>Z-V</b>	Zavorotny-Voronovich (model)

# Chapter 1

## Introduction

### 1.1 Background and Motivation

The progress experienced by the Global Navigation Satellite Systems (GNSS) during the last decades has been astounding. GNSS usage has become nearly ubiquitous, providing accurate three-dimensional position, velocity, and timing (PVT) information to users virtually for free, requiring only a device capable of receiving and processing GNSS signals. The consumer electronics race for cheaper and more powerful devices to satisfy the mass-market has allowed the embedding of GNSS receivers in almost every modern smartphone. It is rare to find someone who has not used the PVT service, directly or indirectly, provided by a single or multiple GNSS to navigate or synchronize some electronic device. Besides, GNSS provides accurate timing to critical services and terrestrial infrastructures, including, e.g., banking and financial services, telecommunications networks and energy distribution grids.

Two decades ago, two GNSS were already operational: the U.S.' Navstar – Global Positioning System (GPS) and the Russian's Globalnaya Navigatsionnaya Sputnikovaya Sistema (GLONASS). Today, GPS and GLONASS are being modernized and two new GNSS are currently being deployed: the European Galileo and the Chinese BeiDou. One regional navigation system, the Navigation with Indian Constellation (NAVIC), is also fully operational and another one, the Japanese Quasi-Zenith Satellite System (QZSS) is being deployed. Altogether, these systems will soon provide more than 130 GNSS transmitters globally distributed [11, 12]. The first GNSS were developed for receivers operating outdoors, preferably with line-of-sight (LOS) signal visibility conditions. Nonetheless, extensive research has been conducted to allow the operation of GNSS receivers in more environments: indoors, under very weak signal conditions [13–15], in urban environments [16–19], and even in space [20, 21].

In many of these environments, the signals reflected and scattered from different surfaces impinging the antenna will interfere with the LOS signal, causing a degradation on the receiver's time-of-arrival (TOA) estimation accuracy. Those interfering signals are known as multipath interference or simply as multipath. The advent of new technologies heavily relying on GNSS positioning, such as unmanned air vehicles (UAVs), or autonomous cars, which are required to operate under potentially severe multipath conditions, are just fostering the need for more efficient techniques to mitigate the effect of multipath.

Lots of research work have already discussed the multipath mitigation problem (e.g.

[22, 23]). Among all the proposed strategies, the use of antenna arrays to implement spatial filtering techniques is considered the most effective. Intuitively, this makes sense because it is highly improbable that the LOS signal and any multipath interference will impinge on the receiver’s antenna from the same angle, therefore, they will have a different direction of arrival (DOA). Unfortunately, traditional arrays are bulky –due to the carrier wavelength of the different GNSS–, require careful calibration, and a more complex receiver hardware. If the spatial processing is done digitally, the receiver requires multiple synchronized RF channels, which substantially increase the complexity of the required hardware and the needed computational power.

However, it is good to remember that “one man’s noise is another man’s signal.” Some initially unforeseen applications of GNSS –beyond PVT– have emerged enhanced by a large number of signals visible at any given time. In particular, GNSS signals have been successfully used as signals of opportunity for remote sensing the atmosphere (GNSS Radio Occultation) or the Earth’s surface (GNSS-Reflectometry). In GNSS-Reflectometry (GNSS-R), modified GNSS receivers are used as passive bistatic or multi-static radars [11]. The NASA Cyclone GNSS (CYGNSS) mission successfully launched a constellation of eight micro-satellites into low earth orbit with onboard GNSS-R instruments to measure wind speeds over the ocean [24, 25]. GNSS signals, transmitted in the L band, are barely attenuated by clouds or rain, which allow them to peer into hurricanes and provide more accurate wind speed measurements. These measurements can significantly improve the hurricane landfall strength predictions.

The time series of signal strength –in the form of carrier-to-noise ratio estimates– measurements recorded by ground-based geodetic GNSS receivers can be used to sense the site’s environment. Specular multipath from satellites observed with low elevation angles will interfere with the line-of-sight signal at the antenna. This multipath will cause a periodic fading or an “interference pattern” on the estimated signal strength. By analyzing this interference pattern, it is possible to retrieve the ground soil moisture, to detect and measure any snow content, or, if the reflection surface is water, measure any water-level change. Any data processing technique used to estimate some of these geophysical magnitudes from the observed interference pattern is generically called Interference Pattern Technique (IPT) [26–28], or GNSS Multipath Reflectometry (GNSS-MR) [29–32]. With little cost or modification, data from many geodetic GNSS receivers can be processed to create meaningful –and constantly updated– datasets for environmental scientists.

The two GNSS-R applications briefly described below, are an example of the GNSS-R techniques’ potential in Earth observation. However, even though the GNSS-R concept was proposed in the early 1990s, only a few works have tried to characterize the theoretical precision limits of GNSS-R techniques, e.g., [6, 33–38]. Moreover, a gap exists for techniques processing data gathered over long –more than a few seconds– observation times, such as the IPT.

Theoretical bounds on the variance or the mean square error (MSE) of estimators are a handy tool to characterize the precision limits when trying to retrieve some parameters from noisy measurements. With a sufficiently good model for the observed measurements, these theoretical bounds explain the estimation precision’s dependency on the current scenario conditions. Besides, they are commonly used to easy benchmark and compare different estimation techniques. Such bounds have been studied for delay, Doppler-shift and direction-of-arrival (DOA) estimation, in the context of GNSS. Unfortunately, only a few works have tried to extend these bounds to GNSS-R estimators, or to DOA estimators based on the antenna motion.



## 1.2 Contributions

This thesis summarizes a set of contributions for the estimation of the multipath experienced by GNSS receivers. These contributions are classified into two groups.

The first group focuses on the estimation of specular multipath’s complex amplitude, and phase parameters, in the context of GNSS-R. These parameters can be used to infer some geophysical parameters of the reflecting surface. These contributions include:

- The derivation of estimation bounds for the receiver’s height and the electrical properties of the reflecting surface by making use of the Cramér-Rao bound (CRB). We concentrated to scenarios where the receiver is static, ground-based and has a single antenna, and a single specular –and therefore, coherent– reflection is dominant. The CRB expressions are derived for short observation times and then extended for observation times up to hundreds of seconds. This CRB for long observation times provides a benchmark on some GNSS-R techniques using the carrier phase information, such as the IPT. The CRB proposed is valid for any GNSS signal, and we study its behavior with GPS and Galileo signals, as a function of the receiver’s bandwidth, and the actual surface’s reflection coefficient and receiver’s height.
- An algorithm to compute the maximum-likelihood estimator (MLE) of the receiver’s height and the electrical properties of the reflecting surface for IPT-like techniques –given a model for the surface’s reflection coefficient– in a computationally efficient way. We have called it: the Segmented maximum-likelihood (SML) algorithm. With the parameters and scenarios considered, the MLE does not have a closed-form expression. Therefore, computing the MLE turns into a multivariable optimization problem that must be addressed by resorting to iterative optimization algorithms. The SML transforms a difficult optimization problem into several simpler –and almost convex– ones by taking advantage of some properties of the cost function specific to this problem. This transformation is achieved by “segmenting” the considered parameter-optimization search space.

The second group of contributions –departing from GNSS-R– is related to the DOA estimation of classical multipath interference and its mitigation by using spatial filtering techniques implemented with synthetic aperture (SA) processing. The main contributions within this group include:

- The derivation of the CRB of the DOA parameters of GNSS signals in the synthetic aperture processing context. The obtained CRB characterizes the best possible precision in the signal’s DOA estimation given any known antenna motion, and with any GNSS signal. The effects of the complex antenna gain have been included within the signal model used to derive the CRB. We use this CRB for two simulation scenarios considering different antenna motions: one simulates an antenna mounted on one end of a rotating arm, while the other simulates a spinning antenna with its boresight slightly tilted from the spinning axis. The proposed CRB is validated using the asymptotic properties of the MLE.
- A signal tracking architecture integrating synthetic aperture processing techniques –both DOA estimation and beamforming–. This architecture is generic enough to support any spatial filtering technique that can be adapted to SA processing.

- Two techniques, named EKF1 and EKF2, to sequentially compensate the phase contribution to the observed carrier phase that would not be already observed by a static receiver. Both EKF1 and EKF2 are based on an extended Kalman filter (EKF), assisting the existing carrier tracking loop in the case of EKF1, and ultimately replacing it in the case of EKF2. The carrier phase compensation is required before attempting any SA processing to prevent biases and distortion in the DOA estimates or on the synthesized antenna pattern.
- An open-loop implementation of the proposed SA tracking architecture, in which SA processing is combined with batch processing of the received signal to increase tracking robustness.
- Validation of the SA tracking architecture with simulated and real recorded GPS L1 C/A signals. The real signal was recorded from an antenna mounted on a mechanical rotating arm that we built to implement uniform circular antenna motions in practice. Experimental results show that the proposed SA tracking architecture can mitigate the bias introduced by multipath interference in the position calculated by the receiver.

Part of the materials presented in this thesis have been the subject of various publications:

### Journals

- M. A. Ribot, C. Botteron, and P.-A. Farine, “Derivation of the Cramér-Rao Bound in the GNSS-Reflectometry Context for Static, Ground-Based Receivers in Scenarios with Coherent Reflection,” *MDPI Sensors* (Switzerland), vol. 16, no. 12, p. 2063, Dec. 2016.
- M. A. Ribot, J. C. Kucwaj, C. Botteron, S. Reboul, G. Stienne, J. Leclère, J. B. Choquel, P. A. Farine, and M. Benjelloun, “Normalized GNSS interference pattern technique for altimetry,” *MDPI Sensors* (Switzerland), vol. 14, no. 6, pp. 10234–10257, 2014.

### Conferences

- M. A. Ribot, J. Cabeza, P. Closas, C. Botteron, P.-A. Farine. “Estimation Bounds for GNSS Synthetic Aperture Techniques,” in *2017 IEEE 7th International Workshop on Computational Advances in Multi-Sensor Adaptive Processing (CAMSAP)*, Curaçao, Dutch Antilles, 2017. (Accepted)
- M. A. Ribot, J. Cabeza, P. Closas, C. Botteron, F. Valdés, B. Alorda, and P.-A. Farine. “Carrier Tracking using Extended Kalman Filters for GNSS Synthetic Aperture Processing with a Rotating Antenna,” in *30th International Technical Meeting of the Satellite Division of the Institute of Navigation, ION GNSS+ 2017*, Portland, USA, 2017.
- M. A. Ribot, J. Cabeza, C. Botteron, F. Valdés, B. Alorda, and P.-A. Farine, “GNSS Multipath Estimation and Mitigation Using a Rotating Antenna,” in *Proceedings of the European Navigation Conference 2017*, Lausanne, Switzerland, 2017.
- M. A. Ribot Sanfeliu, C. Botteron, and P.-A. Farine, “A New Estimation Algorithm for the GNSS-R Interference Pattern Technique: The Segmented Maximum-Likelihood,” in *Proceedings of the 28th International Technical Meeting of The Satellite Division of the Institute of Navigation (ION GNSS+ 2015)*, Tampa, USA, 2015.

- J. C. Kucwaj, M. A. Ribot, G. Stienne, C. Botteron, S. Reboul, J. B. Choquel, P. A. Farine, and M. Benjelloun, “Calibration of the GNSS signal amplitudes in the Interference Pattern Technique for altimetry,” in *International Radar Conference, Radar 2014*, Lille, France, 2014.
- S. Reboul, C. Botteron, M. A. Ribot, G. Stienne, and J. Leclère, “Normalized GNSS Interference Pattern Technique,” in *URSI Commission F Microwave Signatures 2013 - Specialist Symposium on Microwave Remote Sensing of the Earth, Oceans, and Atmosphere*, Espoo, Finland, 2013.

### 1.3 Thesis Outline

This dissertation is structured in five chapters, which combine review material and original contributions. We expect it to be of interest for two kinds of audience: those working on GNSS-Reflectometry, with interest in its theoretical estimation bounds, and those working on GNSS signal processing and GNSS receiver design, particularly interested in array processing and synthetic aperture.

In this dissertation, we describe the carried out research as accurately as possible so that it could be reproduced, or utilized as a starting point for future research in the same direction. Interested readers are encouraged to review the references included –especially those in the first chapter–, which were carefully selected to help the reader get an updated and comprehensive picture of the discussed topics. This section is meant to be a guide to the reader by providing an overview of the document structure.

The thesis has begun with the current **Chapter 1**, which has introduced the background, principal motivations and a general overview of the scope of the thesis. The chapter also summarizes the main contributions of this dissertation.

**Chapter 2** intends to provide the reader with the essential background to understand the rest of the chapters. The chapter provides a general description of GPS, Galileo, and the set of signals considered within this thesis. It continues with a brief description of the GNSS receiver baseband processing chain, focusing on the RF front end, and the signal acquisition and tracking stages. The open-loop tracking architecture is described, as an alternative to the conventional closed-loop tracking. The chapter continues by introducing the GNSS-R concept, and an overview of its state-of-the-art techniques, with particular attention to the IPT. Then, the same is done for synthetic aperture processing with GNSS signals. The chapter finishes by presenting the Cramér-Rao bound, which is a statistical tool extensively utilized in the rest of the thesis.

Chapters 3 and 4 are the core chapters of this thesis. Both follow the same structure: first, we study some estimation precision bounds by computing the CRB in the scenarios of interest, and then, some estimation techniques are introduced, discussed and validated in simulations and with real recorded signals (only GPS L1 C/A).

Following the mentioned structure, **Chapter 3** starts with the derivation of the CRB of the receiver’s height and the surface reflection coefficient –or the parameters of which it is a function of– considering as practical examples the GPS L1 C/A and L5 signals, as well as for Galileo E1 BC and E5 signals. The signal model for the output of the RF front end is particularized for the specular reflection scenario, given a ground-based static receiver with a single antenna. The CRB is studied as a function of receiver’s actual height, or equivalently,

## Chapter 1. Introduction

---

as a function of the propagation path difference between the LOS and the reflected signals. The impact over the CRB of the RF front end's bandwidth and the surface's reflection coefficient is also studied. Chapter 3 also show how to extend the computed CRB in a way that it becomes valid also for long observation times, i.e., as in the case of the IPT. The second half of this chapter introduces the SML algorithm to compute the maximum likelihood estimator of the receiver's height and the complex permittivity of the reflecting surface. The SML is validated with synthetic signal, and the results obtained are cross-validated with the CRB.

**Chapter 4** begins with the derivation of the Fisher information matrix (FIM) for a scenario in which the antenna is moving along a known trajectory, and the channel statistics are known. The chapter continues by studying the CRB – straightforwardly computed– for two different antenna motions. Then, a tracking architecture integrating SA processing within the receiver's baseband signal processing chain is presented. The proposed architecture can be implemented either as closed-loop or open-loop. The chapter continues by describing how to integrate open-loop tracking with simple SA processing. The second part of the chapter presents the results obtained when trying different DOA estimation and beamforming techniques with the proposed architecture: first with synthetic signal generated using a Spirent GSS8000 simulator, and then with real GPS signal recorded using an antenna mounted on a mechanical rotating arm. This rotating arm was deployed in two different sites, each of them with a different level of multipath interference.

Finally, **Chapter 5** closes this dissertation with a summary of the main findings, conclusions and future research directions arising from this work.

## Chapter 2

# GNSS-Reflectometry and Synthetic Aperture Processing: An Overview

This chapter starts by providing a general overview of the GNSS basics required to follow the rest of the dissertation. That includes an overall description of the GNSS working principle, the GPS and Galileo signals considered, and the generic architecture of a GNSS receiver. The open-loop tracking architecture is presented as well.

The chapter continues by introducing the reader to the GNSS-Reflectometry concept and its main applications. Besides, the current state of the art concerning the estimation precision of GNSS-R techniques is sketched. Particular emphasis is placed on the Interference Pattern Technique (IPT). The chapter follows by presenting the concept of synthetic aperture (SA) processing of GNSS signals. A summary of the research carried out to this date with receivers implementing SA processing techniques is presented.

Finally, the chapter concludes by introducing the Cramér-Rao bound, a powerful statistical tool used in the following chapters to compute the theoretical estimation limits of some GNSS-R and SA processing techniques.

### 2.1 GNSS Concept

The term Global Navigation Satellite Systems (GNSS) defines the collection of all satellite navigation systems and their augmentations [12].

A GNSS receiver can determine its position by measuring the distances –or pseudoranges– between itself and the satellites in view. These pseudoranges are obtained by multiplying the signal propagation speed with the estimated time that signals transmitted from each satellite take to reach the receiver, i.e., their propagation time. This method is known as time-of-arrival (TOA) ranging. GNSS satellites broadcast data that allows computing their positions very accurately within a common frame of reference. The receiver only needs to solve a trilateration problem to obtain its position, known as navigation solution. Figure

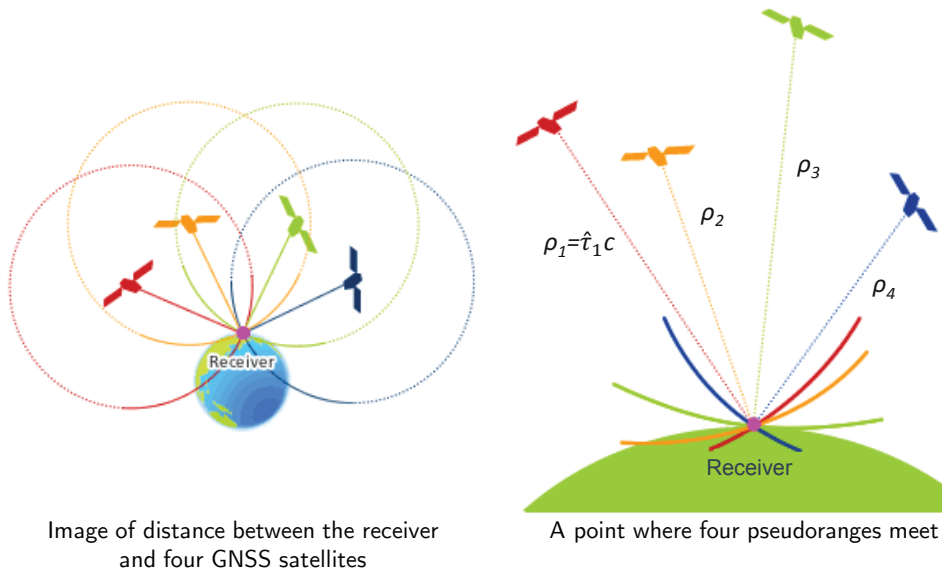


**Figure 2.1** – GNSS positioning concept. The pseudoranges  $\rho_i$  are computed as the product of the signals’ estimated TOA  $\hat{t}_i$ , times the propagation speed  $c$ .

2.1 illustrates this concept<sup>1</sup>. A minimum of four pseudoranges<sup>2</sup> is needed for the receiver to determine its three-dimensional position and a form of Coordinated Universal Time (UTC).

GNSS usage has become critical to several modern day services and infrastructures. With billions of receivers in operation, owning a GNSS has become a valuable strategic resource for any great power. Currently, the U.S.’ GPS and the Russian GLONASS are fully operational, while the European Galileo is at an early operational stage. The Chinese Compass/BeiDou is in the process of being deployed, and already operational in the Asia-Pacific region. Figure 2.2 depicts an overall view of all the operational and planned GNSS signals, their modulations, and their frequency spectrum, while Figure 2.3 shows orbits of the different GNSS.

We provide more details on GPS and Galileo in the sections below, while more details about the other GNSS, regional systems and augmentation systems can be found in [12, 13].

<sup>1</sup>Figure modified from original JAXA source: [http://global.jaxa.jp/countdown/f18/overview/gps\\_e.html](http://global.jaxa.jp/countdown/f18/overview/gps_e.html)

<sup>2</sup>Four pseudorange measurements are needed because the transmitters and the receiver do not share a perfectly synchronized time reference, i.e., the receiver’s clock is not synchronized with the satellites’ clock.

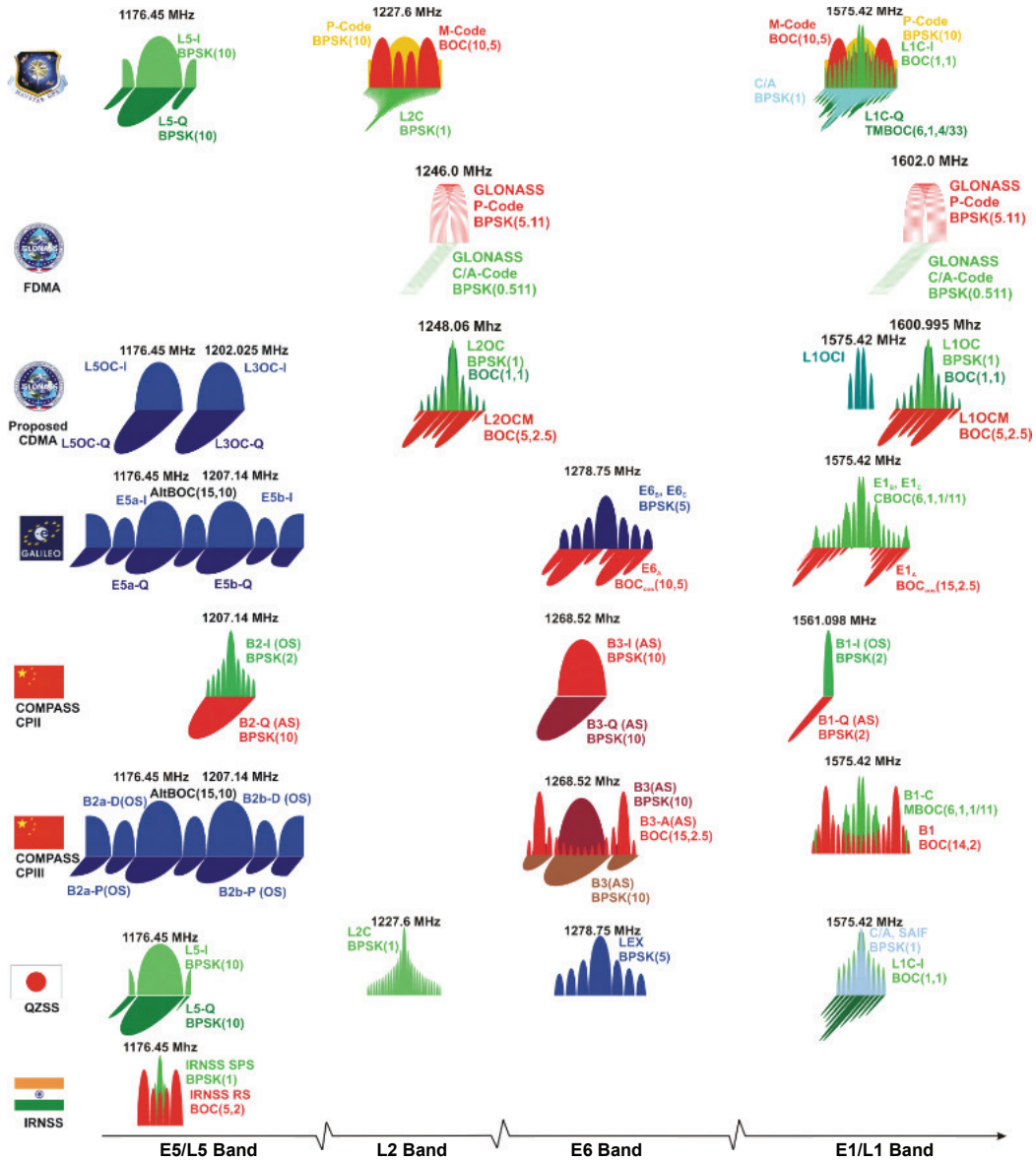


Figure 2.2 – Overview of current and planned GNSS signals: spectrum and modulations. Updated in 2011. [1]

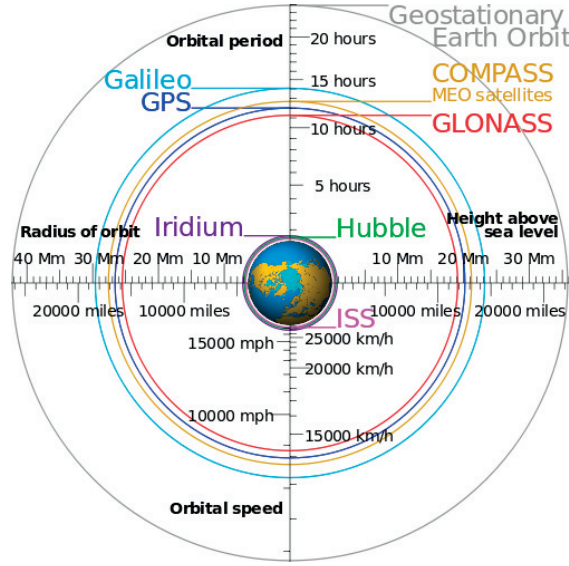


Figure 2.3 – Comparison of the different GNSS orbits (Credit: Cmglee, Ceo. Licensed under CC BY 3.0).

## 2.2 GPS and Galileo Signals

All the satellites within a GNSS constellation are synchronously broadcasting direct sequence spread spectrum (DSSS) signals. DSSS provides the structure for the transmission of ranging signals and essential navigation data, such as satellite ephemeris and satellite health status [12]. DSSS enables the use of Code Division Multiple Access (CDMA), which allows multiple satellites’ transmissions to share the same frequency band, as well as identifying each satellite signal by its specific quasi-orthogonal code. The ranging signals are generated as the product of pseudo-random noise (PRN) codes<sup>3</sup> and navigation data at much lower rate, both modulating the satellite carrier frequencies. The PRN codes are deterministic but have spectral properties similar to random binary sequences, including low autocorrelation for delays other than zero and low cross-correlation. The PRN codes are periodic and can be stored or efficiently and faithfully replicated at the GNSS receiver. For example, the GPS L1 C/A signal transmitted by each GPS satellite is generated using its unique PRN code of 1023 *chips*<sup>4</sup>, the code period is 1 ms, while the navigation data has a rate of 50 bps. Therefore it takes 20 PRN code periods to encode a data bit. Figure 2.4 exemplifies this concept.

The GNSS signals are transmitted using right-hand circular polarization (RHCP). The modulated (bandpass) signal transmitted by the  $p$ th satellite can be expressed as:

$$s_{T,p}(t) = \sqrt{2P_p} (s_{I,p}(t) \cos(2\pi f_c t) - s_{Q,p}(t) \sin(2\pi f_c t)), \quad (2.1)$$

where the subscript  $P_p$  represents the signal power and  $f_c$  the carrier frequency. The power-normalized complex enveloped (baseband equivalent) can be expressed as the sum of the in-phase (subscript  $I$ ) and quadrature (subscript  $Q$ ) components, i.e.,

$$s_p(t) = s_{I,p}(t) + js_{Q,p}(t), \quad (2.2)$$

<sup>3</sup>Also referred to as *spreading* codes.

<sup>4</sup>A *chip* is defined as the minimum time interval between possible transitions in the PRN waveform.



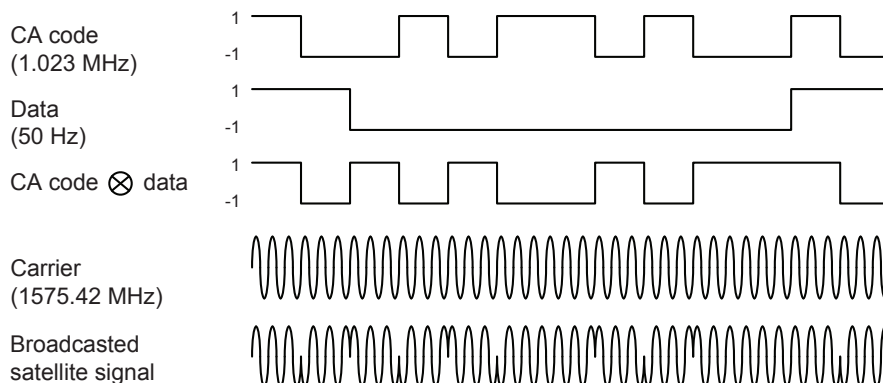


Figure 2.4 – Main components of the GPS L1 C/A signal [2]. The signals are not to scale .

such that

$$s_{T,p}(t) = \sqrt{2P_p} \Re \{ s_p(t) \exp \{ j2\pi f_c t \} \}. \quad (2.3)$$

The travel through the propagation channel will modify the transmitted signals. Indeed, multiple replicas of the same transmitted signal can reach the receiver's antenna due to multipath propagation. These replicas are generally caused by the reflection or the scattering of the direct signal (or line-of-sight (LOS) signal). In the reception scenarios considered in this thesis, this multipath fading channel with  $M$  propagation paths, can be modeled as a linear time-invariant system, which can be described by its (baseband equivalent) impulse response as:

$$h_p(t) = \sum_{m=0}^{M-1} \alpha_{p,m}(t) \exp \{ -j2\pi f_c \tau_{p,m}(t) \} \delta(t - \tau_{p,m}(t)). \quad (2.4)$$

The coefficients  $\alpha_{p,m}(t) \in \mathbb{C}$  represent the complex attenuation for each propagation path, while  $\tau_{p,m}(t)$  represent the time-delay at the instant  $t$ . The subscript  $m = 0$  is assigned to the LOS signal parameters. Depending on the channel assumptions,  $\alpha_{p,m}(t)$  can be statistically modeled as realizations of a random variable with a certain distribution [39, 40]. The time-delays  $\tau_{p,m}(t)$  are usually considered piecewise constant for short observation intervals. The exponential term in (2.4) is related to the Doppler effect on the carrier signal.

Therefore, for a total of  $P$  satellites in view, the signal at the receiver's antenna can be understood as the superposition of the signals transmitted through the multipath propagation channel, corrupted by some additive noise  $n(t)$ . This can be expressed as

$$\begin{aligned} x(t) &= \sum_{p=1}^P \sqrt{2P_p} (s_p(t) * h_m(t)) + n(t) \\ &= \sum_{p=1}^P \sqrt{2P_p} \sum_{m=0}^{M-1} \alpha_{m,p}(t) s_p(t - \tau_{m,p}(t)) \exp \{ -j2\pi f_c \tau_{m,p}(t) \} + n(t). \end{aligned} \quad (2.5)$$

Let us proceed by providing a brief overview of the GPS and Galileo systems, with particular emphasis placed on the description of the signals utilized in this thesis. The main features of these signals have been summarized in Table 2.1, while Figure 2.5 represents their

## Chapter 2. GNSS-R and SA Processing: An Overview

**Table 2.1** – GNSS signal characteristics considered [3, 9, 10].  $f_c$  is the signal’s carrier frequency;  $f_{chip}$  the modulation’s primary code chip rate; and  $B_{Tx}$  the considered transmitted signal bandwidth.  $B_{Tx}$  has been selected to be equal to the receiver’s reference bandwidth, defined in the corresponding Interface Control Documents for each signal. The specs for GPS signals correspond to the Block III satellite vehicles.

	GPS L1 C/A	GPS L5 I Q	Galileo E1 OS E1B E1C	Galileo E5 Full E5a E5b
Minimum received signal power (dBm)	-128.5	-124 -127 -127	-127 -130 -130	-122 -125 -125
$f_c$ (MHz)	1575.42	1176.45	1575.42	1191.795 1176.450 1207.140
Main Lobe BW (MHz)	2.046	20.46	14.322	51.15 20.46 20.46
$B_{Tx}$ (MHz)	30.69	24	24.55	51.15
Modulation	BPSK	QPSK	CBOC(6,1,1/11)	AltBOC(15,10) QPSK QPSK
$f_{chip}$ (MHz)	1.023	10.23	1.023	10.23
Primary code length (chips)	1023	10230	4092	10230
Primary code length (ms)	1	1	4	1
Secondary code chipping rate (chips/s)	-	1000	- 250	1000
Secondary code length (chips)	-	10 20	- 25	20 100 4 100
Secondary code length (ms)	-	10 20	- 100	20 100 4 100
Data rate (bps)	50	100 -	250 -	50 - 250 -

normalized autocorrelation functions (ACF), defined as:

$$R_{ss}(\tau) \triangleq \frac{\int_{\langle T \rangle} s(t)s^*(t-\tau) dt}{\int_{\langle T \rangle} |s(t)|^2 dt}, \quad (2.6)$$

and their power spectral densities, with the respective reference frequency bandwidths<sup>5</sup>.

### 2.2.1 GPS Signals

The U.S. GPS is, by far, the GNSS with the highest number of users. Since its inception for military applications in the 1970s, it has continually evolved, improving its accuracy, integrity, and availability [12]. Once fully deployed, the Galileo space segment will consist of 30 Medium Earth Orbit (MEO) satellites, including 6 spares, in a so-called Walker 24/3/1 constellation [41]. The satellites will be organized in 6 orbital planes with an approximate inclination of  $55^\circ$  with respect to Earth’s equator, with four satellites per plane. The system was designed to provide global coverage with a minimum of 4, and an average of 8, visible satellites at any time. The satellites’ orbital revolution period is approximately half a sidereal day, i.e., 11 hours and 58 minutes, so that they daily pass over the –almost– same locations. Their orbiting altitude is approximately 20200 km above the Earth’s surface.

<sup>5</sup>The receiver reference bandwidth is defined as the bandwidth for which losses due to receiver filtering are less than 0.5 dB.

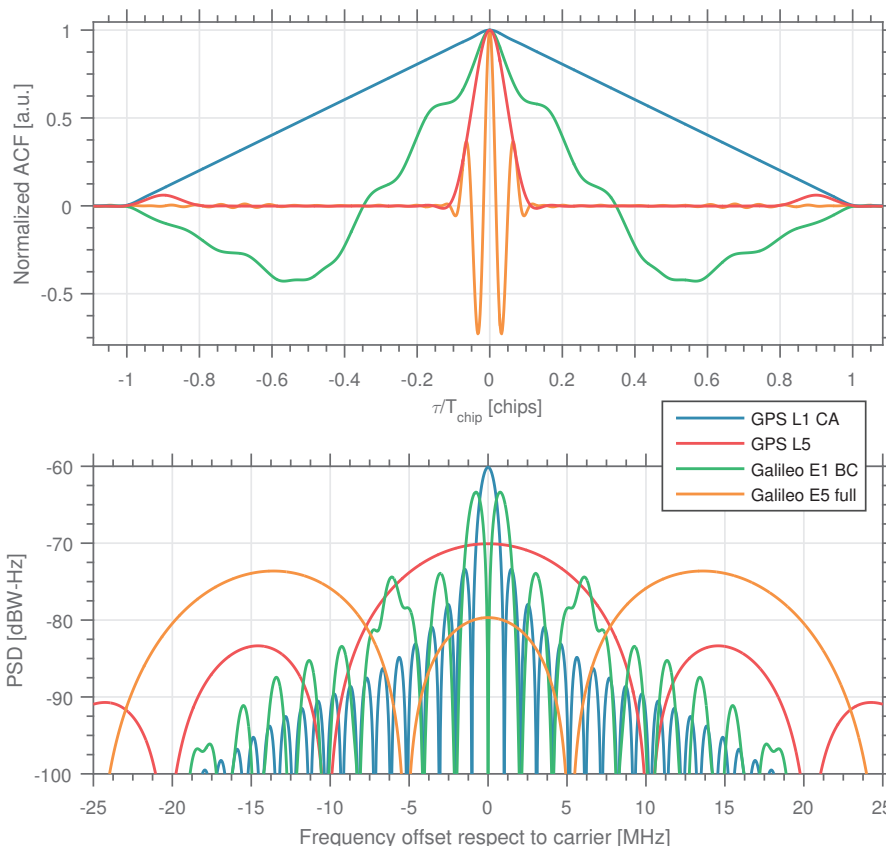


**Figure 2.5** – (Top) Normalized autocorrelation function of the transmitted GNSS signals considered (real part). The  $x$ -axis showing the delay  $\tau$  is normalized to  $T_c = (1.023 \times 10^6)^{-1}$  s. (Bottom) PSD of the signals. See Table 2.1 for more details.

GPS signals are transmitted in 3 different frequency bands, within the L-band of the radio spectrum. These three bands are referred to as L1, L2 and L5. Their nominal carrier frequencies are multiples of fundamental frequency  $f_0 = 10.23$  MHz, i.e.,

$$\begin{aligned} f_c(\text{L1}) &= 154 \cdot f_0 = 1575.42 \text{ MHz} \\ f_c(\text{L2}) &= 120 \cdot f_0 = 1227.60 \text{ MHz} \\ f_c(\text{L5}) &= 115 \cdot f_0 = 1176.45 \text{ MHz}. \end{aligned} \quad (2.7)$$

In this thesis we only consider L1 C/A and L5 signals. L1 C/A signal has reference receiver bandwidth of 30.69 MHz (Block III satellite vehicles), while L5 signal has 24 MHz [9, 10].

### L1 C/A Signal

The L1 carrier is currently modulated by two signals (or ranging codes), unique for each satellite: the Precise (P) code (in-phase) and the Coarse/Acquisition (C/A) code [9]. In this dissertation, we have considered only the C/A code, which is the ranging signal used in civilian receivers and has become the most widely used GNSS signal for mass-market applications. C/A codes are Gold codes [12] of 1 ms length at a chipping rate of 1.023 Mchips/s. The C/A code  $c_{CA}(t)$  is modulated by the navigation data sequence  $b_{CA}(t)$ , transmitted at 50 bps (20

ms of data bit period), i.e.,

$$s_{CA}(t) = b_{CA}(t) c_{CA}(t), \quad (2.8)$$

where  $s_{CA}(t)$  is the power-normalized C/A signal. We emphasize that the P code, in quadrature with the C/A code, was not simulated, and its effect on real GPS recordings disregarded.

## L5 Signal

The L5 signal is the third civilian GPS signal currently in operation –together with L1 C/A and L2C– and was transmitted for the first time on board of Block IIF satellites. L5 signal was designed to meet more demanding requirements for safety-of-life transportation (e.g., aviation) and other applications. Quadrature phase-shift keying (QPSK) is used by combining two synchronized signal components: L5I (in-phase) and L5Q (quadrature), each with different codes. L5I is modulated by a navigation message, while the L5Q signal is not (pilot channel) [10]. The power-normalized baseband equivalent of the L5 signal can be expressed as:

$$s_{L5}(t) = \frac{1}{\sqrt{2}} (b_{L5-I}(t) c_{L5-I}(t) + j c_{L5-Q}(t)), \quad (2.9)$$

where  $b_{L5-I}(t)$  represent the navigation data stream (at 50 bps), and  $c_{L5-I}(t)$  and  $c_{L5-Q}(t)$  are the L5 ranging signals. Each of these signal is binary phase-shift keying (BPSK) modulated by a primary code with a chipping rate of 10.23 Mchips/s with a code period of 1 ms. Secondary or “tiered” codes of different duration are overlaid to the primary code [12].

### 2.2.2 Galileo Signals

Galileo<sup>6</sup> is the European civilian GNSS intended for civilian and commercial use. Galileo aims to provide an independent high-precision positioning system so European nations do not need to rely exclusively on foreign GNSS, which could be degraded or disabled by their operators at any time. Galileo is intended to provide better positioning services at higher latitudes than other GNSS.

When completely deployed, the Galileo space segment will consist of a total of 30 Medium Earth Orbit (MEO) satellites (24 operational and 6 spares) at an approximate orbital altitude of 23222 km. The satellites will be organized in 3 different orbital planes with a 56° inclination with respect to Earth’s equator. They will be evenly spread within each plane with an orbital revolution period of approximately 14 hours and 7 minutes. Galileo’s constellation was designed to provide worldwide coverage with a minimum of 6 visible satellites at any time (elevation mask of 10°).

Galileo started offering early operation capability at the end of 2016, and it is expected to reach full operational capability by 2019. By the last quarter of 2017, 15 satellites Galileo satellites were already usable. Many multi-constellation GNSS receivers already support Galileo –usually in combination with GPS and GLONASS–, but its major mass-market expansion is expected by 2018 since most of the major smartphone manufacturers are including Galileo-ready GNSS receivers within their terminals. Galileo is planned to offer five different services:

---

<sup>6</sup>The system is named after the Italian scientist and astronomer Galileo Galilei (1564-1642) who, among his many achievements, proposed a procedure to calculate the longitude of a point on Earth by observing the orbits of the planet Jupiter’s four natural satellites [40, 42].

1. the free Open Service (OS) for mass-market receivers;
2. the Search and Rescue (SAR) service to help locating 406 MHz distress signals and providing and establishing an emergency communication link with the transmitters;
3. the Public Regulated Service (PRS), using encrypted signals, more robust and intended for security and strategic infrastructure;
4. the Commercial Service (CS), more accurate, using encrypted signals, intended the development of commercial or professional applications;
5. and finally, the Safety-of-Life service (SoL) providing timely warnings to the user when the system fails to meet specific margins of accuracy (integrity).

By 2017, only the three first services listed have started their –still limited– operation. Galileo satellites broadcast their signals in the L-band, which implement the mentioned services. Five carrier frequencies define the five frequency bands: E1, E6, E5, E5a, E5b. As in the GPS, the carrier frequencies are generated from a fundamental frequency  $f_0 = 10.23$  MHz:

$$\begin{aligned}
 f_c(\text{E1}) &= 154 \cdot f_0 = 1575.420 \text{ MHz} \\
 f_c(\text{E6}) &= 125 \cdot f_0 = 1278.750 \text{ MHz} \\
 f_c(\text{E5}) &= 116.5 \cdot f_0 = 1191.795 \text{ MHz} \\
 f_c(\text{E5a}) &= 115 \cdot f_0 = 1176.450 \text{ MHz} \\
 f_c(\text{E5b}) &= 118 \cdot f_0 = 1207.170 \text{ MHz},
 \end{aligned} \tag{2.10}$$

with receiver reference bandwidths of 24.55 MHz for E1, 40.92 MHz for E6, and 51.15 MHz for the full E5. Notice that E1 and E5a carrier frequencies are equivalent, respectively, to GPS L1 and L5. Signals transmitted in E5a and E5b are both parts of the E5 signal in its full bandwidth.

Galileo also uses DSSS to multiplex signals from different satellites and services. Different ranging codes and modulations are used to implement these services. Besides from signals modulated by navigation data (data channels), Galileo also broadcast signals consisting only of the ranging signals, i.e., pilot signals. Data and pilot signals are transmitted with equal power. In this thesis, we have considered only E1 and E5 (full band signals).

### E1 Signal

E1 signal implements the Galileo OS, CS, SoL and PRS services. E1 OS signal multiplexes two signal components: E1-B (in-phase), modulated by the navigation data stream, i.e.,  $e_{E1-B}(t)$ , and E1-C (quadrature), a pilot signal, i.e.,  $e_{E1-C}(t)$ . Both signal components are modulated onto the same carrier component –sharing half of the power– and implemented using composite binary offset carrier (CBOC) modulations, with a sub-carrier rate of 6.138 MHz and a primary code chipping rate of 1.023 MHz. This particular modulation is specified as CBOC(6,1,1/11), where the 1/11 term represents the power ratio used to combine the components forming the sub-carrier [3]. The power-normalized complex envelope of the E1

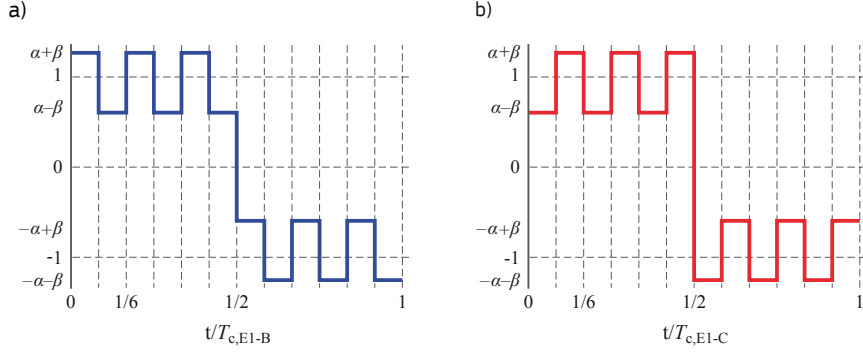


**Figure 2.6** – One period of the CBOC sub-carriers functions for (a) E1-B and (b) E1-C [3].

signal can be expressed as:

$$\begin{aligned}
 s_{E1}(t) = & \frac{1}{\sqrt{2}} e_{E1-B}(t) \underbrace{(\alpha sc_{E1-B,a}(t) + \beta sc_{E1-B,b}(t))}_{\text{Sub-carrier function E1-B}} \\
 & - \frac{1}{\sqrt{2}} e_{E1-C}(t) \underbrace{(\alpha sc_{E1-C,a}(t) + \beta sc_{E1-C,b}(t))}_{\text{Sub-carrier function E1-C}}, \quad (2.11)
 \end{aligned}$$

where the sub-carrier signals are generically defined as<sup>7</sup>:

$$sc_{[X]}(t) = \text{sign} \left( \sin \left( 2\pi f_{[X]} t \right) \right). \quad (2.12)$$

In (2.11), the parameters  $\alpha$  and  $\beta$  are selected such that the combined power of the sub-carriers  $sc_{E1-B,b}(t)$  and  $sc_{E1-C,b}(t)$  equals to 1/11 of the total power of  $e_{E1-B}(t)$  plus  $e_{E1-C}(t)$  [3], before any bandwidth limitation. This constrain yields to:

$$\alpha = \sqrt{\frac{10}{11}}, \quad \beta = \sqrt{\frac{1}{11}}. \quad (2.13)$$

As in [3], we show one period each sub-carrier function in Figure 2.6.

## E5 Signal

Galileo E5 signal implements the OS, CS and SoL services [3]. It is generated with the AltBOC(15,10) modulation, i.e., with a primary code at a chipping rate of 10.23 MHz and a side-band sub-carrier rate of  $f_{E5} = 15.345$ . In this modulation two pairs of data ( $e_{E5a-I}(t)$  and  $e_{E5b-I}(t)$ ) and pilot ( $e_{E5a-Q}(t)$  and  $e_{E5b-Q}(t)$ ) signals are combined onto the E5 carrier signal. The power-normalized complex envelope of the E5 signal can be expressed as:

$$\begin{aligned}
 s_{E5}(t) = & \frac{1}{\sqrt{2}} (e_{E5a-I}(t) + j e_{E5a-Q}(t)) \left( sc_{E5-S}(t) - j sc_{E5-S} \left( t - \frac{T_{s,E5}}{4} \right) \right) \\
 & + \frac{1}{\sqrt{2}} (e_{E5b-I}(t) + j e_{E5b-Q}(t)) \left( sc_{E5-S}(t) - j sc_{E5-S} \left( t - \frac{T_{s,E5}}{4} \right) \right) \\
 & + \frac{1}{\sqrt{2}} (\bar{e}_{E5a-I}(t) + j \bar{e}_{E5a-Q}(t)) \left( sc_{E5-P}(t) - j sc_{E5-P} \left( t - \frac{T_{s,E5}}{4} \right) \right) \\
 & + \frac{1}{\sqrt{2}} (\bar{e}_{E5b-I}(t) + j \bar{e}_{E5b-Q}(t)) \left( sc_{E5-P}(t) - j sc_{E5-P} \left( t - \frac{T_{s,E5}}{4} \right) \right), \quad (2.14)
 \end{aligned}$$

<sup>7</sup>The  $[X]$  symbol is used to represent the specific sub-carrier subscript

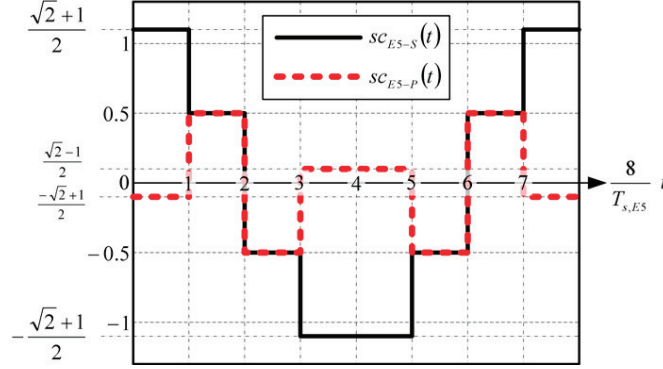


**Figure 2.7** – One period of the two sub-carriers functions, i.e.,  $sc_{E5-S}(t)$  and  $sc_{E5-P}(t)$ , involved in E5 signal’s AltBOC modulation [3].

where  $T_{s,E5} = f_{E5}^{-1}$ , and  $sc_{E5-S}(t)$ ,  $sc_{E5-P}(t)$  representing the two sub-carriers used. The remaining (dashed) product signal terms in (2.14) have been defined as:

$$\bar{e}_{E5a-I}(t) \triangleq e_{E5a-Q}(t) e_{E5b-I}(t) e_{E5b-Q}(t), \quad (2.15)$$

$$\bar{e}_{E5a-Q}(t) \triangleq e_{E5a-I}(t) e_{E5b-I}(t) e_{E5b-Q}(t), \quad (2.16)$$

$$\bar{e}_{E5b-I}(t) \triangleq e_{E5b-Q}(t) e_{E5a-I}(t) e_{E5a-Q}(t), \quad (2.17)$$

$$\bar{e}_{E5b-Q}(t) \triangleq e_{E5b-I}(t) e_{E5a-I}(t) e_{E5a-Q}(t). \quad (2.18)$$

Figure 2.7 represents one period of the sub-carrier functions  $sc_{E5-S}(t)$ ,  $sc_{E5-P}(t)$ . Notice that the AltBOC(15,10) complex baseband signal  $s_{E5}(t)$  can be implemented by an equivalent 8-PSK signal and a predefined look-up table [3].

## 2.3 GNSS Receiver Architecture

The GNSS user receiving equipment, or simply the receiver, is any device capable of receiving and processing the GNSS signals in order to estimate some of their features. In traditional GNSS receivers, these features are the TOA of the signals and the Doppler frequency-shift that these have experienced. Then, the receiver utilizes these parameters for PVT determination [12]. Instead, GNSS-Reflectometry receivers work as bistatic passive radars, i.e., they intend to extract some information out of received GNSS signals that have been previously reflected or scattered. Ultimately, both types of receivers are trying to solve a *signal into noise estimation problem* [43].

As most RF receivers, GNSS receivers have evolved from analog into the world of digital signal processing. Rapid advancement in digital electronics has turned low-cost and low-power GNSS chips into a reality. Nowadays, these chips –or processing modules running inside a more complex circuit– are embedded in billions of devices (e.g. smartphones).

Figure 2.8 shows the common four basic processing blocks of a classical GNSS receiver architecture [12]. Except for the RF front end block, the rest of the processing is done in the digital domain. This blocks can be implemented not only by application-specific integrated circuits (ASICs) (e.g., [44]), but also by field-programmable gate arrays (FPGAs) (e.g. [4, 15, 45, 46]), and software defined radio (SDR) receivers (e.g., [2, 47–50]). All the

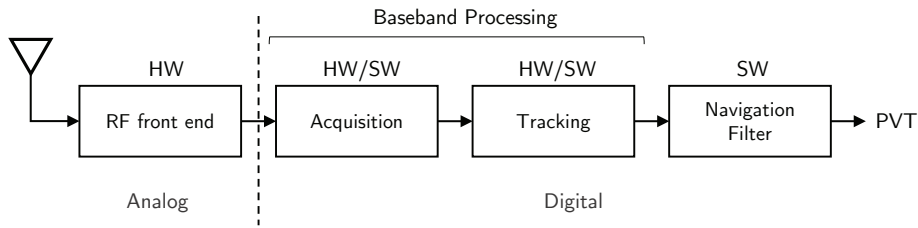


**Figure 2.8** – GNSS receiver main functional blocks. HW: Implementation with specific hardware. SW: Software implementation running on general purpose hardware.

processing techniques described in this thesis have been implemented using an SDR receiver [2]. Obviously, SDR is the most flexible platform among the mentioned ones, and it allows fast prototyping of new techniques.

The navigation filter in Figure 2.8 is responsible for the PVT determination given the code-delay and Doppler-shift measurements provided by at least four parallel tracking channels. GNSS-R receivers do not necessarily include the navigation filter block. Instead, they include a processing block to retrieve the geophysical parameters of interest from the observations. The rest of the processing performed by GNSS-R receivers can be considered, overall, similar to classical GNSS receiver’s processing.

In the following sections, we describe the elements processing blocks depicted in Figure 2.8, except for the navigation filter.

### 2.3.1 The RF Front End

The goal of the RF front end is to condition (amplify, down-convert and filter) and digitize the GNSS signal received at the antenna. Figure 2.9 shows a generic heterodyne RF front end topology typically used in GNSS receivers. A low noise amplifier (LNA) is placed immediately after the antenna. This amplifier, as the first element in the RF chain, is the primary contributor to the receiver’s overall noise figure. Thus the use of an LNA. The first bandpass filter rejects the signal’s RF images and any possible out-of-band interference.

The signal is further amplified and down-converted to an intermediate frequency (IF), more suitable for analog-to-digital conversion. This down-conversion is done by mixing the received signal with two local replicas of the signal’s nominal carrier frequency, one in-phase (I), and the other in quadrature (Q), which results into two processing branches (I branch and Q branch). After low-pass filtering the signals to reject high-frequency images, a variable gain amplifier adjusts the power of the signal to match the analog-to-digital converter’s (ADC) dynamic range and minimize quantization losses [51].

The ADC generates a stream of digital measurements at a sampling rate  $f_s$  [12]. Two-bit quantization per each I and Q components is the most common configuration in RF front ends for mass-market receivers. More quantization levels can improve the signal-to-noise ratio (SNR) and provide additional dynamic range to still be able to decode the signal in the presence of interference, at the cost of increasing the complexity of the receiver. The sampling rate of the ADC,  $f_s$ , must be adjusted appropriately to avoid undesired signal aliasing, and accordingly to the bandwidth of the low-pass filter to avoid unnecessary coloring of the thermal noise.



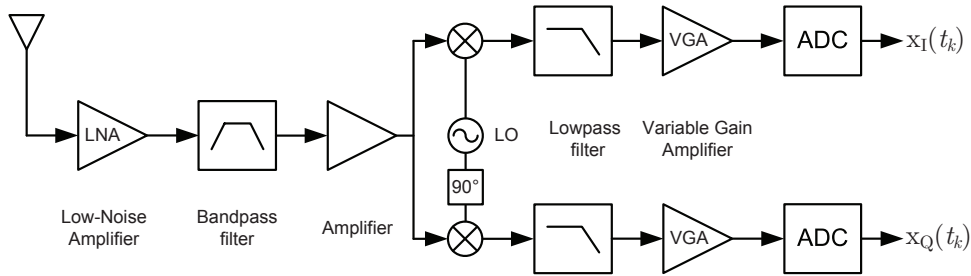


Figure 2.9 – Typical RF front end topology for GNSS receivers [4]

The discrete RF front end output at the sampling instant  $t_k$  is simply

$$x(t_k) = x(t_0 + kf_s^{-1}), \quad (2.19)$$

where  $t_0$  is the initial sampling time. The signal  $x(t_k)$  represents the sampled, quantized, and band-limited signal at the output of the RF front end's processing chain.  $x(t)$  is centered at the IF and models any distortion and additional noise (e.g. thermal noise) introduced by the front end.

The receiver's local oscillator (LO) signal is used to generate the mixing signals to down-convert the RF signal to the IF frequency. This same LO also drives the ADC. It is well-known that the receiver's maximum coherent integration time is limited by the dynamics and the stability of the local oscillator [14]. In this thesis, we assume a receiver equipped with a very stable oscillator. In this way, we can disregard any phase errors caused the LO's phase noise or drift when implementing the discussed processing techniques. That is particularly important in synthetic aperture processing, which coherently combines signal samples for periods of up to a few seconds. In our experimental setups to record GPS signals for its later processing, we have used an oven controlled crystal oscillator (OCXO) to drive our receiver's RF front end (see Chapter 4 for more details).

### 2.3.2 Acquisition

Initially, the receiver has to detect which satellite signals are present –and, therefore, which satellites are visible–. That poses a detection problem that can be classified as a *signal with unknown parameters in noise problem* [52–54], which within the GNSS receiver context is known as *acquisition* [2, 12]. Besides detecting present signals, acquisition provides a coarse estimate of their synchronization parameters, i.e., of the code-delay –in modulo one code period–, and the Doppler frequency shift.

Acquisition is typically performed by correlating the received signal with several noiseless replicas of itself. Each of these replicas is generated using a different code-delay and Doppler-shift hypotheses. The correlation results form a 2-D correlation image<sup>8</sup>, known as Cross-Ambiguity Function (CAF). The CAF's correlation peak must exceed an established threshold above the noise floor for the receiver to consider the signal as detected. As in any detection problem, this threshold is defined as a function of the desired probability of false alarm [54].

<sup>8</sup>This correlation image is known as Cross-Ambiguity Function (CAF) in the GNSS field, or as Delay-Doppler Map (DDM) in the remote sensing field, being the latter term particularly prevalent in the GNSS-Reflectometry literature.

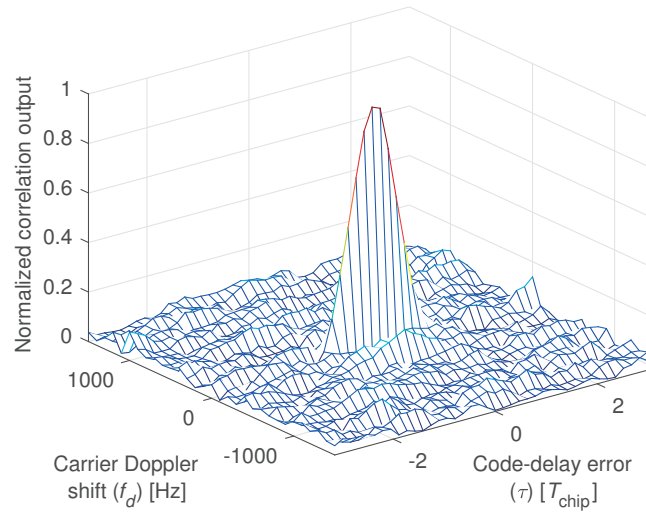


**Figure 2.10** – Example of the CAF for a clearly detectable GPS L1 C/A signal (BPSK modulation) over one code period.

The code-delay and Doppler-shift estimates are the hypotheses corresponding to the CAF’s peak. Figure 2.10 shows an example of a CAF where the signal is clearly detectable. Among the several methods to compute the CAF, the most common ones (e.g. parallel code search and parallel frequency search) use joint time-frequency domain techniques, which can be efficiently implemented using FFT-based methods [12, 55].

Multiple correlation outputs for the same hypotheses, but corresponding to different time periods of the received signal, can be combined –or “integrated”– into a single CAF with enhanced SNR of its peak [56, 57]. If these correlation outputs are coherently averaged over a *dwell* period, the SNR of the CAF’s peak will increase proportionally to the dwell period –assuming zero-mean noise–.

The size of the Doppler-shift search space is defined depending on the application and the expected dynamics of the receiver, i.e., higher dynamics imply possibly higher Doppler-shifts. The search step size, defined as the difference between two consecutive (carrier) Doppler-shift hypotheses, shall be adjusted to a minimum of  $2/3$  of the total coherent dwell time’s inverse to minimize frequency mismatch losses [56]. The longer the dwell time, the smaller the Doppler-shift step size. The default search space in the code-delay dimension covers one code period with a step size no larger than half a chip. With the parallel code search method, the code-delay step size becomes  $f_s^{-1}$ , i.e., the inverse of the signals’ sampling frequency [2, 12].

An interested reader is referred to the references provided in this section, and especially to [55], for further details on the acquisition topic.

### 2.3.3 Tracking

After acquisition, the receiver starts “tracking” the received signal. The coarse estimates of the code-delay and the Doppler-shift generated in acquisition are used to initialize the tracking block. This block’s main purpose is to keep track and refine these estimates, and to decode the navigation message from each tracked signal –if included–. The signal tracking is implemented by continuously adjusting the local signal replica (carrier and code) to match

the received signal, which maximizes the correlation output between them.

If the receiver utilizes the previous code-delay and Doppler-shift estimates to generate a small number of local replicas, the receiver is said to implement a closed-loop for sequential tracking (or closed-loop tracking for short) [5, 12]. In classical tracking architectures, the receiver tracks each satellite signal separately in one of its multiple “tracking channels,” which are working in parallel. Each tracking channel consists of a delay-locked loop (DLL) to track the code-delay, and a phase-locked loop (PLL), or a frequency-locked loop (FLL), to track the carrier frequency, from which the Doppler-shift estimates are obtained.

The DLL is a practical approximation of the Maximum Likelihood Estimator (MLE) of the code-delay, in the absence of multipath [40, 58, 59]. It tries to find the code-delay that maximizes the correlation between the received signal and the local replica. The correlation output corresponding to the current code-delay estimate is called the Prompt correlator. DLLs implement a reduced number of correlators –minimum three, named Early, Late and Prompt– with a small code-delay offset, known as correlator spacing. The output of these correlators are processed according to a specific discrimination function, e.g., Early-Minus-Late [12], which computes an updated raw estimate of the code-delay. This estimate is then filtered and used to drive the numerically controlled oscillator (NCO) generating the local replica of the code.

Similarly, the carrier tracking loop processes the Prompt correlator output –both, its I and Q components– according to a discriminator function, e.g.,  $\text{atan2}()$  [12], to estimate the carrier frequency value to drive the carrier NCO, i.e., the NCO used to generate the local replica of the carrier signal. If the signal contains a navigation message, the receiver can decode it by detecting the abrupt phase changes ( $\approx \pi$  rad) caused by the bit transitions of the BPSK-like modulations.

Given that the carrier tracking loop jitter is significantly less noisy than the code loop jitter, it is possible to use the carrier measurements to remove the LOS dynamics out of the code loop, which allows reducing the order and the bandwidth of the code loop filter. In this case, the noise in the code-delay estimates is reduced while the code-loop can still cope with the receiver dynamics. This architecture is referred to as *carrier-aiding* [12].

Although more resilient to multipath interference, tracking modern GNSS signal with high-order BOC modulations, such as the Galileo signals, becomes more challenging. BOC modulations have autocorrelation functions with multiple secondary peaks, which may cause the receiver to erroneously track a secondary peak, instead of the main one, in this way biasing the code-delay estimates. Unambiguous tracking of the main correlation peak has been the subject of several research works during the last decade, leading to many new code-delay tracking techniques, recently summarized by Lohan et al. in [22]. For more details on the different carrier tracking techniques, we refer to [12, 60].

### 2.3.4 Open-Loop Tracking

The design of tracking loop becomes intricate for challenging reception scenarios, e.g., under weak received signal conditions, in the presence of interfering signals or with high receiver dynamics. Modern receivers work in the discrete-time domain. Therefore, the tracking loops are digital systems, often designed as an approximation of its analog equivalent. For that approximation to reasonably hold, we need  $BT_{int} \ll 1$ , where  $B$  is the loop bandwidth, and  $T_{int}$  is the total integration (or correlation) time considered. If this condition is not fulfilled,

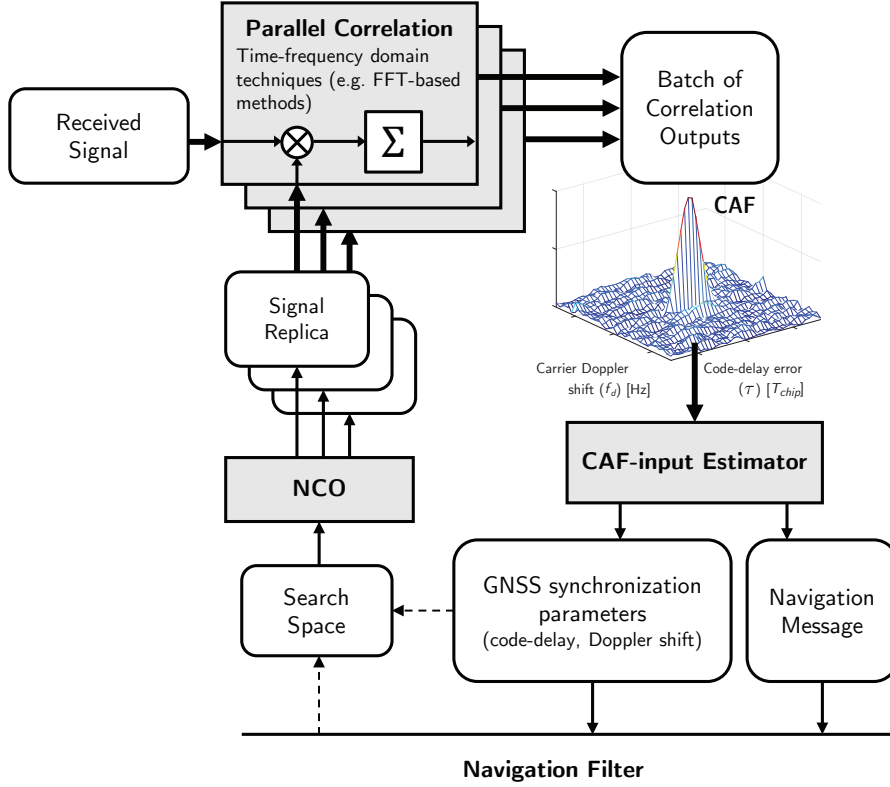


Figure 2.11 – Generalized open-loop tracking architecture (adapted from [5])

the loop becomes unstable, and it is likely to lose lock of the tracked signal. Unfortunately, this condition might be hard to meet in scenarios where, due to the weak signal power received, the receiver needs long integration times, e.g., on the order of hundreds of ms.

The open-loop tracking architecture is an alternative to the traditional sequential tracking loops, i.e., to closed-loop tracking. In this architecture, the receiver continuously correlates batches of the received sampled signal with a large number of signal replicas generated using several code-delay and Doppler hypotheses. This processing is similar to running a continuous signal acquisition resulting in a new CAF computed every  $T_{int}$ , i.e.,  $\chi \in \mathbb{C}^{K_\tau \times K_{f_d}}$ . The size of these CAFs depends on the total number of delay and Doppler-shifts considered, i.e.,  $K_\tau$  and  $K_{f_d}$ , respectively, which define the search space. Figure 2.11 represents a generalized open-loop tracking architecture.

As in acquisition, a particularly efficient way to compute  $\chi$  is to do it in parallel with joint time-frequency domain techniques. Utilizing the parallel code search technique [12], we can compute each column of  $\chi$  as:

$$[\chi]_i = \mathcal{F}^{-1} \{ \mathcal{F} \{ \mathbf{x} \} \odot \mathcal{F} \{ \hat{\mathbf{s}}_i \}^* \}, \quad (2.20)$$

which is the correlation output for the  $i$ th Doppler hypothesis for all the code-delays.  $\hat{\mathbf{s}}_i$  represents the replica of the signal, generated with the Doppler-shift corresponding to the  $i$ th hypothesis within the Doppler search space. This process is repeated for all the  $K_{f_d}$  Doppler hypotheses to compute the entire  $\chi$ . As a result of using the discrete Fourier transform (DFT),

the number of code-delay hypotheses is fixed as  $K_\tau = K$ , where  $K$  is the number of samples in  $\mathbf{x}$  –and in  $\hat{\mathbf{s}}_i$ –. Therefore,  $\tau_k = T_{code}/K$ , where  $T_{code}$  is the signal’s code period.  $K$  is chosen to match exactly one of these period in order to avoid distortions in the representation of the signal in the frequency domain – $\mathcal{F}$  assumes periodic signals–. More code-delay hypothesis can be considered for the same sampling rate of the signal by zero-padding  $\mathbf{x}$ , and then computing the DFT, at the cost of increasing the computational complexity. In practice, expression (2.20) is computed using the Fast Fourier Transform (FFT) algorithm and its inverse.

The CAFs computed for subsequent batches of the received signal can be accumulated to increase the signal-to-noise ratio (SNR). This accumulation, if done coherently, needs to account for possible abrupt phase changes caused by data bit transitions –only if tracking a data channel–. In [5], the authors implement a multi-hypothesis bit transition test to address this issue when tracking GPS L1 C/A signals with an open-loop architecture. This method computes multiple version of the accumulated CAF. Each version assumes a bit transition in one of the individual CAFs accumulated. The position of the bit transition –if there is any– is determined by the accumulated CAF hypothesis with the highest correlation value. This process is repeated every data bit period to decode the navigation message.

The code-delay and Doppler shift estimates can be directly obtained as the hypotheses that maximizes the CAF’s amplitude. In this case, the resolution of the estimates is limited by the step size of the hypotheses used to compute the CAF. However, since the expected shape of the CAF is known, it is possible to utilize some interpolation and fitting methods to get more refined estimates. As in closed-loop tracking architectures, these estimates are continuously fed to the navigation filter to update the computed pseudoranges.

## 2.4 GNSS-Reflectometry

Multipath interference is the most significant error source in many GNSS operational environments, biasing the pseudorange measurements. Mitigating the effects of multipath is challenging because it depends on the environment surrounding the receiver [61–64]. This dependence implies that a multipath signal carries information about the reflecting surface –or surfaces if the multipath signal is received after multiple reflections–. Therefore, it should be possible to retrieve some properties of the reflecting or scattering surface from the received signal. That is the fundamental principle of GNSS-Reflectometry (GNSS-R), i.e., to use the reflected or scattered GNSS signals as signals of opportunity for the remote sensing, primarily, of the Earth’s surface. In this way, GNSS-R receivers work as cost-effective passive bistatic (or multistatic) radars in the L-band.

As early as in 1988, Hall and Cordey reported the first study on the feasibility of implementing a GPS scatterometer in a multistatic configuration<sup>9</sup> [66]. At the time they concluded that, given the low power of the transmitted GPS signals, the performance of such scatterometer would be “inadequate.” Nonetheless, Martín-Neira proposed the use of scattered or reflected GPS signals to implement a mesoscale ocean altimeter on board of satellite, which he named Passive Reflectometry and Interferometry System (PARIS) [67]. Only one year later, in 1994, the first experimental evidence of measured GPS reflected signal

<sup>9</sup>This terminology comes from the radar domain. A *bistatic* radar –or scatterometer– is defined as a radar which transmitting and receiving antennas are at different locations. In this context, *multistatic* is an extension of bistatic, used in the case of having multiple transmitters –and only one receiver– at different locations which are intended to sense the same target [65]

–gathered three years before– was reported in [68]. The receiver installed on board of a French military aircraft locked into a strong multipath reflection, resulting in a temporary erroneous altitude estimates.

In 1998, Garrison et al. proposed the first GNSS-Reflectometer (only using GPS L1 C/A signal), which cross-correlated the reflected GPS signal received using an airborne left-hand circularly polarized (LHCP) antenna, with the locally generated PRN code as a function of the relative code delay [69].

The year 2000 was a landmark year for GNSS-R: Zavorotny and Voronovich proposed a physical model describing the entire sea surface scattering of GPS signals in a relatively simple way to compute. This model –called the Z-V model for brevity– is based on the geometric optics (GO) limit of the Kirchhoff approximation (KA) [11, 64], and it allowed to relate the observed Delay Doppler Map (DDM) for the reflected signal with a set of geophysical parameters. Since then, several models have been proposed, aiming to improve the Z-V, but none of them has been widely adopted. In parallel, Anderson and Kavak proposed the basics of a technique to measure water levels [70], and ground complex permittivity [71], by exploiting the coherent multipath interference measured by a ground-based GPS receiver. In time this will be known as the Interference Pattern Technique (IPT).

Since then, the use of GNSS-R for ocean altimetry, wind speed and sea state determination has gained considerable traction. Several works have been published describing specific GNSS-R instruments and architectures [33, 72, 73], retrieval techniques and algorithms [6, 74], theoretical signal models [62, 63, 75, 76], signal simulators [77–79], and several measurement campaigns carried out from different platforms [6, 80, 81]. Even specific GNSS-R space-based missions have been launched or planned by different space agencies and research institutions [25, 33, 82, 83]. Furthermore, additional remote sensing applications have been also proposed and validated through experimental campaigns, such as: soil moisture monitoring [26, 62, 84–90], snow content monitoring [28, 30, 31, 91–94], sea-ice monitoring [95, 96], ground and calm water altimetry [49, 97–104] and biomass estimation [105, 106].

All the above references confirm the interest that GNSS-R has aroused in the research community working on Earth observation over the last years. GNSS-R receivers, being passive sensors, can be simpler, less power-consuming, and more cost-effective, than active radars. Additionally, signals transmitted in the L-band are particularly suited to sense the Earth’s surface, and they can penetrate clouds [24, 107]. With the new GNSS being deployed, transmitting additional new signals, the number and variety of available signals of opportunity will become even higher, potentially improving the expected accuracy and availability of many GNSS-R applications. The ranging signals used for TOA estimation naturally fit for altimetry applications. However, they reach the Earth’s surface with very weak power, and their bandwidth is certainly limited. This underlines the main drawback of working with signals of opportunity, i.e., not having control any over them.

Some effort has been made to characterize the theoretical estimation performance of certain GNSS-R techniques, mostly in altimetry applications [6, 33–37, 75, 108–114]. The main drawback of theoretical bounds is that they require accurate modeling of the signal statistics as a function of the parameters of interest. Modeling attempts have been made by investigating real signal measurements (e.g. [37, 113]) and with simulations (e.g. [78, 115]). In [33, 36, 114] the different authors tried to assess the impact of specific GNSS-R techniques and architectures, over the attainable precision. Nonetheless, most of these efforts considered only GPS L1 C/A signals in scenarios with diffuse scattering, i.e., assuming noncoherent reflections and short signal measurement times.

Nevertheless, the accuracy of GNSS-R applications is expected to depend strongly on the specific technique, the receiver specs, and the scenario considered. GNSS-R experimental campaigns have confirmed the previous claim. Therefore, establishing a fair comparison among different GNSS-R, solely based on reported performances, is not straightforward. In [6] (Table 4), the authors summarize the accuracies reported by several GNSS-R altimetry experiments.

In the sections below we introduce the signal model for coherently reflected GNSS signals, and then we provide a brief overview of the IPT.

### 2.4.1 Model for Scattered and Reflected GNSS Signals

Let us define a GNSS-R scenario for which we select a frame of reference with its origin of coordinates located at the specular reflection point on the scattering surface. Then, under the KA and GO optics assumptions<sup>10</sup> [63], we can express the baseband equivalent of the reflected signal at output of the receiving antenna as

$$a_r(t) = u_t(t) \int_{S_\rho} G(\boldsymbol{\rho}) s(t - \tau(\boldsymbol{\rho}, t)) \exp\{-j2\pi f_c \tau(\boldsymbol{\rho}, t)\} g(\boldsymbol{\rho}, t) d\boldsymbol{\rho}, \quad (2.21)$$

where:

- $u_t(t) \in \mathbb{C}$  is the amplitude of the GNSS signal impinging on the antenna.
- $s(t) \in \mathbb{C}$  is the GNSS signal modulation.
- $\boldsymbol{\rho} \in \mathbb{R}^{3 \times 1}$  is the vector defining scattering point position within the defined frame of reference.
- $G(\boldsymbol{\rho}) \in \mathbb{C}$  is the amplitude gain of the receiving antenna, which will depend on the angle-of-arrival of the signals, therefore, depending on the reflection scenario geometry through  $\boldsymbol{\rho}$ .
- $f_c$  is the transmitted carrier frequency.
- The scattered signal delay  $\tau(\boldsymbol{\rho}, t)$  can be expressed as

$$\tau(\boldsymbol{\rho}, t) = \frac{|r(\boldsymbol{\rho}, t)| + |r_0(\boldsymbol{\rho}, t)|}{c}, \quad (2.22)$$

where  $c$  is the wave propagation speed,  $r(\boldsymbol{\rho}, t)$  is the distance from each scattering point to the receiving antenna, and  $r_0(\boldsymbol{\rho}, t)$  is the distance from the transmitter to each scattering point.

- $S_\rho$  represents the *glistening area*, i.e., the area from where –under the KA approximation– well-oriented facets might exist under a probability threshold [11, 63]. The rougher the scattering surface, the larger the glistening area. In a more intuitive way, the glistening zone is the surface area from which energy is scattered towards the receiving antenna.

<sup>10</sup>The Kirchhoff –or tangent plane– approximation states that any point on the scattering surface can be approximated by those that would be present on an infinite plane tangent to the surface integration point, called facet plane. Therefore, each contribution to the scattered signal is considered to depend only on the Fresnel reflection coefficient at the facet plane on each surface point [11].

- $g(\boldsymbol{\rho}, t) \in \mathbb{C}$  is the function that models the scattering coefficient of each point of the scattering surface. It is certainly the most important term in expression (2.21). It connects the amplitude of the total scattered signal measured at the receiving antenna with the geophysical parameters of the scattering surface.  $g(\boldsymbol{\rho}, t) \in \mathbb{C}$  is—in most scenarios—defined as a random function of the scattering surface parameters, which implies that  $u_r(t)$  will be a random variable. Very different models are used for different kind of surfaces. The interested reader is referred to [64] for a comprehensive review of models for the scattering of radiowaves from rough surfaces.

The function  $g(\boldsymbol{\rho}, t)$  is usually decomposed into the sum of two contributions: a coherent one, caused by the specular reflection, and a diffuse contribution caused by the surface roughness. Within the context of this dissertation, we are interested on flat and smooth surfaces, where the specular reflection is dominant, and as a result, almost all the scattered energy comes from the first Fresnel zone [64]. Hence, we can approximate  $g(\boldsymbol{\rho}, t)$  as:

$$g(\boldsymbol{\rho}, t) \approx \Gamma_F(t) \exp \left\{ -2 \left( \frac{\pi}{\lambda} \sigma_{s_h} \sin(\theta(t)) \right)^2 \right\} \delta(\boldsymbol{\rho}), \quad (2.23)$$

where  $\Gamma_F(t)$  is the Fresnel Reflectivity<sup>11</sup> of the specular reflection point,  $\sigma_{s_h}$  is the surface roughness coefficient, i.e., the standard deviation of its height,  $\theta(t)$  is the signal's specular grazing angle, and  $\delta(\boldsymbol{\rho})$  is the Dirac delta function. The exponential term in (2.23) is known as the coherence loss factor [64].

In these scenarios, dominated by the specular component, the amplitude of the—now—reflected signal  $a_r(t)$  will be well approximated by substituting expression (2.23) into (2.21), i.e.,

$$\begin{aligned} a_{r, \boldsymbol{\rho}_0}(t) \approx & u_t(t) G(\boldsymbol{\rho}_0) \Gamma_F(t) \exp \left\{ -2 \left( \frac{\pi}{\lambda} \sigma_{s_h} \sin(\theta(t)) \right)^2 \right\} \\ & \times s(t - \tau(\boldsymbol{\rho}_0, t)) \exp \left\{ -j \frac{2\pi}{\lambda} \tau(\boldsymbol{\rho}_0, t) \right\} \end{aligned} \quad (2.24)$$

### 2.4.2 The Interference Pattern Technique (IPT)

Ground-based GNSS receivers, i.e., receivers with their antenna located only a few meters above the ground or a flat potentially reflecting surface, are likely to record oscillations—i.e., periodical slow-fading—on the measured signal power for satellite observed at low elevation angles during extended periods of time—i.e., several minutes—. These so-called “interference patterns” are caused by the interference between the LOS signal and a strong specularly reflected signal. Either received by the same antenna or combined later, if the two signal components have a delay difference shorter than a single modulation's chip period, the change of the satellite's elevation angle will cause an interference pattern on the amplitude of the received composite signal. Obviously, this interference pattern will be observed also in the receiver's SNR (or  $C/N_0$ ) estimates corresponding to the receiver channel tracking the signal

---

<sup>11</sup>Fresnel Reflectivity characterizes the reflection of a transmitted electromagnetic wave at the interface between two dielectric media. It is defined a function of the transmitted and reflected wave angles and the dielectric constant of the scatterer [64].



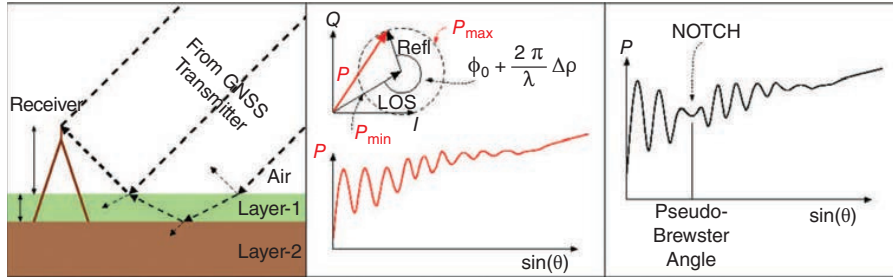


**Figure 2.12** – Sketch of the IPT for ground-based scenarios [6]. The total measured power  $P$  varies the evolution of the observed satellite elevation angle  $\theta$ .  $\phi_0$  is the phase of the LOS signal, and  $\Delta\rho$  is the propagation path difference between the LOS and the reflected signal.

[62, 116, 117]. Figure 2.12 shows an example of these interference patterns on the estimated  $C/N_0$  of a real receiver [6].

A GNSS-R technique that exploits the information about the reflecting surface, embedded in these patterns, is the Interference Pattern Technique (IPT) [26, 118], also known as GNSS multipath reflectometry (GNSS-MR)<sup>12</sup> [29, 30]. The coherent component of the reflected signal will be affected by the permittivity of the reflecting media surface, or even by secondary reflection layers (e.g. vegetation layer). The frequency of the oscillations in the interference pattern depends on the altitude of the receiver above the reflecting surface. Every time that the propagation path difference changes by  $\lambda$ , we observe one of these oscillations. Their amplitude is connected to three main factors: the antenna gain pattern for different polarizations, the roughness of the reflecting surface (contributing to the coherence loss factor in expression (2.23)), and the Fresnel coefficient, related to the surface medium permittivity. These factors also impact the phase of the interference pattern oscillations.

The “notches” observed in the interference pattern correspond to the pseudo-Brewster angle elevations. At this elevation, most of the power received is only from the LOS signal. Therefore, the interference effect almost vanishes, causing the “notch.” The pseudo-Brewster angle is a function of the reflection media complex permittivities, which implies that it is possible to estimate them from the location of the observed notches in the interference pattern. If the reflecting surface media has multiple layers, secondary notches will be observed. In [119], the authors utilize a three-layer model to characterize the reflection coefficient of the surface –i.e., air, one surface layer, on sub-surface layer–. This model has been used in IPT applications aiming to estimate soil moisture, snow [28] and vegetation content [26].

Most commercial GNSS receivers already report estimates on the SNR or  $C/N_0$  of the satellites being tracked, e.g., in NMEA 0183 protocol’s GSV messages. Thus, some research work has already proposed to use these estimates provided by geodetic GNSS receivers to scout the ground surface surrounding the sites where the receivers are deployed. In this way, it is possible to implement a large-scale observation network in a very cost-effective manner since no modification of the receivers is required –only some knowledge about the site surroundings–.

Despite their potential, little research has tried to characterize the estimation performance of IPT-like techniques, beyond reporting the accuracies obtained in specific experiments.

<sup>12</sup>The two terms are arguably interchangeable. Nonetheless, some authors differentiate them by associating GNSS-MR with the cases where most of the interfering signals are co-polar, i.e., RHCP, while they use IPT for dedicated experiments and sometimes a different polarization basis [6].

So far, most efforts to provide some theoretical estimation bounds have mostly considered scenarios dominated by scattered signals [112, 113]. In these scenarios, the reflected or scattered signals are mostly noncoherent, i.e., with a significant amount of speckle noise. In Chapter 3 we address this gap by deriving a precision bound, the CRB, valid for IPT and similar techniques.

## 2.5 Spatial Filtering of GNSS Signals

Interference signals, including multipath, are likely to arrive at the receiver’s antenna from directions different than the direction-of-arrival (DOA) of the LOS signal. Because of that, spatial filtering techniques, which are usually implemented using antenna arrays, are so effective mitigating the error caused by both intentional (e.g. jamming and spoofing signals) and unintentional (e.g., multipath) interferences [120]. With spatial filtering, the receiver can amplify or attenuate the received signals, depending on their DOA [121–123]. Conversely, it can estimate the DOA of those received signals. These two processes are referred to as beamforming and DOA estimation, respectively. In this thesis, we use the term spatial filtering to refer to both of them.

At a given time instant, the propagating source signal will be observed with small delay differences at the different antenna array elements. Assuming a planar wavefront, the signal might have traveled a slightly different distance to reach each element of the array. These traveling distance differences ( $\Delta\rho$ ) will be a function of the array geometry and the DOA of the signal, i.e.,

$$\Delta\rho(\boldsymbol{\psi}, \mathbf{P}), \quad (2.25)$$

where  $\boldsymbol{\psi} \triangleq [\theta, \phi]^T$  is the DOA vector, with  $\theta$  and  $\phi$  used to represent the elevation and azimuth of the received signal in the frame of reference selected. Figure 2.13 shows how these angles are defined. The matrix  $\mathbf{P} \in \mathbb{R}^{N \times 3}$  represents the positions of each of the  $N$  elements of the array.

If the bandwidth of a bandpass signal is much smaller than its carrier frequency, the delays  $\Delta\rho/c$  (where  $c$  is the wave propagation speed) are well approximated as phase shifts (phased-array). This approximation is commonly taken and known as the *narrowband array* assumption. These phase shifts are usually grouped into the steering vector  $\mathbf{k}(\boldsymbol{\psi}) \in \mathbb{R}^{N \times 1}$ ,

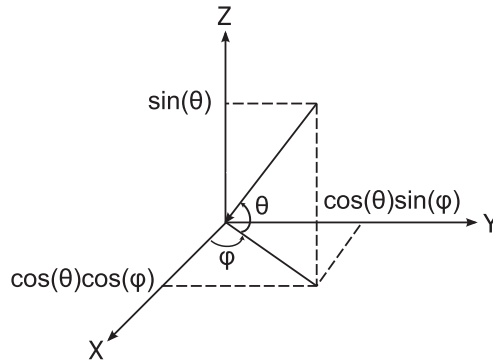


**Figure 2.13** – Definition of the elevation ( $\theta$ ) and azimuth ( $\phi$ ) angles in the selected frame of reference, and Cartesian projection of the steering vector  $\mathbf{k}(\boldsymbol{\psi})$ .

expressed in rad, as:

$$\mathbf{k}(\boldsymbol{\psi}) = -\frac{2\pi}{\lambda} \begin{bmatrix} \cos(\theta) \cos(\phi) \\ \cos(\theta) \sin(\phi) \\ \sin(\theta) \end{bmatrix}, \quad (2.26)$$

where  $\lambda$  is the carrier wavelength.  $\mathbf{k}(\boldsymbol{\psi})$  is used to build the array manifold vector as:

$$\mathbf{v}(\boldsymbol{\psi}) = \exp \left\{ j \mathbf{k}^T(\boldsymbol{\psi}) \mathbf{P} \right\}. \quad (2.27)$$

The output of the array elements simultaneously measured at time  $t$ —referred to a snapshot—can be weighted and summed into a single observation to implement the spatial filtering, i.e.,  $y(t) = \mathbf{w}^H \mathbf{x}(t)$ . If the output of the array elements has been previously digitized, this process is known as digital beamforming (DBF). From now on, we focus on the DBF case.

Besides the specific gain pattern of each antenna elements, and the possible mutual-coupling among them, how the (complex) weight vector  $\mathbf{w}$  is selected will determine the array's gain pattern. There are several techniques to select  $\mathbf{w}$ , which define the specific beamforming techniques. Overall, we can classify them as:

- *Data independent*, if  $\mathbf{w}$  does not directly depend on the received signals, but on other side information (e.g. the known DOA of the signal). The  $\mathbf{w}$  computed with these techniques is used for beam and null steering.
- *Statistically optimum*, if  $\mathbf{w}$  depends on the statistics of the expected signals or on the transmission channel and the signal's DOA. These techniques try to optimize a specific metric, e.g., the output SNR, given the received signal and a set of constraints. The DBF techniques utilizing  $\mathbf{w}$  computed with statistically optimum techniques are also referred to as *adaptive beamforming* techniques, since they adapt to the signal and the channel conditions.

Conversely, the selection of  $\mathbf{w}$  with most of these techniques can be used to determine the DOA of the signals, which is known as bearing or DOA estimation.

In the context of GNSS, antenna arrays have been used successfully for interference mitigation and DOA estimation [40, 120, 124, 125]. However, their usage presents important drawbacks. First, given the carrier wavelength of the GNSS signals, the array sizes can be too bulky for many GNSS applications. The array should have the largest possible aperture<sup>13</sup>. The larger the aperture, the better the spatial resolution. Increasing the number of elements for a given aperture will not increase the array resolution. However, to avoid ambiguities (causing grating nulls), inter-element spacing should be kept equal or less than half a wavelength. Nonetheless, the larger the number of elements, the more degrees of freedom of the array [123]. Secondly, antenna arrays also require to increase the receiver's complexity, particularly of its RF front end. Some data independent beamforming techniques can be implemented directly in the analog domain, at the expense of losing flexibility. On the other hand, the usage of DBF techniques will increase the receiver's computational power requirements.

---

<sup>13</sup>The *aperture* is defined as the area, oriented perpendicular to the direction of an incoming radio wave, which would intercept the same amount of power from that wave as is produced by the antenna receiving it.

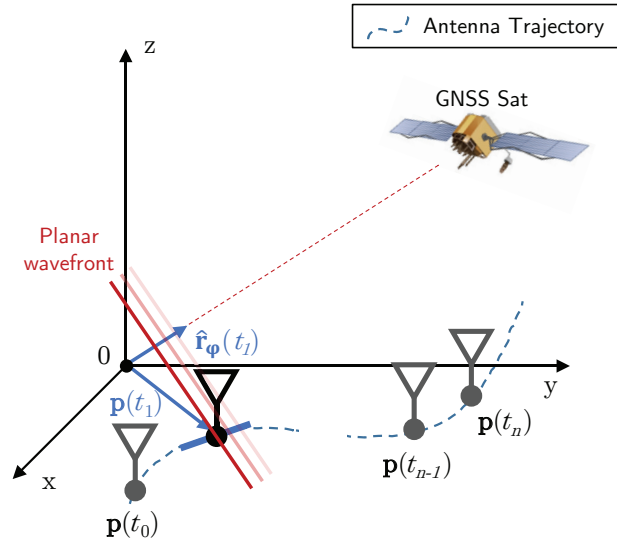


**Figure 2.14** – Synthetic aperture concept: single antenna moving along the trajectory in the selected frame of reference.  $\hat{\mathbf{r}}_\varphi(t)$  represents the unit vector in the direction of the satellite.

In GNSS receivers it is possible to implement the spatial filtering before or after correlating the received signal with its local replica [8, 120, 125, 126]. In this thesis, we consider only the latter case, where the beamforming weights  $\mathbf{w}$  are used to combine correlation outputs. The main reason is that at the post-correlation level, the sampling rate is much lower, which dramatically reduces computational complexity. Besides, post-correlation beamforming allows the simultaneous use of different weights to different satellite signals (in different tracking channels).

### 2.5.1 Synthetic Aperture Processing

Under the assumption of sufficient channel stationarity, the motion of a single antenna –or an array– can be used to synthesize a larger aperture or a “virtual array.” In this thesis, we will refer generically to the signal processing based on this principle as synthetic aperture (SA) processing. The SA processing concept has been widely used during decades in the radar field, where it is known as synthetic aperture radar (SAR) [65, 107, 127]. SAR instruments have been used extensively onboard of aircrafts and satellites in Earth observation applications.

Figure 2.14 depicts the SA processing principle for a single moving antenna. Essentially, the  $N$  observations taken at different locations  $\{\mathbf{p}(t_n)\}$  and times are processed as if they corresponded to the same time instant. Combined, these  $N$  signal observations can mimic one snapshot of physical array of  $N$  elements. We call these  $N$  observations an SA snapshot.

Let us consider an arbitrary static frame of reference, with its origin of coordinates set in the vicinity of the trajectory described by the antenna motion (e.g., in the center of the trajectory). In this frame of reference, the delay  $\tau(t)$  on the GNSS signal observed by the moving antenna can be expressed as the delay that would be observed by the antenna at the origin of coordinates (reference delay) plus an additional component due to the antenna position (relative delay). Assuming knowledge of the trajectory described by the antenna during a time  $T_{SA}$ , i.e., the synthetic aperture time, and after compensating the reference

delay in the observed signal measurements, we can apply some of the same spatial filtering techniques utilized with physical arrays.

We now briefly summarize, in approximate chronological order, the most relevant previous work in the SA processing of GNSS and DSSS signals to perform spatial filtering. Apart from that, the detection of GNSS signals with SA processing has also been studied in [128–131].

An early implementation of the SA processing principle to detect the DOA of multipath signals in mobile communications can be found in [132]. There, De Jong et al. synthesized the equivalent of a uniform circular array (UCA) with the motion of a single antenna. A few years later, in the late 2000s, Broumandan et al. were the first to report the practical implementation of SA processing of GNSS signals to perform DOA estimation of jamming signals [133]. As in [132], Broumandan et al. used a uniform circular motion, implemented by mounting the antenna on a rotating mechanical arm, and implemented the multiple signal classification (MUSIC) algorithm [121, 134]. In [133], the authors used an inertial measurement unit (IMU) to accurately track the antenna motion. Later, in [135], Broumandan et al. also simulated the arbitrary trajectories, but this time, for beamforming to mitigate multipath and improve TOA estimation, using the cumulant-based blind steering approach proposed in [136]. Simultaneously, the same authors experimented with the Estimation of Signal Parameters via Rotational Invariance Techniques (ESPRIT) algorithm in [137], but this time with CDMA IS-95 signals received by two moving antennas, connected to a two-channel receiver.

Approximately at the same time, i.e., in 2008, Pany and Eissfeller published some early results in [138] obtained with their experimental setup to perform DOA estimation by synthesizing a UCA with an antenna rotating with a radius of 79 cm. In this work, the authors highlight two important challenges when implementing SA processing in practice: a) the compensation of the phase component due to the relative delay, and b) the need for a very stable oscillator (they use an OCXO) for antenna motions on the order of 1-s duration.

In 2009, Lin et al. investigated a few classical spatial filtering algorithms adapted to SA processing of GPS L1 C/A signals [8]. The authors considered uniform circular trajectories in RF signal simulations (radius 66 cm) and with the measurements gathered by an antenna mounted on a rotating arm (radius 1 m). In both cases, they considered  $T_{SA} = 2$  s, and an angular speed of  $\pi$  rad/s. In addition, the authors proposed a linear interpolation method and the use of a static antenna to compensate for the carrier phase contribution due to the relative delay (see Section 4.3.2). They conclude [8] by noticing the potential for eigenstructure-based SA beamforming, for random unknown trajectories.

The following year, 2010, Soloviev et. proposed an FFT-based method to synthesize a planar SA with the motion of a physical array of 2 elements [139]. The proposed method implements spatial filtering to process GNSS signals in a computationally efficient way. To validate their method, the authors built a moving array of 2 elements installed on top of a van describing linear motions, perpendicular to the array orientation, at approximately 4 m/s.

In 2011, Nielsen et al. studied the spoofing detection with SA processing techniques for a handled device in indoor environments. The same year, Keshvadi et al. use, one more time, a rotating antenna to implement SA processing for uniform circular motions. This time, however, the authors do it indoors [140] to characterize the multipath.

In 2013, Pany et al. extended their previous work on SA processing [138], by proposing a receiver capable of processing signals recorded over different kinds of motions: uniform

circular with 50 cm radius and an angular speed of  $\pi/2$  rad/s –implemented with a new rotating arm–; vertical; and arbitrary, measured with an IMU or projected with a pedestrian motion model [141]. Also in the same year Dehghanian et al. [142] proposed to use a dual polarization antenna for SA processing to mitigate multipath interference.

The study of specific spatial filtering techniques is outside the scope of this thesis. Instead, we concentrate on the integration of the SA processing into the receiver’s tracking architecture. Hence, we have implemented only a small group of well-known spatial filtering techniques [121–123], with the goal of using them to validate the SA tracking architecture and techniques described in Chapter 4. We have implemented the delay-and-sum beamformer and three DOA estimation algorithms: the Beamscan algorithm, the Capon’s minimum power distortionless response (MPDR-Capon) algorithm, and the MUSIC algorithm [8, 122, 123]. These beamforming and DOA estimation algorithms were previously tested in practice by Lin et al. [8], with an antenna describing a uniform circular motion. Their relative simple implementation, and the fact that they were already validated, strongly motivated our choice.

### 2.5.2 Delay-and-Sum and Beamscan Algorithms

The delay-and-sum is the simplest beamforming algorithm. It is data independent and its weight vector is defined as:

$$\mathbf{w} = \frac{1}{N} \mathbf{v}(\boldsymbol{\psi}), \quad (2.28)$$

where  $\mathbf{v}(\boldsymbol{\psi})$  is the array manifold vector for the direction to which we want to steer the main beam.

Complementary to the delay-and-sum algorithm, we have the Beamscan algorithm, its counterpart for DOA estimation. With the Beamscan algorithm, the DOA of the received signals is found by synthesizing several reception patterns with the main beam steered to different directions. If the power for a particular direction is higher than certain threshold, the Beamscan algorithm considers that there is a signal coming from that direction. This scanning-like process is implemented by defining multiple  $\{\mathbf{v}(\boldsymbol{\psi})\}$  vectors, one for each testing direction. The output magnitudes –or equivalently the power values– generated in this process are depicted in the so-called DOA map. Figure 2.15 shows an example of a DOA computed using the Beamscan algorithm.

The computed DOA map shows that when the direction used to generate  $\mathbf{v}(\boldsymbol{\psi})$  matches the DOA of the signal, the output power is maximized. Otherwise, low output power values are observed as the different signal observations are not coherently combined. The DOA estimation of LOS with the Beamscan algorithm can be stated as:

$$\hat{\boldsymbol{\psi}}_{\text{BS}} = \arg \max_{\boldsymbol{\psi}} \left\{ \mathbf{v}^H(\boldsymbol{\psi}) \left( \mathbf{x}^H \mathbf{x} \right) \mathbf{v}(\boldsymbol{\psi}) \right\}. \quad (2.29)$$

In the previous expression (2.29), the matrix  $(\mathbf{x}^H \mathbf{x})$  can be understood as channel’s sample covariance matrix (SCM), an estimator of the true covariance matrix  $\boldsymbol{\Sigma}_{\mathbf{x}}$ , computed with only one SA snapshot. We refer to the matrix  $\boldsymbol{\Sigma}_{\mathbf{x}}$  also as the spatiotemporal covariance matrix, because in the SA context, each of its samples corresponds to a different time and location.

The accuracy of the Beamscan algorithm will be limited by the distance between adjacent DOA hypotheses in the scanning process. As in any grid search problem, achieving fine resolution will require testing a very large of hypothesis, if we do not use a priori knowledge to limit the DOA’s search space.

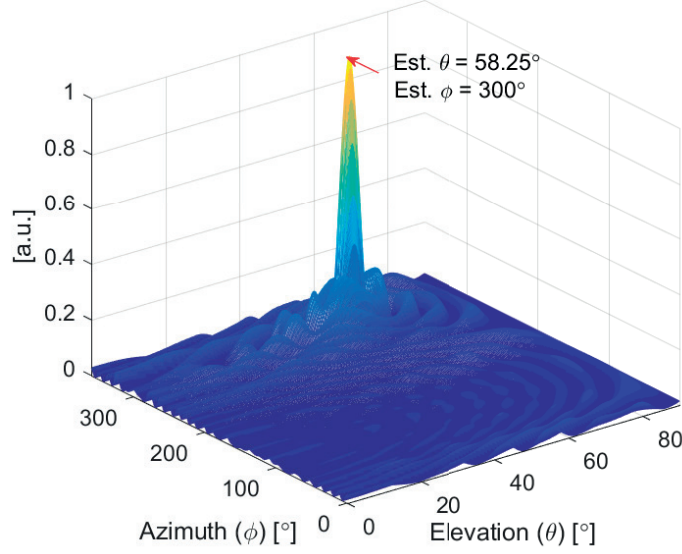


**Figure 2.15** – Example of DOA map computed with the Beamscan algorithm for a uniform circular aperture of 100 elements and a normalized radius of  $4.72\lambda$ . The magnitude is has been normalized and, therefore, represented in arbitrary units (a.u.).

### 2.5.3 Adaptive DOA Estimation: MPDR-Capon and MUSIC

MPDR-Capon and MUSIC are the DOA estimation's counterparts, respectively, to the MPDR and the subspace beamformers [121, 123], which are adaptive algorithms.

MPDR-Capon tries to find the direction that minimizes the total output power, subject to the distortionless constraint [121]. To do so, it requires knowledge of the spatiotemporal covariance matrix  $\Sigma_{\mathbf{x}}$ . In practice, however, the receiver must use an estimate  $\hat{\Sigma}_{\mathbf{x}}$ , computed from the observed measurements, e.g., using the sample covariance matrix (SCM) estimator. MPDR-Capon can achieve better resolution than the Beamscan algorithm, at the cost of computing  $\hat{\Sigma}_{\mathbf{x}}^{-1}$ , which is a full-rank matrix. In the context SA processing,  $\hat{\Sigma}_{\mathbf{x}}$  it is likely to be poorly conditioned. We further discuss this issue later on in Section 4.3.2.

For the practical case, the MPDR-Capon algorithm to estimate the DOA of the signal can be stated as:

$$\hat{\psi}_{\text{Capon}} = \arg \max_{\psi} \left\{ \left( \mathbf{v}^H(\psi) \hat{\Sigma}_{\mathbf{x}}^{-1} \mathbf{v}(\psi) \right)^{-1} \right\}. \quad (2.30)$$

The MUSIC algorithm is a high-resolution classification technique for multiple signals which exploits the eigenstructure of the matrix  $\Sigma_{\mathbf{x}}$  [8, 121]. More specifically, MUSIC exploits the fact that the steering vector corresponding to the DOA of the received signals lies in a subspace orthogonal to the noise subspace. Given the following eigen-decomposition of  $\Sigma_{\mathbf{x}}$ :

$$\Sigma_{\mathbf{x}} = \underbrace{\mathbf{Q}_s \Lambda_s \mathbf{Q}_s^H}_{\text{Signal}} + \underbrace{\mathbf{Q}_n \Lambda_n \mathbf{Q}_n^H}_{\text{Noise}}, \quad (2.31)$$

MUSIC uses the noise subspace  $\mathbf{Q}_n$ , which should fulfill:

$$\mathbf{v}^H(\psi) \mathbf{Q}_n = \mathbf{0}, \quad (2.32)$$

to compute the DOA estimates of the present signals as the peaks in function

$$P_{\text{MUSIC}}(\psi) = \left( \mathbf{v}^H(\psi) \mathbf{Q}_n \mathbf{Q}_n^H \mathbf{v}(\psi) \right)^{-1} \quad (2.33)$$

with the DOA estimate for the LOS signal obtained as:

$$\hat{\psi}_{\text{MUSIC}} = \arg \max_{\psi} \{P_{\text{MUSIC}}(\psi)\}, \quad (2.34)$$

under the assumption that it is strongest signal component present.

We were aware that MPDR-Capon and MUSIC perform poorly in the presence of multiple strongly correlated signals, which is the case of multipath [121, 123]. In the extreme case, where the signals are coherent (e.g., a coherently reflected multipath), the matrix  $\Sigma_{\mathbf{x}}$  –and therefore, its estimates– becomes rank divergent. In the case of MUSIC, that will result in a divergence of a signal eigenvector into the noise subspace and the MUSIC “spectrum” may fail to produce peaks at the DOA locations. In Chapter 4 we use MPDR-Capon and MUSIC in a scenario with a strong coherent multipath signal present. There, we observe how the performance of these algorithms degrades becoming very similar to the Beamscan’s algorithm.

## 2.6 Estimation Precision: The Cramér-Rao Bound

The main goal of any GNSS receiver, no matter its application, is to estimate some unknown signal parameters from a noisy observations. This kind of problem, i.e., the *signal into noise estimation problem*, represents an important part of the statistical signal processing field [43, 54, 143]. In many cases, the observations are a nonlinear function of the unknown parameters.

Given the random nature of the observations, estimators of the unknown parameters will be random variables. Unfortunately, the minimum variance of any estimator –and therefore, its mean square error (MSE)– is lower bounded, no matter the estimator choice: there is always a limit on the accuracy of the estimates obtained from a certain set of random measurements. It is of great interest to investigate variance or MSE bounds for two reasons. First, bounds can be used as performance benchmark to compare different unbiased estimators. Secondly, bounds quantify the best theoretical estimation performance for a given scenario. By comparing the performance of our estimator with a theoretical bound, we can infer if there is any room for improvement.

A comprehensive overview of the most relevant estimation bounds in terms of MSE can be found in [144]. The most commonly used include the Crámer-Rao bound (CRB), the Barankin bound (BB), the Ziv-Zakai bound (ZZB), and the Weiss-Weinstein bound (WWB) [144, 145]. The CRB and the BB are variance bounds belonging to the family of deterministic “covariance inequality” bounds [146], i.e., used to characterize the variance of unbiased estimators of deterministic parameters. The ZZB and the WWB are Bayesian bounds on the MSE of random unknown parameters with a known *a priori* distribution [145]. In this dissertation we consider only long observation times or high SNR scenarios, so that the MSE is small. These conditions are referred to the asymptotic region of operation [144]. Hence, we use the CRB, since it is generally the easiest to evaluate. Along with the standard CRB, several modifications of the CRB can be found in the literature, mostly to deal with nuisance parameters, e.g. the *modified* CRB [147], the *stochastic* CRB [148], the *joint* CRB [149] or the *asymptotic* CRB [43].

The CRB in the context of GNSS signal processing has been already addressed in the literature (e.g., in [150, 151]), even for antenna array receivers (e.g., in [124, 125]). Nonetheless,



## 2.6. Estimation Precision: The Cramér-Rao Bound

---

our aim in this dissertation is to compute the standard CRB to study the theoretical variance bounds of estimators specifically used in:

1. GNSS-R applications for scenarios with specular –coherent– reflection, to retrieve geophysical parameters, and
2. GNSS synthetic aperture processing, to estimate the DOA of the signals.

In essence, given the known probability density function (PDF) of a set of observations –or measurements–, the CRB quantifies the dependency of the observations on the unknown parameters that we desire to estimate. The stronger the PDF’s dependency on these parameters, the lower the CRB. The multiple-parameter CRB states that, for any unbiased estimator of a deterministic, real-valued parameter vector  $\boldsymbol{\xi}$ , the covariance matrix of the estimates

$$\boldsymbol{\Sigma}(\hat{\boldsymbol{\xi}}) = \mathbb{E} \left\{ (\hat{\boldsymbol{\xi}} - \boldsymbol{\xi}) (\hat{\boldsymbol{\xi}} - \boldsymbol{\xi})^T \right\} \quad (2.35)$$

is bounded as

$$\boldsymbol{\Sigma}(\hat{\boldsymbol{\xi}}) \geq \mathbf{J}^{-1}(\boldsymbol{\xi}), \quad (2.36)$$

where  $\mathbf{J}(\boldsymbol{\xi})$  is the so-called Fisher Information Matrix (FIM), whose inverse is the CRB matrix [43, 143]. The matrix inequality (2.36) implies that  $\boldsymbol{\Sigma}_{\hat{\boldsymbol{\xi}}} - \mathbf{J}^{-1}(\boldsymbol{\xi})$  is a positive semidefinite matrix. The elements of the FIM are defined as:

$$\begin{aligned} [\mathbf{J}(\boldsymbol{\xi})]_{ij} &= \mathbb{E} \left\{ \frac{\partial \ln p(\mathbf{x}; \boldsymbol{\xi})}{\partial \xi_i} \frac{\partial \ln p(\mathbf{x}; \boldsymbol{\xi})}{\partial \xi_j} \right\} \\ &= - \mathbb{E} \left\{ \frac{\partial^2 \ln p(\mathbf{x}; \boldsymbol{\xi})}{\partial \xi_i \partial \xi_j} \right\}, \end{aligned} \quad (2.37)$$

where the expectation is taken with respect to the observations  $\mathbf{x}$  conditioned upon  $\boldsymbol{\xi}$ , i.e., the likelihood function  $p(\mathbf{x}, \boldsymbol{\xi})$ . It is assumed that  $p(\mathbf{x}, \boldsymbol{\xi})$  satisfies the “regularity” conditions, i.e.,

$$\mathbb{E} \left\{ \frac{\partial \ln p(\mathbf{x}; \boldsymbol{\xi})}{\partial \boldsymbol{\xi}} \right\} = \mathbf{0} \quad \text{for all } \boldsymbol{\xi}. \quad (2.38)$$

Expression (2.36) provides a lower bound on the variance of any unbiased estimator of the parameter  $\xi_i$ :

$$\sigma_{\hat{\xi}_i}^2 = \mathbb{E} \left\{ (\hat{\xi}_i - \xi_i)^2 \right\} \geq \text{CRB}(\xi_i), \quad (2.39)$$

where  $\text{CRB}(\xi_i) \triangleq [\mathbf{J}^{-1}(\boldsymbol{\xi})]_{ii}$ . An estimator  $\hat{\xi}_i$  is said to be efficient if its variance attains the CRB, i.e., if (2.39) holds with equality.

In the asymptotic region of operation, the maximum-likelihood estimator (MLE)  $\hat{\boldsymbol{\xi}}_{\text{ML}}$  will be distributed according to

$$\hat{\boldsymbol{\xi}}_{\text{ML}} \stackrel{a}{\sim} \mathcal{N}(\boldsymbol{\xi}, \mathbf{J}^{-1}(\boldsymbol{\xi})), \quad (2.40)$$

with the FIM evaluated at  $\boldsymbol{\xi}$ . Expression (2.40) implies that ML estimators are asymptotically unbiased and asymptotically efficient. This property is particularly interesting because it provides a practical way to cross-validate the computed CRB and the estimated variance of the ML estimator.

If we consider a vector of complex observations  $\mathbf{x}$  distributed as

$$\mathbf{x} \sim \mathcal{CN}(\boldsymbol{\mu}(\boldsymbol{\xi}), \boldsymbol{\Sigma}_{\boldsymbol{\xi}}), \quad (2.41)$$

with its likelihood function

$$p(\mathbf{x}; \boldsymbol{\xi}) = \frac{1}{\pi^N \det(\boldsymbol{\Sigma}_{\boldsymbol{\xi}})} \exp\left\{- (\mathbf{x} - \boldsymbol{\mu}(\boldsymbol{\xi}))^H \boldsymbol{\Sigma}_{\boldsymbol{\xi}}^{-1} (\mathbf{x} - \boldsymbol{\mu}(\boldsymbol{\xi}))\right\}, \quad (2.42)$$

we can use the Slepian-Bangs' formula [43] to express the elements of the FIM of  $\boldsymbol{\xi}$  as:

$$[\mathbf{J}(\boldsymbol{\xi})]_{ij} = \text{Tr} \left\{ \boldsymbol{\Sigma}_{\mathbf{x}}^{-1}(\boldsymbol{\xi}) \frac{\partial \boldsymbol{\Sigma}_{\mathbf{x}}(\boldsymbol{\xi})}{\partial \xi_i} \boldsymbol{\Sigma}_{\mathbf{x}}^{-1}(\boldsymbol{\xi}) \frac{\partial \boldsymbol{\Sigma}_{\mathbf{x}}(\boldsymbol{\xi})}{\partial \xi_j} \right\} \quad (2.43)$$

$$+ 2\Re \left\{ \frac{\partial \boldsymbol{\mu}^H(\boldsymbol{\xi})}{\partial \xi_i} \boldsymbol{\Sigma}_{\mathbf{x}}^{-1}(\boldsymbol{\xi}) \frac{\partial \boldsymbol{\mu}(\boldsymbol{\xi})}{\partial \xi_j} \right\}. \quad (2.44)$$

## Chapter 3

# Parameter Estimation in GNSS-Reflectometry Scenarios with Coherent Reflection

The estimation precision achievable using GNSS-Reflectometry sensors in some scenarios is not fully understood yet. This chapter summarizes our attempt to narrow this gap for GNSS-R scenarios dominated by specular reflections when the LOS and reflected signals are received by the same antenna.

First, we compute the Cramér-Rao bound of the receiver's height and the surface's reflection coefficient in that scenario. We do so for the following GNSS signals: GPS L1 C/A and GPS L5 I/Q, which use BPSK, and Galileo E1 B/C and E5, which use BOC modulations. These signal are described in Chapter 2. We assume no specific architecture for the GNSS-R receiver. Thus, we derive the CRB for the signal model at the output of the receiver's front end, which implies that the CRB is taking into account all the information within the received signal. Therefore, the CRB expressions presented in this chapter represent a fundamental precision bound, independent of the considered GNSS receiver architecture.

Then, we evaluate the obtained CRB for the considered GNSS signals, as a function of the front end bandwidth and different scenario parameters, such as the actual propagation path difference between the LOS and the reflected signal, or the actual reflectivity of the reflecting surface. Initially, the CRB is computed for short observation intervals –i.e., up to 1 second– where the LOS signal and an arbitrary number of specular –therefore, coherent– reflections are present. The FIM's parameter transformation approach is used to adapt the general CRB obtained to our particular scenario, and to long observation times.

The second part of the chapter describes the proposed Segmented Maximum Likelihood (SML) algorithm. This algorithm can efficiently obtain the maximum likelihood estimate (MLE) of the same unknown parameters that we have considered when computing the CRB. The SML makes use of the particular properties of the likelihood –or cost– function under consideration transforming a complex optimization problem into several simple ones. To conclude this chapter, the root-mean-square error (RMSE) of the MLE obtained with the SML algorithm and simulated signal, is compared with the CRB as cross-validation.

The materials presented in this chapter have been already presented in [152], and published in [153], [154] (Section 3.1–Section 3.5), and [155] (Section 3.6).

### 3.1 Signal Model and Scenario Assumptions

This section describes the GNSS-R scenario considered in this chapter. Therefore, we summarize all of the relevant assumptions needed to particularize the received signal model at the output of the receiver’s RF front end. The properties of a reflected signal –particularly when compared with a LOS signal in the same scenario– will strongly depend on the scenario geometry and the reflecting/scattering surface [64]. It is precisely this dependency that makes it possible to estimate geophysical parameters from the received signal.

In this chapter, we narrow our analysis to a scenario similar to the one defined in [62]. In such scenario, the GNSS-R receiver is ground-based and stationary during the data acquisition. This receiver has a single antenna simultaneously receiving the LOS signal and a single reflected signal, with the latter being forwardly scattered from the specular reflection point on the surface. The geometry of this scenario is shown in Figure 3.1. RX represents the position of the receiver’s antenna phase center, located at a height  $h$ , defined as its orthogonal distance to the reflection surface. The point  $P$  marks the specular reflection point.

The reflection surface is assumed to be a horizontal planar surface with a homogeneous layered structure, i.e., the dielectric properties of the medium will only depend on the depth, i.e., the  $z$ -axis. These conditions are fulfilled by surfaces such as bare soil, snow or vegetation-covered soil, or calm waters. Because of the large distance separating the satellite and the receiver, the elevation angle of the signal incident at the specular reflection point, and at the receiver antenna can be considered both equal to the angle  $\theta$ . Our scenario’s reflection surface is considered smooth according to the Rayleigh criterion [64], therefore, the standard deviation of the surface height  $\sigma_{sh}$ , i.e., the surface roughness, satisfies

$$\sigma_{sh} < \frac{\lambda}{8 \sin(\theta)}, \quad (3.1)$$

where  $\lambda$  is the carrier signal wavelength. By default, we will assume a  $\sigma_{sh} = 0.01$  m, low enough to fulfill inequality (3.1) for the GNSS L1 and L5 carrier frequencies and  $\theta \leq 35^\circ$ .

According to [64], any reflected signal can be characterized as the sum of two contributions or components: one specular and another one diffuse. Under the smooth surface assumption, the coherent component reflected from the specular reflection point will clearly dominate, therefore, we can disregard the small contribution of the diffuse component in our analysis. Hence, we assume the reflected energy mainly coming from the first Fresnel zone [62, 64]. In this case, the reflected signal can be well approximated by a single delayed and complex-attenuated replica of the LOS signal. The first Fresnel zone is defined by the locus of points for which the trajectory difference (relative to the specular reflection point) is less than  $\lambda/2$ . Therefore, the first Fresnel zone describes an ellipse on the reflection surface (denoted as  $S$  in Figure 3.1) with:

$$a = \frac{b}{\sin(\theta)}; \quad b = \sqrt{\frac{\lambda h}{\sin(\theta)} + \left(\frac{\lambda}{2 \sin(\theta)}\right)^2}, \quad (3.2)$$

where  $a$  represents the ellipse’s semi-major axis –oriented towards the satellite’s azimuth– and  $b$  its semi-minor axis. As was also pointed out in [62, 64], the waves carrying the GNSS signals will acquire some degree of depolarization upon their reflection on dielectric media. While the wave corresponding to the LOS signal will be considered as purely RHCP, the

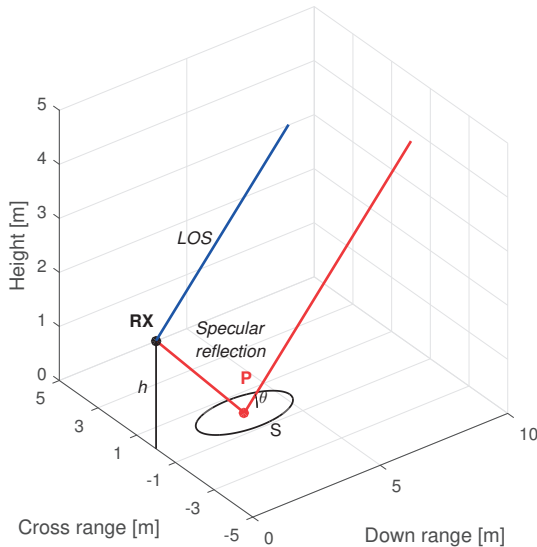


**Figure 3.1** – Scenario geometry depicting the propagation paths of the LOS (blue) and the specular reflection (red) signals. The values  $\theta = 30^\circ$  and  $h = 2$  m were used in this case as an example.

reflected wave can be described as a mix of both RHCP and left-hand circular polarization (LHCP) components.

We will assume a known radiation pattern for the receiving antenna, which effects for different polarizations of the received signals have been already considered within the modeling of the signals’ amplitude. Furthermore, we do not assume any maximum height for the receiver’s antenna phase center position in our scenario, as long as the smooth criterion defined by inequality (3.1) is still respected. In this dissertation, we study only the GPS L1 C/A and GPS L5 (both L5I and L5Q) signals, as well as on the Galileo E1 (E1B: data; and E1C: pilot) and the full Galileo E5 signals.

Although the GNSS signals –see Table 2.1 in Section 2.2– have different typical received powers [3, 9, 10], for comparison purposes, we assume a default carrier-to-noise ratio ( $C/N_0$ ) of the LOS signal impinging on the antenna of 45 dB-Hz in all cases.

### 3.1.1 Signal Model for the LOS Signal with Coherent Multipath

Let us particularize the signal model for the RF front end’s discrete output, described in sections 2.2 and 2.3.1, for the considered GNSS-R scenario. Without loss of generality, we concentrate our analysis to the single-satellite and single-signal scenario. That is reasonable given the low crosstalk among different GNSS signals, as well as the low cross-correlation among the different satellite spreading codes [12, 156]. Over a total observation time  $T_{obs}$ , we collect  $\mathbf{x} \in \mathbb{C}^{K \times 1}$ , at a sampling rate  $f_s$ , such that  $T_{obs} = K f_s^{-1}$ . The front end output at the sampling instant  $t_k = t_0 + k f_s^{-1}$ , where  $t_0$  is the time instant when the first measurement

was taken, can be expressed as

$$x(t_k) \approx \underbrace{\sum_{m=0}^{M-1} a_m d_m(t_k)}_{r(t_k)} + n(t_k), \quad (3.3)$$

where  $a_m$  is the complex amplitude at the instant  $t_0$  –referenced to the receiver’s local oscillator– of the  $m$ th signal component. The amplitudes  $a_m$ , which can be obviously expressed as:

$$a_m = u_m \exp\{j\phi_m\}, \quad (3.4)$$

are assumed deterministic and constant during observation time intervals of up to a 1 s. These amplitudes already include the effects of the receiver antenna’s gain for each specific signal component.  $n(t_k)$  is zero-mean circularly-symmetric complex Gaussian noise with temporal covariance defined by matrix  $\Sigma_{\mathbf{x}}$ . Hence,  $\mathbf{x}$  is a random vector distributed as  $\mathcal{CN}(\mathbf{r}, \Sigma_{\mathbf{x}})$ . The sampled basis-function  $d_m(t_k)$  in (3.3) is defined as:

$$d_m(t_k) = s \left( \left( 1 - \frac{f_{d,m}}{f_c} \right) t_k - \tau_m \right) \exp \{ -j2\pi f_{d,m} t_k \}, \quad (3.5)$$

where we recall  $s(t) \in \mathbb{C}$  representing the received filtered baseband navigation GNSS signal. For each signal component,  $\tau_m$  is the code delay at time  $t_0$ , and  $f_{d,m}$  is the Doppler shift of the carrier frequency.  $f_c$  is the nominal carrier frequency of the transmitted signal. We will also assume  $\tau_m$  and  $f_{d,m}$  over time intervals of up to 1 s. This assumption for  $f_{d,m}$  is justified by the very low rate of change of the Doppler shift observed by a static receiver [157]. Given the maximum rate of change of the relative speed possible in this case, i.e.,  $dv_m/dt|_{Max} \approx 0.178 \text{ m/s}^2$  [157],  $f_{d,m}/f_c$  can vary as little as  $\approx 5.94 \times 10^{-10}$  within a 1-s interval.

In our analysis, the RF front end’s low-pass filter has been simulated with a fifth-order Butterworth filter. Any distortion introduced by this filter is already taken into account in the modeling  $s(t)$ . The sampling frequency of the RF front end is considered equal to the Nyquist rate with complex sampling, i.e.,  $f_s = 2B_{f_e}$ , where  $B_{f_e}$  is the one-sided bandwidth (3 dB) of the low-pass filter. No quantization loss has been considered.

### 3.2 CRB Derivation for GNSS-R Coherent Reflection Scenarios

In this section, we derive the CRB given the output samples of the receiver’s RF front end over a total observation time  $T_{obs} \leq 1$  s. The signal model for these samples, specific for the GNSS-R coherent reflection scenario considered, has been defined in Section 3.1. We derive the general solution for  $M$  signal propagation paths. Then, we particularize this solution for our scenario, i.e., with  $M = 2$ , corresponding to the LOS signal and a single specularly reflected signal.

### 3.2.1 Definition and General Case for $M$ Propagation Paths

In Section 2.6, we have introduced the CRB as a convenient –yet powerful– statistical tool to study the performance of unbiased estimators. It provides a lower bound on the covariance matrix of any unbiased estimator for a set of deterministic parameters, as long as probability density function (PDF) of the measurements is known and depends on these parameters [43]. In fact, we recall that the CRB quantifies this dependency of the measurements’ PDF on the unknown estimation parameters. The stronger the PDF’s dependency on these parameters, the lower the CRB. The CRB of a vector with  $L$  unknown real-valued parameters  $\boldsymbol{\xi} \in \mathbb{R}^{L \times 1}$ , states that the covariance matrix of the estimates, i.e.,  $\boldsymbol{\Sigma}_{\hat{\boldsymbol{\xi}}}$ , must satisfy:

$$\boldsymbol{\Sigma}_{\hat{\boldsymbol{\xi}}} \geq \mathbf{J}^{-1}(\boldsymbol{\xi}), \quad (3.6)$$

where  $\mathbf{J}(\boldsymbol{\xi})$  is the Fisher information matrix (FIM), whose inverse is the CRB matrix. Let us recall from Section 2.6, that the elements in the FIM are given as:

$$[\mathbf{J}(\boldsymbol{\xi})]_{ij} = -E \left\{ \frac{\partial^2 \ln p(\mathbf{x}; \boldsymbol{\xi})}{\partial \xi_i \partial \xi_j} \right\}, \quad (3.7)$$

where  $\ln p(\mathbf{x}; \boldsymbol{\xi})$  is the log-likelihood function of  $\boldsymbol{\xi}$ , given the vector of random measurements  $\mathbf{x}$ . The CRB of the  $i$ th parameter in  $\boldsymbol{\xi}$  is simply the  $i$ th element in the CRB matrix’s main diagonal, i.e.,  $[\mathbf{J}^{-1}(\boldsymbol{\xi})]_{ii}$ .

In Section 3.1.1, we have defined the vector  $\mathbf{x}$ , modeling the discrete output of the receiver’s front end during the time interval  $T_{obs}$ . As previously described there, we assume  $\mathbf{x}$  to obey a circularly-symmetric complex Gaussian distribution. Its expected value vector is defined as  $\boldsymbol{\mu} = \mathbb{E}\{\mathbf{x}\} = \sum \mathbf{r}_m$ , with each of its  $K$  elements described by (3.3). We can express each signal component  $\mathbf{r}_m$  as a function of a subset of parameters in  $\boldsymbol{\xi}$ , i.e., as a function of the vector  $\boldsymbol{\xi}_m$ , which is defined as by grouping the unknown parameters related to the  $m$ th signal component as:

$$\boldsymbol{\xi}_m \triangleq \begin{bmatrix} u_m \\ \phi_m \\ \tau_m \\ f_{d,m} \end{bmatrix}, \quad (3.8)$$

where  $u_m$  represents the amplitude,  $\phi_m$  the phase shift,  $\tau_m$  the time-delay or code-phase, and  $f_{d,m}$  the carrier frequency Doppler. We also define the basis-function vector for the  $m$  signal component as  $\mathbf{d}_m \in \mathbb{C}^{K \times 1}$ , with each of its elements  $d(t_k)$  defined as in (3.5).

We want to jointly estimate the vector  $\boldsymbol{\xi} \in \mathbb{R}^{4M \times 1}$ , which is just the concatenation of all of the  $\boldsymbol{\xi}_m$  vectors. In our signal model we have assumed a Gaussian distribution of  $\mathbf{x}$ , and an additive noise component  $\mathbf{n}$ , independent of the useful signal. Therefore, we assume the covariance of the measurements  $\boldsymbol{\Sigma}_{\mathbf{x}}$  to be known. In such case the Slepian-Bangs’ formula [43] reduces to its second term only (see Section 2.6), and we can express the FIM elements

### Chapter 3. Param. Estimation in GNSS-R Scenarios with Coherent Reflection

simply as:

$$[\mathbf{J}(\boldsymbol{\xi})]_{ij} = 2\Re \left\{ \frac{\partial \boldsymbol{\mu}^H}{\partial \xi_i} \boldsymbol{\Sigma}_x^{-1} \frac{\partial \boldsymbol{\mu}}{\partial \xi_j} \right\}. \quad (3.9)$$

We can express the partial derivatives of  $\boldsymbol{\mu}$  with respect to the parameters in  $\boldsymbol{\xi}$  as

$$\frac{\partial \boldsymbol{\mu}}{\partial u_m} = \frac{\partial \mathbf{r}_m}{\partial u_m} = \mathbf{d}_m \exp \{j\phi_m\}, \quad (3.10)$$

$$\frac{\partial \boldsymbol{\mu}}{\partial \phi_m} = \frac{\partial \mathbf{r}_m}{\partial \phi_m} = ju_m \mathbf{d}_m \exp \{j\phi_m\}, \quad (3.11)$$

$$\frac{\partial \boldsymbol{\mu}}{\partial \tau_m} = \frac{\partial \mathbf{r}_m}{\partial \tau_m} = u_m \frac{\partial \mathbf{d}_m}{\partial \tau_m} \exp \{j\phi_m\}, \quad (3.12)$$

$$\frac{\partial \boldsymbol{\mu}}{\partial f_{d,m}} = \frac{\partial \mathbf{r}_m}{\partial f_{d,m}} = u_m \frac{\partial \mathbf{d}_m}{\partial f_{d,m}} \exp \{j\phi_m\}. \quad (3.13)$$

It is worth noticing that the FIM  $\mathbf{J}(\boldsymbol{\xi}) \in \mathbb{R}^{4M \times 4M}$  can be conveniently expressed as the following symmetric block matrix:

$$\mathbf{J}(\boldsymbol{\xi}) = \begin{pmatrix} \mathbf{J}_{\xi_0 \xi_0} & \mathbf{J}_{\xi_0 \xi_1} & \cdots & \\ \mathbf{J}_{\xi_0 \xi_1}^T & \ddots & & \\ \vdots & & & \mathbf{J}_{\xi_{M-1} \xi_{M-1}} \end{pmatrix}, \quad (3.14)$$

where the elements of each sub-matrix  $\mathbf{J}_{\xi_m \xi_l} \in \mathbb{R}^{4 \times 4}$  are computed as:

$$[\mathbf{J}_{\xi_m \xi_l}]_{ij} = 2\Re \left\{ \frac{\partial \mathbf{r}_m^H}{\partial \xi_i} \boldsymbol{\Sigma}_x^{-1} \frac{\partial \mathbf{r}_l}{\partial \xi_j} \right\}, \quad (3.15)$$

with  $\xi_i \in \{\xi_m\}$  and  $\xi_j \in \{\xi_l\}$ . Expression (3.15) can be used to compute the elements of  $\mathbf{J}(\boldsymbol{\xi})$ , and the CRB of  $\boldsymbol{\xi}$  is then straightforwardly obtained as the main diagonal elements of  $\mathbf{J}^{-1}(\boldsymbol{\xi})$ .

Let us now examine the case where only thermal noise is present. Since we have considered the sampling rate to be a multiple of the Nyquist sampling frequency, the samples in  $\mathbf{x}$  can be considered uncorrelated, which implies a diagonal covariance matrix, i.e.,  $\boldsymbol{\Sigma}_x = \sigma_w^2 \mathbf{I}$ . The noise variance  $\sigma_w^2$  can be computed as:

$$\sigma_w^2 = \frac{N_0}{2} \int_{-\infty}^{\infty} |H_{Rx}(f)|^2 df = N_0 B_n, \quad (3.16)$$

where  $N_0/2$  is the assumed white noise spectral density in W/Hz,  $H_{Rx}(f)$  is the front end's normalized baseband filter response in the frequency domain and  $B_n$  is defined as the equivalent noise bandwidth (one-sided). Thus, for the specific case of complex white Gaussian



noise (CWGN), we can express (3.15) as:

$$\mathbf{J}_{\boldsymbol{\xi}_m \boldsymbol{\xi}_l} = \frac{2}{\sigma_w^2} \Re \left\{ \begin{pmatrix} \mathbf{d}_m^H \mathbf{d}_l & j u_l \mathbf{d}_m^H \mathbf{d}_l & u_l \mathbf{d}_m^H \frac{\partial \mathbf{d}_l}{\partial \tau_l} & u_l \mathbf{d}_m^H \frac{\partial \mathbf{d}_l}{\partial f_{d,l}} \\ -j u_m \mathbf{d}_m^H \mathbf{d}_l & u_m u_l \mathbf{d}_m^H \mathbf{d}_l & -j u_m u_l \mathbf{d}_m^H \frac{\partial \mathbf{d}_l}{\partial \tau_l} & -j u_m u_l \mathbf{d}_m^H \frac{\partial \mathbf{d}_l}{\partial f_{d,l}} \\ u_m \frac{\partial \mathbf{d}_m^H}{\partial \tau_m} \mathbf{d}_l & j u_m u_l \frac{\partial \mathbf{d}_m^H}{\partial \tau_m} \mathbf{d}_l & u_m u_l \frac{\partial \mathbf{d}_m^H}{\partial \tau_m} \frac{\partial \mathbf{d}_l}{\partial \tau_l} & u_m u_l \frac{\partial \mathbf{d}_m^H}{\partial \tau_m} \frac{\partial \mathbf{d}_l}{\partial f_{d,l}} \\ u_m \frac{\partial \mathbf{d}_m^H}{\partial f_{d,m}} \mathbf{d}_l & j u_m u_l \frac{\partial \mathbf{d}_m^H}{\partial f_{d,m}} \mathbf{d}_l & u_m u_l \frac{\partial \mathbf{d}_m^H}{\partial f_{d,m}} \frac{\partial \mathbf{d}_l}{\partial \tau_l} & u_m u_l \frac{\partial \mathbf{d}_m^H}{\partial f_{d,m}} \frac{\partial \mathbf{d}_l}{\partial f_{d,l}} \end{pmatrix} \right\} \times \exp \{-j \phi_{ml}\}, \quad (3.17)$$

with  $m, l \in \{0, \dots, M-1\}$  and  $\phi_{ml} \triangleq \phi_m - \phi_l$ .

On the other hand, if we can take the narrowband signal approximation, which implies  $f_{d,m}/f_c \approx 0$ , then the FIM obtained –and as a result, the CRB– is analogous to the results described in [150], where the CRB was derived for two propagation paths case using a similar approach. In addition, Skournetou et al. used in [158] an approach similar to the one described here, but for the case of up to four signal propagation paths.

### 3.2.2 Two Propagation Path Case for a Ground-Based Static Receiver

To compute the CRB for the scenario described in Section 3.1, we assume  $M = 2$ , with the  $\mathbf{r}_0$  component used to represent the LOS signal and  $\mathbf{r}_1$  used for the specular reflection. In this scenario, we are considering static receiver, where as a result, the LOS signal and the specular reflection will experience the same Doppler shift; thus,  $f_{d,0} = f_{d,1} \triangleq f_d$ . The FIM matrix elements –defined as in (3.17)– related to  $f_{d,0}$  or  $f_{d,1}$ , and a different parameter in  $\boldsymbol{\xi}$ , will become approximately zero. This implies that the Doppler estimates will become uncorrelated to the estimates of the rest of parameters, i.e., they will *decouple*. The same conclusion was reached by Pany et al. in [150] when computing the CRB for two propagation paths with small difference between their carrier Doppler shifts.

Having the Doppler shift parameters decoupled from the rest of unknown parameters allows us to disregard the estimation of the  $f_d$  for the rest of our analysis. The reason is that we are only interested in estimating the geometry of the scenario and the characteristics of the reflecting surface. In a stationary environment,  $f_d$  cannot be related with any of the geophysical parameter that we want to retrieve. Thus, we now redefine the vector of unknown parameters  $\boldsymbol{\xi}$ , by redefining each  $\boldsymbol{\xi}_m$  to just  $[u_m, \phi_m, \tau_m]^T$ . In addition, we define the normalized discrete autocorrelation function (ACF) of the signal  $s(t)$  as:

$$R_{ss}(\tau) = \frac{1}{K} \sum_{k=0}^{K-1} s^* \left( \left(1 - \frac{f_d}{f_c}\right) t_k + \tau \right) s \left( \left(1 - \frac{f_d}{f_c}\right) t_k \right). \quad (3.18)$$

Moreover, we introduce the following identities<sup>1</sup>:

$$R_{ss}(\tau_{ml}) = \frac{1}{K} \mathbf{d}_m^H \mathbf{d}_l, \quad (3.19)$$

$$R'_{ss}(\tau_{ml}) = -\frac{1}{K} \frac{\partial \mathbf{d}_m^H}{\partial \tau_m} \mathbf{d}_l = \frac{1}{K} \mathbf{d}_m^H \frac{\partial \mathbf{d}_l}{\partial \tau_l}, \quad (3.20)$$

$$R''_{ss}(\tau_{ml}) = -\frac{1}{K} \frac{\partial \mathbf{d}_m^H}{\partial \tau_m} \frac{\partial \mathbf{d}_l}{\partial \tau_l}. \quad (3.21)$$

<sup>1</sup>Notice that  $R_{ss}(\tau) = R_{ss}(-\tau)$ ,  $R'_{ss}(\tau) = -R'_{ss}(-\tau)$ , and  $R''_{ss}(\tau) = R''_{ss}(-\tau)$ .

### Chapter 3. Param. Estimation in GNSS-R Scenarios with Coherent Reflection

Notice that in order to keep our notation as simple as possible, we use  $R'_{ss}(\tau_{ml})$  and  $R''_{ss}(\tau_{ml})$  to indicate the 1st and 2nd order partial derivatives of  $R_{ss}(\tau)$  with respect to the  $\tau$ , evaluated at the specific  $\tau_{ml}$  value, which has been defined as  $\tau_{ml} \triangleq \tau_m - \tau_l$ . Identities (3.19)–(3.21) are obtained straightforwardly by applying the chain rule, and they allow to express (3.17) as:

$$\mathbf{J}_{\xi_m \xi_l} = \frac{2K}{\sigma_w^2} \begin{pmatrix} R_{ss}(\tau_{ml}) \cos(\phi_{ml}) & u_l R_{ss}(\tau_{ml}) \sin(\phi_{ml}) & -u_l R'_{ss}(\tau_{ml}) \cos(\phi_{ml}) \\ -u_m R_{ss}(\tau_{ml}) \sin(\phi_{ml}) & u_m u_l R_{ss}(\tau_{ml}) \cos(\phi_{ml}) & -u_m u_l R'_{ss}(\tau_{ml}) \sin(\phi_{ml}) \\ u_m R'_{ss}(\tau_{ml}) \cos(\phi_{ml}) & -u_m u_l R'_{ss}(\tau_{ml}) \sin(\phi_{ml}) & -u_m u_l R''_{ss}(\tau_{ml}) \cos(\phi_{ml}) \end{pmatrix}. \quad (3.22)$$

With only two propagation paths; and using (3.17), the FIM can be expressed as the  $6 \times 6$  block matrix

$$\mathbf{J}(\boldsymbol{\xi}) = \begin{pmatrix} \mathbf{J}_{\xi_0 \xi_0} & \mathbf{J}_{\xi_0 \xi_1} \\ \mathbf{J}_{\xi_0 \xi_1}^T & \mathbf{J}_{\xi_1 \xi_1} \end{pmatrix}, \quad (3.23)$$

where each submatrix is computed as in (3.22).

Given (3.22), we notice that  $\mathbf{J}(\boldsymbol{\xi})$  will be a function of the ACF of  $s(t)$  and first and second order derivatives with respect to the delay, evaluated at  $\tau_{ml}$ . Conveniently, the ACF and its derivatives can be expressed using their relationship with the signal's power spectral density (PSD). By making use of the well-known Wiener–Khinchin theorem [43] and the properties of the Fourier transform, we have that the  $n$ th-order derivative of  $R_{ss}(\tau)$  with respect to  $\tau$ , evaluated at  $\tau = \tau_{ml}$ , can be expressed as:

$$R_{ss}^{(n)}(\tau_{ml}) = \int_{-\infty}^{\infty} (j2\pi f)^n S_{ss}(f) e^{j2\pi f \tau} df \Big|_{\tau=\tau_{ml}}, \quad (3.24)$$

where  $S_{ss}(f)$  represents the PSD of the signal  $s((1 - f_d/f_c)t)$ . Notice that  $s((1 - f_d/f_c)t)$  represents the filtered signal at the output of the receiver's RF front end, scaled in the time domain due to the Doppler effect. In our derivation, any filtering distortion is taken into account within  $R_{ss}(\tau)$  and its derivatives. Nonetheless, if we are interested in evaluating the influence of the front end's filtering on the resulting CRB, it might be more convenient to express  $S_{ss}(f)$  as

$$S_{ss}(f) = |H_{Rx}(f)|^2 S(f), \quad (3.25)$$

where  $S(f)$  is the PSD of the signal received at the antenna. In [36], the authors followed this approach to study the effects of using different front end bandwidths and filter types in the estimation performance of the interferometric GNSS-R technique [6, 111]. They considered also the bandwidth limitation of the signal transmitted by the satellite. Instead, in our approach, we generate a model of  $s(t)$  for samples at the output of the front end –and thus implicitly modeling its effects on the received signal–, and then, we compute the signal  $s(t)$ 's ACF and its derivatives.

The selected front end bandwidth, i.e.,  $B_{fe}$ , will influence the shape of the normalized ACF. The higher the  $B_{fe}$ , the sharper the ACF, as long as  $B_{fe}$  is less or equal than the transmitted signal's bandwidth. Obviously,  $B_{fe}$  will also impact the shape and magnitude of the ACF derivatives  $R_{ss}^{(n)}(\tau)$ . The total number of samples considered within  $T_{obs}$  will also depend on  $B_{fe}$ , as  $K = T_{obs}/(2B_{fe})$ .

### 3.2. CRB Derivation for GNSS-R Coherent Reflection Scenarios

If we consider the support of  $R(\tau_{ss})$  to be approximately limited to the interval  $[-T_c, T_c]$ , where  $T_c$  is the signal's code chip period, then, according to (3.22), we have  $\mathbf{J}_{\xi_m \xi_l} \approx \mathbf{0}$  for propagation path differences greater than  $\rho_{chip} = T_c c$ , where  $c$  is the signal propagation speed. This is a direct consequence of the autocorrelation properties of PRN codes [12]. Moreover,  $\mathbf{J}(\boldsymbol{\xi})$  becomes a diagonal matrix, therefore, all of the parameters in  $\boldsymbol{\xi}$  are now uncoupled. From the FIM calculation point of view, this is equivalent to having a receiver with two synchronized RF front end channels, with uncorrelated noise components, and two different antennas: an up-looking one, exclusively receiving the LOS signal, and a second down-looking antenna, solely receiving the reflected signal.

#### 3.2.3 Introducing Phase Coherence Using FIM's Parameter Transformation

So far, we have obtained  $\mathbf{J}(\boldsymbol{\xi})$ , i.e., an expression for the FIM of  $\boldsymbol{\xi}$  given the scenario defined in Section 3.1. Actually, within the GNSS-R context, we are more interested in a different set of unknown parameters. These parameters must be directly related to the geometry of the scenario, as well as to the electrical properties of the reflecting surface. Up to this point, our signal model has not taken into account the phase coherence presented by specular reflections. Phase coherence implies that the LOS and the reflected signals have approximately the same frequency and a constant phase difference (at least over short periods of time) between them and with respect to the local oscillator, which is used as a reference in the receiver. Phase coherence enables the stationary interference between the signals.

For the sake of flexibility, we have decided to compute the CRB for  $\boldsymbol{\xi}$  and then transform it for a new set of parameters  $\boldsymbol{\Psi}$ . This transformation of  $\mathbf{J}(\boldsymbol{\xi})$  allows us to conveniently introduce the phase coherence assumption. We define the new vector of unknown parameters as

$$\boldsymbol{\Psi} = \begin{bmatrix} u_0 \\ \phi_0 \\ \rho_0 \\ |\Gamma| \\ \phi_\Gamma \\ h \end{bmatrix}, \quad (3.26)$$

where  $u_0$ ,  $\phi_0$ ,  $\rho_0$  are the amplitude, phase and propagation distance ( $\rho_0 = \tau_0 c$ ) for the LOS signal.  $\Gamma = |\Gamma| \exp\{j\phi_\Gamma\}$  is the reflected signal coefficient, which is defined as the complex attenuation experienced by the reflected signal when compared to the LOS signal. Its amplitude is defined as

$$|\Gamma| = \frac{u_1}{u_0}. \quad (3.27)$$

$\Gamma$  takes into account the surface reflectivity coefficient and the antenna complex gain for the received signal's polarization. Thus, it will depend on the satellite's observed elevation angle  $\theta$ , and on the azimuth angle of arrival of the reflected signal to the antenna. Since  $\theta$  varies very slowly over time [157], we assume it to remain constant for observation periods up to 1 s.  $h$  is the height of the receiver, defined as the orthogonal distance between the antenna phase center and the reflection surface. In our horizontal surface scenario,  $h$  can be expressed as a function of the propagation path difference between the LOS and the reflected signals, i.e.,

$\Delta\rho$ , as

$$h = \frac{\Delta\rho}{2 \sin(\theta)}, \quad (3.28)$$

with  $\Delta\rho = (\tau_1 - \tau_0)c$ . In addition, because of the coherence assumption, the phase difference between the two signal components, i.e.,  $\phi_{1,0} = \phi_1 - \phi_0$ , can be expressed as:

$$\phi_{1,0} = \phi_\Gamma - \frac{2\pi}{\lambda} \Delta\rho, \quad (3.29)$$

where  $\lambda$  is the carrier wavelength.

Following the approach described in [143], we can express the FIM for  $\Psi$  as

$$\mathbf{J}(\Psi) = \mathbf{T}\mathbf{J}(\xi)\mathbf{T}^T, \quad (3.30)$$

where  $\mathbf{T} \in \mathbb{R}^{6 \times 6}$  is the transformation matrix defined as

$$\mathbf{T} = \frac{\partial \xi}{\partial \Psi}, \quad (3.31)$$

which is just the transpose of the Jacobian matrix [43]. The specific expressions for each of the elements of  $\mathbf{T}$  are provided in Appendix A. The CRB for the parameters in  $\Psi$  can be directly obtained as the diagonal elements of  $\mathbf{J}^{-1}(\Psi)$ .

This two-step approach, i.e., first computing the FIM for  $\xi$  and then transforming it, has been used due to its simplicity. It allows to redefine the bound for a different set of parameters and to introduce more assumptions into our signal model without having to derive the FIM expression from scratch.

### 3.3 Analysis of the CRB for Short Observation Intervals

The transformed FIM matrix  $\mathbf{J}(\Psi)$ , derived in the previous section, shows that the  $\text{CRB}(\Psi)$  in the specular reflection scenario considered will depend on:

1. **The geometry of the scenario:** through the propagation path difference between the two signal components  $\Delta\rho$ , which is a function of  $h$  and the satellite elevation angle  $\theta$  (and its variation) during the observation time.
2. **The properties of the reflecting surface:** through its reflection coefficient  $\Gamma$ , which can be modeled as a function of the signal's incident angle, the electrical properties of the reflecting medium and the roughness of the reflecting surface.
3. **The GNSS signal considered and the receiver features:** the signal modulation and its transmission bandwidth, the power of the LOS signal, the antenna's radiation pattern and the receiver front end's bandwidth –and its assumed filtering scheme– will all influence the resulting CRB.

### 3.3. Analysis of the CRB for Short Observation Intervals

However, understanding these dependencies only by inspecting the  $\mathbf{J}^{-1}(\Psi)$  matrix is not straightforward. The expressions for  $\mathbf{J}^{-1}(\Psi)$  diagonal elements can be, in the general case, quite cumbersome due to their large number of terms. Nonetheless, we start our analysis by examining the specific case when  $\Delta\rho > \rho_{chip}$ , causing the initial FIM  $\mathbf{J}(\xi)$  to become a diagonal matrix, which greatly simplifies the terms in the final  $\mathbf{J}^{-1}(\Psi)$ . Later on, we also study the other case in which  $\Delta\rho < \rho_{chip}$ .

#### 3.3.1 CRB when $\Delta\rho > \rho_{chip}$

When  $\Delta\rho > \rho_{chip}$ , not only the diagonal terms for the resulting  $\mathbf{J}^{-1}(\Psi)$  matrix, i.e.,  $[\mathbf{J}^{-1}(\Psi)]_{ii}$ , are much simpler, but also this assumption is particularly relevant since it corresponds to the best estimation case, i.e., the CRB for this case lower bounds all other cases with shorter  $\Delta\rho$ . As shown in Appendix A, after some simple algebra, we obtain the following expressions for the CRB of  $h$  and  $|\Gamma|$  in  $\Psi$ :

$$\text{CRB}(h) = -\frac{1}{8\gamma \text{SNR}_0 \sin^2(\theta) \left(\frac{R''_{ss}(0)}{c^2}\right)}, \quad (3.32)$$

$$\text{CRB}(|\Gamma|) = \frac{|\Gamma|^2 + 1}{2 \text{SNR}_0 R_{ss}(0)}, \quad (3.33)$$

where we have introduced the coefficient  $\gamma$ , defined as:

$$\gamma = \frac{|\Gamma|^2}{|\Gamma|^2 + 1}, \quad (3.34)$$

and  $\text{SNR}_0$  represents the equivalent SNR as if only the LOS signal would be present and, as such, it can be expressed as:

$$\text{SNR}_0 = \frac{u_0^2}{\sigma_w^2} K = 2 C/N_0 T_{obs}, \quad (3.35)$$

where  $C/N_0$  is the carrier-to-noise ratio of the LOS signal observed at the receiver's front end output. Notice the amplitude  $u_0$  in (3.35) already takes into account the effects of the receiver's antenna gain pattern for the received LOS signal, which is dependent on the signal incident angle, i.e., a function of  $\theta$  and the orientation of the antenna. From examining Equations (3.32) and (3.33), we can directly deduce the following:

1. As expected, both CRB expressions are inversely proportional to  $\text{SNR}_0$ . However,  $\text{CRB}(h)$  is also inversely proportional to  $\sin^2(\theta)$ . This poses a trade-off: we require low elevations for the smooth surface assumption to hold, but at the same time, the lower the elevation, the higher the  $\text{CRB}(h)$ . Moreover, as shown by Equation (3.2), low elevation angles imply larger first Fresnel zone areas, which decrease the spatial resolution of our estimates.
2. The values that  $\text{CRB}(|\Gamma|)$  can take as a function of  $|\Gamma|$  are bounded, as a consequence of having defined  $\Gamma$  as an amplitude ratio, with  $0 < |\Gamma| \leq 1$ .

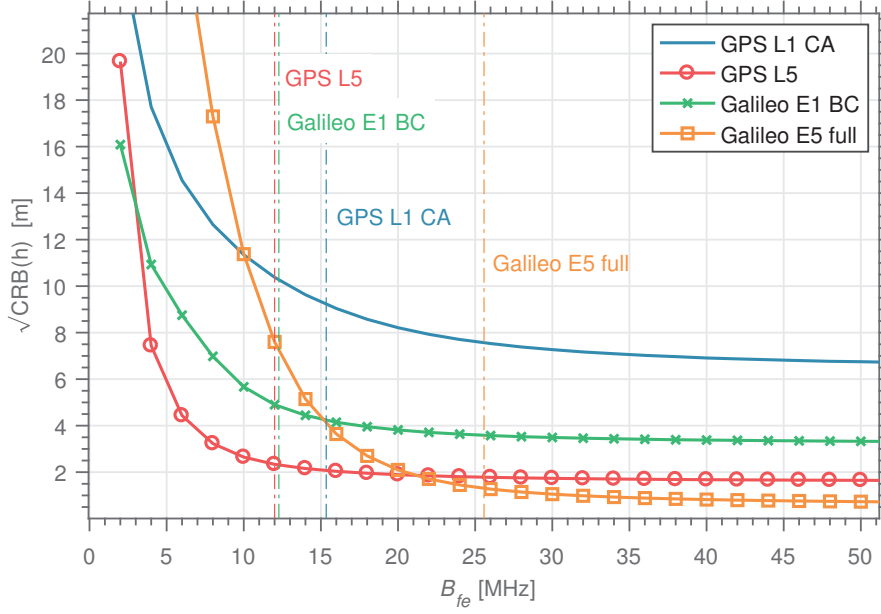


**Figure 3.2** –  $\sqrt{\text{CRB}(h)}$  as a function of the front end’s bandwidth for the different GNSS signals considered. Computed from the inverse of Eq. (3.30). Vertical dashed lines represent the  $B_{Tx}/2$  (one-sided bandwidth) for each signals.

3. In both CRB expressions, the effects of the received signal bandwidth and the front end filtering –possible losses and distortions– are modeled within the  $R''(0)$  and the ACF’s main peak, i.e.,  $R(0)$ .  $R''(0)$  can be understood as the curvature or the sharpness of  $R(0)$ . The higher the front end bandwidth, the larger  $R''(0)$  becomes. This holds only as long as the front end bandwidth is narrower than the received signal bandwidth, otherwise there will be no additional sharpening on the resulting  $R(0)$ . Besides, for a higher front end bandwidth, the  $\text{SNR}_0$  will also increase if the Nyquist sampling rate assumption is maintained, as a consequence of having more samples for the same  $T_{obs}$ .

In Figure 3.2, we show the results obtained when computing  $\text{CRB}(h)$  using expression (3.32) as a function of the front end’s bandwidth  $B_{fe}$ , for the different GNSS signals considered. Notice that in Figure 3.2, the  $y$ -axis represents<sup>2</sup>  $\sqrt{\text{CRB}(\Psi_i)}$ . To obtain these results, we assumed an isotropic antenna, and set  $|\Gamma|$  to  $\sqrt{0.1}$ , which corresponds to an attenuation of 10 dB in the reflected signal power with respect to the LOS signal. The  $T_{obs}$  considered was equal to 1 s.  $\Delta\rho$  was set to 600 m in order to ensure isolation between the LOS and the reflected signal components provided by the code correlation properties. We observe how the  $\text{CRB}(h)$  consistently decreases when increasing  $B_{fe}$  for all the GNSS signals studied, as long as  $B_{fe}$  remains lower than the (one-sided) signal bandwidth  $B_{Tx}$ . The slight decrease in  $\text{CRB}(h)$  for all GNSS signals observed in Figure 3.2 when  $B_{fe} > B_{Tx}/2$  is explained due to the use of a non-ideal low-pass filter, like the one explained in Section 3.1.1, to model the constrained transmission bandwidth. Also in Figure 3.2, we observe how  $\sqrt{\text{CRB}(h)}$  stays in the meter-order, except for the Galileo E5 signal, which reaches decimeter-order precision when  $B_{fe} > 40$  MHz, due to its highest bandwidth. The CRB of the rest of parameters in  $\Psi$  is jointly obtained when computing  $\mathbf{J}^{-1}(\Psi)$ .

In (3.29), we have expressed the phase difference between the two signal components as the sum of two contributions:  $\phi_\Gamma$  and  $(2\pi/\lambda)\Delta\rho$ , with the latter capturing the shift due to

<sup>2</sup>The convention of representing the  $\sqrt{\text{CRB}}$  in the figures is followed consistently along this entire thesis

### 3.3. Analysis of the CRB for Short Observation Intervals

the extra propagation path of the specular reflection. For short observation intervals, where both of these contributions to  $\phi_{1,0}$  remain constant, it is not possible to estimate both of them accurately at the same time. This issue is easily spotted by examining the expression for CRB( $\phi_\Gamma$ ), i.e., the fifth element in  $[\mathbf{J}^{-1}(\boldsymbol{\Psi})]_{ii}$  –derived in Appendix A–, which can be approximated as

$$\text{CRB}(\phi_\Gamma) \approx -\frac{c^2 k^2 R(0)}{2\gamma \text{SNR}_0 R''(0)}, \quad (3.36)$$

where  $k = 2\pi/\lambda$  is the wavenumber for the received signal carrier. The numerator in (3.36) will usually be many orders of magnitude higher than the denominator, causing  $\sqrt{\text{CRB}(\phi_\Gamma)} \gg 2\pi$  rad. This implies that we cannot estimate  $\phi_\Gamma$  properly. Given this ambiguity in separately estimating the two contributions to  $\phi_{1,0}$ , performing precise phase altimetry becomes only possible if we assume  $\phi_\Gamma$  to be known or small enough that it can be neglected. Even if we considered the phase coherence in our derivation of CRB( $h$ ), expression (3.32) becomes equivalent to the CRB for pure GNSS-R code-based altimetry only, i.e., as if no phase information were used.

The CRB of  $h$  for code-based altimetry can also be purposely derived by following the FIM transformation approach described in the previous section. To do so, we just need to assume no phase coherence between the LOS and the reflected signals, i.e., considering  $\phi_{1,0}$  as the difference between two independent phases when computing the  $\mathbf{T}$  transformation matrix defined in (3.31), which leads to the same results as in (3.32).

In [58, 159], the authors characterized the code-tracking precision of GPS receivers by deriving the minimum code thermal noise jitter when using noncoherent DLL discriminators, i.e.,  $\sigma_{\text{DLL}}^2$ . The expressions provided in their results are very frequently used to characterize the tracking performance of different receiver architectures [12]. We can use these same expressions to compute the minimum variance on the  $h$  estimate, i.e.,  $\sigma_h^2$ , in a straightforward way, as

$$\sigma_h^2 \geq \frac{c^2 (\sigma_{\text{DLL}-0}^2 + \sigma_{\text{DLL}-1}^2)}{4 \sin^2(\theta)}, \quad (3.37)$$

where  $\sigma_{\text{DLL}-0}^2$  and  $\sigma_{\text{DLL}-1}^2$  are the minimum variances of the LOS and the reflected signals' code delays, respectively. In (3.37), two independent tracking channels are assumed: one tracking the LOS signal and the other tracking the reflected signal. The results when computing (3.37) match the CRB( $h$ ) values obtained using expression (3.32) when  $\Delta\rho > \rho_{\text{chip}}$ , which correspond to the flat part of the curves later shown in Figure 3.3. Then, it follows that a two-tracking channel architecture for code altimetry is efficient in terms of the bound defined in expression (3.32), given a sufficiently large propagation path difference. In practice, such a scenario might appear unlikely for ground-based receivers. Nonetheless, many of the GNSS modern signals have higher bandwidths, which implies lower  $\rho_{\text{chip}}$  values (e.g., 293 m for GPS L1 C/A signal versus 29.3 m for GPS L5) [12].

In the previous discussion, we have highlighted the problem arising when trying to separately estimate the two contributions to  $\phi_{1,0}$  and how the CRB for the joint estimation of  $\boldsymbol{\Psi}$  captures this effect. However, what if we assume some prior knowledge of one of the two terms in  $\phi_{1,0}$ ? We examine now the impact on the CRB if one of these terms is known, which represents the best case scenario. We study two cases: (1) when  $\phi_\Gamma$  is known, referred

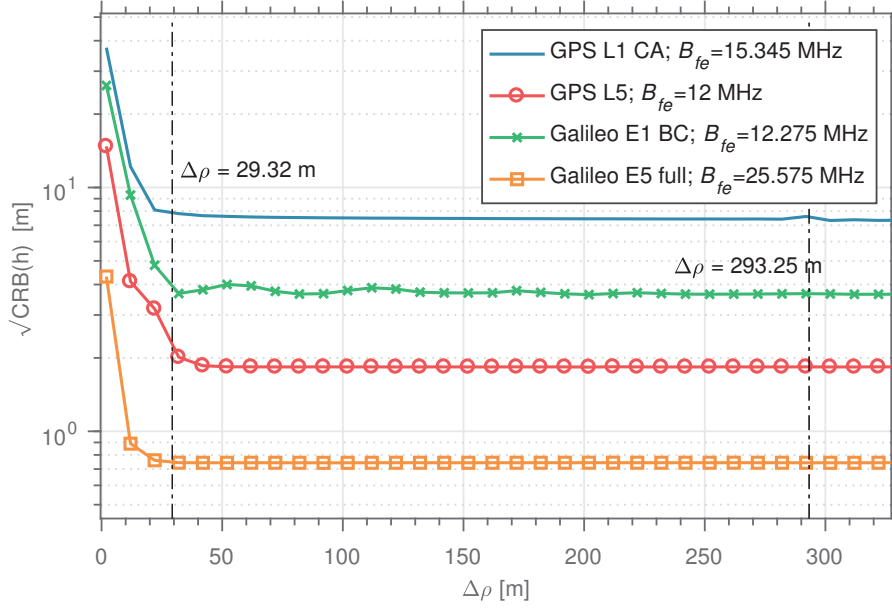


**Figure 3.3** –  $\sqrt{\text{CRB}(h)}$  as a function of  $\Delta\rho$  computed by numerical evaluation of Eq. (3.30)’s inverse.  $B_{fe}$  is the bandwidth of the receiver’s front end assumed for each signal, set to match the signal bandwidth, i.e.,  $B_{Tx}/2$  (see Table 2.1). The two vertical lines represent the chip lengths: 293.25 m, of the GPS L1 CA and Galileo E1 BC signals; and 29.32 m, of the GPS L5 and Galileo E5 signals. The CRB values for the flat regions can be computed using (3.32)

to as “phase altimetry” case; and (2) when  $h$  is known, referred to as “reflection coefficient estimation” case.

### Phase Altimetry

In this case, we assume that the angle  $\phi_\Gamma$  is known. Now, in order to obtain the new  $\text{CRB}_{alt}(h)$  expression, we remove the row and the column of  $\mathbf{J}(\Psi)$  associated with  $\phi_\Gamma$  to later compute the matrix inversion  $\mathbf{J}^{-1}(\Psi)$ , as described in Appendix A. We obtain the following expression:

$$\begin{aligned} \text{CRB}_{alt}(h) &= \frac{1}{8\gamma \text{SNR}_0 \sin^2(\theta) \left( k^2 R(0) - \frac{R''(0)}{c^2} \right)} \\ &\approx \frac{1}{32\gamma \text{SNR}_0 R(0)} \left( \frac{\lambda}{\pi \sin(\theta)} \right)^2, \end{aligned} \quad (3.38)$$

given the fact that  $R''(0)/c^2$  will be very small (e.g.,  $\approx 0.1$  for the worst case, i.e., the Galileo E5 signal with  $B_{fe} = B_{Tx}$ ) compared to  $k^2 R(0)$  (e.g.,  $\approx 623$ ) for the signal bandwidths considered. The phase information is now effectively used and the bound becomes multiple orders of magnitude lower. As expected, it is directly proportional to  $\lambda^2$ , i.e., the lower the carrier wavelength, the higher the possible precision of the  $h$  estimate. We also observe that when comparing expression (3.38) with expression (3.32), the dependence on  $R''(0)$  can be neglected now. This implies the estimation performance of the phase altimetry techniques should be negligibly impacted by the bandwidth of the signal used. As a consequence, the use of the new GNSS with higher bandwidths, but with the same carrier frequency, should



### 3.3. Analysis of the CRB for Short Observation Intervals

bring little improvement to the achievable precision of the phase altimetry techniques for short  $T_{obs}$  when  $\Delta\rho > \rho_{chip}$ .

#### Reflection Coefficient Estimation

Here, similarly to previous section, we compute  $\text{CRB}_r$  of  $|\Gamma|$  and  $\phi_\Gamma$  (subindex  $r$ ), but in this case, we proceed by removing the row and the column associated with  $h$ , as shown, once again, in Appendix A. We obtain the following expressions:

$$\text{CRB}_r(|\Gamma|) = \text{CRB}(|\Gamma|), \quad (3.39)$$

$$\text{CRB}_r(\phi_\Gamma) = \frac{1}{2\gamma \text{SNR}_0 R(0)}. \quad (3.40)$$

As expected,  $\text{CRB}_r(|\Gamma|)$  is the same as in the case of the joint estimation of  $\Psi$ , while  $\text{CRB}_r(\phi_\Gamma)$  is now orders of magnitude smaller when compared to expression (3.36), and well below  $2\pi$ , thus implying that in this case, it is possible to obtain useful phase estimates.

#### 3.3.2 CRB when $\Delta\rho < \rho_{chip}$ : Interference Case

When  $\Delta\rho < \rho_{chip}$ , we cannot process anymore the two signals separately, which was otherwise possible thanks to the small autocorrelation for delays longer than the chip duration exhibited by PRN codes. Now, the initial FIM  $\mathbf{J}(\xi)$  is no longer a diagonal matrix, and the analytic expressions for  $[\mathbf{J}^{-1}(\Psi)]_{ii}$  become quite cumbersome. Thus, from now on, we will rely on numerical evaluation of  $[\mathbf{J}^{-1}(\Psi)]_{ii}$  to compute the CRB.

In Figure 3.3, we show the results of computing  $\text{CRB}(h)$  as a function of  $\Delta\rho$  for the different GNSS signals considered. Once again, we have taken  $|\Gamma|^2 = 0.1$ , and  $T_{obs} = 1$  s.

As expected, we observe that when  $\Delta\rho$  increases, the bound reaches the values obtained using expression (3.32). Moreover, we also observe that the CRB reaches these values even for  $\Delta\rho < \rho_{chip}$ . That is a consequence of the higher transmission bandwidth: the asymptotic value for the bound is reached faster (see Galileo E5), which is related to having sharper ACF peaks. Besides, the higher the signal bandwidth, the lower the value of the bound for any  $\Delta\rho$ .

Figure 3.4 shows the results of computing  $\text{CRB}(h)$  for different  $\Delta\rho$  and  $|\Gamma|$  values. The plots presented allow us to visually determine, approximately, the order of magnitude of the best achievable precision given a  $\Delta\rho$  and  $|\Gamma|$  combination. The  $y$ -axis represents  $|\Gamma|^2$ , which in practice is equivalent to the gain experienced by the reflected signal compared to the LOS signal. As expected, for  $\Delta\rho$  values higher than  $\rho_{chip}$ , the CRB agrees with the one obtained using expression (3.32). Figure 3.3 confirms that the CRB when  $\Delta\rho > \rho_{chip}$  lower bounds all of the other cases, as we had hypothesized at the beginning of this section.

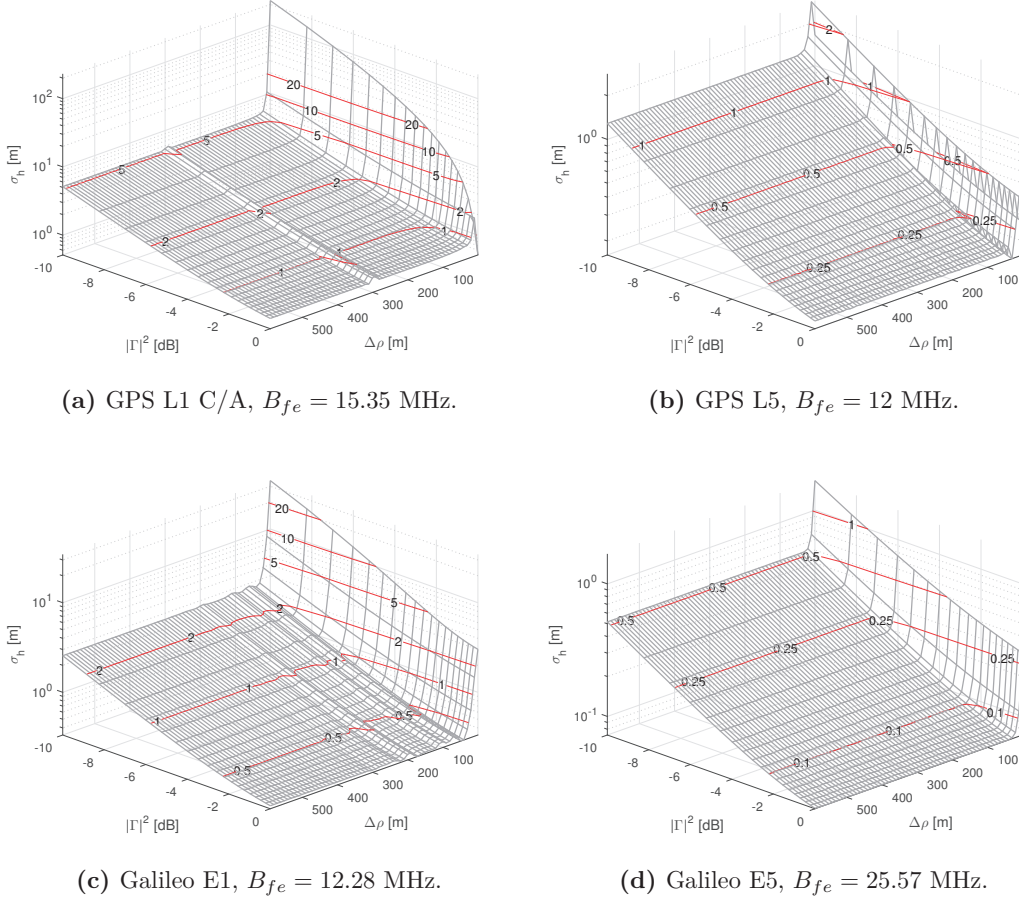


**Figure 3.4** –  $\sqrt{\text{CRB}(h)}$  for different  $|\Gamma|^2$  and  $\Delta\rho$  values. Computed by numerical evaluation of Eq. (3.30). Red lines are used to represent the level curves, each one labeled with its corresponding value of  $\sqrt{\text{CRB}(h)}$  (in m).  $B_{fe}$  represents the assumed front end’s one-sided 3-dB bandwidth.

### 3.4 Derivation of the CRB for Long Observation Intervals: $\text{CRB}(\Psi_{long})$

So far, we have assumed total observation times of up to just one second. However, some GNSS-R techniques, such as the IPT, can use much longer observation times, even reaching on the order of several minutes in some cases. Can we use the CRB expressions obtained in Sections 3.2.3 and 3.3 for such long observation times? Unfortunately, we cannot use them for  $T_{obs}$  longer than one second. This is due to the fact that, for  $T_{obs} \gg 1$  s, the approximation of considering the parameters in  $\Psi$  to be constant over  $T_{obs}$ , described in Section 3.1.1, is no longer valid.

If  $T_{obs} \gg 1$ , the change in the delay of the received LOS signal cannot be well approximated as a linear expression with an initial value of  $\tau_0$  anymore. In addition, neither the Doppler shift observed, nor the phase shift  $\phi_0$  with respect to the receiver oscillator can be considered as constant over such  $T_{obs}$ . That is due to the non-linear relative movement of the satellite and the receiver over long observation times, due to the signal propagating through the atmosphere –which affects the signal as it varies with time–, and due to the phase error introduced by the receiver’s local oscillator noise [12]. In addition, the direction in which

### 3.4. Derivation of the CRB for Long Observation Intervals: $\text{CRB}(\Psi_{long})$

the signals impinge on the antenna –i.e., their direction-of-arrival– will vary over time as a consequence of the variation of the satellite’s elevation, i.e.,  $\theta$ , and the azimuth angles observed. Subsequently, this variation can result in a change in the LOS signal’s amplitude  $u_0$  and an extra phase shift, i.e., a variation of  $\phi_0$ , since these two parameters already account for the effect of the receiver’s antenna gain pattern.

Modeling the reflection coefficient  $\Gamma$  for realistic scenarios, even for homogeneous and horizontal flat surfaces, can be a complex matter. Nonetheless, we still can characterize  $\Gamma$  as a function of the vector  $\mathbf{s}_\Gamma$ , containing the  $L_\Gamma$  parameters related to the reflection surface physical properties; the signal’s impinging angle on the surface; and the antenna gain towards the specular reflection point [64]. The two last terms can be expressed as a function of  $\theta$ . Thus, we have

$$\Gamma(\theta) = f(\theta; \mathbf{s}_\Gamma). \quad (3.41)$$

If we consider  $h$  and the parameters in  $\mathbf{s}_\Gamma$  as constant over  $T_{obs} > 1$  s, then we can compute the CRB for a new vector of unknown parameters  $\Psi_{long}$ , defined as:

$$\Psi_{long} \triangleq \begin{bmatrix} \mathbf{u}_0 \\ \phi_0 \\ \boldsymbol{\rho}_0 \\ \mathbf{s}_\Gamma \\ h \end{bmatrix}, \quad (3.42)$$

where  $\mathbf{u}_0$ ,  $\phi_0$  and  $\boldsymbol{\rho}_0$  are column vectors of  $L$  elements, which we refer to as “fast-varying” parameters. In our analysis, these parameters are associated with the values of  $u_0$ ,  $\phi_0$  and  $\tau_0$  at the  $l$ -th time interval of  $T_{coh} = 1$  s duration, with  $L = T_{obs}/T_{coh}$  being the total number of these intervals for  $T_{obs}$ . We assume that  $\theta$  remains constant over each  $T_{coh}$  interval. This assumption is very reasonable given the fact that the rate of change of  $\theta$  over time observed by ground-based static receivers is very low, i.e., on the order of  $10^{-3}$  °/s [157].

Now, we can use the kind of FIM parameter transformation approach introduced in Section 3.2.3, to obtain  $\text{CRB}(\Psi_{long})$ . This approach allows us to compute  $\mathbf{J}(\Psi_{long})$  as a function of the  $\mathbf{J}(\Psi)$  for each of the different  $L$  short time intervals  $T_{coh}$ . In order to do so, we first need to define the vector  $\Psi_{ext}$  of unknown parameters as:

$$\Psi_{ext} \triangleq \begin{bmatrix} \Psi_0 \\ \vdots \\ \Psi_{L-1} \end{bmatrix}, \quad (3.43)$$

where each subvector  $\Psi_l$  corresponds to the  $l$ -th  $T_{coh}$  observation interval. We build now the –block diagonal– “extended” FIM matrix  $\mathbf{J}(\Psi_{ext})$  as:

$$\mathbf{J}(\Psi_{ext}) \triangleq \begin{pmatrix} \mathbf{J}(\Psi_0) & & \mathbf{0} \\ & \ddots & \\ \mathbf{0} & & \mathbf{J}(\Psi_{L-1}) \end{pmatrix} \quad (3.44)$$

$$= \text{diag} \{ \mathbf{J}(\Psi_0), \dots, \mathbf{J}(\Psi_{L-1}) \}, \quad (3.45)$$

where each  $\mathbf{J}(\Psi_l)$  is the FIM computed using expressions (3.23)–(3.31) for the  $l$ -th  $T_{coh}$  observation interval. The  $\mathbf{J}(\Psi_{ext})$  generated is equivalent to assuming all of the parameters in any  $\Psi_l$  are independent from any of the parameters in a different subvector  $\Psi_k$ . This assumption is only used as a tool to introduce the parameter dependencies between observation intervals by transforming  $\mathbf{J}(\Psi_{ext})$ , once again, using a new transformation matrix  $\mathbf{T}_{long} \in \mathbb{R}^{6L \times P}$  [143], defined as:

$$\mathbf{T}_{long} = \frac{\partial \Psi_{ext}}{\partial \Psi_{long}}. \quad (3.46)$$

The number of columns in the matrix  $\mathbf{T}_{long}$ ,  $P$ , is equal to the number of parameters in  $\Psi_{long}$ , i.e.,  $P = 3L + L_\Gamma + 1$ . Since the parameter  $h$  was already in  $\Psi$  and is considered constant for all of the  $L$  intervals,  $\partial h_l / \partial h = 1, \forall l$ . Finally,  $\mathbf{J}(\Psi_{long})$  is obtained as:

$$\mathbf{J}(\Psi_{long}) = \mathbf{T}_{long} \mathbf{J}(\Psi_{ext}) \mathbf{T}_{long}^T. \quad (3.47)$$

A more detailed description of how the matrix  $\mathbf{T}_{long}$  is constructed is provided in Appendix A. The CRB of the  $i$ th parameter can be obtained directly as  $[\mathbf{J}^{-1}(\Psi_{long})]_{ii}$ . Furthermore, we shall emphasize that the previous derivation is independent of the model of  $\Gamma$  considered, as long as the gradients of  $|\Gamma|$  and  $\phi_\Gamma$  with respect to  $\mathbf{s}_\Gamma$  exist. No assumption was made regarding the number of parameters in  $\mathbf{s}_\Gamma$ . Nonetheless, it is well known that the CRB can only increase with the number of unknown parameters considered, which intuitively makes sense, given the increased uncertainty [43, 143].

### 3.5 Analysis of the CRB for Long Observation Times

In this section, we compute the CRB using expression (3.47) for different simulation cases. Our goal is to study the effect of the received signal's elevation change during the observation time ( $\Delta\theta$ ), and the impact of the GNSS signal modulation, over the theoretical achievable precision in the estimation of the parameters in  $\Psi_{long}$ .

The variation of  $\theta$  during the observation time has the following implications:

1.  $\Delta\rho$  will change due to the displacement of the specular reflection point. In addition, the angle of arrival of the LOS and reflected signals to the antenna will also vary.
2. If the reflection coefficient  $\Gamma$  is assumed to depend on  $\theta$ , this will also change during the observation time.

Up to this point, we have not selected any specific model for the reflection coefficient  $\Gamma$ . From now on, we will use the model for a single-layer bare soil introduced in [62], which we will call the Zavorotny–Larson model (Z-L). This model is described in Appendix B, but basically, it specifies  $\Gamma$  as a function of  $\theta$  and the following parameters:

$$\mathbf{s}_\Gamma = [\varepsilon_r, \sigma]^T, \quad (3.48)$$

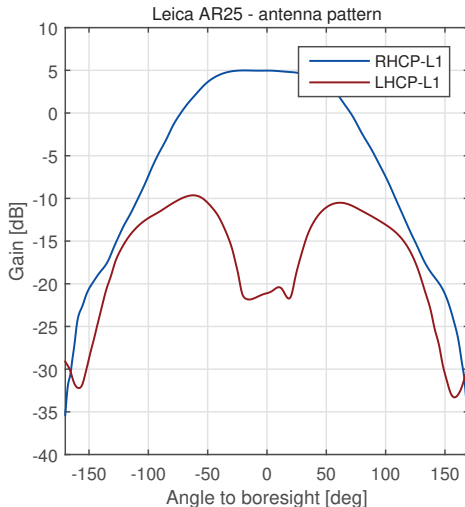


**Figure 3.5** – Leica GNSS AR25 antenna’s gain as a function of the angle to the boresight for RHCP and LHCP at L1 carrier frequency

where  $\varepsilon_r$  and  $\sigma$  are the real part of the surface’s relative permittivity and the surface conductivity, respectively, which are considered constant over the entire observation interval. Notice that this model for  $\Gamma$  is used as an example in our analysis and that the approach proposed to obtain  $\mathbf{J}(\Psi_{long})$  can accommodate other models for  $\Gamma(\theta; \mathbf{s}_\Gamma)$ .

Furthermore, the gain of the receiving antenna will have an important impact on the CRB. To characterize it, we consider two possible antenna cases in our analysis:

1. An ideal case, with an isotropic antenna model.
2. A Leica GNSS AR25 antenna [160] model. Only the antenna gain’s amplitude has been modeled. The antenna phase center is assumed to be located at the distance  $h$  perpendicular to the reflection surface. The antenna boresight is pointing upwards, parallel to the surface normal vector (i.e., with an elevation of  $90^\circ$ ). We have used the pattern model provided as part of the open source GPS multipath simulator [161], depicted in Figure 3.5.

In both cases, we take the assumption that the antenna complex gain is accurately known and that the entire available signal’s energy is considered, by defining the receiver’s front end bandwidth as  $B_{fe} = B_{Tx}/2$ .

### 3.5.1 CRB( $\Psi_{long}$ ) vs. $\Delta\theta$

In this first case, we compute the CRB for different  $h$  values and elevation spans  $\Delta\theta$ , covering from  $\theta_0 = 10^\circ$  to  $\theta = 35^\circ$ . In the results presented herein, the first individual  $\Delta\theta$  value represents a particular case, corresponding to a single short observation interval of  $T_{obs} = 1$  s, with no change in  $\theta$ , set to  $10^\circ$ . In this case, the bound matches the results obtained using the short-period CRB derived in Section 3.2. The reflected signal has perfect LHCP reflection with constant  $|\Gamma|^2 = -10$  dB.

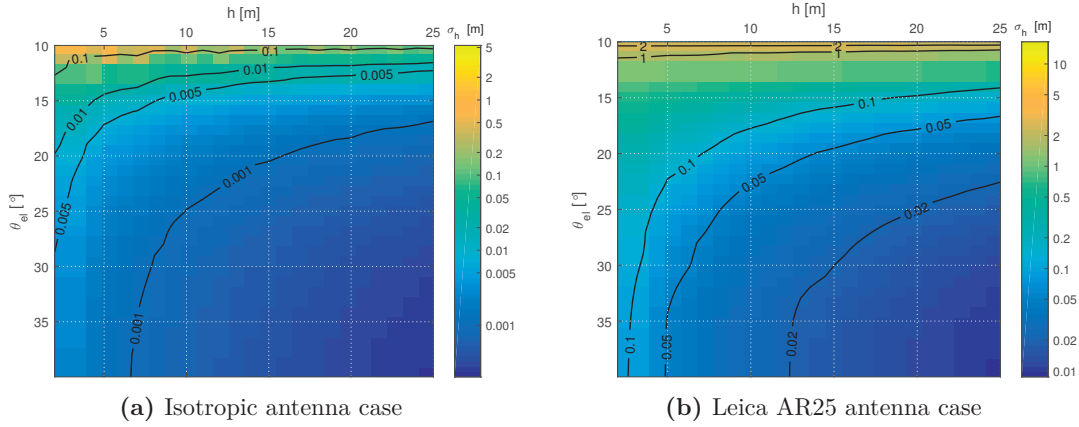


**Figure 3.6** –  $\sqrt{\text{CRB}(h)}$  for different  $\Delta\theta$ 's (vertical axis), starting from an initial elevation of  $10^\circ$ , and true receiver heights  $h$  (horizontal axis). Computed by numerically evaluating the inverse of Eq. (3.47). Black lines represent the level curves for the values labeled on top of them.

Figure 3.6 shows the  $\text{CRB}(h)$  computed in the isotropic antenna and the AR25 antenna cases, with GPS L1 C/A signal. The highest CRB values depicted in the figure are located at the left-upper corner. They correspond to the low antenna height values (below 5 m) and short elevation spans (below  $15^\circ$ ). The CRB values decrease almost monotonically with both, the increase of  $h$ , and the elevation span covered. As expected, the plots show that the antenna pattern has a very significant impact on  $\text{CRB}(h)$  given the same  $h$  and  $\Delta\theta$ .

Besides, Figure 3.6a shows that sub-millimeter precision could be attained in the ideal isotropic antenna case. In the AR25 antenna case, however, the plot in Figure 3.6b shows that only centimeter precision can be achieved. These CRB values are significantly lower than the CRB values computed previously in Section 3.2. Firstly, given the considered satellite elevation rate of  $5 \times 10^{-3} \text{ }^\circ/\text{s}$ , the observation time is above the hour duration for  $\Delta\theta > 18^\circ$ . The longer the observation time considered, the more independent samples we collect, thus the lower CRB values obtained. Secondly, the CRB computed now takes into account the phase difference information, which can be used for the estimation of  $h$ . Intuitively, it is possible to estimate the sum of two contributions conforming the reflected signal's phase because they have a different rate of change: the phase shift due to the scenario geometry (related to  $h$ ) and the phase shift due to the polarization change due to the reflecting surface properties, i.e., to  $\Gamma$ .

Having a higher true  $h$  has two main implications. First, the higher the  $h$  gets, the faster the oscillation rate of the interference pattern observed in the composite amplitude of the received signal with the change of satellite elevation. Second, the  $\Delta\rho$  will be larger, which makes it easier to isolate the two signal components, given the code's autocorrelation properties, and the resulting CRB can be lower, as we have shown in Section 3.2. However, techniques like the IPT only use the output of the estimated SNR, or the prompt correlator (single output), and they can only work if there is interference between the LOS and the reflected signals, i.e., when  $\Delta\rho < \rho_{chip}$  [26]. Thus, with the IPT, we face a trade-off: we require low  $\Delta\rho$  values in order to observe the interference pattern, but according to the CRB expressions obtained, low  $\Delta\rho$  values degrade the achievable estimation precision.

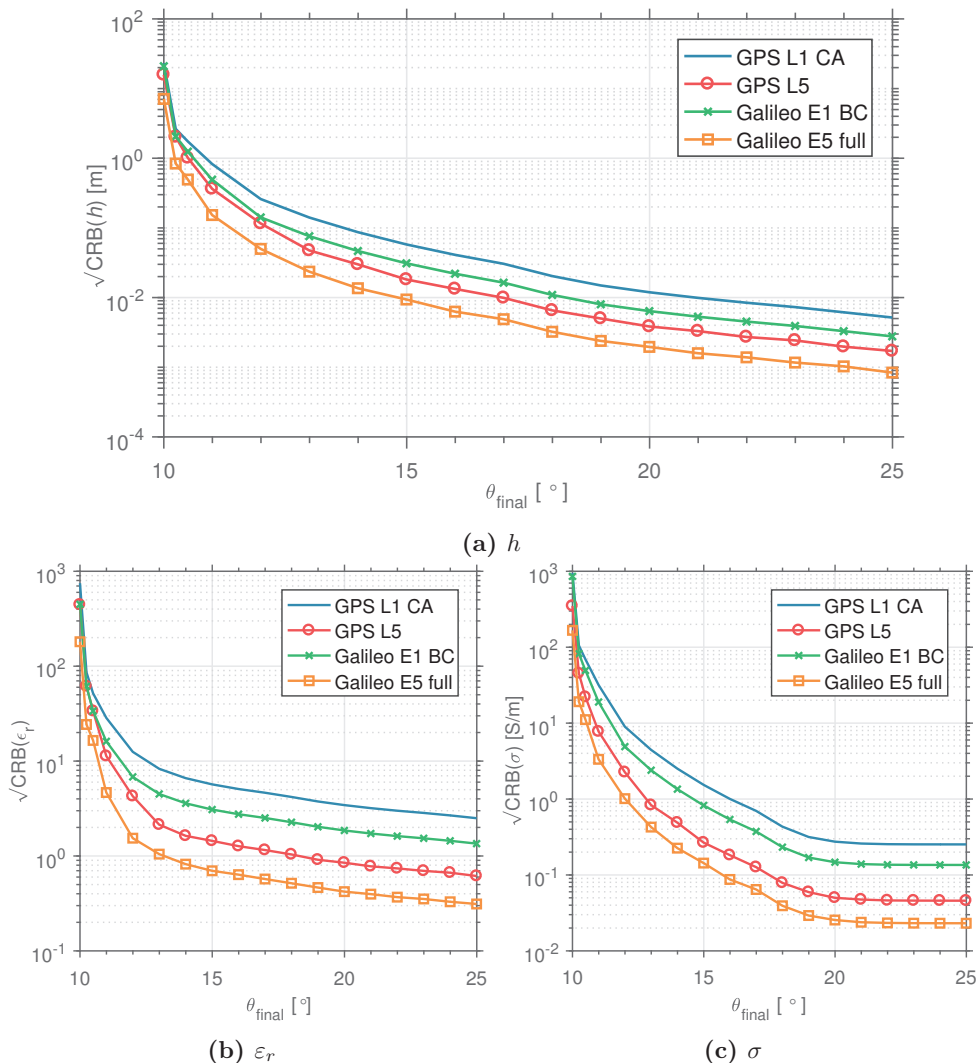


**Figure 3.7** –  $\sqrt{\text{CRB}}$  for different  $\Delta\theta$  starting from an initial  $\theta_0 = 10^\circ$ . Computed by numerically evaluating the inverse of Eq. (3.47).

### 3.5.2 Effects of the Signal Modulation on the $\text{CRB}(\Psi_{long})$

We now present the results of computing the CRB of  $\mathbf{s}_\Gamma$  and  $h$ , given  $\Delta\theta$  spans of different lengths and the considered GNSS signals. For each signal, we have considered a particular  $B_{fe} = B_{Tx}/2$ . We have considered the Leica AR25 antenna model [160, 162], and a true receiver height  $h = 3$  m. We have also used the Z-L model to define  $\Gamma(\theta)$ , given a wet ground surface with a permittivity (real part)  $\epsilon_r = 30$  and a conductivity  $\sigma = 0.2$  S/m [163]. The initial  $\theta$  is  $10^\circ$  for all of the elevation spans considered.

The results obtained are summarized in Figure 3.7. Each data point represented in the figure corresponds to the results for a particular  $\Delta\theta$ , with its value on the  $x$ -axis representing the final  $\theta$  angle achieved in that span. The first data point (left of the plot) corresponds to a single  $T_{coh}$  observation. As expected, the longer the  $\Delta\theta$  covered during the observation time, the lower the CRB values obtained, for all three parameters. However, this improvement is not linear. We observe how the CRB decreases significantly for  $\Delta\theta$ s covering up to  $\sim 2^\circ$ , while it decreases at a much slower rate when extending  $\Delta\theta$  beyond that value. This observed

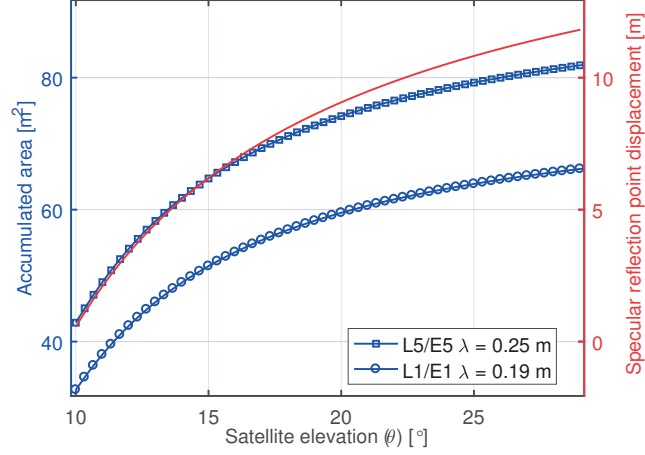


**Figure 3.8** – Accumulated area within the first Fresnel zone for  $h = 3$  m with the variation of  $\theta$ . Right axis shows the displacement of the specular reflection point from its initial location when  $\theta = 10^\circ$ .

behavior can be explained as follows. For our scenario and given the GNSS signals' carrier wavelength, i.e., from 0.19–0.25 m, a  $\Delta\theta$  of  $\sim 2^\circ$  is required to observe a  $2\pi$  phase shift in the reflected signal phase, caused exclusively due to the change in  $\Delta\rho$ . In the IPT context, this corresponds to observing a single complete oscillation of the SNR interference pattern.

Longer  $\Delta\theta$ , i.e., longer observation times still provide some improvement. It is important to highlight the existing trade-off between extending  $\Delta\theta$ , i.e., extending the observation time, and the displacement of the specular reflection point over the reflection surface. The change in  $\theta$  also changes the size of the first Fresnel zone. For low elevation angles, such as the ones needed to consider to ensure the smooth surface assumption, the change in the area covered by the first Fresnel zone and the displacement of the specular reflection point is significant, as shown in Figure 3.8. The GPS L5 and Galileo E5 signals have slightly different carrier frequencies (1176.45 MHz and 1191.795 MHz, respectively), but both of their wavelengths have been approximated to the same  $\lambda = 0.25$  m for Figure 3.8. In practice, it is unlikely to find real surfaces that are that flat and homogeneous –and with no obstacles–, except maybe for the case of calm water surfaces. On the other hand, the antennas used in practice (e.g., in geodetic sites) have lower cross-coupling at lower elevation angles, i.e., less attenuation on the LHCP signal for these elevations. Therefore, we observe higher oscillation amplitudes of the SNR interference pattern for low  $\theta$  angles in standard GNSS geodetic receivers [62, 116].

We shall also notice that even for long observation times, where we can use the signal's phase information in the parameter estimation, the higher the signal's bandwidth, the lower the CRB for all of the parameters. This relationship is because for a  $h = 3$  m,  $\Delta\rho$  is small enough for the two signal components to interfere, and the separability provided by the PRN code's autocorrelation properties acts only partially. This separability is needed to measure the code delay difference between the two components, which is required to unambiguously estimating  $h$ . That cannot be done by using only the phase difference  $\phi_{1,0}$ .

We would like to highlight that, if, over the  $\Delta\theta$  covered, the  $\Gamma$  coefficient changes substantially, lower CRB values of  $\varepsilon_r$  or  $\sigma$  can be achieved with shorter  $\Delta\theta$ . These substantial changes are likely to be observed when the current  $\Delta\theta$  covers the Brewster angle [26, 64]. Intuitively, if the pdf of the observed signal changes significantly with the variation of the unknown parameters, such as  $\varepsilon_r$  or  $\sigma$ , then it is easier to estimate these parameters from



the observed samples, resulting in lower CRB values. Likewise, when the  $\Gamma$  coefficient barely changes during the observation time considered, it becomes harder to unambiguously retrieve the  $\varepsilon_r$  or  $\sigma$  parameters from the observed samples, thus resulting in higher CRB values.

Figure 3.7 shows that centimeter precision can be theoretically achieved when estimating  $h$  over elevation spans larger than  $20^\circ$  for all GNSS signals. The CRB results also show that millimeter precision can be theoretically achieved for  $\Delta\theta = [10^\circ, 25^\circ]$ , in the case of the Galileo E5 signal, i.e., when using its full bandwidth. In practice, however, it is unlikely to find real surfaces that are that flat and homogeneous (and with no obstacles), except maybe for very calm water surfaces. Thus, the millimeter precision is unlikely to be achieved by any estimator in a practical scenario, even with the assumptions made in this chapter (e.g., perfect knowledge of the antenna gain pattern, and the satellite elevation angle). The asymptotic behavior observed over long observation times of the CRB of the conductivity  $\sigma$  can be related to the small dependency and change of  $\Gamma$  during the considered elevation spans for the dry ground surface.

## 3.6 The Segmented ML Algorithm

So far in this chapter, we have computed the CRB that determines the best estimation precision achievable by GNSS-R techniques using the phase information and working with long observation times –on the order of tens or hundreds of seconds–. The Interference Pattern Technique (IPT) –described in Section 2.4.2– is probably the most popular among those. However, there is still no consensus about the optimal estimation technique to retrieve the height of the receiver and the permittivity of the reflecting surface from the noisy interference pattern observed, either on the estimated SNR, the estimated  $C/N_0$ , or the correlator’s output (see e.g., [61, 103, 164, 165]).

In the sections below we propose to use the maximum likelihood estimator in combination with the Z-L model for the reflection coefficient  $\Gamma$ . Unfortunately, this estimator does not have a closed-form expression. In addition, the measurements’ dependency on the parameters that we want to estimate is highly non-linear, resulting into a computationally demanding optimization problem. To overcome this limitation, we propose a new computationally efficient way to compute the MLE, the Segmented Maximum Likelihood (SML) algorithm.

### 3.6.1 Signal Model at the Output of the Prompt Correlator

The SML algorithm utilizes the receiver’s prompt correlator –complex– as its input. According to the scenario considered, described in Section 3.1, we assume the receiver is tracking the sum of the LOS signal and a single specularly reflected signal. The height  $h$  of the receiver antenna considered is sufficiently small to fulfill  $\Delta\rho < \rho_{chip}$ . For simplicity, we assume that the satellite azimuth ( $\phi$ ) remains constant. Under this assumption, the satellite and the receiver are contained within the same vertical plane over the entire signal observation period.

The receiver tracking loop selected here to study the SML is the widely used combination of DLL for the code tracking and a PLL for the carrier tracking [12]. Without loss of generality, we can assume that the total carrier frequency observed has been completely removed by the tracking loop. As previously described in Section 3.2.2, in a scenario where the receiver is stationary, LOS and specularly reflected signals will experience the same Doppler shift [11]. Moreover, we ignore the data bit transitions in our analysis by assuming that the receiver

### Chapter 3. Param. Estimation in GNSS-R Scenarios with Coherent Reflection

has already achieved bit synchronization and that external assistance –providing the data sequence– is available.

During the tracking stage, we can express the –complex– output of the prompt correlator at instant  $t_n = nT_{int}$ , with  $T_{int}$  as the correlation time, as:

$$y(t_n) = y_n = \underbrace{a_{0,n} R_{s\hat{s}}(\tau_{0,n} - \hat{\tau}_n)}_{r_{0,n}} + \underbrace{a_{1,n} R_{s\hat{s}}\left(\tau_{0,n} + \frac{\Delta\rho_n}{c} - \hat{\tau}_n\right)}_{r_{1,n}} + \eta_n \quad (3.49)$$

where  $r_{0,n}$  and  $r_{1,n}$  are the LOS and reflected signal components, respectively.  $\eta_n$  is zero-mean complex white Gaussian noise, which is generated after correlating the noise at the front end output with the local replica of the signal.  $R_{s\hat{s}}(\tau)$  is the discrete correlation of the received signal's code  $s(t)$  –after being filtered by the receiver's front end– with the locally generated signal replica  $\hat{s}(t)$ . It is expressed as

$$R_{s\hat{s}}(\tau) = \frac{1}{K} \sum_{k=0}^{K-1} \hat{s}^*(t'_k - \tau) s(t'_k), \quad (3.50)$$

where we recall  $K$  being the number of samples per  $T_{int}$ .  $t'_k$  is the sampling instant stretched due to the Doppler effect on  $s(t)$  [12], i.e.,  $t'_k = (1 - f_d/f_c) t_k$ . Under the assumption taken that carrier Doppler  $f_d$  can be (almost) perfectly compensated, the local replica is generated with the same code Doppler as the receiver signal.  $\Delta\rho_n$  is the path difference between the LOS and the reflected component –previously introduced in expression (3.28), in Section 3.2.3– at  $t_n$ . We recall that  $\Delta\rho$  in the considered scenario can be expressed as:

$$\Delta\rho_n = \Delta\rho(t_n) = 2h \sin(\theta(t_n)). \quad (3.51)$$

Finally, the complex amplitudes  $a_{0,n}$  and  $a_{1,n}$  in (3.49) can be expressed as

$$a_{0,n} = u_0 G_{\text{RHCP},n} \exp\{j\Delta\phi_{0,n}\}, \quad (3.52)$$

$$a_{1,n} = u_0 \Gamma_n \exp\left\{j\left(\Delta\phi_{0,n} + \frac{2\pi}{\lambda}\Delta\rho_n\right)\right\}, \quad (3.53)$$

where:

- $u_0$  is the amplitude of the LOS signal impinging on the antenna, i.e., before any antenna gain. In here, we assume it remains approximately constant over the entire observation time.
- $\Delta\phi_{0,n}$  is the phase difference between the true LOS carrier phase and the PLL estimate at time  $t_n$ , i.e.,  $\Delta\phi_{0,n} \triangleq \phi_{0,n} - \hat{\phi}_n$ .
- $G_{\text{RHCP},n}$  is the antenna complex amplitude gain for RHCP polarization. As such, it is a function of the received signal's direction-of-arrival at time  $t_n$ .
- $\lambda$  is the carrier wavelength, e.g.,  $\approx 0.1904$  m for the GPS L1 signal.
- $\Gamma_n \in \mathbb{C}$  is the reflectivity coefficient –we recall it from Section 3.2.3–, that depends on the surface electrical properties and the signal incidence angle at time  $t_n$ .

As in Section 3.5, we utilize again the Z-L model for single layer bare-soil surfaces, proposed in [62] and described in Appendix B. We also utilize this model for calm water surfaces. The Z-L model actually captures the depolarization of the GPS signal upon its reflection, the attenuation or loss of coherence due to the surface roughness, and the effect of the antenna gain. Therefore, we can express  $\Gamma_n$  as:

$$\Gamma_n = f\left(\theta(t_n), \varepsilon, \sigma_{sh}, G_{[R/L]HCP,n}\right), \quad (3.54)$$

which states it is a function of the observed satellite elevation  $\theta(t_n)$  changing over time, the surface relative permittivity  $\varepsilon$ , the surface roughness coefficient  $\sigma_{sh}$  and the antenna gain for RCHP and LHCP signals.

During the signal tracking, the presence of the specularly reflected component will introduce a bias in the estimated code phase delay and the carrier phase estimates, causing  $\Delta\tau_0 = b_{\tau,n}$  and  $\Delta\phi_{0,n} = b_{\phi,n}$ . These biases will depend on the reflected signal, but also on the receiver's tracking architecture considered. Here, and for the sake of simplicity, we neglect these biases, i.e.,  $\Delta\tau_0, \Delta\phi_{0,n} \approx 0$ , by assuming that they can be small enough given a tracking architecture implementing some multipath mitigation scheme, such as narrow correlator or double delta correlator techniques.

Given  $\theta_n$ 's slow rate of change, we have reduced the number of samples by averaging the correlator outputs over one second intervals. By doing so, we assume that the mean of  $y_n$  remains approximately constant over each second interval. From now on until the end of this chapter, we will be referring to the samples obtained after this 1-second averaging.

#### 3.6.2 SML Description

Given the model for averaged prompt correlator's output described in (3.49-3.53) from section above, we will use the maximum likelihood estimator (MLE) to jointly estimate the vector of unknown deterministic parameters

$$\xi_{\text{SML}} = \begin{bmatrix} u_0 \\ \beta \end{bmatrix} \in \mathbb{R}^{4 \times 1}, \text{ with } \beta \triangleq \begin{bmatrix} \varepsilon_r \\ \varepsilon_i \\ h \end{bmatrix}, \quad (3.55)$$

from the set of noisy measurements  $\mathbf{y} \in \mathbb{C}^{N \times 1}$ . In (3.55) we have defined  $\beta$  as the vector that groups the unknown parameters of the Z-L model (see Appendix B) that are not linear with the data measurements. We recall  $\varepsilon_r$  and  $\varepsilon_i$  representing the real and imaginary parts, respectively, of the surface permittivity.  $h$  corresponds to our definition of the receiver's height, i.e., the orthogonal distance between the reflection surface and the antenna phase centre's nominal position. The usage of the MLE is motivated by its asymptotically efficient properties in terms of mean square error, given a sufficiently large data record or for high SNR values (asymptotic region) [43]. In this case, we have observation times on the order of a few minutes, and high SNR, due to the 1 second averaging. Therefore, the MLE appears to be particularly well suited in this case.

The MLE of  $\xi$  is defined for the general case as

$$\hat{\xi}_{\text{ML}} = \arg \max_{\xi} p(\mathbf{y}; \xi) = \arg \max_{\xi} \ln(\mathbf{y}; \xi), \quad (3.56)$$

### Chapter 3. Param. Estimation in GNSS-R Scenarios with Coherent Reflection

where  $\ln p(\mathbf{y}; \boldsymbol{\xi})$  is log-likelihood function. The vector of measurements  $\mathbf{y}$  is distributed as  $\mathcal{CN}(u_0 \mathbf{r}(\boldsymbol{\beta}), \sigma_\eta^2 \mathbf{I})$ , where  $\mathbf{r}(\boldsymbol{\beta}) = u_0^{-1} \mathbb{E}\{\mathbf{y}\}$  is the expected value of  $\mathbf{y}$  normalized by the LOS signal's amplitude  $u_0$ , and  $\sigma_\eta^2$  is the variance of  $y_n$ . Under this assumption, (3.56) becomes equivalent to

$$\hat{\boldsymbol{\xi}}_{\text{SML}} = \arg \min_{\{u_0, \boldsymbol{\beta}\}} |\mathbf{y} - u_0 \mathbf{r}(\boldsymbol{\beta})|^2. \quad (3.57)$$

In this case the MLE becomes equivalent to the least squares estimator (LSE) [43]. Since  $u_0$  is linear in the data, the MLE of  $u_0$  has the following analytic expression

$$\hat{u}_{0, \text{SML}} = \left( \mathbf{r}^H(\boldsymbol{\beta}) \mathbf{r}(\boldsymbol{\beta}) \right)^{-1} \mathbf{r}^H(\boldsymbol{\beta}) \mathbf{y} \Big|_{\boldsymbol{\beta} = \hat{\boldsymbol{\beta}}_{\text{SML}}}. \quad (3.58)$$

We can now replace (3.58) into (3.57) to obtain

$$|\mathbf{y} - u_0 \mathbf{r}(\boldsymbol{\beta})|^2 \Big|_{u_0 = \hat{u}_{0, \text{SML}}} = \mathbf{y}^H \mathbf{y} - \underbrace{\left( \mathbf{r}^H(\boldsymbol{\beta}) \mathbf{r}(\boldsymbol{\beta}) \right)^{-1} \left| \mathbf{y}^H \mathbf{r}(\boldsymbol{\beta}) \right|^2}_{J_{\text{SML}}(\boldsymbol{\beta})}. \quad (3.59)$$

By doing so, finding  $\hat{\boldsymbol{\xi}}_{\text{SML}}$  has been reduced to minimizing the cost function  $J_{\text{SML}}(\boldsymbol{\beta})$ .  $J_{\text{SML}}(\boldsymbol{\beta})$  is a non-linear, non-convex, multimodal scalar function of 3 independent variables. As a consequence, computing  $\hat{\boldsymbol{\beta}}_{\text{SML}}$  is clearly not straightforward. Grid search methods can be computationally very expensive, and the precision of the method will be linked to the grid's step size. Since  $J_{\text{SML}}(\boldsymbol{\beta})$  presents several local minima, if an arbitrary initial  $\boldsymbol{\beta}_0$  is used, simple steepest descent algorithms are more likely to converge to a local minimum instead of the global minimum. Although a vast amount of optimization methods have been described in the existing literature (e.g., [166, 167]) to address this kind of problems, here we describe a simple alternative by taking advantage of the specific properties shown by our  $J_{\text{SML}}(\boldsymbol{\beta})$ .

By examining  $J_{\text{SML}}(\boldsymbol{\beta})$ , we have spotted a strong quasi-periodic behavior in the  $h$  dimension. If we assume  $\varepsilon$  known, we have  $J_{\text{SML}}(h)$ , i.e., it now depends only on the parameter  $h$ . Heuristically, we determined that the average distance between local minima in  $h$ ,  $d_h$  can be well-approximated as

$$d_h \approx \frac{\lambda}{2} \left( \frac{1}{N} \sum_{n=0}^{N-1} \sin(\theta(t_n)) \right)^{-1}. \quad (3.60)$$

In order to verify hypothetical periodicity, we have computed the DFT of  $J_{\text{SML}}$  averaged over 1000 Monte Carlo<sup>3</sup> iterations for different  $\varepsilon$  values and satellite elevation spans. We generated  $J_{\text{SML}}(h)$  for a 600-sample measurement vector with a  $\text{SNR}_0 = 25$  dB. We depict the results obtained in Figure 3.9. They show a peak approximately at  $d_h^{-1}$  for each of the considered cases. In agreement with (3.60), the position of the peak, and thus the periodicity of the local minima, does not seem to depend on the surface properties or the height of the

<sup>3</sup>Monte Carlo simulations generate a large synthetic data sets with prescribed noise characteristics. Then, these data sets are used to evaluate parameters obtained by inverse modeling, e.g., the average magnitude's value of the DFT of  $J_{\text{SML}}$  in this case.

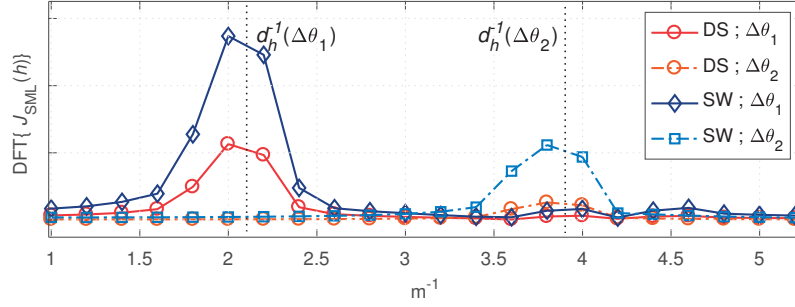


**Figure 3.9** – Mean value of the magnitude of  $\text{DFT}\{|J_{\text{SML}}(h)|\}$  for  $\Delta\theta_1 = [10^\circ, 13^\circ]$ , with  $d_h(\Delta\theta_1) = 0.47$  m, and  $\Delta\theta_2 = [20^\circ, 23^\circ]$ , with  $d_h(\Delta\theta_2) = 0.26$  m; and two surfaces: “Dry Surface” (DS):  $\epsilon_{\text{DS}} = 4 - j1.14$ , and “Sea Water” (SW):  $\epsilon_{\text{SW}} = 20 - j45.69$ .

receiver. This behavior for  $J_{\text{SML}}(\beta)$  is also observed, together with a much smoother one in the  $\epsilon_r$  and  $\epsilon_i$  dimensions, i.e., for most of  $\beta$  values, we have that

$$\frac{\partial J_{\text{SML}}(\beta)}{\partial \epsilon_{[r,i]}} \ll \frac{\partial J_{\text{SML}}(\beta)}{\partial h}. \quad (3.61)$$

Since the distance between two contiguous local minima can be roughly determined in advance as  $d_h$ , we now describe a new method or algorithm tailored to our specific  $J_{\text{SML}}(\beta)$  to efficiently obtain  $\hat{\beta}_{\text{SML}}$ . The proposed algorithm relies on two principles:

1. For any given scenario, it is reasonable to assume some knowledge of the range of values that  $\beta$  might take. Using this knowledge, we can constrain our search space to  $S \subset \mathbb{R}^3$ , such that  $\beta \in S : \beta_{\min} \leq \beta \leq \beta_{\max}$ .
2. It is possible to divide or “segment” the subspace  $S$  into  $K$  subspaces  $\{S_k\}$ , with their centers separated a  $d_h$  distance in the  $h$  dimension. Each  $S_k$  should contain a single local minimum of  $J_{\text{SML}}(\beta)$ .

By applying these two principles, we are able to “segment” or divide the original optimization problem into  $K$  simpler and faster to solve problems. In the section below, we describe how the SML algorithm works.

### Algorithm Description

In its initialization stage, the SML algorithm computes  $d_h$ , as in (3.60), for the satellite elevation span  $\Delta\theta$  covered during the entire observation time considered  $T_{\text{obs}}$ . In addition, the algorithm defines  $S$  by setting the search space boundaries, i.e.,  $\{\beta_{\min}, \beta_{\max}\}$  using the a priori information for the current scenario. The total number of subspaces,  $K$ , is obtained as

$$K = \left\lceil \frac{h_{\max} - h_{\min}}{d_h} \right\rceil. \quad (3.62)$$

---

**Algorithm 1** Segmented Maximum Likelihood (SML)

---

**Require:**  $d_h$  and  $\beta_{\min}, \beta_{\max}$  defining  $S$

**Ensure:**  $\hat{\beta}_{\text{SML}} = \arg \min_{\beta \in S} J_{\text{SML}}(\beta)$

*Initialization:*

- 1: Select  $\beta_{S_0} \in S$
- 2: Define  $S_0 \subset S$  centered at  $\beta_{S_0}$
- 3: Compute  $\hat{\beta}_{S_0} = \arg \min_{\beta \in S_0} J(\beta)$

*Algorithm iterations:*

- 4: **for**  $k = 1$  to  $K - 1$  **do**
  - 5:     Define  $S_k \subset S$  centered at  $\beta_{S_k}$
  - 6:     Compute  $\hat{\beta}_k = \arg \min_{\beta \in S_k} J(\beta)$
  - 7: **end for**
  - 8:  $\hat{\beta}_{\text{SML}} = \arg \min_{\hat{\beta}_k} J_{\text{SML}}(\hat{\beta}_{S_k}), \quad k = 0, \dots, K - 1$
- 

Then, an initial guess  $\beta_{\text{init}} \in S$  is selected.  $S_0$  is defined around  $\beta_{\text{init}}$ , as

$$\beta \in S_0 : \begin{cases} \varepsilon_{r,\min} \leq \varepsilon_r \leq \varepsilon_{r,\max} \\ \varepsilon_{i,\min} \leq \varepsilon_i \leq \varepsilon_{i,\max} \\ h_{\text{init}} - \frac{d_h}{2} \leq h \leq h_{\text{init}} + \frac{d_h}{2} \end{cases} . \quad (3.63)$$

Now, we compute the first local minimum  $\hat{\beta}_{S_0}$ , the nearest to  $\beta_{\text{init}}$ , as

$$\hat{\beta}_{S_0} = \arg \min_{\beta \in S_0} J_{\text{SML}}(\beta) \quad (3.64)$$

using a gradient-descent like algorithm. After obtaining  $\hat{\beta}_{S_0}$ , we can define every subspace  $S_k$ , with  $k \in \{1, \dots, K - 1\}$ , such that

$$\beta \in S_k : \begin{cases} \varepsilon_{r,\min} \leq \varepsilon_r \leq \varepsilon_{r,\max}, \\ \varepsilon_{i,\min} \leq \varepsilon_i \leq \varepsilon_{i,\max}, \\ h_{k,\text{lb}} \leq h \leq h_{k,\text{ub}} \end{cases} \quad (3.65)$$

and

$$h_{k, [\text{lb}/\text{up}]} = h_{\hat{\beta}_{S_0}} + \left( m_k \pm \frac{1}{4} \right) d_h. \quad (3.66)$$

$m_k \in \mathbb{Z}$  is defined as the multiple of  $d_h$  separating  $h_{\hat{\beta}_{S_0}}$  from the center of  $S_k$  in the  $h$  dimension. Then,  $\hat{\beta}_{S_k}$  is computed in the same way as  $\hat{\beta}_{S_0}$ , but with  $\beta \in S_k$  instead. Finally, the global minimum, corresponding to  $\hat{\beta}_{\text{SML}}$ , is determined by choosing the  $\hat{\beta}_{S_k}$  that minimizes  $J_{\text{SML}}(\beta)$ . All these steps are summarized in Algorithm 1.

Figure 3.10 depicts an example of the segmentation performed by the SML algorithm in the case of  $J_{\text{SML}}(h)$ . The  $J_{\text{SML}}(h)$  shown was generated for a 600-sample vector of measurements with  $\text{SNR}_0 = 25$  dB. The top plot in Figure 3.10 shows how many local minima  $J_{\text{SML}}(h)$  there are for an  $h$  range between 0 and 7 m, for a true receiver's height  $h = 2.25$  m and a

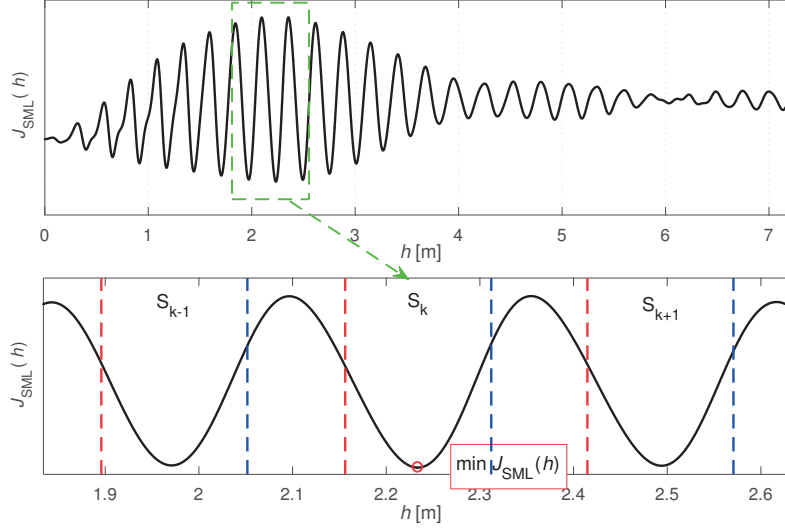


**Figure 3.10** – (Top) Example of  $J_{\text{SML}}(h)$  evaluated for  $h = [0, 7]$  m. (Bottom) Magnified version around the global minimum of  $J_{\text{SML}}(h)$  (dashed green rectangle). Dashed-red and dashed-blue lines are used for the subspaces’ bounds computed by the SML.

satellite elevation span  $\Delta\theta = [20^\circ, 23^\circ]$ . We want to highlight the relative small difference between the global minimum value of  $J_{\text{SML}}(h)$  and the near local minima. The bottom plot in Figure 3.10 shows the segmentation into different  $S_k$  computed by the SML on a magnified section around the global minimum.

### Performance Assessment with Synthetic Data

In this section we test the proposed SML with synthetic signal to validate it and assess its performance by comparing it with the CRB previously derived in Section 3.4. That CRB was computed considering the measurements at the output of the receiver’s front end, while the SML computes the MLE using correlation output samples. Correlating the received signal a local replica is a linear operation, and therefore, if only coherent integration is used, the samples at the correlator output shall be a sufficient statistics of the unknown parameters. As a result, computing the CRB using the correlation output to model the log-likelihood function leads to the same CRB results as when considering the front end’s output.

We compute the RMSE of the SML estimates using Monte Carlo simulation in different cases. In all of them, we have considered a fixed antenna height  $h = 2.25$  m and an isotropic antenna, with an attenuation of 20 dB for the LHCP received signals. We set the true surface’s reflectivity as  $\varepsilon_{\text{DS}} = 4 - j1.14 \times 10^{-4}$ , which according to [168] corresponds to a “dry surface”.  $\sigma_{sh}$  was set to  $5 \cdot 10^{-3}$  m.

We expect to observe the asymptotically efficient behavior –characteristic of the MLE–, which shall validate the SML algorithm. We have used the SML to obtain  $\hat{\beta}_{\text{SML}}$  for different elevation span lengths,  $\Delta\theta$ , ranging from  $1.5^\circ$  to  $6^\circ$ , but with all of them starting at the initial elevation  $\theta_0 = 15^\circ$ . For all the  $\Delta\theta$  considered, we have simulated a  $5 \times 10^{-3} \text{ }^\circ/\text{s}$  constant elevation rate. The SML uses a single sample per second as input, computed by averaging the prompt correlator output during the same time, as explained in Section 3.6.1. Therefore, the number of input samples for the SML will vary for each different  $\Delta\theta$  considered. For the

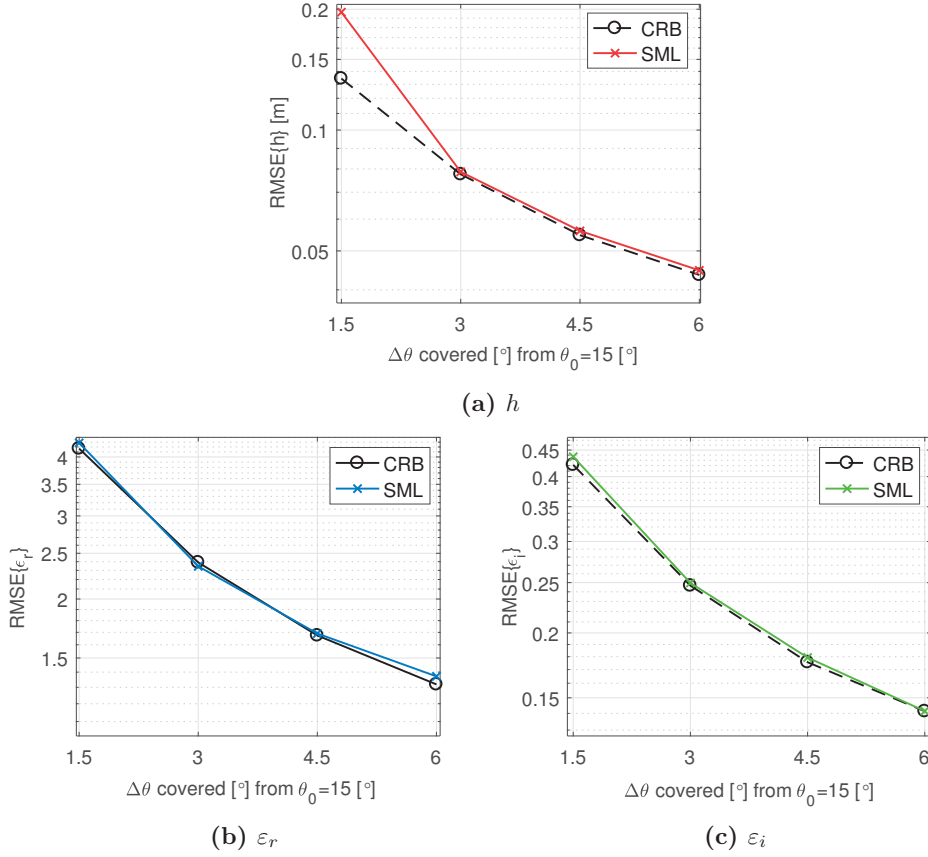


**Figure 3.11** – RMSE of the MLE computed using the SML compared with the  $\sqrt{\text{CRB}}$  for the joint estimation of  $\beta$  for different elevation spans  $\Delta\rho$  starting at  $\theta_0 = 15^\circ$ .

shortest span,  $\Delta\theta = [15^\circ, 16.5^\circ]$ , which corresponds to a total observation time of 5 min, we obtain 300 samples. We have defined the remaining elevation spans to increase the number of samples by multiple of 300, until reaching 1200 samples for  $\Delta\theta = [15^\circ, 21^\circ]$ , i.e., a 20 min observation time. Since the SNR of the total received signal will vary over time due to the interference pattern observed, we make use of  $\text{SNR}_0$ , defined in (3.35) instead, corresponding to the SNR that will be observed if only the LOS signal were present. In the carried out simulations,  $\text{SNR}_0$  was set to a fixed value of 35 dB, which is a reasonable value considering the 1-second averaging of the correlator output.

Figure 3.11 shows the RMSE results obtained for the estimates  $\hat{\epsilon}_r$ ,  $\hat{\epsilon}_i$  and  $h$ , for the different elevation spans considered. In the plots depicted, each point corresponds to a different elevation span, computed with 1000 Monte Carlo iterations using the signal model described by (3.49) (see Section 3.6.1). Each RMSE value was computed as

$$\text{RMSE} \{ \hat{\beta}_{\text{SML}} \} = \sqrt{\mathbb{E} \left\{ \left| \hat{\beta}_{\text{SML}} - \beta \right|^2 \right\}} \quad (3.67)$$

$$\approx \sqrt{\frac{1}{M} \sum_{m=1}^M \left| \hat{\mathbf{B}}_{\text{SML},m} - \beta \right|^2}, \quad (3.68)$$



where the matrix  $\hat{\mathbf{B}}_{\text{SML}} \in \mathbb{R}^{3 \times M}$  contains the  $\hat{\beta}_{\text{SML}}$  for the  $M$  Monte Carlo iterations.

As expected, the results show that the ML estimates computed with the SML algorithm are consistent and asymptotically efficient. In fact, the RMSE values observed almost attain the CRB for elevations spans as short only  $3^\circ$ , i.e., for an observation time of 10 min. Even though the RMSE of  $\hat{\varepsilon}_r$  almost reaches the CRB even for the  $1.5^\circ$  elevation span as shown in Figure 3.11, the error obtained will be too large for the retrieval of meaningful surface properties (e.g., soil moisture), at least with the assumed  $\text{SNR}_0$  of 35 dB. Figure 3.11 also shows that it is possible to reach sub-decimeter precision already with the  $\Delta\rho = [15^\circ, 18^\circ]$ . The higher RMSE of  $\hat{h}$  corresponding to  $\Delta\rho = [15^\circ, 16.5^\circ]$  is explained because the number of samples is not large enough for the SML to reach the asymptotic behavior.

### 3.7 Chapter Conclusion

In the first half of the chapter, we derived a theoretical precision bound on the joint estimation of the receiver's height and the reflected signal coefficient for the GNSS-R specular –and therefore, coherent– reflection scenario, for static ground-based receivers. The CRB was derived first for observation times of up to 1 s (short observation intervals), and later on, extended to long observation intervals of up to hundreds of seconds, where the satellite elevation angle was changing during the observation time. We computed the CRB for GPS and Galileo signals with different bandwidths and different modulations, i.e., BPSK, CBOC(6,1,1/11) and AltBOC(15,10). For short observation times and  $\Delta\rho > \rho_{chip}$ , it was possible to obtain simple analytic expressions of the CRB. Next, we have extended the CRB to be valid for long observation periods, by using the FIM transformation approach. This transformation approach can easily accommodate different models for the surface's reflection coefficient  $\Gamma$ .

We selected the Z-L model to describe  $\Gamma$ , and then, computed the CRB as a function of satellite elevation spans, of different sizes, covered during the observation time. The impact of the antenna radiation pattern was considered within the modeling of  $\Gamma$ . We studied a particular case –receiver height, antenna pattern and surface properties– as an example to understand the CRB's dependency on the signal properties and the scenario parameters.

The results for short observation times of up to 1 s have shown that, even for antennas designed to mitigate multipath, it is still theoretically possible to achieve meter precision height's estimation –or even decimeter precision using Galileo E5 signal's full bandwidth– given a front end with high enough bandwidth. That is the case even for antennas installed with their boresight perpendicular to the ground. For long observation intervals, the computed CRB confirms the link between the variation in the satellite elevation and the attainable precision. Moreover, the presented CRB evaluation confirms the cm level precision that has been reported by many works, e.g., [31, 94, 100, 103, 169–171], among others, some of them using standard GNSS geodetic stations [172]. The CRB results show that it is possible to achieve reasonable precision in the –joint– estimation of  $\varepsilon_r$  and  $\sigma$  over observation times covering satellite elevation variations above  $10^\circ$ . According to the CRB results computed, the considered modernized GNSS signals, i.e., GPS L5, Galileo E1 and Galileo E5 can potentially provide better estimation precision for all of the parameters when compared to the GPS L1.

The second part of this chapter described the SML algorithm, a computationally efficient way to obtain the joint MLE of the receiver's height and the surface permittivity. We tested the SML algorithm using synthetic data generated using a signal model describing

### **Chapter 3. Param. Estimation in GNSS-R Scenarios with Coherent Reflection**

---

the Prompt correlator's output while tracking of the sum of the LOS and the specularly reflected signals. As expected, the ML estimates obtained showed an asymptotically efficient behavior for satellite elevation spans  $\geq 3^\circ$ . The matching of the estimated RMSE with the CRB –computed as described in the first part of the chapter– cross-validated both the SML and the CRB. By using the SML algorithm during long observation times, we seek to attain the optimal estimation precision for a given observation time or a significant reduction of the required observation time for a given estimation precision, which means a higher spatial and temporal resolutions.

As a final remark, we want to point out an obvious, yet essential, limitation of the precision bounds and the SML described in this chapter: the chosen signal model for coherent reflection might not accurately match the actual reflected signal. In many practical scenarios, the reflected signal is better described as the sum of two contributions: a coherent (or specular), and the other incoherent (or diffuse). The importance of each signal component will depend on the considered scenario. In any case, the CRB results presented in this chapter should lower bound the results obtained with more complete signal model considering the incoherent reflections.

## Chapter 4

# Spatial Filtering of GNSS Signals with Synthetic Aperture Processing

GNSS usage for PVT applications has become nearly ubiquitous in our modern society. Modern GNSS receivers are expected to operate accurately and reliably in environments with some amount of interference, e.g., multipath in dense urban environments. In previous Chapter 1, we studied the estimation bounds for GNSS-R techniques in the presence of coherent multipath. For GNSS-R applications, the stronger the power of the reflected signal, the better. In contrast, in this chapter, we are interested in estimating the DOA of the received signals and, ultimately, mitigating any interference or multipath. To do so, we implement the spatial filtering techniques described in Section 2.5.1 in a synthetic aperture (SA) GPS receiver, which has a single moving antenna.

In the first part of this chapter (sections 4.1 and 4.2), we particularize our signal model—introduced in Section 2.2—for scenarios with slow-moving receivers, to then study the DOA estimation bounds with SA in this context. The performance of DOA estimation techniques using static antenna arrays in the context of GNSS has been extensively studied, see e.g., [120, 124], but not that much when these arrays are onboard of a moving platform. Antenna—or antenna array—motion allows to synthesize a large aperture that can be treated as a “virtual” array. The number and position of the elements of this virtual array will depend on the trajectory described by the antenna during the considered observation time.

In the second part of this chapter (Section 4.3), we propose a simple tracking architecture to integrate SA processing into the receiver’s baseband processing chain. This tracking architecture has been implemented by modifying a GPS software defined radio (SDR) receiver, which can serve as SA development framework for spatial filtering techniques. The proposed architecture can be adapted for closed-loop or open-loop tracking. With closed-loop tracking, it is required to isolate the phase component contribution due to the antenna motion only, before any SA processing. In practice, this poses a formidable problem. In Section 4.3.4, we propose two new techniques addressing this task. The core of these techniques is an extended Kalman filter (EKF) that integrates the model for the assumed antenna motion. In Section 4.3.3 we describe a new open-loop tracking scheme supporting SA processing, which has been integrated within the proposed architecture.

In the third, and final, part of this chapter, we present the results obtained after validating the proposed tracking architecture and the SA techniques described in Section 4.3. These results mainly focus on two aspects: the DOA estimation performance, and the multipath-

induced bias compensation in the receiver’s navigation solution. Section 4.4 summarizes the results obtained with a synthetic signal, generated using a GPS simulator. Mostly by following the same outline, Section 4.5 summarizes the results obtained with real GPS signals recorded with an antenna mounted on a rotating mechanical arm.

Some of the materials presented in this chapter have been already published in [173] (Section 4.2) and [174] (Section 4.5).

## 4.1 Signal Model for Synthetic Aperture Processing

According to the model defined by Expression (2.5), back in Section 2.2, the baseband equivalent representation of the RF signal measured at the output of a GNSS antenna can be described as the superposition of  $M$  scaled and delayed signals with known structure, corrupted by additive noise. We recall this signal being expressed as:

$$x(t) = \sum_{m=0}^{M-1} a_m(t) s_m(t - \tau_m(t)) \exp \{-j2\pi f_c \tau_m(t)\} + n(t), \quad (4.1)$$

where  $M$  accounts for the sum of the LOS signal and the multipath components. The rest of terms in Expression (4.1) have been defined as follows:

- $s_m(t) \in \mathbb{C}$  represents the  $m$ th received baseband GNSS signal, including the code and the navigation message (if present). The subscript  $m$  may correspond to the different multipath signal components originating from the same or a different GNSS signal transmitter.
- $a_m(t)$ ,  $\tau_m(t)$  represent, respectively, the complex amplitude and the group delay for each signal component. The group delay –or just delay, for short– includes the sum of dispersive and nondispersive delays caused by the signal propagation through the atmosphere [175, 176]. The carrier signal is affected differently by these delays, and the resulting phase difference –which is assumed to remain approximately constant over the considered observation times– is already taken into account within the phase of  $a_m(t)$ . The amplitude  $a_m(t)$  also takes into account the antenna gain, given the polarization of the received signal, i.e.,  $G(t)$ , and can be subsequently expressed as:

$$a_m(t) = G(t)u_m(t), \quad (4.2)$$

where  $u_m(t)$  is the amplitude of the signal when impinging on the antenna.

- $f_c$  is the nominal carrier frequency of the transmitted GNSS signal under consideration.
- $n(t)$  represents the noise and any interfering signals present, except for the multipath. We consider it complex, zero-mean, and circularly symmetric Gaussian distributed.

For a moving receiver, it is possible to decompose the delay  $\tau_m(t)$  experienced by each signal component as the sum of two delay components: the *reference* delay and the *relative* delay, i.e.,

$$\tau(t) = \tau_{\text{ref}}(t) + \tau_{\text{rel}}(t), \quad (4.3)$$

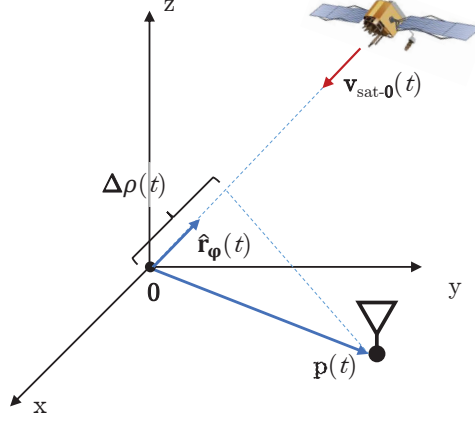


**Figure 4.1** – Additional propagation path  $\Delta\rho(t)$  within the defined frame of reference

where the index  $m$  is omitted for notation simplicity.

Given an arbitrary frame of reference, we have defined the *reference* delay  $\tau_{\text{ref}}(t)$  as the transmitted signal's travel time from the satellite to the origin of coordinates, i.e.,  $\mathbf{0}$ . For a receiver in motion, by default, we will set  $\mathbf{0}$  to the geometric center of the trajectory described by the receiver's antenna phase center. For observation times on the order of a few seconds,  $\tau_{\text{ref}}(t)$  can be accurately approximated using Taylor's second-order expansion [12], as

$$\tau_{\text{ref}}(t) \approx \tau_0 + \alpha t + \frac{\dot{\alpha}}{2} t^2, \quad (4.4)$$

where  $\tau_0$  is the delay at time  $t_0$ , i.e., the beginning of our observation;  $\alpha \triangleq c^{-1}v_{\text{sat}-\mathbf{0}}$  is the Doppler coefficient, with  $v_{\text{sat}-\mathbf{0}}$  being the relative speed between the satellite and the origin of coordinates  $\mathbf{0}$ ;  $c$  stands for the signal propagation speed; and  $\dot{\alpha} \triangleq d\alpha/dt$  is the Doppler coefficient rate.

On the other hand, we have defined the *relative* delay  $\tau_{\text{rel}}(t)$  as the additional signal's travel time due to the antenna position with respect to  $\mathbf{0}$ . Therefore, it can be expressed as:

$$\tau_{\text{rel}}(t) = \frac{\Delta\rho(t)}{c} = \frac{\hat{\mathbf{r}}_{\psi}^T \mathbf{p}(t)}{c}, \quad (4.5)$$

where  $\Delta\rho(t)$  is the additional propagation path, which can be described as the receiver position at time instant  $t$ , i.e.,  $\mathbf{p}(t)$ , projected into the unit vector pointing towards the signal's DOA  $\hat{\mathbf{r}}_{\psi}$ . Figure 4.1 depicts this description.

After sampling the down-converted signal at the Nyquist rate over an observation interval of  $T_{\text{SA}}$  seconds, we obtain the vector of measurements  $\mathbf{x} \in \mathbb{C}^{K \times 1}$  distributed as  $\mathbf{x} \sim \mathcal{CN}(\boldsymbol{\mu}, \boldsymbol{\Sigma}_{\mathbf{x}})$ . For a moving antenna, every sample corresponds not only to a different point in time, but also to a different position within the defined frame of reference. Hence, we refer to the matrix  $\boldsymbol{\Sigma}_{\mathbf{x}}$  as the spatiotemporal covariance matrix, since it simultaneously describes the noise's temporal and spatial correlations.

Making use of (4.1), it is possible to express  $\mathbf{x}$  as<sup>1</sup>:

$$\mathbf{x} = (\mathbf{D} \odot \mathbf{G}) \mathbf{u} + \mathbf{n}, \quad (4.6)$$

where we define  $\mathbf{D} \in \mathbb{C}^{K \times M}$  as the basis-function matrix, where its elements are expressed as:

$$[\mathbf{D}]_{km} = s_m(t - \tau_m(t_k)) \exp(-j2\pi f_c \tau_m(t_k)). \quad (4.7)$$

$\mathbf{u} \in \mathbb{C}^{M \times 1}$  is the vector of complex amplitudes of the received signals when impinging on the receiver's antenna.  $\mathbf{n} \in \mathbb{C}^{K \times 1}$  is the noise vector. The matrix  $\mathbf{G} \in \mathbb{C}^{K \times M}$  describes the antenna's complex gain for every received signal over time, given their corresponding DOAs and observed polarization, i.e.,  $[\mathbf{G}]_{km} = G_m(t_k)$ .

The *narrowband* signal and array assumptions are often made when modeling the GNSS signals received by an antenna array. The narrowband signal assumption implies that the Doppler effect experienced by the signal received by a single antenna element can be modeled by a carrier frequency shift [120, 123]. This assumption allows to ignore the Doppler effect on  $s_m(t)$ , known as code Doppler. However, according to [176], the assumption only holds whenever

$$\frac{c}{vB} \gg T_{\text{SA}}, \quad (4.8)$$

where  $v$  is the relative speed between the transmitter and the receiver,  $B$  denotes the signal bandwidth, and we recall  $T_{\text{SA}}$  as the considered –coherent– observation interval. Assuming a receiver with a sufficiently accurate local oscillator,  $T_{\text{SA}}$  intervals of a few seconds are possible, e.g., in SA processing. With these  $T_{\text{SA}}$  values, Inequality (4.8) might not hold in some scenarios. Therefore, for the sake of generality, the signal model proposed will explicitly consider the Doppler effect on the GNSS signal  $s_m(t)$ , i.e., we will not use the narrowband signal assumption.

On the other hand, the narrowband array assumption, often used in the GNSS antenna array context, considers that the propagation time for a signal along the array is much smaller than the inverse of the signal's bandwidth. As a result, a phase-shift can be used to describe the delay difference in the signal received by the different elements of the array. In [177], Zatman defines a more rigorous threshold to identify if the narrowband array assumption holds, i.e., only when<sup>2</sup>

$$\text{sinc}(B\tau_{max}) \simeq 1, \quad (4.9)$$

where  $\tau_{max}$  is the propagation delay between two farthest elements of the antenna array. In the context of the SA processing, Equation (4.9) constrains the maximum trajectory size for which the narrowband assumption still holds for a specific GNSS signal. In order to avoid this constraint in our analysis, the signal model considered when deriving the CRB in the following section does rely on this assumption.

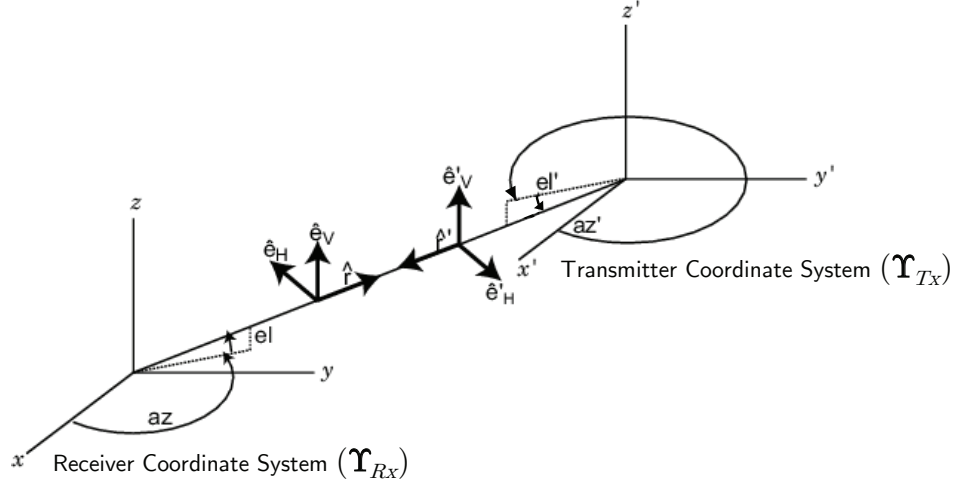


**Figure 4.2** – Construction of the transmitter and receiver spherical basis vectors to compute polarization mismatch coefficient ([7] - “Polarized Fields” entry).

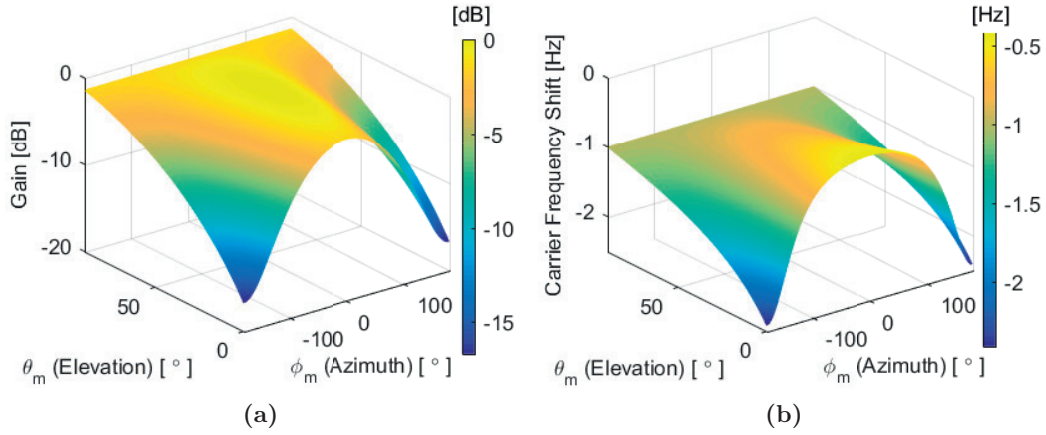


**Figure 4.3** – Polarization mismatch coefficient as a function of the signal’s DOA for the RHCP signal - RHCP receiving antenna case. Antenna boresight tilted  $45^\circ$  with respect to the vertical ( $z$ ) axis. (a) Power losses due to the mismatch. (b) Induced carrier frequency shift.

#### 4.1.1 Antenna Pattern and Polarization Mismatch Effects

At any given instant, the amplitudes of the received signal components,  $a_m(t)$ , can be expressed as

$$a_m(t) = \underbrace{F_m(t)\gamma_m(t)}_{G_m(t)} u_m \quad (4.10)$$

where  $u_m$  is the complex amplitude of the signal impinging on the antenna, which can be reasonably assumed to remain constant during the considered observation time  $T_{SA}$ .  $F_m(t)$ ,

<sup>1</sup>The operator  $\odot$  stands for the Hadamard product.

<sup>2</sup>To be rigorous, the results described in [177] consider a uniform linear array (ULA). Nonetheless, and according to the author, they can be easily extended to an arbitrary array geometry.

$\gamma_m(t)$  are the complex gain introduced by the antenna, and polarization mismatch coefficient, respectively. It is common to express these two parameters as a single term for a defined antenna polarization, i.e., the partial directive gain  $G_m(t)$ . However, it is important to notice that even if  $|F_m(t)| \approx 1$ , any real antenna will have a certain directivity due to any possible polarization mismatch between the antenna and received signal.

Both,  $F_m(t)$  and  $\gamma_m(t)$ , depend on the relative position and orientation between the receiver and the transmitter. Therefore, it is relevant to model this dependency since, if the receiver and transmitter antennas' attitude and polarization are known, any variations over time in the measured amplitude  $a_m(t)$  convey potentially useful information for estimating the DOA of the received signal. Phase variations in  $\gamma_m(t)$  due to the change in the relative orientation of the transmitting and the receiver antennas can be measured by the receiver during the signal's carrier tracking. These phase variations are usually referred as phase wrap-up or wind-up [178–180], and must be taken into account in GNSS receivers that use carrier phase measurements. According to [181], the polarization mismatch coefficient  $\gamma_m(t)$  can be obtained as:

$$\gamma_m(t; \theta_m, \phi_m, \mathbf{Y}_{Rx}, \mathbf{Y}_{Tx}) = \boldsymbol{\varphi}_{gTx}^H \boldsymbol{\varphi}_{gRx}, \quad (4.11)$$

where  $\theta_m, \phi_m$  are the elevation and azimuth of the received signal in a common (global) frame of reference; and  $\{\mathbf{Y}_{Rx}, \mathbf{Y}_{Tx}\} \in \mathbb{R}^{3 \times 3}$  are the receiver and transmitter antennas' orthonormal basis, characterizing their respective frames of reference. They are defined such as the antenna's boresight is parallel to the  $z$  axis. The vectors  $\boldsymbol{\varphi}_{gTx}, \boldsymbol{\varphi}_{gRx}$  represent, respectively, the transmitter and receiver antennas' Jones polarization vectors in the global frame of reference. They can be expressed as a function of the transmitter's and receiver's spherical basis as:

$$\boldsymbol{\varphi}_{gTx} = \varphi_{gTx,H} \hat{\mathbf{e}}'_H + \varphi_{gTx,V} \hat{\mathbf{e}}'_V \quad (4.12)$$

$$\boldsymbol{\varphi}_{gRx} = \varphi_{gRx,H} \hat{\mathbf{e}}_H + \varphi_{gRx,V} \hat{\mathbf{e}}_V. \quad (4.13)$$

Figure 4.2 shows how the unit vectors  $\hat{\mathbf{e}}'_H, \hat{\mathbf{e}}_H$  and  $\hat{\mathbf{e}}'_V, \hat{\mathbf{e}}_V$ , already expressed in the global frame of reference, are defined. The change of basis required to express the polarization vectors in the global frame of reference, given the orientations of the transmitter and the receiver defined in spherical coordinates, can be carried out using Euler angle matrices, as described in detail in [181]. When the transmitter and receiver antennas are not aligned, this change of basis allows to compute the coefficients  $\varphi_{gTx,H}, \varphi_{gRx,H}$  and  $\varphi_{gTx,V}, \varphi_{gRx,V}$  from the normalized Jones vector for a specific polarization, e.g., from  $1/\sqrt{2} [1, -j]^T$  corresponding to the RHCP.

As an example, Figure 4.3 represents the polarization coefficient  $\gamma_m$ , as a function of the received signal's DOA when the receiving antenna and signal are both RHCP. We used expression (4.11) to compute  $\gamma_m$ . In this particular case, the receiving antenna is tilted, with its boresight pointing towards a  $45^\circ$  elevation angle. In addition, the antenna is spinning at 1 rev/s around the vertical axis. Figure 4.3 demonstrates the dependency of  $\gamma_m$  on the received signal's elevation angle. For elevation angles near  $90^\circ$ , the phase of  $\gamma_m$  varies almost linearly with the change in azimuth. Hence, for such high elevations, the observed phase wrap-up on the carrier signal depends almost exclusively on the antenna's spinning speed.

In short, for a known receiving antenna attitude, gain pattern and polarization; the phase and amplitude of  $\gamma_m$  will depend on the received signal DOA, which might improve the DOA



estimation. This dependency is more pronounced for low elevation angles. We intend to validate this hypothesis in the following section.

## 4.2 Estimation Bounds: CRB Derivation

As described in Section 2.6, the CRB provides a lower bound on the covariance matrix for the joint –unbiased– estimation of a deterministic real-valued parameter vector  $\boldsymbol{\xi}$ . This lower bound is obtained by taking the inverse of the Fisher information matrix, i.e.,  $\mathbf{J}^{-1}(\boldsymbol{\xi})$ . Let us recall that the FIM is defined as

$$[\mathbf{J}(\boldsymbol{\xi})]_{ij} = -\mathbb{E} \left\{ \frac{\partial^2 \ln p(\mathbf{x}; \boldsymbol{\xi})}{\partial \xi_i \partial \xi_j} \right\}, \quad (4.14)$$

with  $\ln p(\mathbf{x}; \boldsymbol{\xi})$  being the log-likelihood function of  $\boldsymbol{\xi}$  given the measurements in  $\mathbf{x}$  [43]. Under the assumption of the vector of measurements being distributed as  $\mathbf{x} \sim \mathcal{CN}(\boldsymbol{\mu}(\boldsymbol{\xi}), \boldsymbol{\Sigma}_{\mathbf{x}})$ , which implies an additive Gaussian noise independent of  $\boldsymbol{\xi}$ , we can use the Slepian-Bang’s formula [43] to compute the elements of the FIM simply as

$$[\mathbf{J}(\boldsymbol{\xi})]_{ij} = 2\Re \left\{ \frac{\partial \boldsymbol{\mu}^H(\boldsymbol{\xi})}{\partial \xi_i} \boldsymbol{\Sigma}_{\mathbf{x}}^{-1} \frac{\partial \boldsymbol{\mu}(\boldsymbol{\xi})}{\partial \xi_j} \right\}. \quad (4.15)$$

For the signal model under consideration, defined in (4.6), we have

$$\boldsymbol{\mu}(\boldsymbol{\xi}) = (\mathbf{D}(\mathbf{v}, \boldsymbol{\psi}) \odot \mathbf{G}(\boldsymbol{\psi})) \mathbf{u}, \quad (4.16)$$

with the vector of unknown parameters  $\boldsymbol{\xi} \in \mathbb{R}^{7M \times 1}$  defined as

$$\boldsymbol{\xi} = \begin{bmatrix} \mathbf{u} \\ \boldsymbol{\psi} \\ \mathbf{v} \end{bmatrix}, \quad (4.17)$$

which we have split in the amplitude vector  $\mathbf{u} \in \mathbb{R}^{2M \times 1}$ , the DOA parameters vector  $\boldsymbol{\psi} \in \mathbb{R}^{2M \times 1}$ , and the synchronization parameters vector  $\mathbf{v} \in \mathbb{R}^{3M \times 1}$ , defined as

$$\mathbf{u} = \begin{bmatrix} \Re\{\mathbf{u}\} \\ \Im\{\mathbf{u}\} \end{bmatrix}; \quad \boldsymbol{\psi} = \begin{bmatrix} \boldsymbol{\theta} \\ \boldsymbol{\phi} \end{bmatrix}; \quad \mathbf{v} = \begin{bmatrix} \tau_0 \\ \boldsymbol{\alpha} \\ \dot{\boldsymbol{\alpha}} \end{bmatrix}. \quad (4.18)$$

The vectors  $\{\boldsymbol{\theta}, \boldsymbol{\phi}\} \in \mathbb{R}^{M \times 1}$  contain the elevation and azimuth angles, respectively, of each received signal component. These angles are defined with respect to the common (or global) frame of reference introduced in Section 4.1. The vectors  $\{\tau_0, \boldsymbol{\alpha}, \dot{\boldsymbol{\alpha}}\} \in \mathbb{R}^{M \times 1}$  contain the time delay, Doppler coefficient, and Doppler coefficient rate, respectively, for each received signal. All the parameters in  $\boldsymbol{\xi}$  are assumed to remain constant during the observation time  $T_{\text{SA}}$ .

Under the assumption of a known channel’s spatio-temporal covariance matrix  $\boldsymbol{\Sigma}_{\mathbf{x}}$ , we only need to compute the gradient of  $\boldsymbol{\mu}(\boldsymbol{\xi})$  with respect to  $\boldsymbol{\xi}$ , to fully determine the FIM elements. Moreover, the FIM can be expressed using submatrices as

$$\mathbf{J}(\boldsymbol{\xi}) = \begin{pmatrix} \mathbf{J}_{uu} & \mathbf{J}_{u\psi} & \mathbf{J}_{uv} \\ \mathbf{J}_{u\psi}^T & \mathbf{J}_{\psi\psi} & \mathbf{J}_{\psi v} \\ \mathbf{J}_{uv}^T & \mathbf{J}_{\psi v}^T & \mathbf{J}_{vv} \end{pmatrix}. \quad (4.19)$$

The elements of the submatrices in (4.19) are obtained as described by expression (4.15), i.e.,

$$\mathbf{J}_{u_i u_j} = 2\Re \left\{ \frac{\partial \mathbf{u}^H}{\partial u_i} (\mathbf{D} \odot \mathbf{G})^H \boldsymbol{\Sigma}_{\mathbf{x}}^{-1} (\mathbf{D} \odot \mathbf{G}) \frac{\partial \mathbf{u}}{\partial u_j} \right\}, \quad (4.20)$$

$$\mathbf{J}_{u_i \psi_j} = 2\Re \left\{ \frac{\partial \mathbf{u}^H}{\partial u_i} (\mathbf{D} \odot \mathbf{G})^H \boldsymbol{\Sigma}_{\mathbf{x}}^{-1} \left( \frac{\partial \mathbf{D}}{\partial \psi_j} \odot \mathbf{G} + \mathbf{D} \odot \frac{\partial \mathbf{G}}{\partial \psi_j} \right) \mathbf{u} \right\}, \quad (4.21)$$

$$\mathbf{J}_{u_i v_j} = 2\Re \left\{ \frac{\partial \mathbf{u}^H}{\partial u_i} (\mathbf{D} \odot \mathbf{G})^H \boldsymbol{\Sigma}_{\mathbf{x}}^{-1} \left( \frac{\partial \mathbf{D}}{\partial v_j} \odot \mathbf{G} \right) \mathbf{u} \right\}, \quad (4.22)$$

$$\mathbf{J}_{\psi_i \psi_j} = 2\Re \left\{ \mathbf{u}^H \left( \frac{\partial \mathbf{D}}{\partial \psi_i} \odot \mathbf{G} + \mathbf{D} \odot \frac{\partial \mathbf{G}}{\partial \psi_i} \right)^H \boldsymbol{\Sigma}_{\mathbf{x}}^{-1} \left( \frac{\partial \mathbf{D}}{\partial \psi_j} \odot \mathbf{G} + \mathbf{D} \odot \frac{\partial \mathbf{G}}{\partial \psi_j} \right) \mathbf{u} \right\}, \quad (4.23)$$

$$\mathbf{J}_{\psi_i v_j} = 2\Re \left\{ \mathbf{u}^H \left( \frac{\partial \mathbf{D}}{\partial \psi_i} \odot \mathbf{G} + \mathbf{D} \odot \frac{\partial \mathbf{G}}{\partial \psi_i} \right)^H \boldsymbol{\Sigma}_{\mathbf{x}}^{-1} \left( \frac{\partial \mathbf{D}}{\partial v_j} \odot \mathbf{G} \right) \mathbf{u} \right\}, \quad (4.24)$$

$$\mathbf{J}_{v_i v_j} = 2\Re \left\{ \mathbf{u}^H \left( \frac{\partial \mathbf{D}}{\partial v_i} \odot \mathbf{G} \right)^H \boldsymbol{\Sigma}_{\mathbf{x}}^{-1} \left( \frac{\partial \mathbf{D}}{\partial v_j} \odot \mathbf{G} \right) \mathbf{u} \right\}. \quad (4.25)$$

The partial derivatives of  $\mathbf{D}$  with respect to the parameters in  $\boldsymbol{\xi}$  can be expressed using the chain rule as

$$\frac{\partial \mathbf{D}}{\partial \xi_i} = \frac{\partial \mathbf{D}}{\partial \boldsymbol{\tau}(t_k)} \frac{\partial \boldsymbol{\tau}(t_k)}{\partial \xi_i}. \quad (4.26)$$

The first term in (4.26) can be expressed as

$$\begin{aligned} \left[ \frac{\partial \mathbf{D}}{\partial \boldsymbol{\tau}(t_k)} \right]_{km} &= -(\dot{s}_m(t_k - \tau_m(t_k)) + j2\pi f_c s_m(t_k - \tau_m(t_k))) \\ &\quad \times \exp\{-j2\pi f_c \tau_m(t_k)\}, \end{aligned} \quad (4.27)$$

with  $\dot{s}_m(t)$  used to represent the time derivative of the waveform  $s_m$  evaluated at time  $t$ ; while the latter can be expressed as a zero vector, except for the  $i$ th position, i.e.,

$$\left[ \frac{\partial \boldsymbol{\tau}(t_k)}{\partial \xi_i} \right]_i = \begin{cases} 1, & \text{if } \xi_i \in \boldsymbol{\tau}_0 \\ t_k, & \text{if } \xi_i \in \boldsymbol{\alpha} \\ \frac{1}{2}t_k^2, & \text{if } \xi_i \in \dot{\boldsymbol{\alpha}} \\ c^{-1} \frac{\partial \Delta \rho(t_k)}{\partial \xi_i}, & \text{if } \xi_i \in \boldsymbol{\psi}. \end{cases} \quad (4.28)$$

$\partial \mathbf{u} / \partial \xi_i$ , is an all-zero  $2M \times 1$  vector except for the  $i$ th position. This position will be equal to 1 if  $i \leq M$ , and equal to the imaginary operator  $j$  otherwise. In the case of  $\partial \mathbf{G} / \partial \psi_i$  in (4.25), we need to take the partial derivatives of the basis transformation matrix with respect to the parameters in  $\boldsymbol{\psi}$ .

The antenna's gain matrix  $\mathbf{G}$  depends on  $\boldsymbol{\psi}$ , i.e., including any polarization mismatch effect. Therefore, in most practical cases  $\mathbf{G}$  cannot be modeled analytically. Instead, it is more likely to have a descriptive model of this gain as a function of the DOA of the impinging signal for a given polarization. This model can be obtained either empirically, by characterizing a specific antenna in the anechoic chamber, or it can be approximated from

the reference antenna pattern, provided by its manufacturer. In any case, we can still resort to numerical estimation of the partial derivatives of  $\mathbf{G}$  with respect to  $\boldsymbol{\psi}$  for a particular antenna trajectory.

Interestingly, applying the chain rule to get expression (4.26) highlights that FIM values related to the DOA parameters  $\boldsymbol{\psi}$  are proportional to  $\partial\Delta\rho(t_k)/\partial\psi_i$ . This confirms the intuition that, along a certain trajectory, the larger the variation in  $\Delta\rho$  with the change in the DOA of the signal, the larger the FIM values related to the DOA, and therefore, the lower the resulting CRB.

The FIM expressions obtained in this section are valid for any deterministic trajectory, as well as for any kind of GNSS signal.

### 4.2.1 CRB Evaluation

Up to this point, the CRB of  $\boldsymbol{\xi}$  has not been explicitly derived, but instead, it has been expressed as the diagonal terms of the obtained FIM's inverse. As a result of the matrix inversion operation, expressing the CRB analytically becomes very cumbersome. However, we continue to be interested in:

1. Determining the minimum theoretical variance of an unbiased DOA estimator in plausible SA scenarios.
2. Understanding the dependency of the CRB on the antenna motion, as well as on the true DOA of the received signal.

To help us in achieving these goals, we have defined two different simulation scenarios, for which we have numerically computed the CRB. Before describing each scenario below, we list the common simulation settings used in both of them:

- We consider only a single GPS satellite to be visible. This satellite only transmits the L1 C/A signal using an ideal RHCP antenna [176].
- The receiving antenna is assumed to be omnidirectional and RHCP in the boresight direction only, e.g., a patch or a crossed-dipole antenna. Therefore, it is assumed that the attenuation –characterized by the gain matrix  $\mathbf{G}$ – of any received signal coming from a direction different from the antenna boresight depends only on the polarization mismatch effects.
- At any given time, the antenna attitude is known and defined by  $\theta_{ant}$  and  $\phi_{ant}$ , i.e., the elevation and azimuth angles of the antenna's boresight in the defined frame of reference.
- The simulated receiver front end low-pass filter has an equivalent noise bandwidth (one-sided)  $B_{fe}=3.25$  MHz, with a sampling frequency  $f_s=2B_{fe}$ , which for the GPS L1 C/A signal, implies  $K = 6500$  samples per code period.
- For the sake of validating the selected signal model and the derived CRB, only the LOS signal component in the presence of thermal noise is considered. Therefore,  $M=1$  and  $\boldsymbol{\Sigma}_x=\sigma_n^2\mathbf{I}$ . No multipath components were modeled into the simulated scenarios.
- The  $C/N_0$  of the signal impinging on the receiver is set to a constant value of 45 dB-Hz.

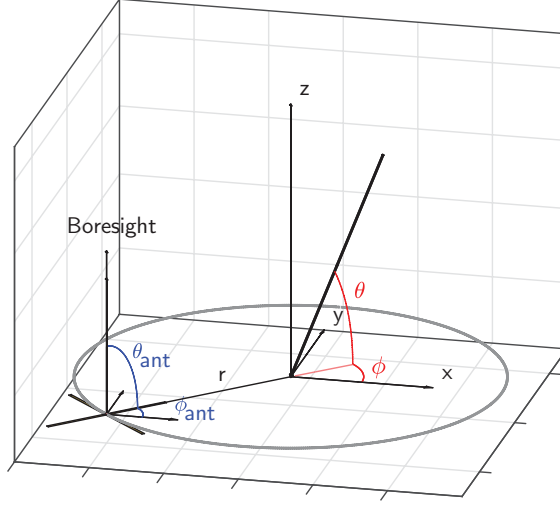


Figure 4.4 – CRB Scenario I geometry: Antenna mounted on a rotating arm

Even though the chosen sampling frequency, i.e.,  $f_s = 6.5$  MHz, cannot be considered as particularly high, the total number of samples corresponding to an entire  $T_{SA}$  of a few seconds becomes very large, e.g.,  $K = 13 \times 10^6$  for  $T_{SA} = 2$  s. In practice, directly computing the FIM expression strictly as described earlier in Section 4.2 becomes computationally intractable in the case of colored noise. The matrix  $\Sigma_{\mathbf{x}} \in \mathbb{C}^{K \times K}$  will require a tremendous amount of memory<sup>3</sup> and computational effort to obtain each value in the FIM  $\mathbf{J}(\boldsymbol{\theta})$ .

A first approach to overcome this limitation is to compress the matrix  $\Sigma_{\mathbf{x}}$ , primarily by taking advantage of its inherent structure as covariance matrix and its sparsity. Moreover, for receivers moving at low speeds, we can approximate the observed relative delay as constant over the duration of one signal's code period, e.g., 1 ms. Implicitly, this is equivalent to approximating small trajectory spans, covered by the receiver during short time periods, as individual points located in the middle of these spans. We also assume the channel to remain stationary during each of these short time periods. Under these two assumptions, several adjacent elements of the matrix  $\Sigma_{\mathbf{x}}$  will have the same value. Besides, the basis-function matrix  $\mathbf{D}$  and its partial derivatives can also be equal. These two facts allow us to avoid the unnecessary repetition of the same computations, thus, significantly reducing the required memory and computational burden. In this dissertation, we constrained ourselves to the case where only white noise is present, in which there is no need for strictly computing  $\Sigma_{\mathbf{x}}$  to obtain the FIM.

### CRB Scenario I: Antenna Mounted on a Rotating Arm

In this first scenario, depicted in Figure 4.4, the antenna moves along a uniform circular trajectory, while simultaneously spinning around its vertical ( $z$ ) axis at the same angular speed  $\omega_{rot} = \pi$  rad/s (i.e., 0.5 Hz or 30 rpm). In the figure, the angles defining the receiver's antenna attitude are represented in blue, while the angles defining the received signal's DOA, set to  $\theta = 60^\circ$  and  $\phi = 45^\circ$  as an example, are depicted in red. The antenna trajectory is represented in gray, with  $r$  being its radius. The antenna's boresight elevation is set to

<sup>3</sup>With no compression and 8 bytes to represent each one of the total  $K(K+1)/2$  unique values in the covariance matrix, it would require  $\approx 676$  TB of memory.

$\theta_{ant}=90^\circ$ . We have chosen this trajectory in order to replicate the motion of an antenna mounted on a mechanical rotating arm, implemented by the experimental setup described in Section 4.5. Actually, similar experimental setups implementing this kind of antenna motion are reported in [179, 180, 182]. For this reason, the CRB results that we have obtained could be compared with the reported performance of the SA DOA algorithms implemented with those experiments.

Figure 4.5 shows the  $\sqrt{\text{CRB}}$  results for the received signal’s DOA estimation, i.e., the observed elevation  $\theta$  and azimuth  $\phi$  angles, as a function of the true  $\theta$  of the received signal and the radius  $r$  of the described trajectory. The radius  $r$  has been normalized by the carrier signal wavelength. The values depicted correspond to true radii from 0.25 m to 5 m, for  $\lambda_{\text{GPS-L1}} \approx 0.1904$  m. As expected, larger  $r$  values imply larger synthesized apertures, which lead to better achievable precision in the signal’s DOA estimation.  $\text{CRB}(\theta)$  depends on the true  $\theta$  value, showing an improvement in the precision for higher elevation angles. For low elevation angles, the value of  $\text{CRB}(\theta)$  significantly increases, in the same manner as in a physical uniform circular array [123]. On the other hand,  $\text{CRB}(\phi)$  shows a complementary behavior, with improving precision for lower  $\theta$  angles. As expected given the circular symmetry of the antenna motion, the  $\text{CRB}(\phi)$  is independent of the  $\phi$ ’s true value.

### CRB Scenario II: Antenna Spinning Around Vertical Axis

In this second scenario, the antenna spins around the  $z$  axis of the global reference frame, i.e., the vertical axis, at an angular speed  $\omega_{rot}=\pi$  rad/s, while remaining at the same location. More rigorously, the spinning axis crosses the antenna phase center, which remains static within the defined reference frame. Therefore, only the antenna’s attitude varies over time.

Figure 4.6 shows the  $\sqrt{\text{CRB}}$  results for  $\theta$  and  $\phi$ , as a function of the received signal’s true elevation angle, and the antenna’s boresight elevation, i.e.,  $\theta_{ant}$ . In this case,  $\theta_{ant}$  is not necessarily parallel to the spinning axis, except when  $\theta_{ant} = 90^\circ$ . The results show that if the antenna is sufficiently tilted, its orientation change alone can enable the use DOA estimation techniques, with a theoretical achievable precision on the order of  $1^\circ$  or less. This is a direct consequence of the diversity provided by the antenna’s complex gain, in this case exclusively due to the polarization mismatch between the receiving antenna and the received signal.

### CRB Discussion

The CRB results presented for the two simulated scenario show that it is possible to achieve high precision on the GNSS signal DOA estimation using the known motion or orientation change of the receiving antenna. The CRB quantifies the dependency of the DOA estimation precision on the antenna motion when using SA processing. The results for the CRB Scenario II, corresponding to a spinning antenna show that, DOA estimation of received signals is possible when the antenna is spinning alone. This is possible, even with an omnidirectional antenna, because the observed signal’s phase will change depending on the polarization mismatch between the antenna and the received signal. Given the duality existing between DOA estimation and beamforming [123], these results underline the feasibility of implementing GNSS receivers using SA beamforming also based on the polarization diversity resulting from the antenna’s orientation change. Let us remark that, in our CRB derivation, we have assumed the antenna complex gain as perfectly known. In practice, deviations from the antenna gain assumed might introduce biases and distortions during the SA processing, which

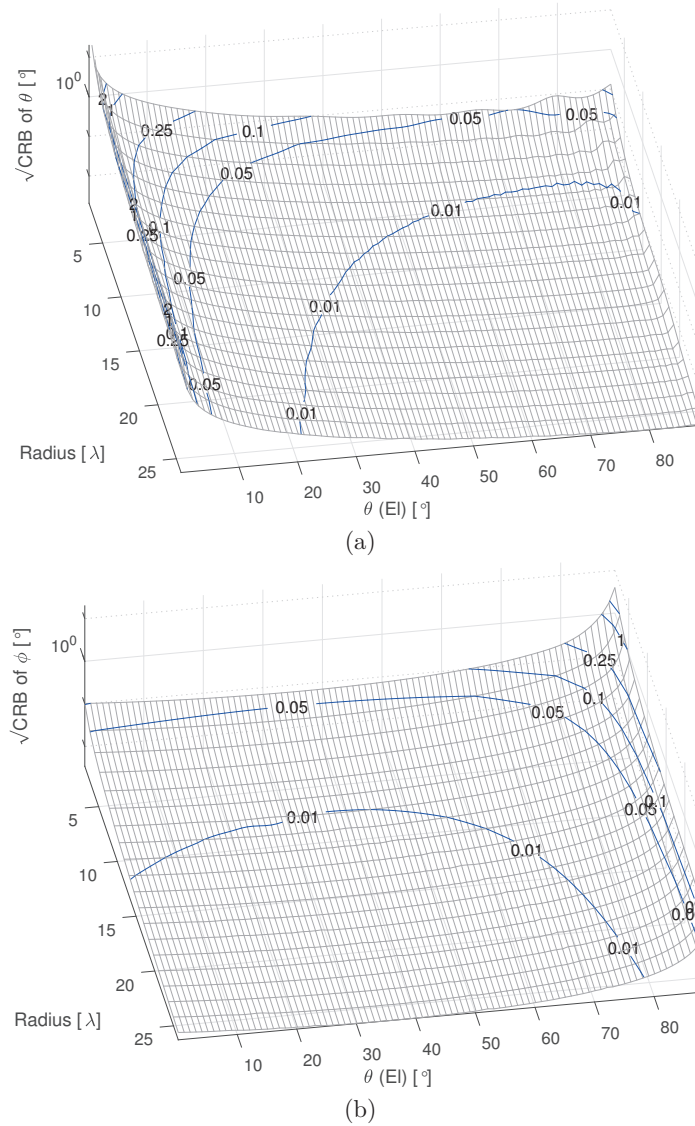
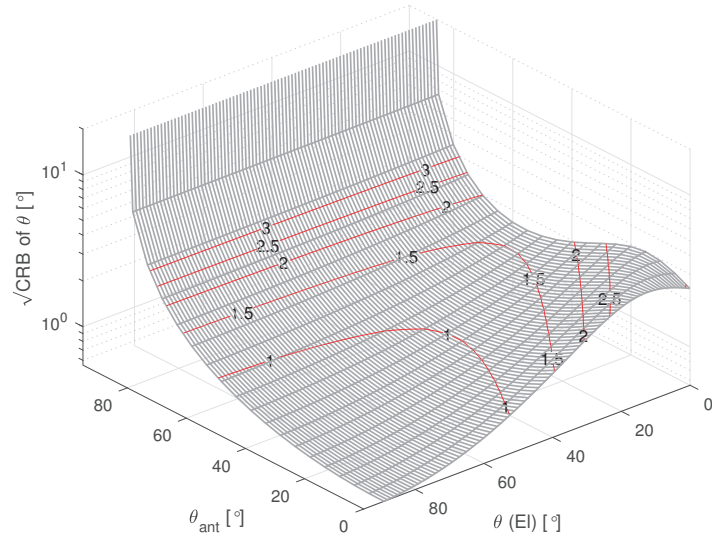


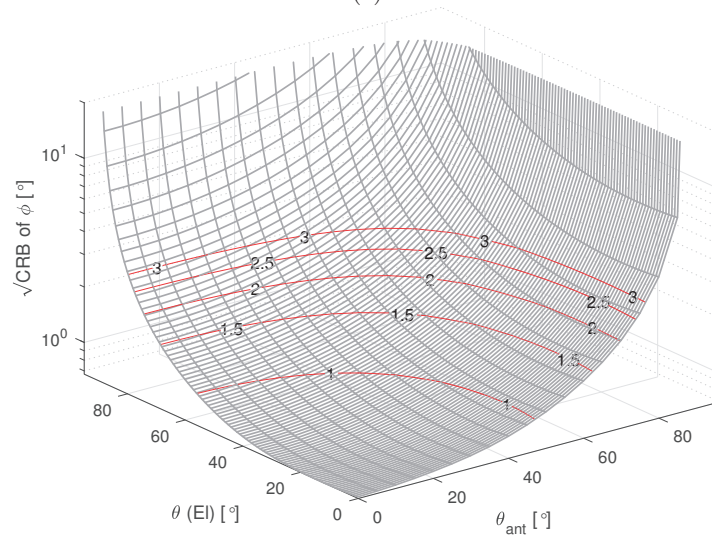
**Figure 4.5** –  $\sqrt{\text{CRB}}$  of  $\theta$  (a), and  $\phi$  (b) in Scenario I, for different true values of  $\theta$  and normalized trajectory radius  $r$ . Blue contours represent level curves.

will degrade the accuracy of techniques making use of the antenna’s orientation change.

Even though the CRB results presented in this thesis were obtained considering a single signal component, we would like to remind that the CRB expressions provided in this section are valid for multiple coherent signal components. However, extending these CRB expression to consider the estimation of the parameters in  $\xi$  together with an unknown channel’s spatio-temporal covariance  $\Sigma_x$  is not straightforward, mostly due to the large number of unknown parameters that we must estimate. In addition, the partial derivative of  $\Sigma_x$  with respect to the unknown parameters will not be zero anymore in this case. Thus, we will need to use the complete expression for the Slepian-Bang’s formula, instead of only one of its terms.



(a)



(b)

**Figure 4.6** –  $\sqrt{\text{CRB}}$  of  $\theta$  (a), and  $\phi$  (b) in Scenario II, for different true values of  $\theta$  and antenna boresight elevations  $\theta_{ant}$ . Red contours represent level curves. Axes are exchanged from (a) to (b) for clarity.

### 4.2.2 CRB Comparison to Maximum Likelihood Estimator

The maximum likelihood estimator (MLE) is known for having asymptotic –for large data records– properties of being unbiased, efficient, i.e., achieving the CRB, and having a Gaussian distribution [43, 123]. Therefore, it is considered *asymptotically optimal*. Moreover, for signal in noise problems, the MLE achieves the CRB for high SNRs [43].

The asymptotic efficiency property of the MLE is often used to validate CRB derivations. In this section we follow this approach to validate the results presented in Section 4.2.1. Now, we derive the MLE estimator for the LOS signal’s DOA estimation scenario, but only for a few selected cases. The variance –estimated– of the MLE obtained should closely match the minimum variance predicted by the CRB. Clearly, the MLE shall jointly estimate the parameters in the CRB’s unknown parameter vector  $\boldsymbol{\xi}$ , defined in (4.17). Hence, let us derive now the MLE for the signal model described in Section 4.1.

Under the noise statistics assumptions introduced in Section 4.1, we recap having the received signal measurements distributed as  $\mathbf{x} \sim \mathcal{CN}(\boldsymbol{\mu}(\boldsymbol{\xi}), \boldsymbol{\Sigma}_{\mathbf{x}})$ , which implies the following likelihood function<sup>4</sup>

$$p(\mathbf{x}; \boldsymbol{\xi}) = \frac{1}{\pi^N \det(\boldsymbol{\Sigma}_{\mathbf{x}}(\boldsymbol{\xi}))} \exp \left\{ -(\mathbf{x} - \boldsymbol{\mu}(\boldsymbol{\xi}))^H \boldsymbol{\Sigma}_{\mathbf{x}}^{-1}(\boldsymbol{\xi}) (\mathbf{x} - \boldsymbol{\mu}(\boldsymbol{\xi})) \right\}. \quad (4.29)$$

The MLE for the unknown parameter vector  $\boldsymbol{\xi}$  is defined as

$$\hat{\boldsymbol{\xi}}_{\text{ML}} = \arg \max_{\boldsymbol{\xi}} p(\mathbf{x}; \boldsymbol{\xi}) = \arg \max_{\boldsymbol{\xi}} \ln(\mathbf{x}; \boldsymbol{\xi}), \quad (4.30)$$

where  $\ln p(\mathbf{x}; \boldsymbol{\xi})$  is the log-likelihood function.

Since the noise is assumed to be independent from the signal, therefore,  $\boldsymbol{\Sigma}_{\mathbf{x}}(\boldsymbol{\xi}) = \boldsymbol{\Sigma}_{\mathbf{x}}$ . In addition, the noise covariance matrix is assumed to be known. As a result, the MLE estimator can be stated as

$$\hat{\boldsymbol{\xi}}_{\text{ML}} = \arg \min_{\boldsymbol{\xi}} (\mathbf{x} - \boldsymbol{\mu}(\boldsymbol{\xi}))^H \boldsymbol{\Sigma}_{\mathbf{x}}^{-1} (\mathbf{x} - \boldsymbol{\mu}(\boldsymbol{\xi})), \quad (4.31)$$

with the mean vector of the measurements defined as

$$\boldsymbol{\mu}(\boldsymbol{\xi}) = \mathbb{E}\{\mathbf{x}\} = \mathbf{H}\mathbf{u}, \quad (4.32)$$

where, for convenience, we have defined  $\mathbf{H} \triangleq (\mathbf{D} \odot \mathbf{G})$ . In this case, the MLE is equivalent to a weighted least squares estimator.

From this point, obtaining the MLE turns into solving an optimization problem, with the following cost function

$$\Lambda(\boldsymbol{\xi}) \triangleq (\mathbf{x} - \mathbf{H}\mathbf{u})^H \boldsymbol{\Sigma}_{\mathbf{x}}^{-1} (\mathbf{x} - \mathbf{H}\mathbf{u}). \quad (4.33)$$

Let us define now the following correlation terms

$$\begin{aligned} \hat{r}_{xx} &= \mathbf{x}^H \boldsymbol{\Sigma}_{\mathbf{x}}^{-1} \mathbf{x}, \\ \hat{r}_{hx} &= \mathbf{H}^H \boldsymbol{\Sigma}_{\mathbf{x}}^{-1} \mathbf{x}, \\ \hat{\mathbf{R}}_{hh} &= \mathbf{H}^H \boldsymbol{\Sigma}_{\mathbf{x}}^{-1} \mathbf{H}. \end{aligned} \quad (4.34)$$

<sup>4</sup>The likelihood function is defined as the probability density function for a given data as a function of the set of unknown parameters, i.e.,  $\boldsymbol{\xi}$ .



## 4.2. Estimation Bounds: CRB Derivation

Since  $\boldsymbol{\mu}(\boldsymbol{\xi})$  is linear in the complex amplitudes  $\mathbf{u}$ , it is straightforward to express the MLE for  $\mathbf{u}$  as

$$\hat{\mathbf{u}}_{\text{ML}} = \left( \mathbf{H}^H \boldsymbol{\Sigma}_{\mathbf{x}}^{-1} \mathbf{H} \right)^{-1} \mathbf{H}^H \boldsymbol{\Sigma}_{\mathbf{x}}^{-1} \mathbf{x}, \quad (4.35)$$

which can also be expressed by making use of the definitions in (4.34) as

$$\hat{\mathbf{u}}_{\text{ML}} = \hat{\mathbf{R}}_{hh}^{-1} \hat{\mathbf{r}}_{hx}. \quad (4.36)$$

As a consequence of the linearity in  $\mathbf{u}$ , the  $\mathbf{u}_{\text{ML}}$  is unbiased and has the following covariance matrix

$$\boldsymbol{\Sigma}_{\hat{\mathbf{u}}_{\text{ML}}} = \left( \mathbf{H}^H \boldsymbol{\Sigma}_{\mathbf{x}}^{-1} \mathbf{H} \right)^{-1}. \quad (4.37)$$

Now, by replacing the  $\hat{\mathbf{u}}_{\text{ML}}$  expression into the log-likelihood expression, we get

$$\begin{aligned} [\Lambda(\boldsymbol{\xi})]_{\mathbf{u}=\hat{\mathbf{u}}_{\text{ML}}} &= \mathbf{x}^H \boldsymbol{\Sigma}_{\mathbf{x}}^{-1} \mathbf{x} - \mathbf{x}^H \boldsymbol{\Sigma}_{\mathbf{x}}^{-1} \mathbf{H} \left( \mathbf{H}^H \boldsymbol{\Sigma}_{\mathbf{x}}^{-1} \mathbf{H} \right)^{-1} \mathbf{H}^H \boldsymbol{\Sigma}_{\mathbf{x}}^{-1} \mathbf{x} \\ &= \hat{r}_{xx} - \hat{\mathbf{r}}_{hx}^H \hat{\mathbf{R}}_{hh}^{-1} \hat{\mathbf{r}}_{hx}. \end{aligned} \quad (4.38)$$

We know that the covariance matrix  $\boldsymbol{\Sigma}_{\mathbf{x}} \in \mathbb{C}^{K \times K}$  is Hermitian, and it is assumed positive definite so that it is invertible as  $\boldsymbol{\Sigma}_{\mathbf{x}}^{-1}$  [43]. Therefore,  $\hat{r}_{xx} = \mathbf{x}^H \boldsymbol{\Sigma}_{\mathbf{x}}^{-1} \mathbf{x} > 0$ , since the inverse of a positive definite matrix is also positive definite. As a consequence, it is enough to maximize  $\hat{\mathbf{r}}_{hx}^H \hat{\mathbf{R}}_{hh}^{-1} \hat{\mathbf{r}}_{hx}$  to obtain the MLE of  $\boldsymbol{\xi}$ .

Unlike in the case of  $\hat{\mathbf{u}}_{\text{ML}}$ , there is no closed expression for the rest of parameters in  $\hat{\boldsymbol{\xi}}_{\text{ML}}$ . In this particular case, our cost function  $\Lambda(\boldsymbol{\xi})$  is multivariate, non-linear and non-convex. Fortunately, a distinct advantage of the MLE is that it can always be found numerically for a given data set. In this case, we shall resort to iterative optimization procedures [43, 167]. These procedures will likely produce the MLE if the initial guess, i.e.,  $\hat{\boldsymbol{\xi}}_{\text{ML},0}$ , is close enough to the cost function's global minimum. However, the convergence of these methods to the global minimum is not guaranteed, especially for a non-convex cost function. One shall notice that the function to optimize, i.e.,  $\Lambda(\boldsymbol{\xi})$ , is not known a priori and it will be different for each different data set  $\mathbf{x}$ .

There are several iterative optimization algorithms suitable to obtain  $\hat{\boldsymbol{\xi}}_{\text{ML}}$ , each with different singularities [40, 43, 167]. For convenience we have selected the popular Nelder-Mead simplex algorithm [7, 183]. This algorithm is a direct search method for multidimensional unconstrained minimization. The motivation for using this particular algorithm is twofold: first, it does not require the numerical computation of the gradient of the cost function, and second, it is already implemented very efficiently within the MATLAB's `fminsearch()` function [7].

We are particularly interested in the case where there is only AWGN, i.e., when  $\boldsymbol{\Sigma}_{\mathbf{x}} = \sigma^2 \mathbf{I}$ , since this same assumption was taken to obtain CRB results presented in Section 4.2.1. Under such assumption, it is worth noticing the MLE's behavior is equivalent to the matched filter's [43]. Therefore, an alternative procedure to obtain  $\hat{\boldsymbol{\xi}}_{\text{ML}}$  would be generating a local replica of the signal, with the assumed  $\hat{\boldsymbol{\xi}}$  and correlating it with the received signal  $\mathbf{x}$ . The values of  $\hat{\boldsymbol{\xi}}$  that maximize the absolute square of the correlation are also the ML estimates.

The plots in Figure 4.7 show the comparison of the CRB computed versus the MLE's standard deviation for different true elevation angles of the received signal, in the CRB scenarios I and II. These scenarios, i.e., a uniform circular movement and a 45° tilted antenna spinning, were previously defined in Section 4.2.1. For Scenario I, the antenna boresight is pointing towards a  $\theta = 90^\circ$ . Even though only the results for  $\theta$  and  $\phi$  are shown, both CRB

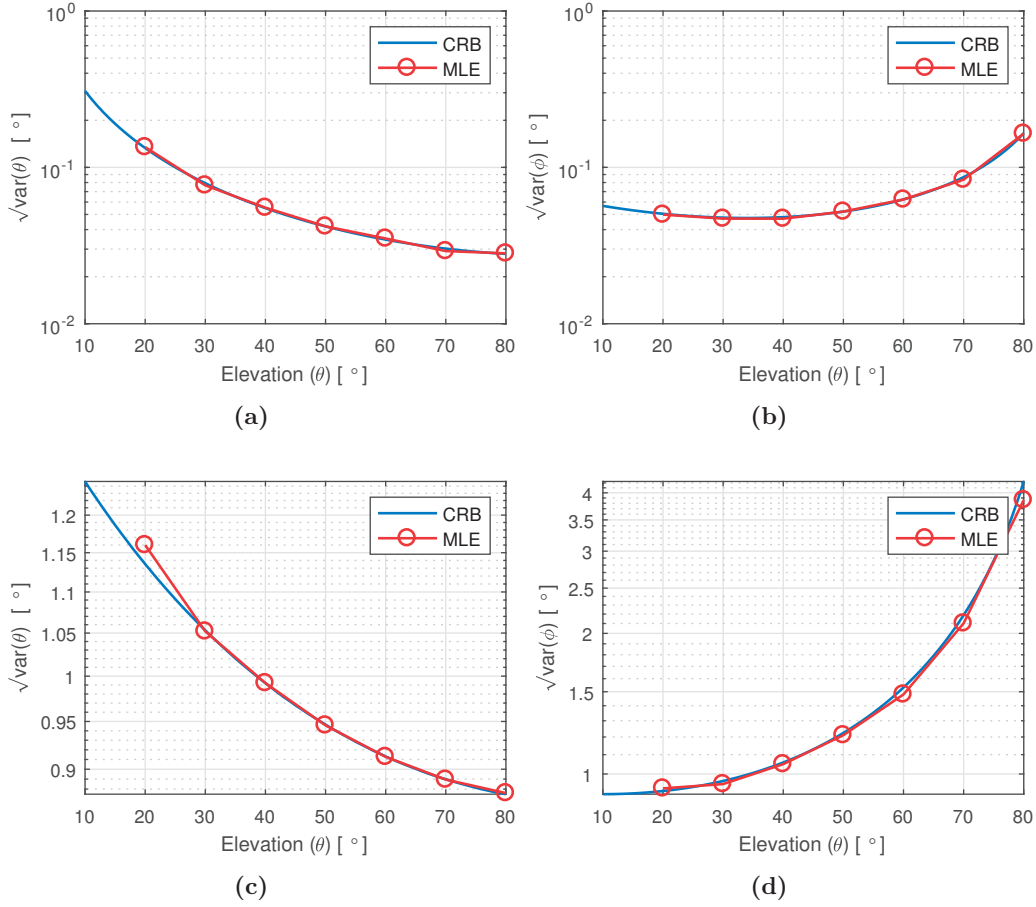


**Figure 4.7** – CRB vs MLE’s standard deviation for CRB Scenario I –(a), (b)–, and CRB Scenario II –(c), (d)–.

and MLE were computed for the joint estimate of all the parameters in  $\xi$ . The MLE’s RMSE values were computed with 1000 simulation iterations. Given the sufficient SNR and number of samples, the results in Figure 4.7 manifest the expected agreement between the CRB and the MLE. Assuming our signal model as correct, the agreement shown validates the CRB expressions and results described so far.

### 4.3 A Tracking Architecture for SA Processing with Uniform Circular Motion

In Section 4.2 we have examined the DOA estimation bounds of the GNSS SA processing by computing the CRB. By contrast, this section introduces a tracking architecture supporting SA processing techniques. Similar tracking architectures to experiment with the SA processing of GNSS signals were necessarily developed in previous research works, e.g., in [8, 141, 180, 184], and have been documented with different level of detail.

To implement this so-called SA tracking architecture, we have modified an SDR GPS receiver to serve as development framework to validate, test and benchmark new and existing SA processing techniques.

### 4.3. A Tracking Architecture for SA Processing with Uniform Circular Motion

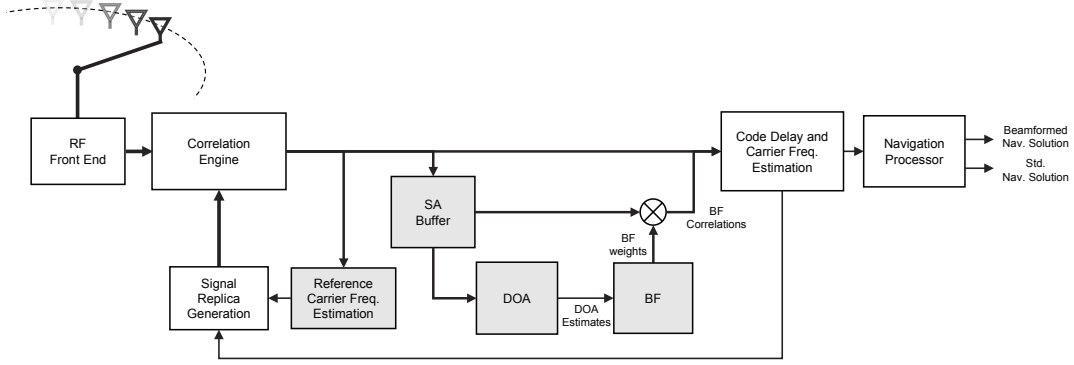


**Figure 4.8** – Proposed tracking architecture (single channel) supporting SA processing. Newly introduced blocks specific to SA are depicted with gray background.

As in [8, 141, 180], we started by focusing on SA processing for a uniform circular motion –with up to 1 m radius, and angular speeds up to  $2\pi$  rad/s–. This kind of motion is very convenient, since it is two-dimensional and symmetric; periodic, which enables long continuous data recordings; it is easy to reproduce in practice and it allows to synthesize the equivalent of a physical circular array. But more importantly, the circular motion can be analytically modeled in a simple manner as a function of a reduced number of parameters. For example, the uniform circular motion can be fully determined by the antenna radius, a constant angular speed and the initial azimuth of the antenna.

To implement this kind of antenna motion, we have built a mechanical rotating arm mounting a GNSS antenna, which complements the modified SDR GPS receiver and allowed us to experiment with real signal. The mechanical arm implements an antenna motion that closely matches a uniform circular translation combined with a synchronized antenna spinning around its vertical axis. This same kind of motion was considered in the CRB Scenario I, described in Section 4.2.1. Further details on the mechanical arm are provided in Section 4.5.

Although only circular motions is discussed in this thesis, the proposed SA tracking architecture can be also adapted for receivers moving along any arbitrary trajectory, either known or estimated by an additional sensor unit. With the proper signal processing, SA techniques have the potential to improve the robustness of any kind of mobile receiver.

The proposed SA tracking architecture implements continuously updated DOA estimation combined with digital beamforming at post-correlation level. Figure 4.8 depicts the SA architecture to track the signal of an individual satellite. It performs the correlation of the received signal with a locally generated replica, using the code delay  $\hat{\tau}$  and Doppler coefficient  $\hat{\alpha}$  estimates obtained from beamformed correlation outputs. These estimates are also fed to the navigation processor and –together with the correlation output– to the new *reference carrier frequency estimation block*. The latter is responsible for estimating the frequency shift coefficient  $\hat{\alpha}_{ref}$ , that is only caused by the reference delay (defined in Section 4.1), and to output it as the carrier frequency shift  $\hat{f}_{d,n}$ . This task, far from trivial in practice, must be performed before attempting any SA processing.

The SA processing of the correlators output is processed by three SA blocks before serving as input for any code tracking scheme:

1. An SA Buffer, where correlation outputs collected during the last  $T_{SA}$  period are stored.

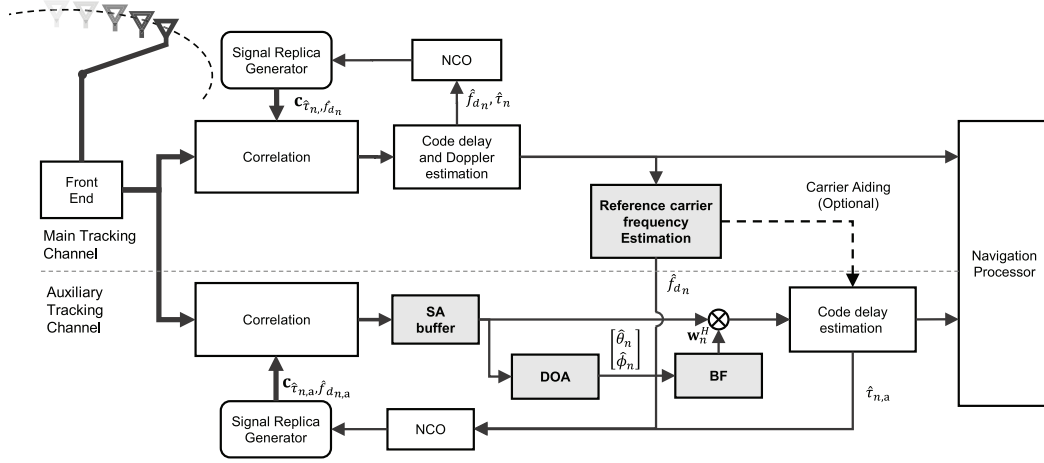


**Figure 4.9** – SA tracking architecture (single channel) in a closed-loop scheme. This architecture implements an auxiliary tracking channel to generate “beamformed” code delay estimates. Blocks depicted with gray background are specific to SA processing.

$T_{SA}$  is the time required to complete SA trajectory. Every time there is a new correlation output available, the buffer is updated and the oldest stored correlation samples are discarded.

2. The DOA block, where DOA estimates for the LOS signal, namely  $\hat{\theta}$  and  $\hat{\phi}$ , are continuously generated. These estimates can be externally provided, e.g., obtained from available navigation solutions or provided by some external assistance. They also can be computed by a DOA estimation algorithm implemented within this block using the samples in the SA Buffer as input. This block is meant to be generic enough to support any DOA estimation algorithm. The DOA estimates are recorded for signal monitoring purposes, and used as input for the beamforming block if needed.
3. The Beamforming block, where digital beamforming is applied using the samples in the SA buffer, or their covariance estimate, as input. Again, this block is purposely kept generic enough to support any beamforming algorithm, either data independent or adaptive, such as the ones described in Section 2.5.1. Depending on the implemented algorithm, this block may or may not make use of the DOA estimates previously generated at the DOA block.

When the SA processing is active, the navigation solution is computed using the code delay and carrier frequency estimates generated from the beamformed correlation outputs.

Figure 4.9 shows the implementation of the SA tracking architecture in a closed-loop scheme. As shown in the figure, for each traditional tracking channel –referred to as *main* tracking channel–, the SA architecture is implemented with an *auxiliary* channel, responsible for most of the SA processing. The samples at the output of the RF front end are simultaneously fed to the main and the auxiliary channels. The main channel operates just as a regular tracking channel [12]: it performs the correlation of the received signal with a locally generated replica, using the code delay  $\hat{\tau}$  and Doppler coefficient  $\hat{\alpha}$  estimates obtained from previous filtered correlation outputs. The auxiliary channel uses  $\hat{f}_{d,n}$  to generate its local replica of the signal, therefore, it does not have any carrier tracking loop.

### 4.3. A Tracking Architecture for SA Processing with Uniform Circular Motion

The proposed SA tracking architecture can be implemented as with an open-loop tracking scheme, as described in Section 2.3.4.

Many beamforming algorithms require the DOA of the LOS signal (spatial reference beamforming) [123]. In the proposed architecture, the DOA block is supposed to provide these DOA estimates. Then, the DOA block output becomes critical. If a wrong DOA estimate is provided to the Beamforming block, this might attenuate the LOS signal, and in closed-loop schemes, eventually lead to the loss-of-lock of the Auxiliary channel. Inaccurate DOA estimations can be caused by intense multipath, which can introduce biases; when the LOS signal is received with very low  $C/N_0$ ; or by the presence of a strong spoofing signal, obviously with a different DOA [126]. To minimize the likelihood of considering an erroneous DOA in those scenarios, it is possible to take advantage of the very low –and approximately linear over short time spans– rate of change of the LOS signal’s DOA (when the receiver attitude is known). We have implemented a sliding window method, which limits the next DOA estimate to a  $\pm 10^\circ$  difference, both in elevation and azimuth, from the current DOA estimate. This method effectively reduces the size of the search space of the DOA estimation algorithms. If a search grid approach is used, and for a given grid step size, reducing the search space will reduce the total number of to be tested. Besides, the sliding window method also contributes to protecting the receiver from tracking spoofed signals, unless their DOA becomes very close to the LOS signal’s DOA.

#### 4.3.1 Receiver Baseband Processing Prior to SA

In this section, we describe the signal model for the correlation output of a moving receiver. This post-correlation model particularly relevant, since the SA processing performed by the techniques described in the rest of this chapter, relies on it.

Let us start by noticing that for receivers moving at speeds of up to a few m/s, we can approximate Expression (4.7), which defines the elements of the basis-function matrix  $\mathbf{D}$ , as:

$$[\mathbf{D}]_{km} \approx s_m \left( \left( 1 - \frac{f_{d,m}}{f_c} \right) t_k - \tau_{0,m} \right) \exp \left\{ -j2\pi \left( f_{d,m} t_k + \frac{\dot{f}_{d,m}}{2} t_k^2 + \frac{\Delta\rho(t_k)}{\lambda} + f_c \tau_{0,m} \right) \right\}. \quad (4.39)$$

In the previous equation, the effects of the relative delay have been approximated as a carrier phase shift only. This approximation is equivalent to taking the narrowband array assumption. Equation (4.39) introduces the terms  $f_{d,m} \triangleq \alpha_m f_c$  and  $\dot{f}_{d,m} \triangleq \dot{\alpha}_m f_c$ , as the equivalent carrier Doppler shift and Doppler shift rate for the  $m$ th signal component, respectively. For static or slow moving receivers, typical values for  $\dot{f}_d$  are on the order of a few  $\text{Hz}^2$  [176], which allows to safely neglect the effect of the Doppler rate on  $s_m(t)$ , in other words, to neglect the code delay.

GNSS receivers correlate the signal at the output of the RF front end with a locally generated replica of the desired satellite signal, over a time  $T_{int} = K f_s^{-1}$ , which is referred to as correlation –or integration– time. We recall  $f_s$  as the sampling frequency. This approach, known as matched filtering, is optimal for maximizing the SNR in the presence of additive noise, and it allows to estimate the delay and Doppler shift experienced by the received signal [123]. Every  $T_{int}$  period, the receiver computes a new correlation output that can be

expressed as:

$$y_n = \frac{1}{K} \sum_{k=0}^{K-1} x(t_k) s^* \left( \left( 1 - \frac{\hat{f}_{d,n}}{f_c} \right) t_k - \hat{\tau}_n \right) \exp \{ j 2 \pi \hat{f}_{d,n} t_k \}, \quad (4.40)$$

where  $\hat{\tau}_n$  and  $\hat{f}_{d,n}$  are, respectively, the delay and the carrier Doppler frequency shift, estimated by the receiver for the  $n$ th  $T_{int}$  interval.  $s(t_k)$  represents the local replica of the PRN sequence for the satellite of interest, sampled at  $f_s$ . Given the low cross-correlation among the pseudorandom codes of the different satellites [12], it is possible to approximate Expression (4.40) as:

$$y_n \approx \frac{1}{K} \sum_{k=0}^{K-1} \sum_{m=0}^{M_p-1} a_m(t_k) [\mathbf{D}]_{km} s^* \left( \left( 1 - \frac{\hat{f}_d}{f_c} \right) t_k - \hat{\tau}_n \right) \exp \{ j 2 \pi \hat{f}_{d,n} t_k \} + \eta_n, \quad (4.41)$$

where  $M_p$  is the number of different signal components (LOS plus multipath) for the considered satellite, and  $\eta_n$  is the resulting filtered noise, which is expressed as:

$$\eta_n = \frac{1}{K} \sum_{k=0}^{K-1} n(t_k) s^* \left( \left( 1 - \frac{\hat{f}_d}{f_c} \right) t_k - \hat{\tau}_n \right) \exp \{ j 2 \pi \hat{f}_{d,n} t_k \}. \quad (4.42)$$

In the GNSS literature, e.g., in [156, 185], when Equation (4.41) is expressed as a function of  $\hat{\tau}_n$  and  $\hat{f}_{d,n}$ , it is known as the discrete version of the cross-ambiguity function (CAF), already introduced in Section 2.3.2.

The correlation of the received signal with the locally generated replica is a linear operation. Therefore, Expression (4.41), is just the sum of each signal component correlated with the signal's local replica. Hence, it follows that the correlation output  $y_n$  can be expressed as:

$$\begin{aligned} y_n &\approx \sum_{m=0}^{M_p-1} \beta'_{m,n} + \eta_n \\ &= \sum_{m=0}^{M_p-1} \left( \beta_{m,n} + \frac{1}{\sqrt{2}} \sigma_{\beta_{m,n}} Z_{m,n} \right) + \eta_n \\ &= \sum_{m=0}^{M_p-1} \beta_{m,n} + \underbrace{\frac{1}{\sqrt{2}} \sum_{m=0}^{M_p-1} \sigma_{\beta_{m,n}} Z_{m,n}}_{\eta'_n} + \eta_n, \end{aligned} \quad (4.43)$$

where the coefficients  $\{\beta'_{m,n}\}$  are independent and, by the central limit theorem, distributed as circularly-symmetric complex Gaussian random variables with mean  $\{\beta_{m,n}\} \in \mathbb{C}$  and variance  $\sigma_{\beta_{m,n}}^2$  [64]. Hence, in Equation (4.43),  $\{Z_{m,n}\}$  represent *iid* circularly-symmetric complex normal random variables. The new noise term  $\eta'_n$ , which combines the thermal noise and statistical part of the multipath, will follow a zero-mean complex Gaussian distribution.

As any complex number, the deterministic coefficients  $\{\beta_{m,n}\}$  can be expressed as  $|\beta_{m,n}| \exp \{ j \varphi_{m,n} \}$ , where  $\varphi_{m,n}$  represents the phase of  $m$ th correlation output component, with respect to the receiver's local oscillator phase.

### 4.3. A Tracking Architecture for SA Processing with Uniform Circular Motion

It is possible to take the approach used to express (4.43) even further, and express the correlation output right after the  $n$ th integration period as:

$$y_n \approx |\beta_{\Sigma,n}| \exp \{j\varphi_{\Sigma,n}\} + \eta'_n, \quad (4.44)$$

with

$$|\beta_{\Sigma,n}| = \sqrt{\left(\sum_{m=0}^{M_p-1} |\beta_{m,n}| \cos(\varphi_{m,n})\right)^2 + \left(\sum_{m=0}^{M_p-1} |\beta_{m,n}| \sin(\varphi_{m,n})\right)^2}, \quad (4.45)$$

and

$$\varphi_{\Sigma,n} = \text{atan} \left( \frac{\sum_{m=0}^{M_p-1} |\beta_{m,n}| \sin(\varphi_{m,n})}{\sum_{m=0}^{M_p-1} |\beta_{m,n}| \cos(\varphi_{m,n})} \right). \quad (4.46)$$

Depending on the considered scenario, we can make two alternative assumptions about the statistics of  $y_n$ :

1. The LOS signal is received and there is no significant coherent multipath component. This is equivalent to setting  $\beta_{m,n} \approx 0$  for  $m > 0$ , which implies  $\varphi_{\Sigma,n} \approx \varphi_{0,n}$  and  $\beta_{m,n} \approx \beta_{0,n}$ . Hence,  $y_n$  will follow a complex Gaussian distribution with mean approximately equal to  $\beta_{0,n} \exp \{j\varphi_{0,n}\}$  and the variance of  $\eta_n$ .
2. The LOS signal is received together with a  $M_p - 1$  coherent multipath components. Similarly, this corresponds to  $\beta_{m,n} = 0$  for  $m > M_p$ . For example, this assumption would hold for static receivers in dense urban environments.

In both cases,  $|y_n|^2$  will follow a non-central chi-squared distribution, while the amplitude  $|y_n|$  will follow a Rice distribution [64].

Let us focus on the case where the LOS component clearly dominates, i.e.,  $\beta_{0,n} \gg \beta_{m,n}$ , which corresponds –approximately– to the first of the two previous assumptions. Besides, we assume any multipath contribution to be zero-mean and already considered as part of the noise term  $\eta_n$ . Under these assumptions, the noiseless correlator's output phase,  $\varphi_{\Sigma,n}$  at the receiver's tracking stage, can be expressed as:

$$\varphi_n = \underbrace{\vartheta_{init} + 2\pi \left( f_d t_n + \frac{\dot{f}_d}{2} t_n^2 \right)}_{\text{Reference phase delay component}} + \underbrace{\frac{2\pi}{\lambda} \Delta \rho(t_n)}_{\text{Relative phase delay component}} + \vartheta_a(t_n) - \hat{\varphi}_n, \quad (4.47)$$

where, from now on, we drop the subscript ' $\Sigma$ ' for readability.  $\vartheta_{init}$  is the phase with respect to the local oscillator at  $t = 0$ ;  $\vartheta_a(t)$  is the phase shift due to the receiving antenna, assumed constant during each  $T_{int}$  interval, and caused by the antenna's complex gain and the polarization mismatch; and  $\hat{\varphi}_n$  is the phase estimate related to the local replica of the signal. The phase terms labeled as *reference phase delay component* in Equation (4.47), are related to the reference delay  $\tau_{ref}$ , introduced in Section 4.1, i.e., the phase observed by a hypothetical receiver with its antenna's phase center located at the origin of coordinates of the defined reference frame. Conversely, the phase terms labeled as *relative phase delay component* in Equation (4.47), are related to the relative delay  $\tau_{rel}$ , also defined in Section 4.1. We recall  $\tau_{rel}$  as the propagation delay difference caused by the receiver's position being different than the origin of coordinates. Thus, it is only related with the antenna motion within the frame of reference.

As previously described in Section 4.3, we are particularly interested in the scenario where the antenna is supported by a rotating arm. In this scenario, the antenna describes a uniform circular motion parallel to the ground plane at a rotation speed  $\omega_{rot}$ . The propagation path difference  $\Delta\rho(t)$  for this particular motion can be expressed as

$$\Delta\rho(t) = r \cos(\theta) \cos(\omega_{rot}t + \Delta\phi), \quad (4.48)$$

where  $r$  is the trajectory radius;  $\theta$  is the observed elevation angle for the LOS signal; and  $\Delta\phi = \phi_{ant-0} - \phi$  is the azimuth difference between the LOS azimuth  $\phi$ , and the azimuth defining the antenna position at the beginning of the measurement, i.e.,  $\phi_{ant-0}$ . All these angles are defined in the considered reference frame, which remains static.

Being attached to the mechanical arm, the antenna is simultaneously spinning around the vertical axis at the same rate  $\omega_{rot}$ . The phase term  $\vartheta_a$  will potentially change in orientation of the receiving antenna with respect to the transmitting antenna, i.e., the GNSS satellite antenna. The  $\vartheta_a(t)$  phase contribution is responsible for the so-called phase *wrap-up*, or phase *wind-up* effect [140, 178, 180]. Compensating the phase wrap-up effect is particularly important in GNSS receiver designs using carrier phase measurements. In the context of SA processing, and for satellites observed at a high elevation angles, the phase wrap-up can be approximated as a constant frequency offset in the carrier measurements. This implies that  $\vartheta_a(t)$  is evolving linearly with time as a function of the antenna spinning speed only [180]. The phase wrap-up effect must be corrected, otherwise, it will degrade the performance of the SA processing techniques, e.g., biasing the DOA estimates.

### 4.3.2 Practical Challenges of SA Processing

Adapting spatial filtering techniques used with physical antenna arrays, either for beamforming or DOA estimation, to use them in the SA processing context entails practical challenges. Here, we described the three most important ones that we have identified during the designing the proposed SA tracking architecture and its implementation within our GPS SDR receiver.

First, the position of the antenna during the SA interval must be accurately known. In practice, this usually satisfied by measuring the antenna position using some kind of sensor [127, 141]. Even in the case of an antenna mounted on a rotating arm with a fixed radius, the angular speed will likely experience some small variations over time, caused by the motor itself or external factors, such as the presence of wind when operating outdoors. For other arbitrary trajectories, an inertial measurement unit (IMU) can be used, like different authors did in [133, 141, 184, 186]. The antenna position measurements must be synchronized with the RF measurements, which increases the system complexity.

As described in Section 2.5.1, the SA processing of GNSS signals depends on the stationary channel assumption holding over the considered  $T_{SA}$  period. In scenarios with severe multipath, such as in urban environments, this assumption barely holds in practice, particularly for long  $T_{SA}$  periods, e.g., of a few seconds. Even assuming that it holds, the receiver still needs to estimate the spatiotemporal covariance matrix  $\Sigma_{\mathbf{x}}$ , if adaptive algorithms are to be used. With physical GNSS antenna arrays, the collection of a few milliseconds of signal usually implies a number of samples large enough to estimate the channel's spatial correlation by using the Sample Covariance Matrix (SCM) method [187]. However, in SA processing at post-correlation level, each sample corresponds to a different antenna position. Therefore, the number of samples is equal to the number of available snapshots, which is referred as small sample size regime [187]. If the SCM is used within the adaptive algorithms –e.g., within those described in Section 2.5.1– under this regime, these algorithms might display



### 4.3. A Tracking Architecture for SA Processing with Uniform Circular Motion

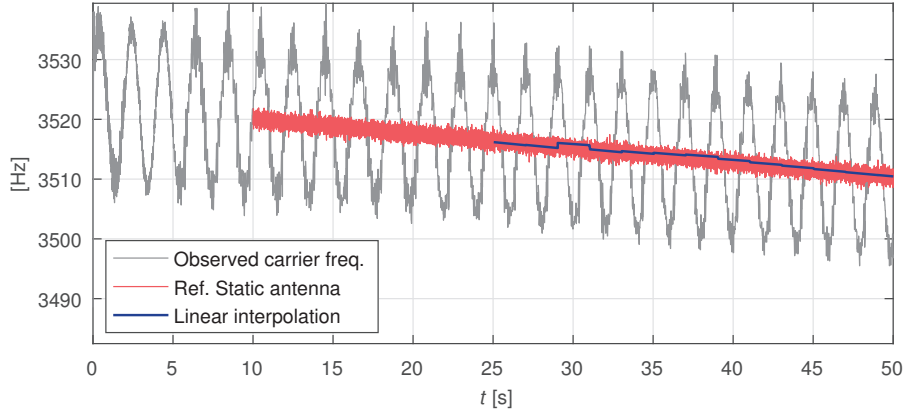


**Figure 4.10** – Comparison of the reference carrier frequency estimation methods described in [8].

severe performance degradation. The reason for this behavior is that the SCM is not a well conditioned estimator of the covariance matrix. Therefore, in the small sample size regime, inverting the SCM drastically amplifies the estimation error [187]. Several approaches to address this issue can be found in the literature, e.g., in [187–189]. Most of them seek to find an estimator of the covariance matrix that behaves better than the SCM or that regularizes it. How to apply these approaches within the GNSS SA processing context is beyond the scope of this thesis. By default, we use only the SCM method when implementing any of the adaptive algorithms considered.

Finally, even in an interference free scenario where only LOS signal is received, the isolation of the relative phase delay component from the observed phase, expressed as in Equation (4.47), is not straightforward. In [8], the authors describe the following two methods to do so:

- A first method consists in approximating the reference carrier frequency as linear, and using a least squares estimation (LSE) algorithm to estimate the regression coefficients, which correspond to a constant frequency shift  $f_d$  and a frequency rate  $\dot{f}_d$ . The input to this LSE algorithm is a batch of carrier frequency estimates obtained from the carrier tracking loop. The length of the selected batch strongly impacts the LSE accuracy. In this thesis, we refer to this method as the *linear interpolation method*.
- A second method consists in using an additional static antenna, ideally placed in the origin of coordinates of the considered reference frame, to track the reference carrier frequency. The carrier frequency observed by the static antenna is dominated by the satellite-receiver motion. Hence, the reference carrier estimate obtained with the static antenna can be used to compensate the total carrier frequency observed by the moving antenna. However, this approach increases the receiver’s complexity and the amount of required signal processing. Moreover, having an extra static antenna can be unfeasible for some applications. We refer to this method as the *reference static antenna method*.

Figure 4.10 shows an example comparing these two methods with real GPS signal measured by an antenna mounted on a rotating arm. The setup to collect these measurements is later discussed in Section 4.5.

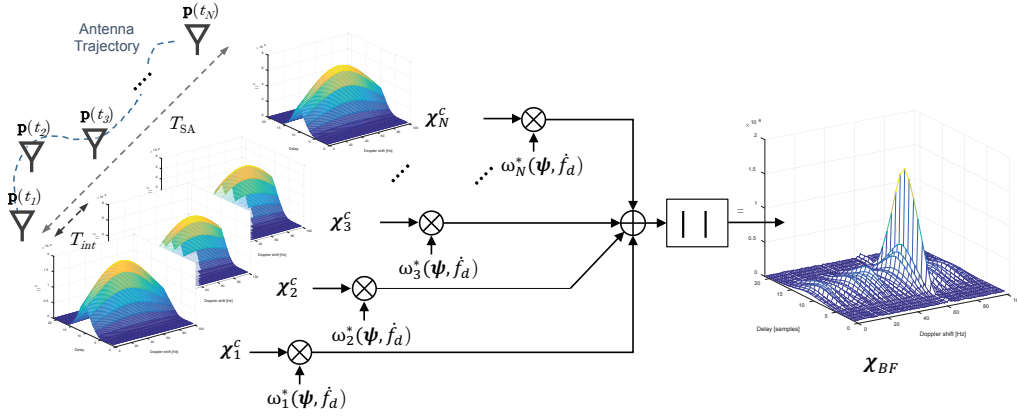


Figure 4.11 – Proposed SA open-loop beamforming scheme flow diagram

### 4.3.3 Open-Loop Tracking with SA Processing

The classic open-loop tracking of GNSS signals has been described in Section 2.3.4. In this section, we concentrate only on describing how it can be adapted for SA processing by computing a new –SA– CAF, as the weighted sum of the CAFs computed for the considered SA interval  $T_{SA}$ . Figure 4.11 shows this simple principle.

For every correlation interval  $T_{int}$ , the receiver processes the signal as described in Section 4.3.1. During this interval, the received signal is correlated –possibly in parallel– with not a single, but with multiple local replicas. These replicas correspond to the code delay  $\hat{\tau} \in \mathbb{R}^{K_\tau}$  and Doppler frequency shift  $\hat{f}_d \in \mathbb{R}^{K_{f_d}}$  hypotheses. As described in Section 2.3.4, for a specific Doppler hypothesis, the correlation for all the code delay hypothesis can be efficiently computed in parallel in the frequency domain resorting to FFT-based methods. The correlation results for all the hypothesis are organized into the CAF matrix, defined as:

$$\chi_n(\hat{\tau}, \hat{f}_d) \in \mathbb{C}^{K_\tau \times K_{f_d}}. \quad (4.49)$$

The hypotheses in  $\hat{\tau}$ , and  $\hat{f}_d$  define the open-loop tracking search space. Besides, the number of code delay hypotheses is constrained to  $K_\tau \leq T_{int} f_s^{-1}$ .

Since the open-loop tracking generates CAFs corresponding  $T_{int}$  periods, it convenient to select the SA interval as a multiple of  $T_{int}$ , i.e.,  $T_{SA} = NT_{int}$ . For GPS L1 C/A signals, we choose  $T_{int} = 20$  ms, i.e., an exact multiple of the their code period. We assume that data bit synchronization has been achieved, such that possible bit transitions coincide with the end of every  $T_{int}$  period. Moreover, we also assume the receiver is either assisted –i.e., the data sequence is provided via another communication channel and compensated in the received signals– or the receiver is processing pilot channel signals.

At this point, we introduce the *corrected*-CAF matrix for as a modified version of (4.49), which ensures the coherence of the signal replicas across consecutive  $T_{int}$  intervals. This matrix can be computed as<sup>5</sup>:

$$\text{vec}(\chi_n^c(\hat{\tau}, \hat{f}_d)) = (\hat{\mathbf{D}}(\hat{\tau}, \hat{f}_d) \Phi_n)^H \mathbf{x}_n, \quad (4.50)$$

<sup>5</sup>  $\text{vec}(\cdot)$  is the vectorization operator, a linear operator that rearranges the matrix into a column vector.

### 4.3. A Tracking Architecture for SA Processing with Uniform Circular Motion

where  $\chi_n^c(\hat{\tau}, \hat{\mathbf{f}}_d)$  is the corrected-CAF for the  $n$ th  $T_{int}$  interval. The matrix  $\hat{\mathbf{D}}(\hat{\tau}, \hat{\mathbf{f}}_d) \in \mathbb{C}^{K \times P}$  groups all signal local replicas generated for a single integration interval and a total number of hypotheses  $P = K_\tau K_{f_d}$ . The elements of this matrix are expressed as:

$$[\hat{\mathbf{D}}(\hat{\tau}, \hat{\mathbf{f}}_d)]_{kp} = s \left( \left( 1 - \frac{\hat{f}_{d,p}}{f_c} \right) t_k - \hat{\tau}_p \right) \exp \{ -j2\pi \hat{f}_{d,p} t_k \}, \quad (4.51)$$

where  $0 \leq k \leq K - 1$ , and  $1 \leq p \leq (K_\tau K_{f_d})$ . The diagonal matrix  $\Phi_n \in \mathbb{C}^{P \times P}$  contains the correction coefficients to maintain phase coherence among signal replicas for the same  $\hat{\mathbf{f}}_d$  over the different correlation intervals. It is expressed as<sup>6</sup>:

$$\Phi_n = \text{diag} \{ \mathbf{b}_n(\hat{\mathbf{f}}_d) \} \otimes \mathbf{I}_{K_\tau}, \quad (4.52)$$

where  $\mathbf{b}_n(\hat{\mathbf{f}}_d) \in \mathbb{C}^{K_{f_d}}$  is the vector of phase coefficients, with its components defined as:

$$b_{n,i} = \exp \{ j2\pi \hat{f}_{d,i} t_n \}. \quad (4.53)$$

$t_n$  is the sampling instant corresponding to the center of the  $n$ th correlation interval duration, i.e.,  $t_n = (n - 1/2)T_{int}$ .

Subsequently, we define the *beamformed* CAF matrix, computed using the  $N$  corrected-CAF matrices obtained during the entire  $T_{SA}$  as:

$$\chi_{BF} = \sum_{n=0}^{N-1} \chi_n'(\hat{\tau}_n, \hat{\mathbf{f}}_{d,n}) \omega_n^*, \quad (4.54)$$

where  $\omega_n \in \mathbb{C}$  is the  $n$ th *modified* beamforming coefficient. These beamforming coefficients shall also compensate for the carrier's Doppler rate  $\dot{f}_d$  effect on the carrier phase observed during  $T_{SA}$ . Hence, we have defined them as

$$\boldsymbol{\omega} = \mathbf{w} \odot \boldsymbol{\gamma}, \quad (4.55)$$

where the vector  $\mathbf{w}$  is the beamforming weight vector –defined in Section 2.5.1–. The components in the vector  $\boldsymbol{\gamma} \in \mathbb{C}^N$  are expressed as:

$$\gamma_n = \exp \{ j\pi \dot{f}_d t_n^2 \}. \quad (4.56)$$

Given that  $\dot{f}_d$  is usually very small, i.e.,  $< \pm 2$  Hz/s [157], its effect on the observed carrier phase can be well approximated as a constant phase offset over correlation intervals of up to a few milliseconds. That is equivalent to taking a second-order approximation of the local signal replicas' carrier phase. If this phase offset is not corrected, the receiver will not be able to properly compensate the entire phase contribution due to the reference delay. Hence, the performance of any SA processing technique might be severely impacted.

Finally, the code delay and Doppler frequency estimates correspond to the values in  $\hat{\tau}$  and  $\hat{\mathbf{f}}_d$  for which  $|\chi_{BF}|$  is maximized. Any possible distortion in  $\chi_{BF}$  –from the ideal CAF with a  $T_{int} = T_{SA}$  – caused by the presence of interfering signals given the right  $\mathbf{w}$  and  $\dot{f}_d$  selection, should be minimized as a result of the beamforming.

The SA open-loop processing described can be implemented using the tracking architecture proposed in Section 4.3. In this case, the SA buffer now the  $N$  modified CAF matrices corresponding to the last  $T_{SA}$  seconds. The DOA and the beamforming are performed within

<sup>6</sup> $\otimes$  operator represents the Kronecker product.

the respective blocks. However, the receiver can estimate the Doppler rate  $\dot{f}_d$  together with the DOA parameters –through the definition of the modified beamforming coefficient vector– within the DOA estimation block.

Within the current open-loop context, the weights  $\mathbf{w}$  for the Delay-and-sum beamformer are obtained exactly as described in Section 2.5.1, since they do not depend on the signal’s statistics. However, computing  $\mathbf{w}$  for adaptive methods in this same is more complicated. Essentially, it is not obvious how to define the covariance matrix for the  $P$  corrected-CAF elements across several  $T_{int}$  intervals. Moreover, the receiver needs to be capable of estimating this matrix in practice, i.e., to estimate the channel’s spatiotemporal covariance matrix from the corrected-CAFs computed. For this reason, we concentrate on adapting only the Delay-and-sum and the Beamscan algorithms.

Adapting the Beamscan algorithm is straightforward. The vector of beamforming coefficients  $\mathbf{w}$  is computed exactly as defined by Expressions (2.28-2.27) and (2.28), from Section 2.5.1, i.e., as

$$\mathbf{w} = \mathbf{v}(\theta, \phi) = \frac{1}{N} \exp \left\{ j \mathbf{k}^T(\theta, \phi) \mathbf{P} \right\}, \quad (4.57)$$

where  $\mathbf{k}(\theta, \phi)$  is the steering vector for a particular DOA and is defined as

$$\mathbf{k}(\theta, \phi) = -\frac{2\pi}{\lambda} \begin{bmatrix} \cos(\theta) \cos(\phi) \\ \cos(\theta) \sin(\phi) \\ \sin(\theta) \end{bmatrix}, \quad (4.58)$$

where this time, the matrix  $\mathbf{P} \in \mathbb{R}^{3 \times N}$  describes the position of the antenna during its motion. Each row in  $\mathbf{P}$  represents the average position of the antenna’s phase center during each of the  $N$   $T_{int}$  intervals included in the total SA time  $T_{SA}$ .

The DOA parameters can be estimated together with the carrier frequency’s by computing

$$\left\{ \hat{\theta}, \hat{\phi}, \hat{\dot{f}}_d \right\} = \arg \max_{\left\{ \theta, \phi, \dot{f}_d \right\}} \left( \max \left( \left| \chi_{BF}(\theta, \phi, \dot{f}_d) \right| \right) \right). \quad (4.59)$$

This maximization can be performed using iterative optimization methods, such as we have done for computing the MLE in Section 4.2.2, or using a 3D grid search. The latter approach is more robust –there is no risk of misidentifying a local maximum as the global one– but, unless the search space is small, it rapidly becomes computationally prohibitive given the large number of hypotheses to test.

Figure 4.12 shows an example of the beamformed CAF –using the Delay-and-sum algorithm– depicted in three different cases. In the first case (a) the DOA of the received signal matches the beamforming direction. Since SA processing is coherent, the width of the beamformed CAF –i.e., from null-to-null– in the  $f_d$  dimension is reduced to  $1/T_{SA}$ . In the second case (b), the beamforming direction does not match the DOA of the received signal, so we can appreciate a significant attenuation (17.3 dB in power) and major distortion caused by the beamforming process. Lastly, in case (c) the DOA of the received signal matches the beamforming direction, but there is a 0.5 Hz<sup>2</sup> error on the Doppler rate  $\dot{f}_d$  assumption used

### 4.3. A Tracking Architecture for SA Processing with Uniform Circular Motion

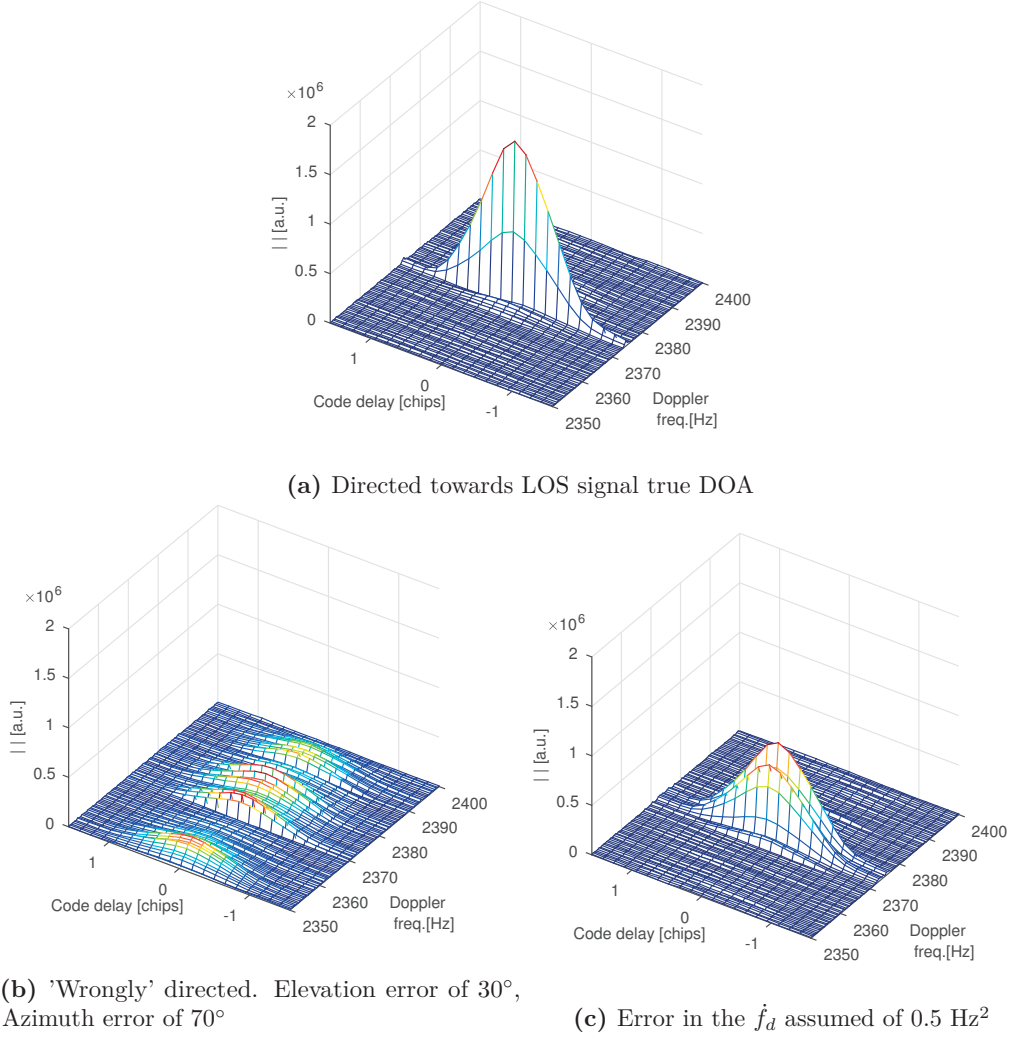


**Figure 4.12** – Beamformed CAFs for 3 different cases using Delay-and-sum

to generated the modified beamforming coefficients. We observe how this error introduces an attenuation of 5.2 dB and some distortion in the carrier Doppler dimension.

The SA open-loop tracking proposed is inherently more robust than its closed-loop counterpart. In the context of the proposed tracking architecture, closed-loop tracking requires the Main tracking channel to maintain the signal lock if any SA processing is performed in the Auxiliary channel. This problem is common to all closed-loop schemes supporting any SA processing. At the moment of writing this thesis, and to the best of our knowledge, all the previous work implementing SA processing in the GNSS context has been implemented closed-loop tracking schemes (e.g., [8, 133, 141]). Unless the DOA of the LOS signal is known a priori, as in [141], the proposed open-loop scheme should be more resilient to interfering signals. For example, we can think of a receiver operating in hostile environments, where the presence of some interfering signal(s), prior to the SA processing start, prevents our receiver from applying any spatial filtering. In such scenario, the SA open-loop tracking can seamlessly start its operation immediately after the signal acquisition. Moreover, as described in Section 2.3.4, the open-loop tracking itself can be understood as a continuous acquisition of the signal, –usually– only over a smaller search space. Therefore, just by adjusting the initial search space for synchronization parameters  $\tau$  and  $f_d$ , the described SA open-loop

processing can be directly used to implement spatial filtering with SA directly in the receiver’s acquisition stage. Unfortunately, any kind of open-loop tracking architecture usually has higher computational cost than its closed-loop counterpart. SA processing only makes this cost even higher. Compared to the closed-loop case, with the Delay-and-sum and Beamscan algorithms, the total number of operations required is multiplied by  $P$  times, i.e., the total number of hypotheses. The amount of memory needed by the SA buffer is also increased by a factor  $P$ , in order to store the  $N$  corrected-CAF matrices.

#### 4.3.4 Closed-Loop Tracking: Estimation the Reference Carrier Frequency

In closed-loop tracking architectures, the receiver sequentially processes the correlation output to generate the code delay and carrier Doppler frequency estimates, i.e.,  $\{\hat{\tau}_n, \hat{f}_{d,n}\}$ , for the next correlation period  $T_{int}$ . The simplest closed-loop tracking architectures implement a delay-locked loop (DLL) to estimate the code delay, combined with a phase-locked loop (PLL) or a frequency-locked loop (FLL) to track the signal’s carrier phase, or carrier frequency, respectively [12].

Nonetheless, the use of Kalman filters (KFs) to replace traditional tracking loops has received significant attention during the last years. Particularly for carrier tracking, KFs have demonstrated several advantages under harsh tracking conditions [60, 190–192]. A KF might be thought of as a sequential minimum mean square error (MSE) estimator which exploits a statistical and dynamical model to predict and estimate the parameters of interest representing the filter states [123, 193].

Within the SA processing context, a KF can efficiently integrate our knowledge about the antenna motion and decouple the measured signal phase into its different contributions. If the KF converges successfully, it can provide an efficient solution to the reference carrier frequency compensation challenge. In this thesis, we propose a new approach to do so by using an extended Kalman filter (EKF). EKFs are used with to linearize non-linear state and measurement transition functions about the working point [193]. This approach can potentially overcome many of the limitations of the existing methods, described in Section 4.3.2. The EKF sequentially updates the parameter estimates, which naturally solves the issue of the LSE’s batch length selection faced by the linear interpolation method, and does not require an extra static antenna element.

For the rotating antenna scenario, equations (4.47) and (4.48), describing the carrier phase measurements, can be used to develop the state model for an EKF. The formulation for this EKF carrier tracking problem is sketched in Algorithm 2. We use a fairly standard KF notation, as in [192], for the estimated variables, i.e., the subscript  $n|n-1$  for the predicted estimate at time  $t_n$  using measurements up to time  $t_{n-1}$ , while  $n|n$  is used for the estimated value at time  $t_n$  using measurements up to time  $t_n$ . In Algorithm 2,  $\hat{\mathbf{x}}$  represents the state vector estimate;  $\mathbf{P}_n$  represents the process noise covariance matrix;  $\mathbf{F}_n$  is the state transition matrix;  $\mathbf{Q}_n$  is the system noise covariance matrix; the vector  $\mathbf{z}_n$  represents the measurements with their covariance expressed by  $\mathbf{R}_n$ ; and  $\mathbf{H}_n$  stands for the observation matrix, which describes the relationship between measurements and the state vector. In general, the design of a KF requires defining and initializing  $\mathbf{R}_n$ ,  $\mathbf{Q}_n$  and  $\mathbf{P}_{0|0}$ . In non-adaptive KF tracking architectures, these matrices must be carefully defined a priori [191–193]. This definition has a major impact on the performance of the KF. While  $\mathbf{R}$  can be estimated from observed measurements, choosing  $\mathbf{Q}_n$  is more problematic. We have followed the common approach of

### 4.3. A Tracking Architecture for SA Processing with Uniform Circular Motion

using a discretization of the continuous noise model for the process noise, obtained as

$$\mathbf{Q}_n = \int_0^{T_{int}} \mathbf{F}_n \mathbf{Q}_c \mathbf{F}_n^T, \quad (4.60)$$

where  $\mathbf{Q}_c$  can be defined as a diagonal matrix with its non-zero elements being the spectral densities of each of the individual processes noises, as in [191].

In this thesis, we propose two different methods, both implemented using an EKF, to estimate the reference phase delay, referred –for simplicity– as EKF1 and EKF2. The two methods are implemented as part of the Main tracking channel within the proposed SA tracking architecture (see Section 4.3).

With the EKF1 method, the receiver tracks the carrier frequency using a traditional FLL. The EKF does not directly intervene in the carrier tracking. Instead, the carrier frequency estimates are fed to an EKF, which tries to estimate the carrier frequency due to the change in the reference phase delay contribution. This estimate is used to compensate the correlation output. Subsequently, the only remaining carrier frequency is due to the relative phase delay contribution. In contrast, with the EKF2 method the receiver implements a deep coupling integration scheme [193], in which an EKF is entirely responsible for the carrier tracking, while simultaneously estimates the reference phase delay component from the correlation outputs. This reference phase delay estimate is directly used to generate the carrier frequency estimate for the auxiliary channel  $\hat{f}_{d,n}$ .

More detailed descriptions of EKF1 and EKF2 methods are presented in the sections below. We shall remark that both methods assume an almost linear phase wrap-up contribution, which is observed as constant frequency offset on the carrier frequency. This offset is assumed to be already modeled within the constant carrier term  $f_d$ . Besides, these methods assume neither significant coherent multipath interference, nor atmospheric errors on the observed signal's carrier phase.

#### EKF1: FLL Carrier Tracking Combined With an EKF for Reference Frequency Tracking

When using this method, the receiver implements a standard second-order FLL to track the carrier frequency of the received signal. The frequency estimated by the FLL at the time instant  $t_n$  can be expressed using (4.48) and the time derivative of (4.47) as

$$\hat{f}_n = \underbrace{f_d + \dot{f}_d t_n}_{f_{\text{ref}}} - \omega_{\text{rot}} \kappa \sin(\underbrace{\omega_{\text{rot}} t_n + \Delta\phi}_{\phi_a}) + \eta_{f,n}, \quad (4.61)$$

with  $\kappa \triangleq r \cos(\theta)$ , since the trajectory's radius  $r$  is considered fixed and known; and  $\eta_{f,n}$  represents the frequency noise.  $f_{\text{ref}}$  is the reference Doppler contribution, and  $\phi_a$  has been defined as the accumulated antenna azimuth. This frequency estimate is used as the measurement for an EKF filter, i.e.,  $z_n = \hat{f}_n$ , defined together with the following state vector

$$\mathbf{x} \triangleq [f_{\text{ref}}, \dot{f}_d, \kappa, \phi_a, \omega_{\text{rot}}]^T. \quad (4.62)$$

The process equation is formulated as

$$\mathbf{x}_n = \underbrace{\begin{pmatrix} \mathbf{F}_{\text{ref}} & \mathbf{0} \\ \mathbf{0}^T & \mathbf{F}_{\Delta\rho} \end{pmatrix}}_{\mathbf{F}} \mathbf{x}_{n-1} + \mathbf{w}_n, \quad (4.63)$$

**Algorithm 2** Generic formulation for the (E)KF [192]

---

**Require:**  $\hat{\mathbf{x}}_0, \mathbf{P}_{x,0|0}, \mathbf{F}_n, \mathbf{H}_n, \mathbf{z}_n, \mathbf{Q}_n$  and  $\mathbf{R}_n \forall n$

1:  $n := 1$

**Prediction (time update)**

2: Estimate the predicted state vector:

$$\hat{\mathbf{x}}_{n|n-1} = \mathbf{F}_n \hat{\mathbf{x}}_{n-1|n-1}.$$

3: Estimate the predicted error covariance:

$$\mathbf{P}_{x,n|n-1} = \mathbf{F}_n \mathbf{P}_{x,n-1|n-1} \mathbf{F}_n^T + \mathbf{Q}_n.$$

**Estimation (measurement update)**

4: Estimate the predicted measurement vector:

$$\hat{\mathbf{z}}_{n|n-1} = \mathbf{H}_n \hat{\mathbf{x}}_{n|n-1}.$$

5: Estimate the innovation covariance matrix:

$$\mathbf{P}_{z,n|n-1} = \mathbf{H}_n \mathbf{P}_{x,n-1|n-1} \mathbf{H}_n^T + \mathbf{R}_n.$$

6: Estimate the Kalman gain:

$$\mathbf{K}_n = \mathbf{P}_{x,n|n-1} \mathbf{H}_n^T \mathbf{P}_{z,n|n-1}^{-1}.$$

7: Estimate the updated state vector:

$$\hat{\mathbf{x}}_{n|n} = \hat{\mathbf{x}}_{n|n-1} + \mathbf{K}_n (\mathbf{z}_n - \hat{\mathbf{z}}_{n|n-1}).$$

8: Estimate the error covariance matrix:

$$\mathbf{P}_{x,n|n} = \mathbf{P}_{x,n|n-1} - \mathbf{K}_n \mathbf{H}_n \mathbf{P}_{x,n|n-1}.$$

9:  $n := n + 1$  and go to Step 2.

---

where the state transition matrix  $\mathbf{F}$  has been expressed using the matrices

$$\mathbf{F}_{\text{ref}} = \begin{pmatrix} 1 & T_{\text{int}} \\ 0 & 1 \end{pmatrix}, \quad \mathbf{F}_{\Delta\rho} = \begin{pmatrix} 1 & 0 & 0 \\ 0 & 1 & T_{\text{int}} \\ 0 & 0 & 1 \end{pmatrix}, \quad (4.64)$$

representing the reference and relative frequency state transition matrices, respectively. The process noise  $\mathbf{w}_n \sim \mathcal{N}(\mathbf{0}, \mathbf{P}_n)$  stands for any possible uncertainties or mismatches in the state model. The process noise covariance  $\mathbf{P}_n$  is initialized to  $\mathbf{P}_{0|0}$ , which is defined as a diagonal matrix and updated according to Algorithm 2. The values selected for the main diagonal of  $\mathbf{P}_{0|0}$  are shown in Table 4.1. We have defined the system noise covariance  $\mathbf{Q}_n$  as constant using (4.60), with

$$\mathbf{Q}_c = \text{diag} \left\{ \left[ Q_{f_{\text{ref}}}, Q_{f_d}, Q_{\kappa}, Q_{\phi_a}, Q_{\omega_{\text{rot}}} \right]^T \right\}, \quad (4.65)$$

where the different  $Q_c$  parameters, shown in Table 4.1, stand for the power spectral densities of the expected errors for each state in  $\hat{\mathbf{x}}$ . The model for  $Q_{f_{\text{ref}}}$ , corresponding to the carrier reference frequency errors parameter, is assuming the receiver oscillator error as the dominant error source. The parameter  $h_{-2}$  depends on the type of oscillator used [191]. In this case it was set  $h_{-2} = 2 \times 10^{-20}$  Hz, which is a reference value for a receiver's clock using an oven controlled crystal oscillator (OCXO).  $Q_{f_d}$ , i.e., the spectral density of the reference Doppler rate, is driven by the acceleration along the line-of-sight between the origin of coordinates of the frame of reference and the satellite. The remaining parameters in  $\mathbf{Q}_c$  are tuned to match the expected slow variation of the parameters to be estimated. As hinted in Section 4.3.2,  $\omega_{\text{rot}}$



### 4.3. A Tracking Architecture for SA Processing with Uniform Circular Motion

**Table 4.1** – Tuning parameters selected in the system noise description for the the EKF1 case.

$\mathbf{Q}_c$ diag. terms	$\mathbf{Q}_c$ values	$\mathbf{P}_{0 0}$ diag. terms	$\mathbf{P}_{0 0}$ values
$Q_{f_{\text{ref}}}$	$\frac{4\pi^3 f^2 h_{-2}}{2\pi^2} 0.1 = 0.0156 \text{ Hz}$	$\sigma_{f_{\text{ref}}}^2$	$20^2 \text{ Hz}^2$
$Q_{f_d}$	$\frac{0.01^2}{2\pi^4} = 6.41 \times 10^{-6} \text{ Hz}^3$	$\sigma_{\dot{f}_d}^2$	$0.25 \text{ Hz}^4$
$Q_\kappa$	$0.01 \text{ m}^2/\text{Hz}$	$\sigma_\kappa^2$	$0.25 \text{ m}^2$
$Q_{\phi_a}$	$0.001 \text{ rad}^2/\text{Hz}$	$\sigma_{\phi_a}^2$	$\pi^2/3 \text{ rad}^2$
$Q_{\omega_{\text{rot}}}$	$0.001 \text{ rad}^2/\text{Hz}^3$	$\sigma_{\omega_{\text{rot}}}^2$	$0.5^2 (\text{rad/s})^2$

will not remain exactly constant in a real measurement scenario. Therefore  $Q_{\omega_{\text{rot}}} > 0$ .  $Q_\kappa$  and  $Q_{\phi_a}$  account for the small evolution of the observed signal's DOA.

In the EKF1 approach there is only one measurement available: the frequency estimated by the FLL, i.e.,  $z_n = \hat{f}_n$ . The measurement model is described as

$$z_n = \mathbf{H}_n \mathbf{x}_n + v_n, \quad (4.66)$$

where  $v_n \sim \mathcal{N}(0, \sigma_{f_n}^2)$  is the measurement's noise. The linearized observation matrix in equation (4.66), i.e.,  $\mathbf{H}_n \in \mathbb{R}^{1 \times 5}$ , is defined as

$$\mathbf{H}_n^T = \begin{bmatrix} 1 \\ 0 \\ -\omega_{\text{rot},n|n-1} \sin(\phi_{a,n|n-1}) \\ -\omega_{\text{rot},n|n-1} \kappa_{n|n-1} \cos(\phi_{a,n|n-1}) \\ -\kappa_{n|n-1} \sin(\phi_{a,n|n-1}) \end{bmatrix}. \quad (4.67)$$

When using the EKF1, we assume that the noise variance of the FLL output is mainly caused by thermal noise. This assumption is reasonable for the kind of antenna motion considered in this thesis, and allows us to disregard the dynamic stress error. We have selected the measurement  $z_n$  noise variance to match the thermal noise variance [12], i.e.,

$$R_n = \sigma_{f_n}^2 \approx \frac{1}{2C/N_0 T_{\text{int}}} \left( 1 + \frac{1}{2C/N_0 T_{\text{int}}} \right), \quad (4.68)$$

where  $C/N_0$  is the carrier-to-noise density of the received signal at the instant  $n$ . In practice, the true  $C/N_0$  is not known and the receiver must estimate it. In this case, we have implemented an additional *noise tracking channel*, in which the received signal is correlated with the PRN code of a satellite not present in the considered scenario. The variance of this channel's correlation output –after low-pass filtering it– is taken as the noise variance estimate  $\hat{\sigma}_w^2$ . Then, we  $\hat{C}/N_0$  as:

$$\hat{C}/N_0 = 10 \log \left( \frac{P}{\hat{\sigma}_w^2 T_{\text{int}}} \right) \text{ dB}, \quad (4.69)$$

where  $P$  is the absolute square of the Prompt correlator's output after low-pass filtering –with a simple moving average spanning 200 ms–.

#### **EKF2: Carrier Phase Tracking using an EKF for Deep Coupling Integration with the Antenna Motion Model**

In this method, carrier phase tracking is performed using an EKF that integrates, in a deep coupling scheme [193], the information provided by the antenna motion model, with its effects

**Table 4.2** – Tuning parameters selected in the system noise description for the the EKF2 case.

$\mathbf{Q}_c$ diag. terms	$\mathbf{Q}_c$ values	$\mathbf{P}_{0 0}$ diag. terms	$\mathbf{P}_{0 0}$ values
$Q_{\varphi_{\text{ref}}}$	$\pi f^2 h_0 = 3.898 \times 10^{-3} \text{ rad}^2/\text{Hz}$	$\sigma_{\varphi_{\text{ref}}}^2$	$\pi^2/3 \text{ rad}^2$
$Q_{f_{\text{ref}}}$	$\frac{4\pi^3 f^2 h_{-2}}{2\pi^2} = 0.156 \text{ Hz}$	$\sigma_{f_{\text{ref}}}^2$	$10^2 \text{ Hz}^2$
$Q_{\dot{f}_d}$	$\frac{5}{2\pi^4} \text{ Hz}^3$	$\sigma_{\dot{f}_d}^2$	$4 \text{ Hz}^4$
$Q_{\kappa}$	$0.01 \text{ m}^2/\text{Hz}$	$\sigma_{\kappa}^2$	$0.25 \text{ m}^2$
$Q_{\phi_a}$	$0.001 \text{ rad}^2/\text{Hz}$	$\sigma_{\phi_a}^2$	$\pi^2/3 \text{ rad}^2$
$Q_{\omega_{\text{rot}}}$	$0.001 \text{ rad}^2/\text{Hz}^3$	$\sigma_{\omega_{\text{rot}}}^2$	$0.05^2 \text{ (rad/s)}^2$
$Q_{\beta}$	$(200 T_{\text{int}})^2$	$\sigma_{\beta}^2$	$10^2$

on the observed phase described by equation (4.47). The state vector for this EKF is defined as

$$\mathbf{x} \triangleq [\varphi_{\text{ref}}, f_{\text{ref}}, \dot{f}_d, \kappa, \phi_a, \omega_{\text{rot}}, \beta]^T, \quad (4.70)$$

where  $\varphi_{\text{ref}}$  represents the accumulated phase due to the reference Doppler, and  $\beta$  is the amplitude of the prompt correlator output [12]. The process equation is formulated as shown in equation (4.63), with the state transition matrix  $\mathbf{F}$  expressed now using the following matrices

$$\mathbf{F}_{\text{ref}} = \begin{pmatrix} 1 & 2\pi T_{\text{int}} & \pi T_{\text{int}}^2 \\ 0 & 1 & T_{\text{int}} \\ 0 & 0 & 1 \end{pmatrix}, \quad \mathbf{F}_{\Delta\rho} = \begin{pmatrix} 1 & 0 & 0 & 0 \\ 0 & 1 & T_{\text{int}} & 0 \\ 0 & 0 & 1 & 0 \\ 0 & 0 & 0 & 1 \end{pmatrix}. \quad (4.71)$$

The values selected to initialize  $\mathbf{P}_n$ , i.e.,  $\mathbf{P}_{0|0}$ , are shown in Table 4.2. We have defined the system's noise covariance  $\mathbf{Q}_n$  as constant using expression (4.60), with

$$\mathbf{Q}_c = \text{diag} \left\{ [Q_{\varphi_{\text{ref}}}, Q_{f_{\text{ref}}}, Q_{\dot{f}_d}, Q_{\kappa}, Q_{\phi_a}, Q_{\omega_{\text{rot}}}, Q_{\beta}]^T \right\}. \quad (4.72)$$

Most of the parameters in  $\mathbf{Q}_c$  are defined in the same way as in expression (4.65) for EKF1.  $Q_{\beta}$  accounts for any slow drift on the observed signal amplitude, which the process model assumes constant.  $Q_{\varphi_{\text{ref}}}$  stands for the power spectral density of the expected error on the reference Doppler phase, which we assume that is due to the receiver clock error [191, 192]. The parameters selected for  $\mathbf{Q}_c$  are shown in Table 4.2. The model for  $Q_{\varphi_{\text{ref}}}$  is defined as a function of the parameter  $h_0 = 8 \times 10^{-20} \text{ s}$ , for a receiver driven by an OCXO [191].

The measurement vector  $\mathbf{z}_n$  for EKF2 has been defined as  $\mathbf{z}_n = [\Re\{y_n\}, \Im\{y_n\}]^T$ , i.e., the in-phase and quadrature components of the receiver's prompt correlator output. The linearized observation matrix describing the measurement model has been computed as

$$\mathbf{h}_n(\mathbf{x}_n) = \begin{bmatrix} \beta_n \cos \left( 2\pi \left( \varphi_{\text{ref},n} - \hat{\varphi}_{\text{ref},n-1|n-1} + \kappa_n \cos(\phi_{a,n}) - \hat{\kappa}_{n-1|n-1} \cos(\hat{\phi}_{a,n-1|n-1}) \right) \right) \\ \beta_n \sin \left( 2\pi \left( \varphi_{\text{ref},n} - \hat{\varphi}_{\text{ref},n-1|n-1} + \kappa_n \cos(\phi_{a,n}) - \hat{\kappa}_{n-1|n-1} \cos(\hat{\phi}_{a,n-1|n-1}) \right) \right) \end{bmatrix}. \quad (4.73)$$

The covariance matrix of the measurement vector  $\mathbf{z}_n$  is therefore characterized as

$$\mathbf{R}_n = \frac{\sigma_{\eta,n}^2}{2} \mathbf{I}, \quad (4.74)$$

where  $\sigma_{\eta,n}^2$  is the noise variance of the correlator output samples, which is a function of the observed  $C/N_0$  and  $T_{\text{int}}$ . In practice, the receiver must estimate the value for  $\sigma_{\eta,n}^2$ . As for the EKF1's case, we have implemented a *noise tracking channel* to obtain this estimate.

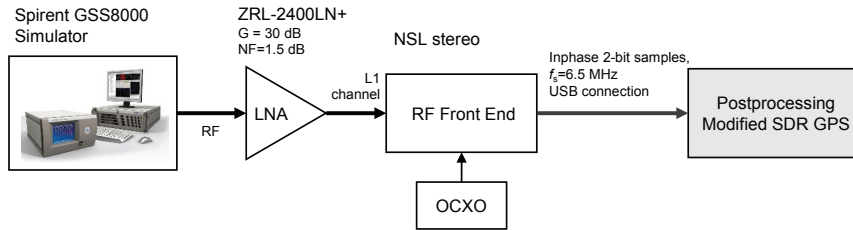


Figure 4.13 – Simulation test bench diagram

## 4.4 Results with Simulated Signal

In this section we present a selection of the results obtained with the SA processing techniques described in sections 4.3 and 2.5.1, when using synthetic GPS L1 C/A signal<sup>7</sup>. This section’s goal is twofold: first, validating the proposed SA tracking architecture in a controlled simulation environment; and secondly, demonstrating that SA techniques can effectively detect and mitigate multipath. In addition, we identify and characterize some of the main practical challenges faced by these techniques.

Simulating GNSS signals is a powerful tool to develop and test new GNSS receivers, techniques, and algorithms because it provides precise control over the signal characteristics and the scenario of interest. Therefore, when experimenting with new techniques, it is standard practice to begin working with simulated or synthetic signals, before using real measured signals. In this case, as shown in Figure 4.13, we have implemented a simulation test bench composed of three main elements:

1. A Spirent GSS8000 Simulator [194] to generate the GPS L1 C/A RF signal. The Spirent is a full constellation simulator that provides complete control over the signals features and the environmental conditions. Within its capabilities, Spirent allows user-defined antenna trajectories and gain patterns for the receiver. Spirent can also simulate –limited– multipath interference, either fixed by the user; or using a statistical model to simulate different types of environments.
2. An NSL stereo RF front end [195]. The RF output of the Spirent simulator is amplified using a Mini-Circuits ZRL-2400LN+ LNA<sup>8</sup> [196], and used as input for the front end. The front end amplifies, down-converts, filters and samples the signal. It can synchronously sample two RF channels, named L1 and L-Band. The processing chain for the L1 channel uses a MAX2769B RF front end chip (see [195]) with a single In-phase output. The L-Band channel processing chain is implemented with a MAX2112 RF front end chip (see [195]) with In-phase and Quadrature outputs. The sampling rate was configured to 6.5 MHz for both RF channels, with 2 bits per sample. The front end uses USB as output interface. The front end was driven by an external Oscilloquartz 8663 OCXO [197] to minimize the clock error impact over long integration times.
3. A modified Kai-Borre’s GPS SDR Receiver [2]. This receiver has been extensively modified to support the SA tracking architecture proposed in Section 4.3. It is implemented in MATLAB [7] and it works in post-processing, i.e., it processes previously recorded

<sup>7</sup>The term “synthetic signal” describes the RF signal generated using a GPS signal simulator.

<sup>8</sup>The Mini-Circuits ZRL-2400LN+ LNA has a nominal gain of 30 dB and a typical noise figure of 1 dB (nominal values) for the 1400–1900 MHz frequency band.

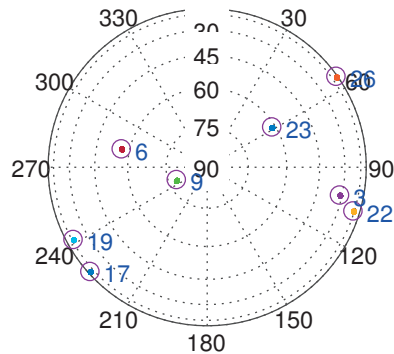


**Figure 4.14** – Skyplot for the scenario simulated using the Spirent GSS8800 simulating the a receiver located at the position:  $46^{\circ} 59' 52.73''$  N,  $6^{\circ} 56' 44.83''$  E; at time 14h41 UTC+1 on 28/11/2016.

signals. It is widely used among the GNSS research community because it allows the rapid prototyping of new GNSS algorithms.

In all the simulation cases described bellow, we consider the uniform circular motion of an isotropic antenna. Therefore, no effect due to the antenna gain or polarization mismatch, e.g., phase wrap-up, shall be observed. The signal's data bit sequence is considered known a priori, and therefore, it is errorlessly compensated during the signal tracking. Spirent was configured to simulate a receiver –or the center of its trajectory– located at the position:  $46^{\circ} 59' 52.73''$  N,  $6^{\circ} 56' 44.83''$  E; with the simulation starting at 14h40 UTC+1 on 28/11/2016. This scenario was selected to match one of our experimental scenarios: the MC Rooftop, which is described in Section 4.5. The skyplot showing the GPS satellites observed by the receiver in this scenario is displayed in Figure 4.14. Unless stated otherwise, the  $C/N_0$  for all the visible satellites is constant and approximately to 45 dB-Hz. These equal  $C/N_0$  conditions were achieved by manually adjusting the transmitted powers of the satellites in the Spirent. The simulation of atmospheric effects was turned-off when computing the results presented below.

#### 4.4.1 SA Closed-Loop Tracking: Direction-of-Arrival Estimation (I)

We have adapted the Beamscan, MPDR-Capon and MUSIC algorithms for estimation algorithms –described in Section 2.5.1– within the SA processing context. These algorithms were implemented within the DOA block of the SA tracking architecture proposed in Section 4.3. Under ideal conditions, a uniform circular motion should synthesize an aperture equivalent to a UCA. Therefore, if we correctly adapted the DOA estimation algorithms, we should observe behaviors equivalent to those of a physical UCA. We first start by assuming almost perfect cancellation of the reference carrier frequency contribution, since it can be recovered from the Spirent's simulation data logs [194].

Figure 4.15 shows two DOA maps computed for the PRN 3, using different rotation radii:  $r = 0.5$  m and  $r = 0.9$  m, at angular speed  $\omega_{rot} = \pi$  rad/s. At the time of computing the DOA maps, the true DOA of PRN 3 signal was  $\theta_3 = 31.35^{\circ}$  and  $\phi_3 = 102.05^{\circ}$ . All the DOA maps were computed using the samples gathered during one rotation period, i.e.,  $T_{SA} = 2\pi/\omega_{rot} = 2$  s. As confirmed by Figure 4.15, a smaller radius implies a smaller SA, and therefore, a wider main beam when using Beamscan. Moreover, the synthesized aperture

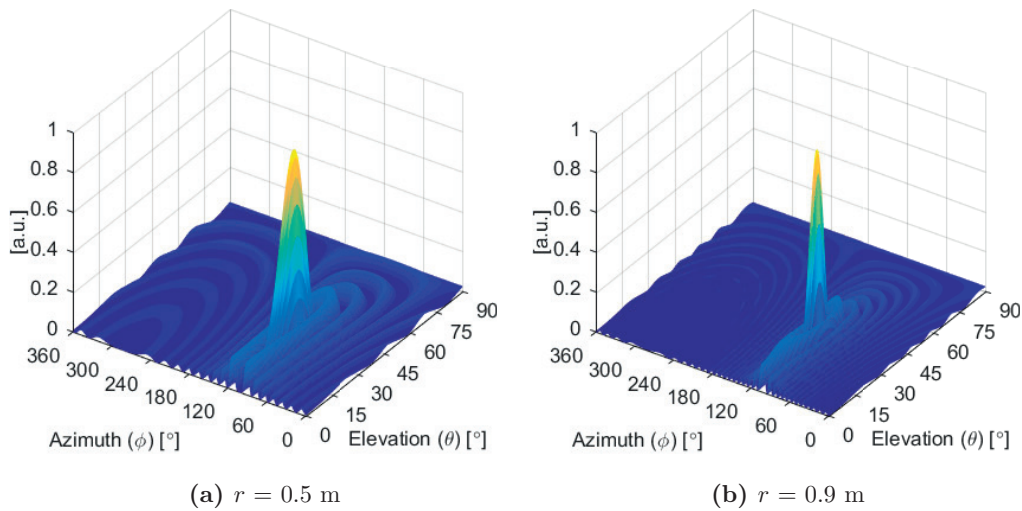


Figure 4.15 – Radius effect on the DOA map when using the Beamscan algorithm (PRN 3)

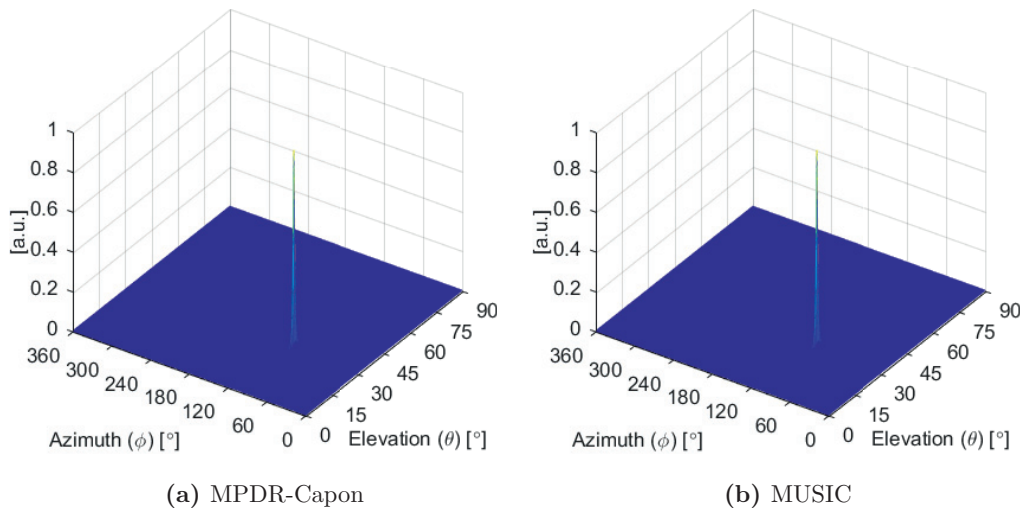
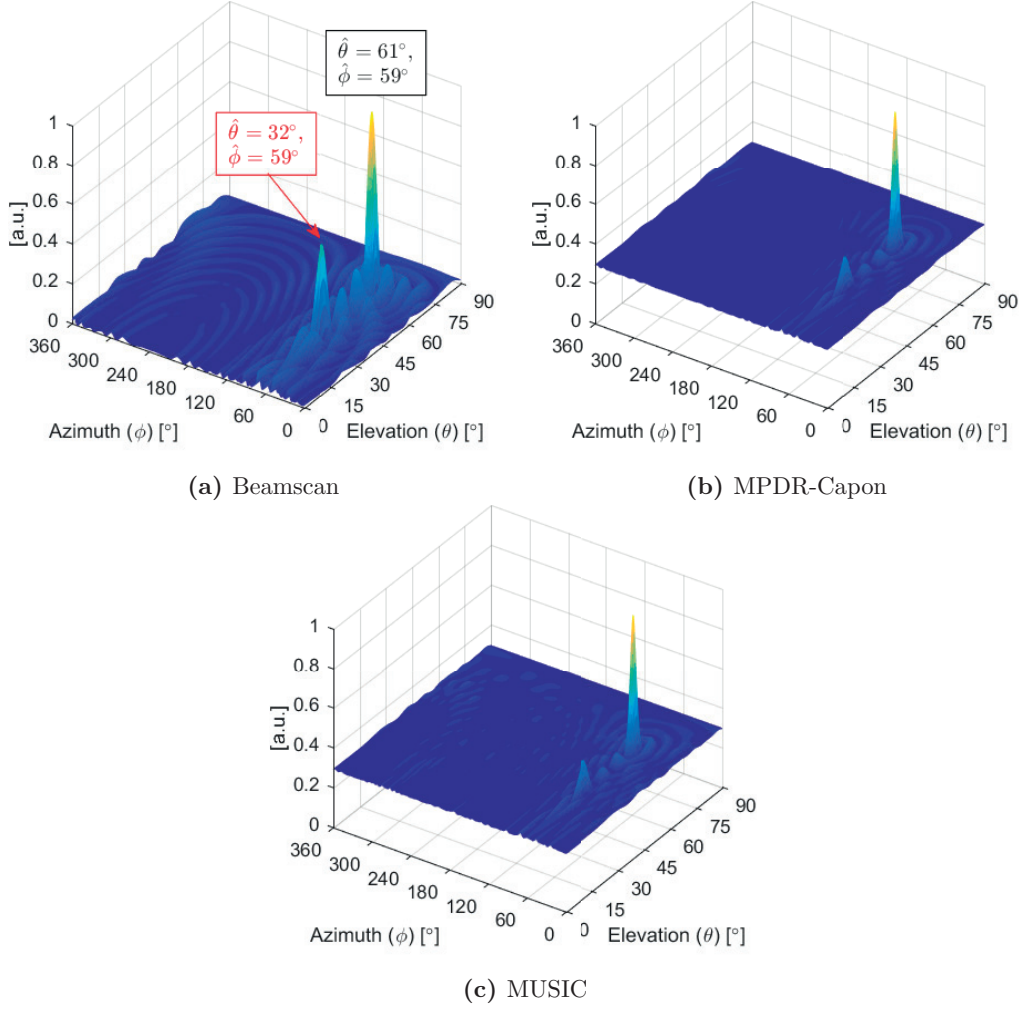


Figure 4.16 – DOA maps computed using adaptive algorithms (PRN 3)

behaves as a UCA with  $N$  elements, equally spaced by  $2\pi/N$  rad, where  $N$  is the number of correlation intervals used for the SA processing, i.e.,  $N = T_{SA}/T_{int}$ . As in a physical UCA, when using the Delay-and-sum beamformer –the Beamscan algorithm’s counterpart–, the width of the beam depends on the elevation steering angle. The lower the steering elevation, the wider the beam.

Figure 4.16 shows DOA maps computed using MPDR-Capon and MUSIC algorithms, in the same scenario. The SCM method was used to estimate the covariance matrix  $\hat{\Sigma}_{\mathbf{x}}$  for both algorithms. As expected, these adaptive techniques generate much narrower peaks/beams. Moreover, the maximum in the DOA map corresponds to the exact same DOA as with the Beamscan.

Next, we modify the previous simulation scenario by introducing a single coherent multipath component. This multipath component has been generated using the Spirent simulator’s fixed multipath mode, with 0.05 L1 C/A chips of extra delay and 3 dB power attenuation, with respect to the LOS signal for PRN 23, which had a true DOA of  $\theta_{23} = 61.65^\circ$



**Figure 4.17** – Multipath effect on DOA estimation for PRN 23. Synthetic signal. The DOAs for the two peaks in the 3 subfigures are the same, but it has been represented only once on (a). Red font is used for the multipath DOA estimates.

and  $\phi_{23} = 58.9^\circ$ . The multipath’s DOA has been set to match the LOS signal azimuth, and be exactly half of its elevation, i.e., on average  $\phi_m \approx 59^\circ$  and  $\theta_m \approx 32.25^\circ$ .

In Figure 4.17 we show the DOA maps computed using the same three DOA estimation algorithms, but this time for PRN 23. The multipath component is clearly identifiable in the DOA map in all cases. The peaks/beams for the LOS signal’s DOA when using the adaptive algorithms are not as narrow as in the LOS signal only case previously shown. Moreover, the normalized base-level of the DOA map is not close to zero anymore. The coherence of the multipath signal is responsible for these two described behaviors [121, 123]. On top of that, we expect the multipath presence to bias the LOS signal’s DOA estimates. Results in Figure 4.18 confirm this hypothesis. The smaller the angular distance difference between the signal components, the larger the bias observed. Similarly, in the same scenario, multipath with higher power it is likely to introduce a higher bias. If as in this case, multipath and LOS signal have the same azimuth, there is no bias observed in the LOS’s signal azimuth estimate.

So far, we have assumed a good knowledge of the reference carrier frequency, which allowed to compensate it, except for any deviations between the nominal values of the simulator and actual ones –small and caused by the oscillators errors–. In practice, this compensation must be done using some of the methods described in Sections 4.3.2 and 4.3.4. Errors in that

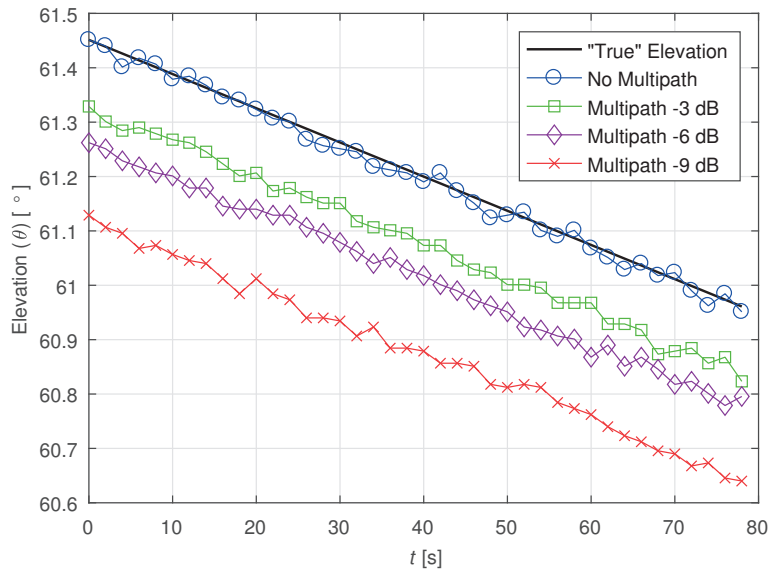


**Figure 4.18** – Elevation estimation using Beamscan algorithm during 80 s, for different coherent multipath power values, defined with respect to the LOS signal power, i.e., from -3 dB to -9 dB of attenuation.

compensation can also impact the DOA estimation, as it is discussed below.

#### 4.4.2 Reference Frequency Estimation Methods Comparison (I)

In Section 4.3.2 we have identified the challenge of isolating the relative phase –or equivalently, frequency– component in the correlation outputs. This challenge needs to be addressed before attempting any spatial filtering. In this section, we compare three different methods to do so by estimating the carrier reference phase: the linear interpolation method using a LSE; and the two EKF-based proposed methods, i.e., EKF1 and EKF2. The linear interpolation method has been described in Section 4.3.2, while EKF1 and EKF2 have been thoroughly described in Section 4.3.4.

Figure 4.19 shows the reference frequency estimates obtained with the three methods, for two different satellites: PRN 22 and PRN 23. Figure 4.19.(a) displays only the first 30 s of the carrier tracking results. The total carrier frequency observed –depicted in gray– is noisier at the start of the recording, mostly because the integration time is increased, from 1 ms to 20 ms, and the carrier tracking loop bandwidth is decreased (see Table 4.3). The observed oscillations are caused by the relative frequency component, with their period exactly matching the antenna rotation period. Abrupt changes, in the shape of small steps, are expected when using the linear interpolation method. These steps appear every time the LSE output is updated. We have selected sample batch duration of 5 s as input for the LSE. The resulting estimate is used to interpolate the reference frequency for the next 5 s. EKF1 and EKF2 methods take approximately 10 s to converge. However, the zoomed view in Figure 4.19.(b) shows a small offset of EKF1 with respect to the two other methods. This small offset does not significantly decrease, even after several seconds.

We are now interested in assessing the impact of the reference frequency compensation on the DOA estimation of the LOS signal.

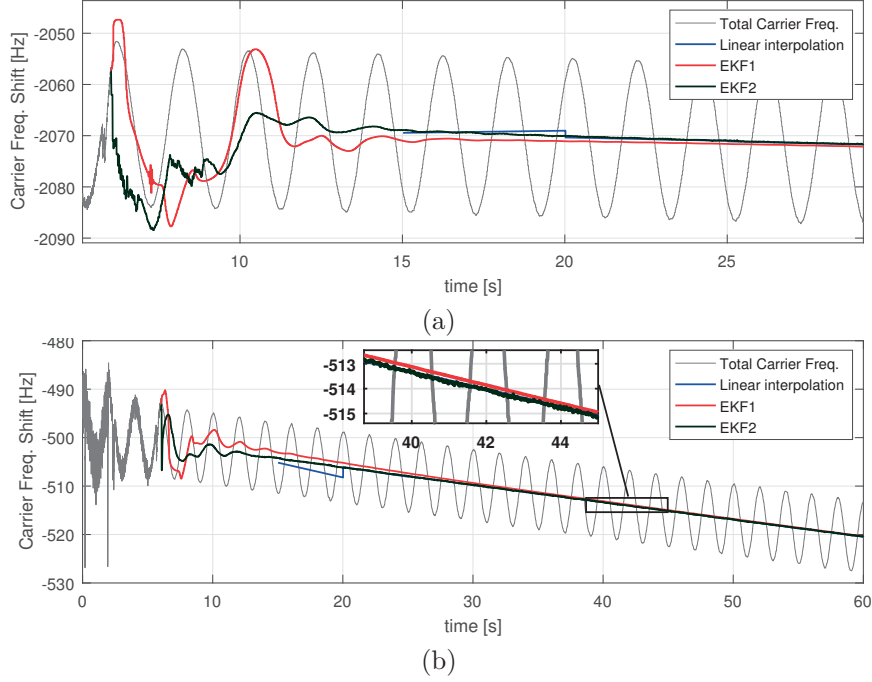


**Figure 4.19** – Estimated reference Doppler for (a) PRN 22, and (b) PRN 23. Synthetic signal. For each method, the beginning of the line marks the first estimation.

**Table 4.3** – Tracking channel settings for reference carrier frequency estimation methods comparison.  $d$  is the Early-Late correlator spacing.  $B_{(D/P/F)LL}$  represent the filter bandwidth.

time	$T_{int}$	Code Tracking (2nd-order DLL) Settings	Carrier Tracking Settings
0 – 2 s	1	$d = 1$ chips, $B_{DLL} = 1$ Hz	FLL: $B_{FLL} = 20$ Hz
2 – 5 s	1	$d = 1$ chips, $B_{DLL} = 1$ Hz	FLL: $B_{FLL} = 10$ Hz
5 – 6 s	20	$d = 0.5$ chips, $B_{DLL} = 0.5$ Hz	FLL: $B_{FLL} = 5$ Hz + PLL: $B_{PLL} = 18$ Hz
6 –	20	$d = 0.2$ chips, $B_{DLL} = 0.25$ Hz	<b>Linear interp.:</b> PLL: $B_{PLL} = 20$ Hz <b>EKF1:</b> FLL: $B_{PLL} = 20$ Hz <b>EKF2:</b> EKF

Figure 4.20 shows the DOA map computed using the Beamscan algorithm for the PRN 23. The Beamscan input are the prompt correlator output samples after the compensation of the reference carrier frequency, using EKF1 method, over one full antenna rotation, i.e., during a rotation period  $T_{SA} = 2$  s. The first input sample corresponds to the instant  $t = 40$  s, shown in Figure 4.19.(b). The projections of the DOA map’s maximum into the  $XY$  and  $YZ$  planes have been depicted, respectively, in red and gray in Figure 4.20. We use these projections or “slices” as reference to evaluate the distortion on the computed DOA map versus an ideal scenario. We have defined this ideal scenario as the one corresponding to an ideal physical UCA with  $N = T_{SA}/T_{int}$  elements. In such case, the DOA of the received signal is assumed to be perfectly known and the DOA map is computed using the analytic expressions for the UCA [123].

In Figure 4.21, we show these “slices” for the elevation and azimuth estimation for PRN 23’s DOA map, obtained using the considered reference frequency compensation methods. Interestingly, we observe a significant error in the estimated elevation  $\hat{\theta}$  for the EKF1 method,



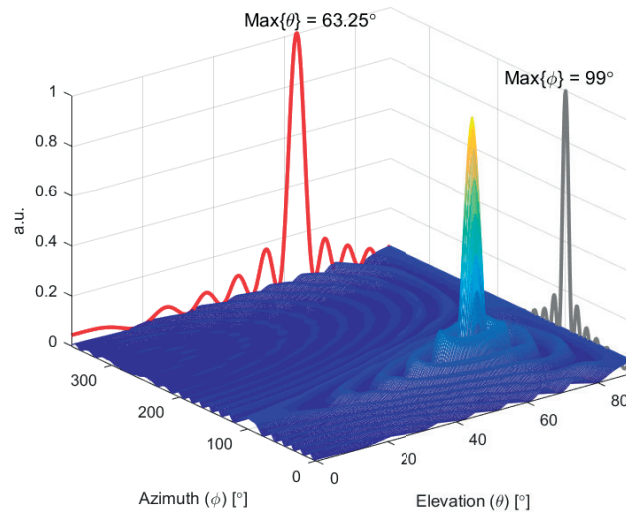


**Figure 4.20** – DOA map for PRN 23 with reference frequency compensated using EKF1 method. Synthetic signal.

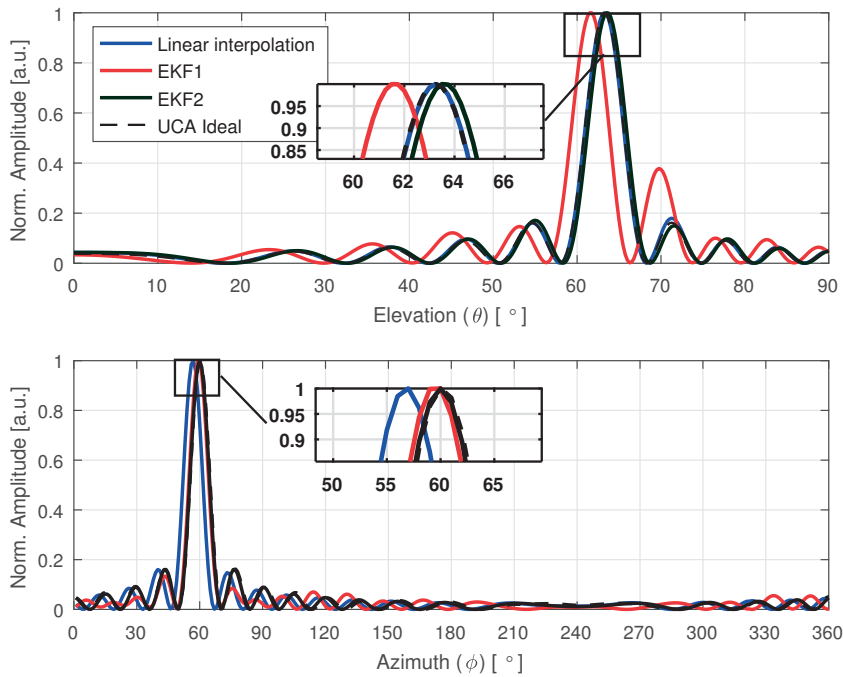


**Figure 4.21** – DOA map peak's projections in azimuth (top) and elevation (bottom) for PRN 23, using different reference frequency compensation methods. Synthetic signal.

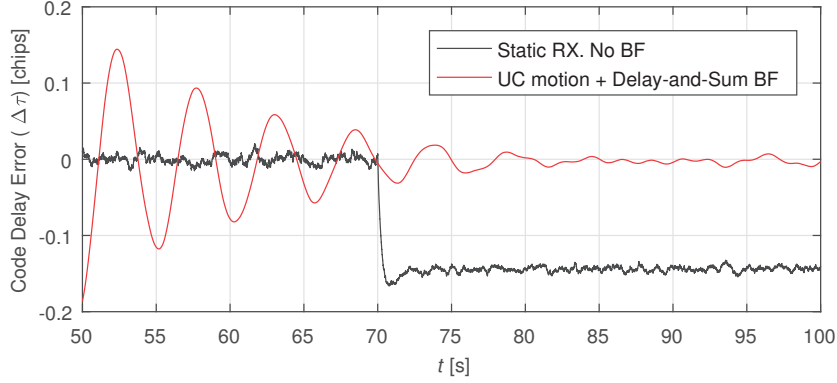


**Figure 4.22** – Code delay error over time for the tracking of PRN 23’s signal in the presence of multipath from  $t = 70$  s.

with a larger secondary peak at  $\theta \approx 70^\circ$ . EKF2 shows a smaller error in the estimated elevation, while the linear interpolation method closely matches the ideal UCA case. However, the linear interpolation method shows the largest error in its azimuth estimate.

#### 4.4.3 Corrected Code-Delays with SA Closed-Loop Tracking

The SA tracking architecture proposed in Section 4.3 should be able to estimate DOA of the LOS signal, and then, by means of beamforming, mitigating the effect of the simulated multipath component. To proof this hypothesis, we introduce again a multipath component to PRN 23’s signal; with a constant additional code delay of 0.15 chips ( $\sim 44$  m) and 3 dB power attenuation, with respect to the LOS signal. The multipath’s DOA is set to be equal to the LOS signal’s azimuth, and exactly half of its elevation, i.e., on average  $\phi_m \approx 59^\circ$  and  $\theta_m \approx 32.25^\circ$ . The multipath component is introduced 70 s after the start of the recorded simulation.

With a standard DLL [12], the coherent multipath presence in stationary scenarios will add a constant bias to the code delay estimates. This bias is observed clearly after  $t = 70$  s in Figure 4.22, where the code delay error ( $\Delta\tau$ ) over time is depicted. The code delay error is defined as the difference between the code delay estimate and the true code delay, computed from the Spirent simulator data logs.

We consider now the case where the receiver’s antenna is rotating with  $\omega_{rot} = \pi$  rad/s –i.e., 0.5 rev/s– with a radius of 0.9 m. Now, the receiver can take advantage of the SA processing using the proposed SA tracking architecture. In the main tracking channel, the linear interpolation method is used to compensate for the reference carrier frequency. After this, the auxiliary tracking channel fills the SA buffer with the  $N = 100$  compensated correlator outputs –the correlation period is 20 ms– for the last  $T_{SA} = 2$  s, corresponding to a complete antenna rotation. Using the buffer content as input, the Beamscan algorithm is executed within the DOA estimation block. This block tries to estimate only the DOA of the LOS signal. Then, the Delay-and-sum, implemented in the Beamforming block, synthesizes a radiation pattern with the main beam steered towards the estimated LOS signal’s DOA. The code delay error for PRN 23 when considering the code delay estimates generated in the auxiliary tracking channel, i.e.,  $\hat{\tau}_{aux}$ , is also shown in Figure 4.22. These estimates are generated by processing the “beamformed” correlation outputs.

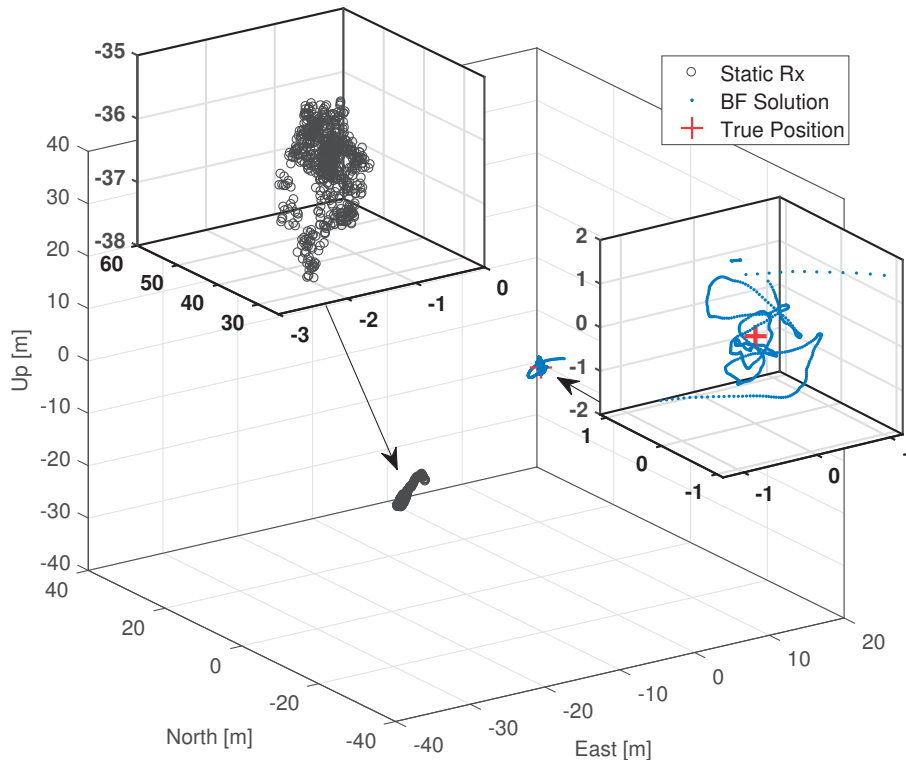


**Figure 4.23** – Navigation Solution Comparison in Simulated Scenario. ENU coordinates with respect to the true position.

The auxiliary channel’s DLL was initialized at  $t = 50$  s. It was configured with a bandwidth of 0.25 Hz, an early-late correlator spacing of 0.1 chips, and was carrier aided [12]. During the first 30 s, the DLL is still settling. After that we observe how the code error varies around zero. The  $\hat{\tau}_{aux}$  values are updated every correlation period, but they are computed by the beamforming block using the last  $N$  correlation outputs. Hence, each new  $\hat{\tau}_{aux}$  is computed with a single new sample in the SA buffer, when compared to the previous estimate. That explains the high correlation observed between succeeding  $\hat{\tau}_{aux}$  values.

The receiver is using the code delay estimates to compute the pseudoranges. Therefore, unless corrected somehow, the bias induced by the multipath in the PRN 23 signal should also bias the navigation solution computed by the receiver. Figure 4.23 confirms this hypothesis. In it, we show the navigation solutions –in ENU coordinates– computed by the receiver using 5 satellites: PRN 3, PRN 6, PRN 9, PRN 19 and PRN 23; every 100 ms over a total observation time of 120 s. In this case, multipath component in PRN 23 is present from the start of the simulation. In fact, the plot represents the differences between the navigation solution obtained and the receiver’s true position –corresponding to the plot’s origin of coordinates and marked with a red cross–. As expected, for the static receiver case, we observe a bias, mostly in the north and up directions. In contrast, the receiver implementing SA processing is able to cancel the bias very effectively. Oscillations on the order of 1 m around the true position are due to the antenna motion. They could be compensated, given a known DOA of the LOS signal, by subtracting the code delay variations due to the antenna motion from the pseudoranges, as proposed in [141], to compute the navigation solution corresponding to the center of the antenna’s trajectory. The larger error observed corresponds to the initialization

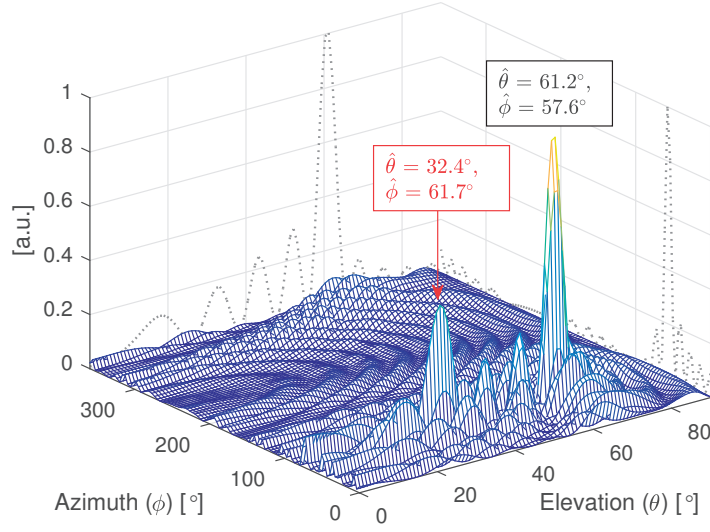


**Figure 4.24** – DOA map computed with Open-Loop version of the Beamscan algorithm for PRN 23 in the presence of coherent multipath with an additional delay of 0.15 chips. Doppler rate of  $-0.26 \text{ Hz}^2$ . Synthetic signal.

stage.

#### 4.4.4 ACF Correction with SA Open-Loop Tracking (I)

In Section 4.3.3, we proposed an Open-Loop implementation of the SA tracking architecture implementing the combination of Beamscan for the DOA estimation and Delay-and-sum for the beamforming. Here, we aim to validate this SA Open-Loop tracking by processing synthetic GPS L1 C/A, generated with our Spirent signal simulator, to mitigate coherent multipath effects. We compare two cases: a static receiver, and a receiver in uniform circular motion, with radius 0.9 m and angular speed  $\pi \text{ rad/s}$ .

As in sections 4.4.1 and 4.4.3, we introduce a coherent multipath component for the PRN 23 signal. This multipath signal has an attenuation of 3 dB with respect to the LOS signal, which is simulated for an equivalent 45 dB-Hz at the front end output. The DOA of the multipath signal was set to  $\theta = 30.82^\circ$  and  $\phi = 58.9^\circ$ , which is half the elevation of the LOS signal and the same azimuth. We assume the receiver motion does not alter it (in the chosen static reference frame with its origin at the center of the circular trajectory). We have simulated two alternative cases with additional multipath delays of 0.15 chip and 0.5 chip, respectively. The 0.5 chip case has been selected to better observe any multipath distortion in the delay dimension of the computed CAF.

Every 20 ms, the receiver computes a new CAF that is included within the SA Buffer of the proposed SA tracking architecture (see Section 4.3). We have defined a frequency search space of 50 Hz, with steps of 0.1 Hz, and a code delay search space of 3.14 chips, with steps of  $f_c/f_s = 0.157$  chips.

When the SA Buffer is full, the Open-Loop version of the DOA block jointly estimates the DOA of the LOS and the Doppler rate using the adapted version Beamscan algorithm,

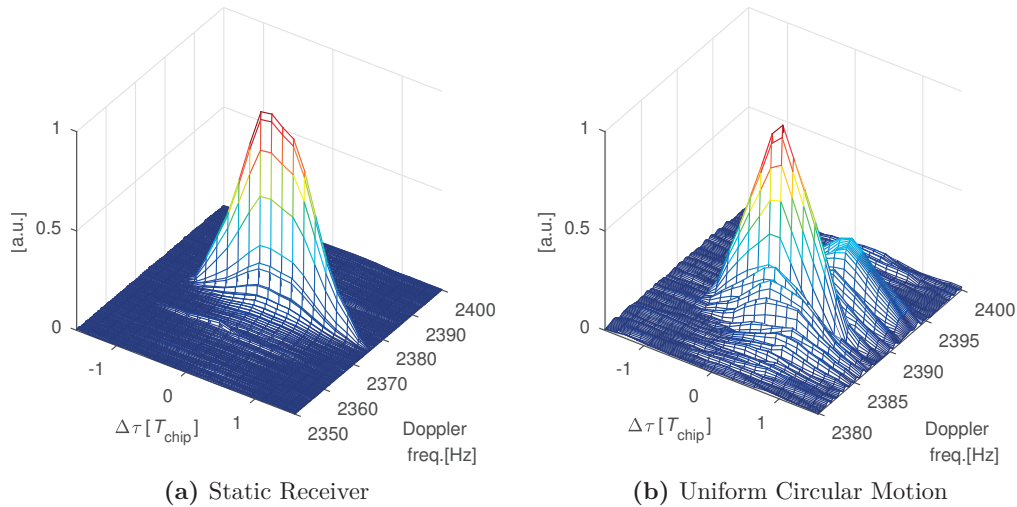


**Figure 4.25** – Accumulated and Beamformed CAFs, respectively, for the static receiver and for the SA Open-Loop receiver. Coherent multipath component with additional delay of 0.5 chips. Synthetic signal.

described by Expression (4.59). The search grid implementation of the Beamscan algorithm, i.e., computing the DOA map, is implemented by selecting the highest value for of the Beamformed CAF for each DOA hypothesis. Moreover, we recall that the DOA block considers the signal received with the highest power to be the LOS signal. In Figure 4.24, we show the DOA map –computed at  $t = 2$  s– for the estimated Doppler rate, i.e.,  $-0.26 \text{ Hz}^2$ , in the case of of a multipath delay of 0.15 chips. We observe two clear peaks corresponding to the two LOS and multipath signals. The LOS signal DOA estimate is very close to the true values. The peak for the multipath signal shows a small error. The limited resolution of the DOA map computed in this case, i.e.,  $0.9^\circ$  in  $\theta$ , and  $3.6^\circ$  in  $\phi$ , can be partially contributing to this error.

Using the LOS’ DOA estimates generated by the DOA block, the Beamforming block computes the Open-Loop version of the Delay-and-sum to obtain the beamformed CAF  $\chi_{BF}$ , as described by Expression (4.54). Figure 4.25 represents: (a) the CAF for the static receiver case, with a 2-seconds coherent integration time, and (b), the beamformed CAF for the receiver moving along the circular trajectory, computed using Delay-and-sum steered towards the LOS signal’s estimated DOA. In both cases, the multipath’s additional delay was 0.5 chip. The distortion in the CAF due to the multipath is quite noticeable in Figure 4.25.(a). In the absence of any distortion, the CAF should have a triangular-like shape with a rounded peak (due to the signal’s bandwidth limitation) in the code delay dimension. The multipath-caused distortion in Figure 4.25.(a) implies that a standard DLL will return biased code delay estimates. On the other hand, the main CAF peak in Figure 4.25.(b), i.e., in the beamformed CAF, is barely distorted. Interestingly, we also observe an additional group correlation peaks with a delay difference of approximately 0.5 chips with respect to the main correlation peak, spanning over a few Hz from the main peak, in the frequency dimension. This group of secondary peaks, with its larger peak within a few Hz distance from the CAF main peak is due to the coherent multipath presence. The beamforming has “separated” the multipath signal in the frequency domain.

In Figure 4.26, we have represented the evolution of the normalized ACF during 5 s. The normalized ACF is obtained as a “slice” of the CAF taken at carrier frequency of its main peak. In other words, the normalized ACF includes the correlation values for the all the

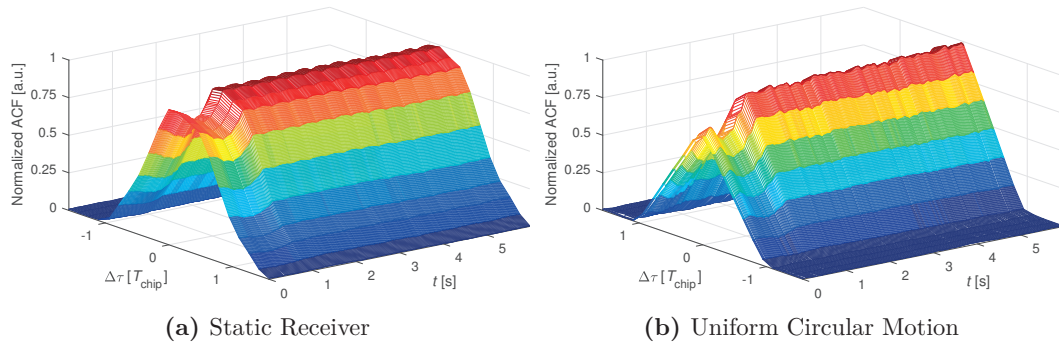
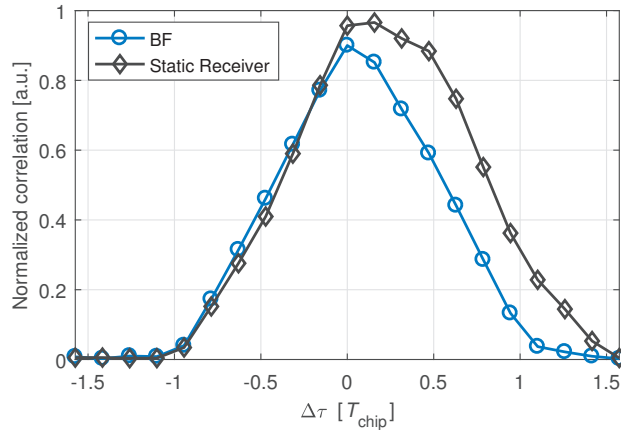


**Figure 4.26** – Normalized ACF over time, obtained from the accumulated CAF and the beamformed CAF, respectively, for the static receiver and the SA tracking architecture.

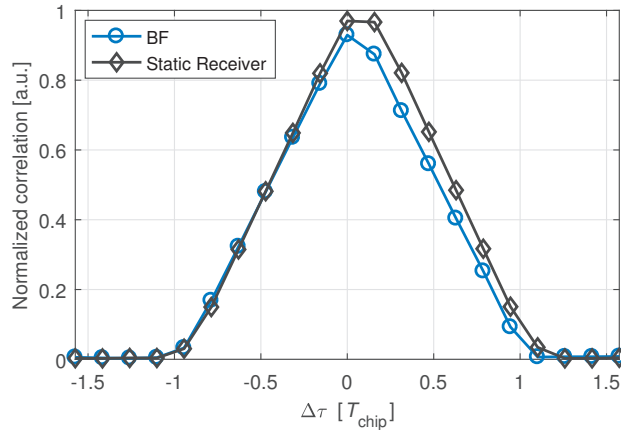
code delay hypotheses given a single carrier frequency, which is selected as the frequency corresponding to the CAF’s peak. Two cases are depicted: in Figure 4.26.(a) we observe the evolution of the accumulated CAF for the static receiver, while in Figure 4.26.(b) we observe the evolution the beamformed CAF. By comparing both figures, we observe how the beamforming significantly mitigates the multipath-caused distortion in the ACF. In the beamformed CAF case, the output of the DOA block was used every 100 ms to update the steering direction of the Delay-and-sum beamformer to the estimated LOS signal’s DOA. In both cases, during the first second, the Open-Loop tracking is refining the coarse delay estimate obtained in the acquisition stage, thus the transitional behavior.

Finally, in Figure 4.27, we compare the averaged normalized ACFs for the static receiver and the beamformed case. Figure 4.27.(a) shows the results for the multipath with a delay difference of 0.5 chips (equivalent to averaging Figure 4.26 in the time dimension), while Figure 4.27.(b) shows the results for 0.15 chips. In both cases, it is clear how the beamforming mitigates the multipath-caused distortion, which shall reduce the bias in the code-delay estimates.

#### 4.5. Experimental Results with Real Signals Recorded with a Rotating Arm



(a) Multipath additional delay of 0.5 chips



(b) Multipath additional delay of 0.15 chips

Figure 4.27 – Average ACFs over 6 s in the presence of coherent multipath. Synthetic Signal.

### 4.5 Experimental Results with Real Signals Recorded with a Rotating Arm

The results obtained with simulated signals, presented in the previous section, were considered as preliminary validation of the proposed tracking architecture and the implemented SA processing techniques. In this section, we move on to processing real GPS signals. In the real world, there are various sources of error –not modeled in our simulations– that can impact the SA processing: errors in the assumed antenna trajectory, e.g., due to unexpected changes of the angular speed; variations in the observed LOS signal’s amplitude during the SA interval, caused by the non-modeled antenna gain; phase-wrap; signal blockage or multipath; the channel not being sufficiently stationary; or an assumed spatiotemporal covariance matrix far from the true one; are some of them. These errors will have a significant impact on the SA processing.

The experimental setup used to record the GPS L1 C/A signal using an antenna mounted on a mechanical rotating arm is depicted in Figure 4.28. As in the simulation test bench –described in Section 4.4–, the same sterero NSL RF front end [195], and the same modified GPS software receiver were used. This time, the GPS signal simulator has been replaced by

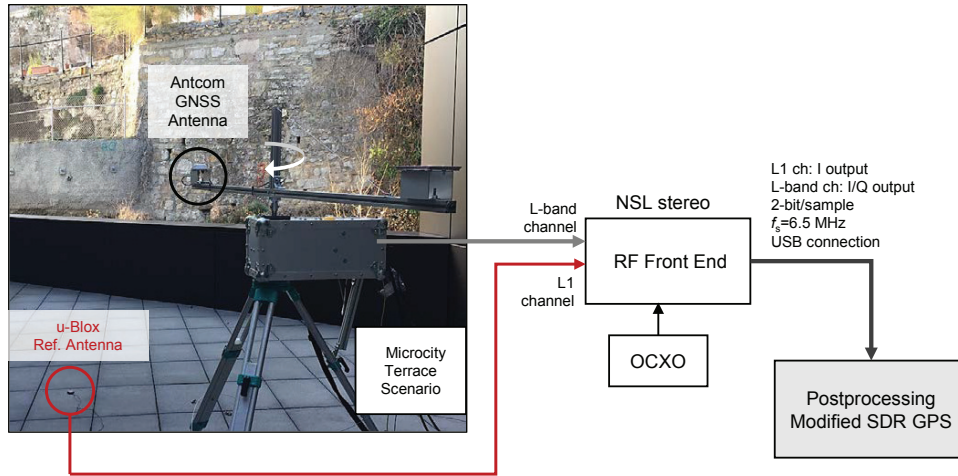


Figure 4.28 – Experimental setup for the antenna mounted on the rotating arm

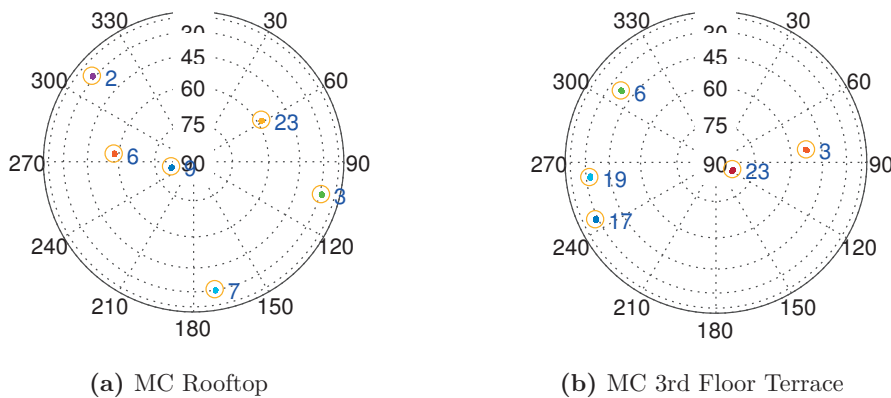


Figure 4.29 – Skyplot for the two data collection sites considered when the signal recording took place.

an Antcom 42GNSSA-RL-XT-1 antenna<sup>9</sup> [198] mounted on the rotating arm. The arm was designed and built in-house in collaboration with the University of Balearic Islands. The rotating arm is supported by a fully-adjustable tripod as shown in Figure 4.28. It allows to manually adjust the antenna rotation radius from 0.5 m to 0.95 m. Vertical oscillations of the antenna during the arm’s rotation were minimized by carefully counterbalancing the loaded arm. The arm’s rotation speed can be adjusted in real time from a minimum of  $\approx \pi/2$  rad/s (0.25 Hz or 15 rpm), up to  $\approx 10\pi/3$  rad/s (1.66 Hz or 100 rpm). This maximum speed limitation is mainly caused by the mechanical limitations of the arm’s built-in RF rotary joint [199]. This RF joint is aligned with the arm rotation axis and is used to connect the antenna with the RF front end –located inside the arm’s box–.

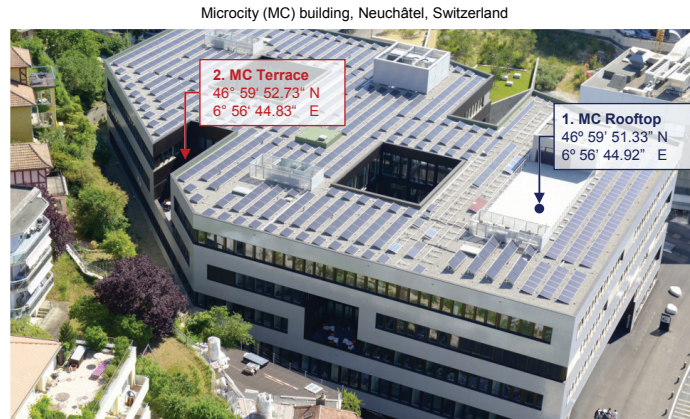
As also shown in Figure 4.28, we included an additional u-blox ANN-MS active GPS antenna<sup>10</sup>, connected to the RF front end’s L1-Band channel. The RF signal from the rotating antenna was connected to the L-channel. The u-blox antenna remained static at approximately 2.5 meters from the arm’s rotation axis. In practice, this distance proved

<sup>9</sup>The Antcom 42GNSSA-RL-XT-1 has a built-in LNA with a gain of 33 dB and a noise figure of 3 dB.

<sup>10</sup>The u-blox ANN-MS GPS antenna has a built-in LNA with 27 dB gain and 1.8 dB noise figure.



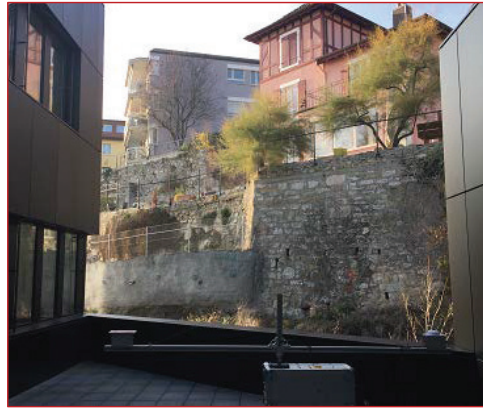
#### 4.5. Experimental Results with Real Signals Recorded with a Rotating Arm



(a) Deployment locations of the rotating arm



(b) MC Rooftop: Clear-sky



(c) MC 3rd Floor Terrace: Severe multipath

**Figure 4.30** – Experimental sites where the rotating arm was deployed for the recording of real GPS L1 signal.

sufficient to prevent any observable blockage or interference effect caused by the rotating arm's vicinity when tracking the signal. The static antenna was required to implement the *reference static antenna method* used to compensate the reference carrier frequency (see Section 4.3.2).

The setup described was used to record 120 s of GPS L1 signal in two different sites, shown in Figure 4.30:

**MC Rooftop:** A Clear-sky scenario. The rotating antenna was deployed on the rooftop of the Microcity building (Neuchâtel, Switzerland). The skyplot showing the visible GPS satellites at this site during the recording time is shown in Figure 4.29.(a). This scenario was selected in order to validate the SA processing implemented within the receiver, hence, in a scenario where little multipath interference –at least for satellites with an elevation higher than 30°– is expected.

**MC 3rd Floor Terrace:** A severe multipath scenario. Conversely, the skyplot for this site is shown in Figure 4.29.(b). This scenario was selected with the expectation to observe severe multipath interference, especially of coherent nature. As it is shown in Figure's 4.30.(a) and 4.30.(c) pictures, the terrace has a U shape, open eastwards. This environment, with metal plates covering the facade, gave us highly likelihood of

capturing some clear multipath effects. Prior to applying any SA processing, tracking the signal proved to be particularly difficult in this scenario. We needed to use the signal from the reference antenna to correctly compensate the data bit transitions in the signal received by the rotating antenna. Otherwise, too many errors in the bit transition detection would severely degrade the SA processing performance.

The “true” arm location at the MC Rooftop site, defined as the position of its rotation axis, was measured using map matching and u-blox EVK-6PPP-0 GPS receiver with differential GPS measurements [200]. In the case of the MC 3rd Floor Terrace we used the MC building plans and map matching to define the arm’s location from the MC Rooftop true location. Defining the true position in this convoluted way was necessary to avoid any possible multipath effect. These true locations, together with the exact starting time of the measurements, is summarized in Table 4.4.

In the sections bellow, we present a selection of the obtained results. They are presented following the same structure as in the simulated signals case, i.e., as in Section 4.4.

#### 4.5.1 SA Closed-Loop Tracking: Direction-of-Arrival Estimation (II)

Let us start the analysis of the results obtained from the SA processing of real signals, by examining the DOA maps computed for the MC Rooftop scenario. The Beamscan, MPDR-Capon and MUSIC DOA estimation algorithms are considered, again –implemented inside the DOA block– within the SA tracking architecture proposed in Section 4.3. As a representative example of the results obtained, Figure 4.31 shows the DOA maps computed using the three DOA algorithms, for PRN 7 at time  $t = 30$  s. At this instant, the true observed elevation –obtained from the receiver’s navigation solution– was  $\theta_7 = 29.74^\circ$ . The arm rotation speed  $\omega_{rot}$  was set to a nominal value of  $\pi$  rad/s (30 rpm), which implies a  $T_{SA} = 2$  s. The linear interpolation method was used to compensate the reference carrier frequency when generating these results. The DOA maps for the three algorithms show the presence of only a single strong signal, corresponding to the LOS.

With Beamscan, we do not appreciate any significant distortion in the synthesized beam shape when compared to the simulation results, even despite the small error in the assumed antenna trajectory caused by the actual non-constant rotation speed. Also, any possible non-linear phase wrap-up due to the antenna gain did not distort the DOA map significantly.

MPDR-Capon and MUSIC, in contrast, show peaks wider than their equivalent in the

**Table 4.4** – Experimental sites selected where the rotating antenna was deployed to record GPS L1 signal.

	MC Rooftop	MC 3rd Floor Terrace
Location	46° 59' 52.73" N 6° 56' 44.83" E	46° 59' 51.33" N 6° 56' 44.92" E
Starting recording time Time / Date	14h47 UTC+1 / 28.11.2016	14h55 UTC+1 / 15.11.2016
Nominal Arm’s Rotation speed	$\pi$ rad/s (30 rpm)	
Radius	0.90 m	
Goal	SA Processing validation in an almost multipath-free scenario	Severe multipath scenario with possible coherent reflections

#### 4.5. Experimental Results with Real Signals Recorded with a Rotating Arm

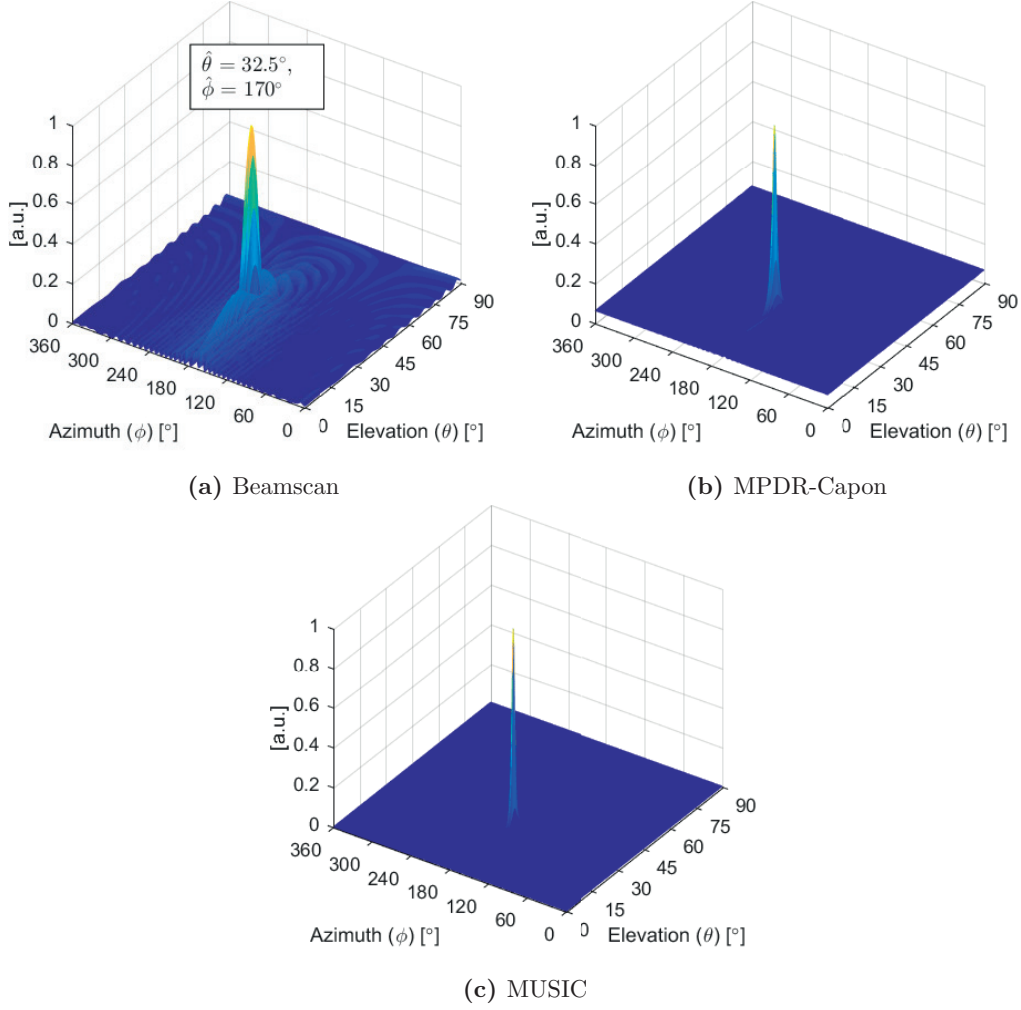


**Figure 4.31** – DOA estimation for PRN 7 with measurements from Microcity Rooftop Scenario. The DOAs for the peaks in the 3 subfigures are the same, but it has been represented only once on (a).

simulations. This effect can be related to a mix of causes, such as: the previously mentioned error in the assumed antenna trajectory; having a channel that is not stationary enough; a poor spatiotemporal covariance matrix estimate  $\hat{\Sigma}_x$ ; a very weak multipath contribution; or even to the phase wrap-up effect. Figure 4.31.(c) shows that the DOA map’s base-level value for the MPDR-Capon algorithm has increased when compared to the simulated case. This effect was also observed in simulations when multipath was present.

The estimated DOA obtained with the three algorithms is the same. This might be a result of the DOA map’s limited resolution:  $0.25^\circ$  in  $\theta$ , and  $1^\circ$  in  $\phi$ . The peak of the DOA map is used as DOA estimate. The three algorithm exhibit a bias in elevation of  $+2.76^\circ$ . This bias is likely caused by some nonlinear phase wrap-up, and by the fact that we considered a constant rotation speed during  $T_{SA}$ , which is not fully accurate. Subsequently, that translates into errors in the assumed antenna positions during the SA trajectory. Also, we hypothesize this bias to depend on the elevation of the observed signal given a specific receiver’s antenna orientation, becoming more significant for low elevations. Although we tried to carefully level and balance the mechanical arm, there still might be a small contribution to the observed bias due to the rotation plane not being completely horizontal.

Accurately measuring the bias in the estimated azimuth is more complicated in practice. First, it requires the receiver knowing either the arm’s absolute azimuth (or orientation) at any

time or this absolute azimuth at a specific time instant, and then propagate the arm's position with a very accurate measure of its rotation speed. Unfortunately, the mechanical arm did not implement any sensor to measure its absolute orientation when the data recordings took place. Therefore, we concentrate our discussion on the elevation estimates. Nevertheless, we adjusted the azimuth in the DOA maps using the azimuth obtained from the navigation solution. We acknowledge that it should be possible to use the azimuth estimates of all the satellites in view in combination to the azimuth values obtained from the navigation solutions to estimate the arm's absolute azimuth.

We move on to examining the results for the MC 3rd Floor Terrace scenario. Given the site's environment, we expected to detect some coherent multipath interference, resulting in additional peaks in the DOA maps computed. Figure 4.32 shows the DOA map computed with Beamscan for PRN 23. Its true elevation at the signal time interval for which the DOA map is computed was  $\theta_{23} = 82.92^\circ$ , while the azimuth was  $\phi_{23} = 119.48^\circ$ . Figure 4.32 also shows the estimated DOA. The elevation estimate is very accurate, with an observed error of  $\sim 0.1^\circ$ . The DOA map shows several small peaks, which were not observed with simulated signal, that deviate from the sinc-like shape expected in the ideal UCA-like case.

In Figure 4.33 we show the DOA map for PRN 19 when using Beamscan once again. PRN 19's estimated elevation was  $\hat{\theta}_{19} = 31.75^\circ$ . The elevation obtained from the navigation solution, which we consider as reference, was  $\theta_{19} = 33.17^\circ$ .

Besides from the LOS signal's peak, we observed a small group of peaks at elevations scattered around  $\hat{\theta}_{19}$  and azimuth distances of approximately  $180^\circ$  from  $\hat{\phi}_{19}$ . Among these peaks, the main one has an elevation closely matching  $\hat{\theta}_{19}$ . That supports the hypothesis of these group of peaks being the result of multipath interference caused by a single reflection, as shown in Figure 4.34. According to the law of reflection, the elevation observed for this reflected signal should be the same as for the LOS signal. Figure 4.35 shows the DOA map computed using MPDR-Capon algorithm. The main peak, which has clearly become wider than its counterpart with simulated signal and the –normalized– DOA map's base-level, has increased to 0.34. Besides, although not as clearly as with Beamscan, we can also observed an additional peak, i.e., the hypothetical multipath signal at the same DOA as with Beamscan, i.e., the second peak has an approximate difference of  $180^\circ$  with respect to the main (LOS) peak.

Finally, Figure 4.36 shows the DOA map computed with Beamscan for PRN 17. The estimated elevation is  $\hat{\theta}_{17} = 28.5^\circ$ , which accurately matches (within  $0.1^\circ$  error) the true elevation for PRN 17. We observe again a secondary peak, but this time it has approximately the same magnitude as the main one corresponding to the LOS signal. This peak's presence confirms our hypothesis that its presence is caused by coherent multipath. PRN 19 and PRN 17 both have low elevations and approximate azimuth angles, thus the similar secondary peaks in their respective DOA maps. Interestingly, when using adaptive DOA estimation algorithms for PRN 17, the DOA map obtained (not represented) closely matched the Beamscan's case. We assume this behavior to be caused by the presence of such strong multipath signal, that being coherent, is, obviously, correlated with the LOS signal component. We recall that classical MPDR-Capon and MUSIC are suitable for DOA estimation of correlated signals [121, 123].

In the section below, we repeat Section 4.4.2's analysis to compare the different reference carrier frequency estimation methods. This time, instead, it is done with real recorded signals.

#### 4.5. Experimental Results with Real Signals Recorded with a Rotating Arm

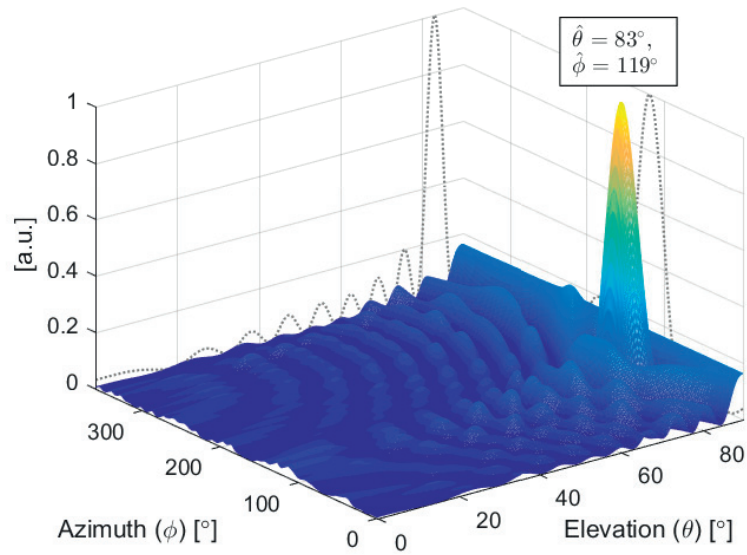


Figure 4.32 – DOA map computed using Beamscan for PRN 23 in MC 3rd Floor Terrace Scenario.

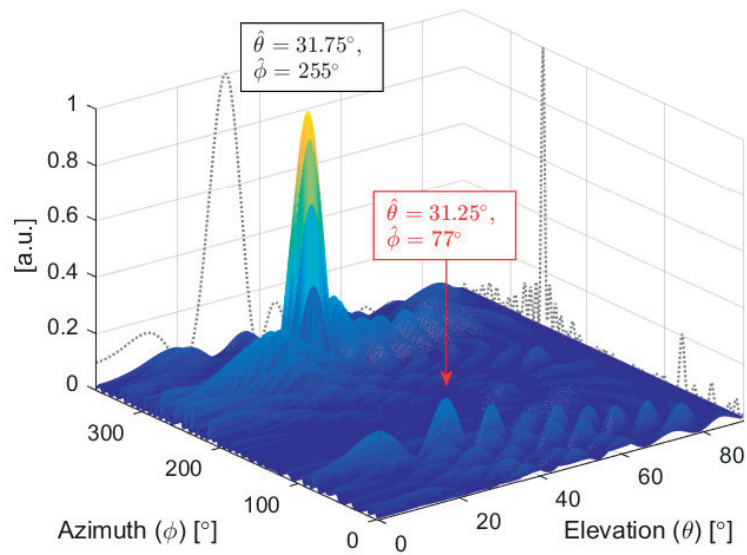


Figure 4.33 – DOA map computed using Beamscan for PRN 19 in MC 3rd Floor Terrace Scenario.



**Figure 4.34** – Single specular reflection hypothesis to explain the main secondary peak in the DOA map for PRN 19.

#### 4.5.2 Reference Frequency Estimation Methods Comparison (II)

The linear interpolation method described in Section 4.3.2, and the EKF1 and EKF2 algorithms proposed in Section 4.3.4, have proved themselves capable of compensating the reference carrier frequency quite efficiently –with synthetic signal– when only the LOS signal is present. In this section, we put them to the test with real GPS signal measurements. In addition to the linear interpolation method, EKF1 and EKF2, this time we also include the reference static antenna method, which was not previously tested with synthetic signal. We test these methods with signal recorded in the MC Rooftop scenario, for which we recall the antenna radius fixed to 0.9 m and a nominal rotation speed set to  $\pi$  rad/s (30 rpm). However, small deviations from this speed value were expected –and observed– since it is very complicated to generate a uniform motion, particularly outdoors under some mild wind conditions.

This section’s primary goal is to validate the EKF1 and EKF2 methods in practice and assess their impact on the DOA estimation techniques. Obviously, poorer results are foreseen in comparison with those obtained with simulated signals. We shall notice that EKF1, EKF2 and the linear interpolation method do not explicitly model any coherent multipath component, nor the phase wrap-up effect. Their performance depends heavily on the accuracy of the  $C/N_0$  estimates (used to compute the  $\mathbf{R}$  matrix), and the assumptions made to define the EKF’s process covariance matrix  $\mathbf{Q}_n$ , which might not be accurate.

We start by presenting the results obtained in the MC Rooftop site. In Figure 4.37, we have depicted the reference carrier frequency estimated by the different methods for PRN 7 and PRN 23. The linear interpolation method performs poorly, and in some time intervals the difference with respect to the actual reference frequency can be larger than 1 Hz. EKF2 estimates show some residual periodic oscillation, matching the antenna rotation period. EKF1 appears to provide the smoothest estimate. The variance of the reference frequency estimates provided by the static antenna method depends on the noise bandwidth of the carrier tracking loop used to track the signal received by the static antenna. We recall that a second-order FLL with 1 Hz of bandwidth was used. The phase-wrap up effect cannot be compensated with the reference static antenna method. Thus, we manually added a frequency offset to its reference carrier estimates, i.e., +1.8 Hz for PRN 7 and 1.5 Hz for PRN 23, to

#### 4.5. Experimental Results with Real Signals Recorded with a Rotating Arm

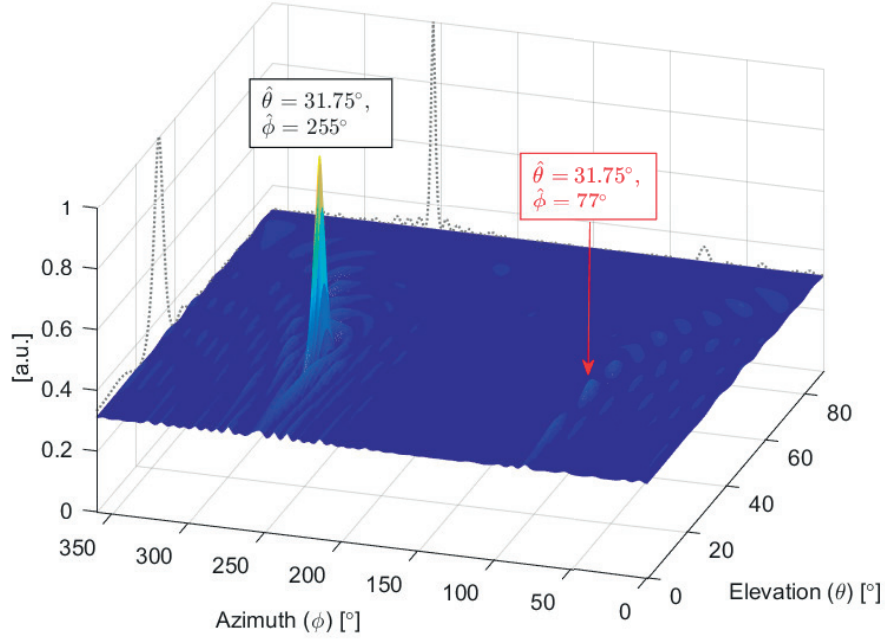


Figure 4.35 – DOA map computed using MPDR-Capon for PRN 19 in MC 3rd Floor Terrace Scenario.

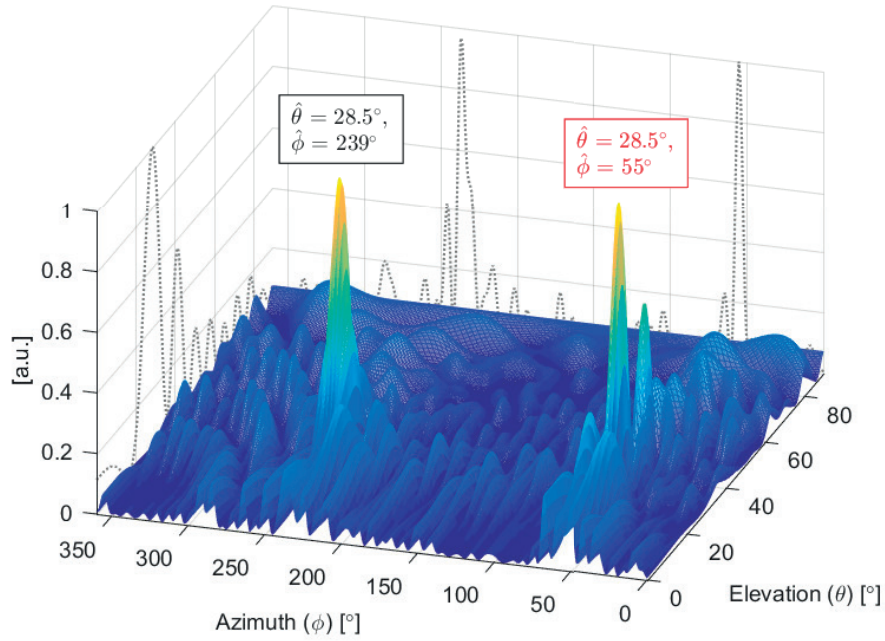
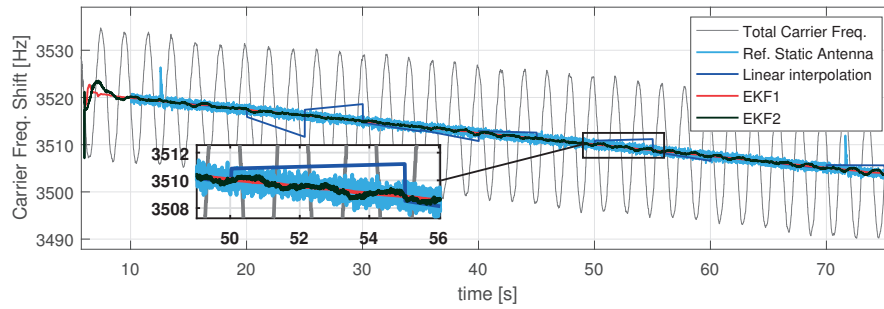
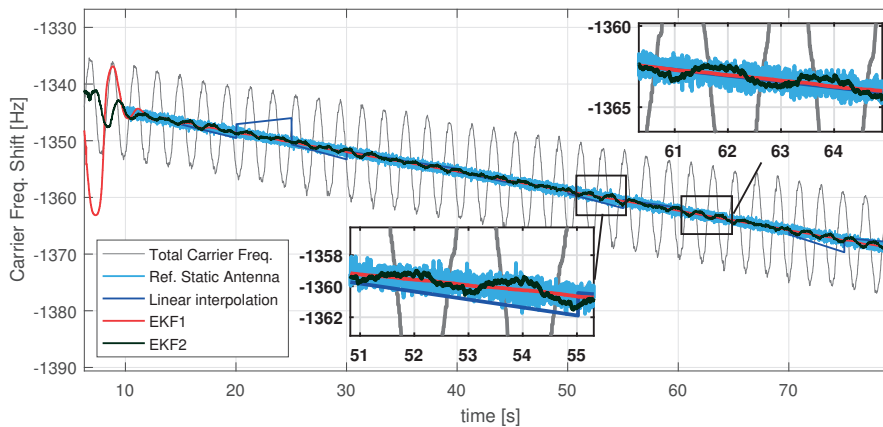


Figure 4.36 – DOA map computed using Beamscan for PRN 17 in MC 3rd Floor Terrace Scenario.



(a) PRN 7



(b) PRN 23

**Figure 4.37** – Estimated reference carrier frequency for the MC Rooftop scenario. For each method, the beginning of the line marks the first estimation.

match the average trend observed by the other methods.

In Figure 4.38 we present the DOA maps computed using the Beamscan algorithm for PRN 23 (top row) and PRN 7 (bottom row) for the considered reference carrier estimation methods, starting at time  $t = 52$  s in the recorded measurements. The reference carrier estimation around  $t = 52$  s has been magnified within Figure 4.37. The linear interpolation and EKF1 methods were used to obtain the results shown, respectively, in Figure 4.38.(a-b). Analogously for PRN 7, but this time with the EKF2 method instead of EKF1, the DOA maps obtained with Beamscan are presented in Figure 4.38.(c-d). The instant  $t = 52$  s was deliberately chosen because of the deviation shown by the linear interpolation method estimates from what appears to be the actual reference carrier frequency, for both PRNs under consideration.

In a similar way as in Section 4.4, we examine some DOA map “slices” for PRN at two different time instant. In Figure 4.39, we do it for  $t_1 = 62$  s, and in Figure 4.40 for  $t_2 = 52$  s. Let us recall these “slices” being defined as the projections in elevation and azimuth axes of the DOA map’s peak. Figure 4.37.(b) shows that, in  $t_1 = 62$  s, the reference carrier frequency estimates from the different methods closely match, including the linear interpolation method. Hence, in Figure 4.39, all the methods display a similar behavior. Nonetheless, EKF1 and the static antenna methods show a small bias in the elevation estimate when compared to the ideal DOA shape. Figure 4.40, on the other hand, exemplifies the case where the linear interpolation method is significantly off from the actual reference carrier, which results in a



#### 4.5. Experimental Results with Real Signals Recorded with a Rotating Arm

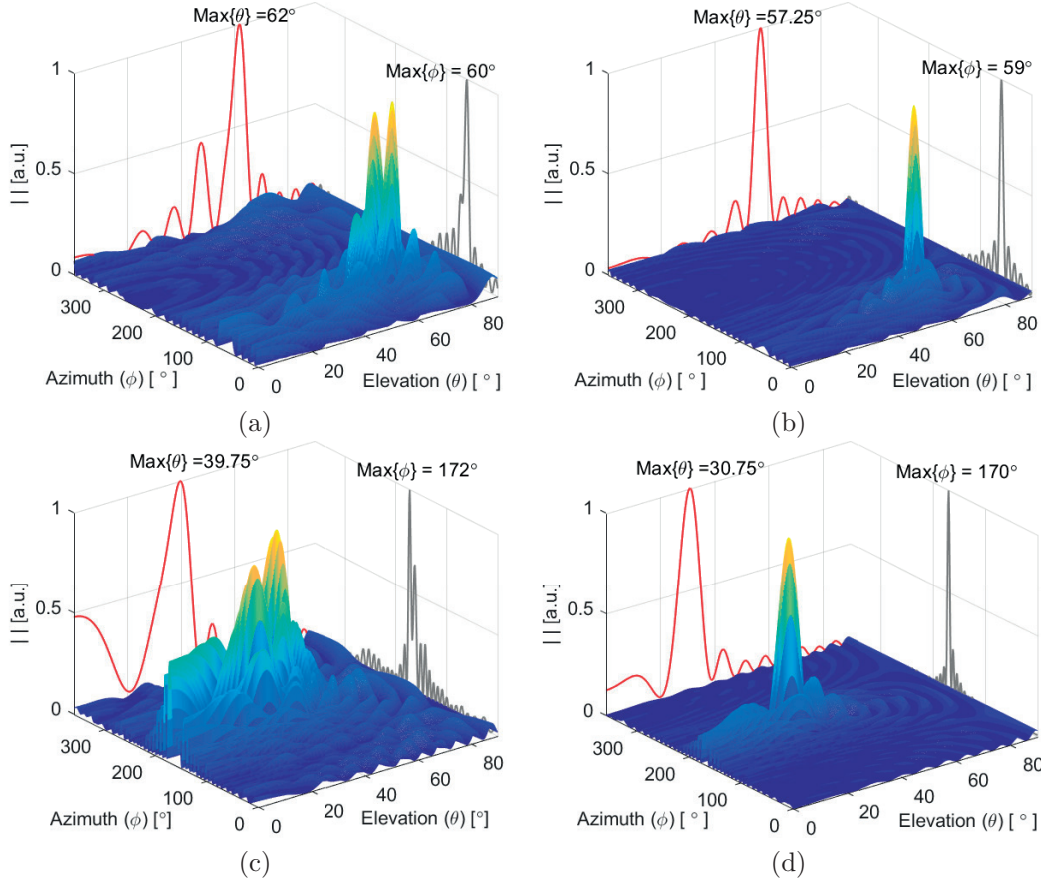
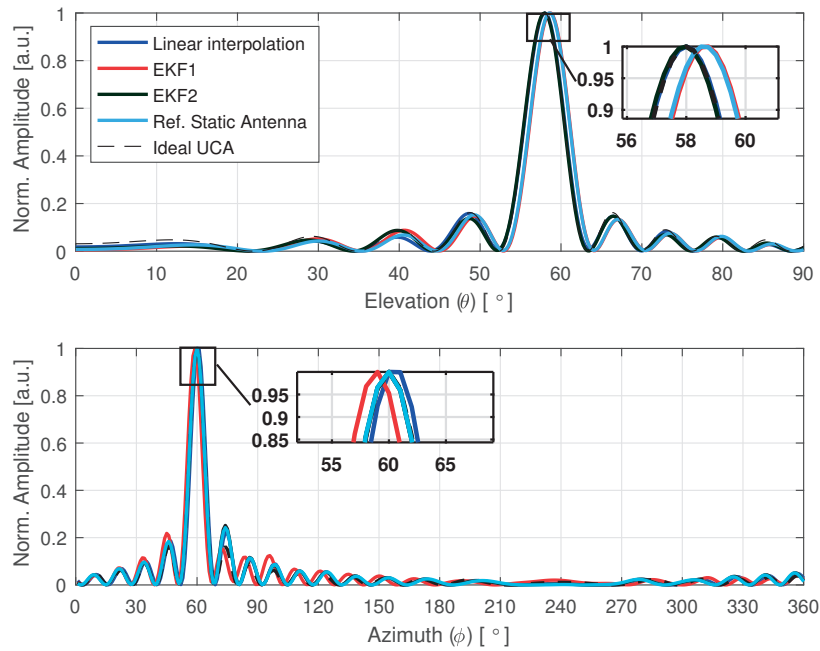


**Figure 4.38** – DOA maps computed for the MC Rooftop scenario, starting at the instant  $t = 52$  s. (a) PRN 23 and linear interpolation; (b) PRN 23 and EKF1; (c) PRN 7 and linear interpolation; and (d) PRN 7 with EKF2.

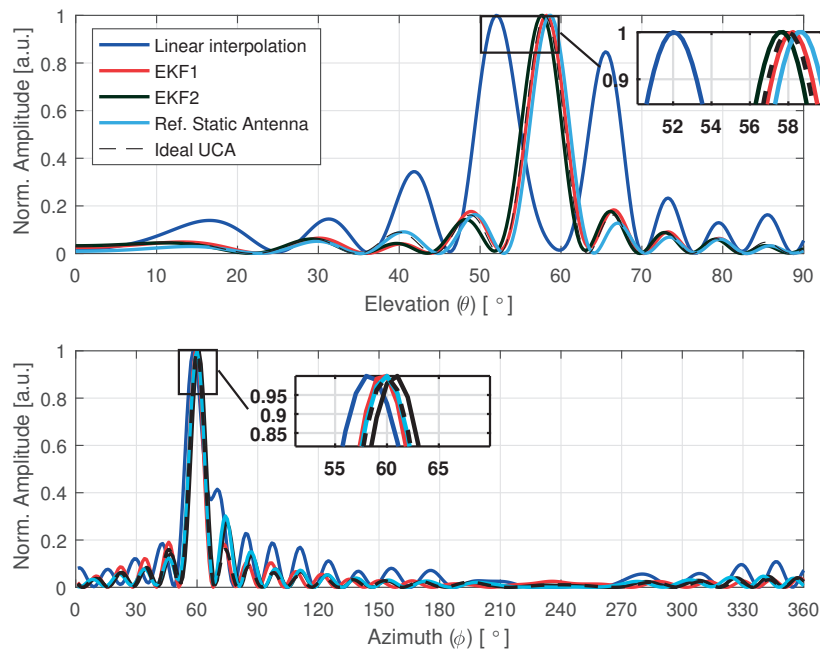
considerably distorted DOA map.

Figure 4.41 and Figure 4.42 depict the received signal’s elevation error over time for PRN 23 and PRN 7, respectively, when compensating the correlation outputs with the reference carrier estimates obtained with the different methods. The elevation error is shown for a 30 s interval, starting from the signal recording time  $t = 40$  s, in order to ensure that EKF1 and EKF2 filters had already converged. The satellite elevations used as true values were obtained from the navigation solution computed by the receiver. Given their much superior accuracy, there were used as reference. Table 4.5 summarizes the RMSE of the elevation estimates for the considered methods.

We recall that the EKF1 and EKF2 methods estimate the arm’s rotation speed –actually, it is one of the parameters in their state vector–. In Figure 4.43 we show the rotation speed estimates (i.e., for the MC Rooftop site) generated by these methods, as well as the estimate produced as a side product of the LSE when using the linear interpolation method. Figure 4.43 shows how, after approximately 20 s, required by the EKFs to converge, the actual rotation speed oscillates around the nominal  $\pi$  rad/s value. As mentioned before, these small variations were expected, and they can be explained mostly by the mechanical limitations of the arm, and by mild wind conditions during the signal recording. Errors in the assumed rotation speed translate into errors in the assumed antenna trajectory, required by



**Figure 4.39** – DOA map peak’s projections in azimuth (top) and elevation (bottom) for PRN 23 for the signal recorded at the MC Rooftop site, starting at  $t_1 = 62$  s, using different reference carrier estimation methods.



**Figure 4.40** – DOA map peak’s projections in azimuth (top) and elevation (bottom) for PRN 23 for the signal recorded at the MC Rooftop site, starting at  $t_2 = 52$  s, using different reference carrier estimation methods.

#### 4.5. Experimental Results with Real Signals Recorded with a Rotating Arm

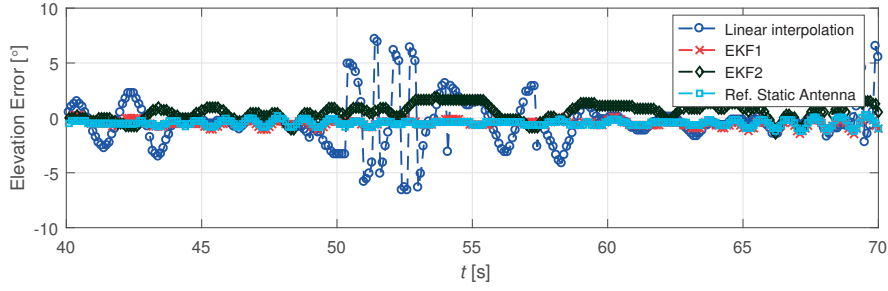


**Figure 4.41** – Elevation error for PRN 23, using the Beamscan algorithm, for the different reference carrier estimation methods. MC Rooftop site.

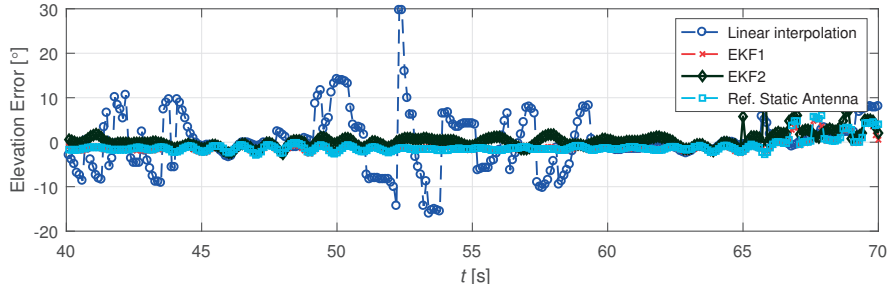


**Figure 4.42** – Elevation error for PRN 7, using the Beamscan algorithm, for the different reference carrier estimation methods. MC Rooftop site.

**Table 4.5** – RMSE of the LOS signal elevation estimate ( $\hat{\theta}$ ) for PRNs 23 and 7, obtained using the Beamscan DOA estimation algorithm after removing the reference carrier frequency with the different methods considered. MC Rooftop site.

Method/Sat	PRN 23	PRN 7
Linear interpolation	2.169°	6.113°
EKF1	0.568°	1.676°
EKF2	1.037°	1.809°
Ref. Static Antenna	0.535°	1.779°

the DOA estimation algorithms. Within the GNSS context, this kind of errors have shown to severely impact the SA processing, as it has been shown in [133]. This effect may additionally contribute to the poor results for the linear interpolation method at  $t = 52$  s. Indeed, Figure 4.43 shows that at that time instant, the rotation speed diverges from  $0.5 \pi$  rad/s, while for  $t = 62$  s the estimated rotation speed is much closer to that value.

Finally, we tried the four methods with the signal recorded at the MC 3rd Floor site. For the satellite signals showing strong coherent multipath, all the methods, except the reference static antenna, presented an offset in their reference carrier estimates. We illustrate this issue in Figure 4.44, where the reason for such behaviour becomes obvious: the distortion in the total carrier frequency observed, –with more frequency estimates below the reference carrier frequency– is responsible for the bias. Unless the EKF1 and EKF2 state transition models are modified, perhaps including an extra parameter to cope with these effects, these methods will show poor performances in environments with strong coherent multipath present.

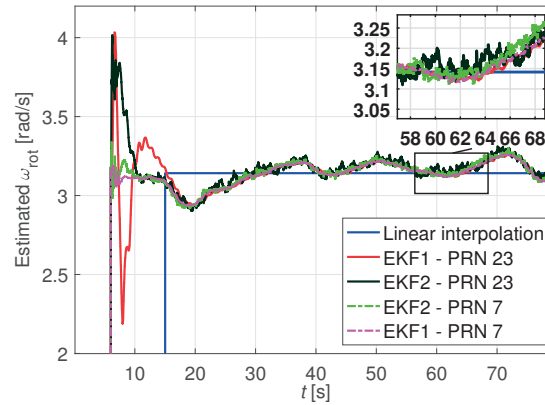


**Figure 4.43** – Estimated antenna rotation speed using PRN 23 and PRN 7 signals in the MC Rooftop scenario.

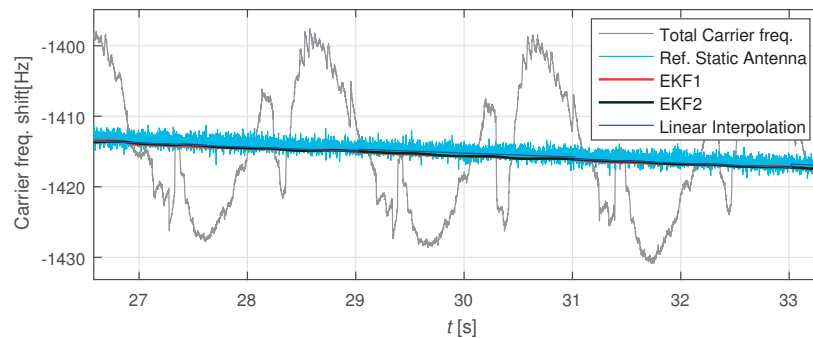


**Figure 4.44** – Estimated reference carrier for PRN 19 for the MC 3rd Floor Terrace scenario. Magnified view from  $t = 26.7$  s to  $t = 33.2$  s.

### 4.5.3 SA Spatial Filtering Effect on the Navigation Solution

Just as done in Section 4.4 with simulated signal, we seek to validate the proposed SA tracking architecture (see Section 4.3) by processing real GPS signals, and assess its impact on the navigation solution. We have implemented the Beamscan algorithm within the DOA–estimation– block, to use the estimates generated for steering the Delay-and-sum algorithm, implemented within the Beamforming block. The auxiliary tracking channel produces an updated correlation output every 20 ms. These correlation outputs drive the auxiliary channel’s DLL. We resorted to the reference static antenna method to estimate the reference carrier frequency. This decision had a twofold motivation: firstly, we observed how the static antenna tracking is less prone to errors when decoding the data bit sequence; and secondly, tracking the static antenna’s signal in the main tracking channel yield code delay estimates synchronized to those obtained in the auxiliary channel. The latter allows us to compare results corresponding to the same exact time periods. The setup for the code and carrier channels, used to obtain the results in this section, is summarized in Table 4.6.

We have concentrated on the MC 3rd floor terrace site, where the multipath mitigation provided by the SA tracking architecture is expected to provide a higher improvement –by reducing the bias in the position–. In Figure 4.46a, we show the 2D positions computed with the main code delay estimates –which are used to compute the pseudoranges–, obtained from processing the static antenna’s signal; and the positions computed with the auxiliary channel’s

#### 4.5. Experimental Results with Real Signals Recorded with a Rotating Arm

**Table 4.6** – Code and carrier tracking settings used in the receiver at the MC 3rd Floor Terrace Scenario when comparing navigation solutions. Main and Auxiliary tracking channels (bold) are part of the SA tracking architecture processing the signal from the rotating antenna.

	<b>Main Tracking Channel</b>	<b>Auxiliary Tracking Channel</b>	Static Receiver
Integration time (s)	$1 \times 10^{-3}$	2	1
Carrier Loop Bandwidth (Hz)	5 (FLL)	-	5 (PLL)
DLL Bandwidth (Hz)	1	0.25	0.25
E-L correlator spacing (chips)	0.2	0.2	0.25

**Table 4.7** – RMSE and standard deviation comparison between the navigation solutions.

<b>RMSE (m)</b>	E	N	U
Static Receiver	10.052	12.217	23.401
SA Tracking BF	2.274	1.774	13.498

<b>Std (m)</b>	E	N	U
Static Receiver	4.230	9.050	8.699
SA Tracking BF	2.273	1.165	4.762

code delay estimates, i.e., making use of the signal from the rotating antenna processed with the SA tracking architecture. In both cases, the navigation solution was recomputed every 100 ms for a total time of 64 s, which corresponds to each point in Figure 4.46a. The true and average computed positions are depicted in the figure.

Figures 4.46b and 4.46c compare the distributions of the computed latitude and longitude values, respectively, in each case. These figures show that the bias in the average position is significantly reduced when the rotating antenna’s signal is processed using the SA tracking architecture. Smaller variance in the SA tracking case was expected since the samples of a  $T_{SA} = 2$  s are used to compute the code delay estimates. This also implies a high correlation among successive samples observed in Figure 4.46a (explaining the ‘worm-like’ pattern), and more clearly observed in Figure 4.45, where the RMSE over time is depicted. Table 4.7 summarizes the results obtained. In the light of these results, we can conclude that the proposed SA tracking architecture can significantly mitigate the bias in the navigation solution due to multipath presence.

#### 4.5.4 ACF Correction with SA Open-Loop Tracking (II)

In previous Section 4.4.4, we validated the Open-Loop version of the proposed SA tracking architecture by processing simulated signals. Now, just like in the previous sections, we present the results obtained after processing the real GPS L1 C/A signals recorded in the MC 3rd Floor Terrace scenario. We present the results following a similar structure as in Section 4.4.4.

We focus on PRN 19 and PRN 17 signals, whose DOA maps computed in Section 4.5.1 showed the presence of strong coherent multipath reflections. We processed PRN 23 as well, to have a reference signal with little multipath interference and observed at a high elevation angle.

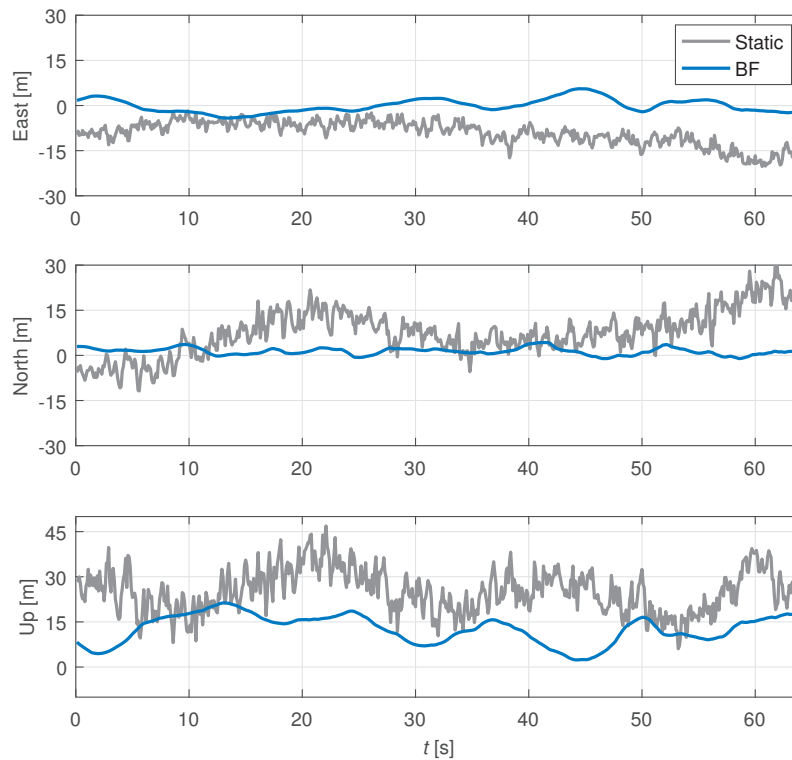
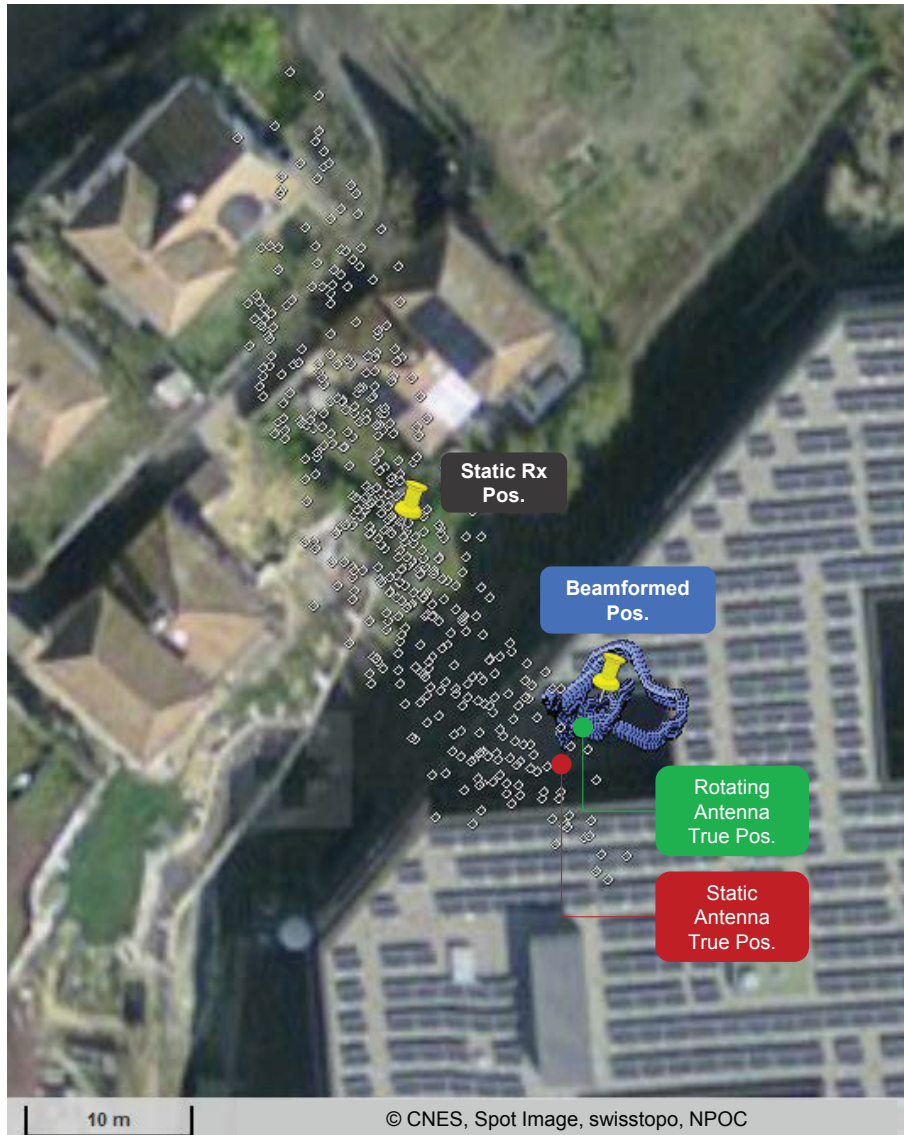


**Figure 4.45** – Error comparison over time: static receiver versus rotating antenna with SA tracking architecture.

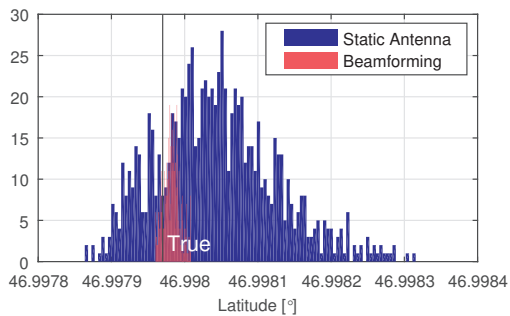
Figure 4.47 shows the beamformed CAFs for PRN 19 and PRN 17 at  $t = 3$  s. In this case we used a smaller frequency search space spanning 20 Hz with a resolution of 0.05 Hz. We observe again smaller secondary replicas of the main CAF peak, spanning the considered frequency search space, however, we cannot directly relate them to multipath interference. They could also be related caused by the complex antenna gain (nonlinear phase wrap-up) or by the deviations of the rotation speed with respect to the nominal value.

In Figure 4.47 we show the evolution of the normalized ACF over time (see Section 4.4.4 for more details). This time however, we have cut off the first second after acquisition. While Figure 4.47.(a) shows a very constant ACF, Figure 4.47.(b) presents variations in the amplitude of the ACF. We recall that the DOA Block implements the Beamscan algorithm and updates the DOA estimates every 100 ms. In Figure 4.48 we show the elevation error over time, i.e., the difference between the elevation output from the DOA Block and the reference elevation obtained from the navigation solution. As expected, a part from a small bias of  $0.35^\circ$ , the elevation estimate for PRN 23 is very steady, with a standard deviation of only  $0.08^\circ$ . The elevation estimates for PRN 19 have a standard deviation of  $0.72^\circ$  and a bias of  $-0.66^\circ$ . In the case of PRN 17, the elevation estimates show higher variability, which was constrained due to the constrained search space for the elevation estimate in the DOA block, set to  $\pm 3^\circ$ . The variations in the ACF in Figure 4.47.(b) show some weak correlation with the error in the elevation estimates for PRN 17, but we cannot link these ACF variations only to the poor DOA estimation. We tried providing the DOA computed from the navigation solution to the Beamforming block, but we got similar results with variations on the ACF

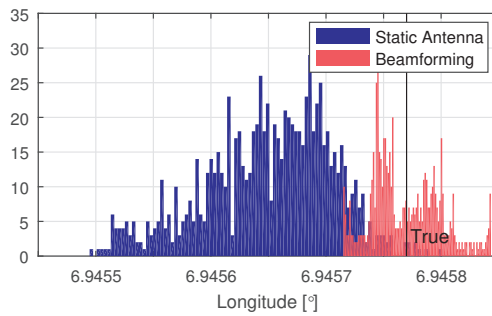
#### 4.5. Experimental Results with Real Signals Recorded with a Rotating Arm



(a) Computed positions: blue for the rotating arm, gray for the static antenna.



(b) Latitude histogram



(c) Longitude histogram

**Figure 4.46** – 2D navigation solutions using the static antenna signal versus the rotating antenna signal with the proposed SA tracking architecture at the MC 3rd Floor Terrace site. The yellow push pins represent the average positions.

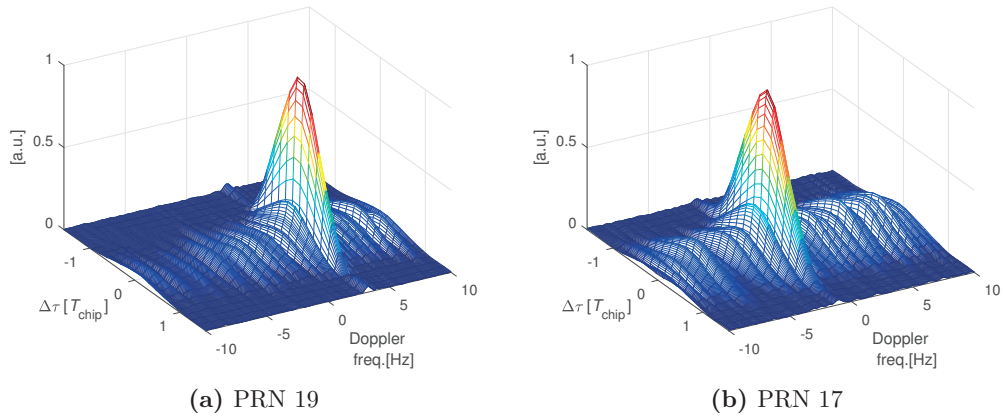


Figure 4.47 – Beamformed CAFs at  $t = 3$  s. MC 3rd Floor Terrace scenario.

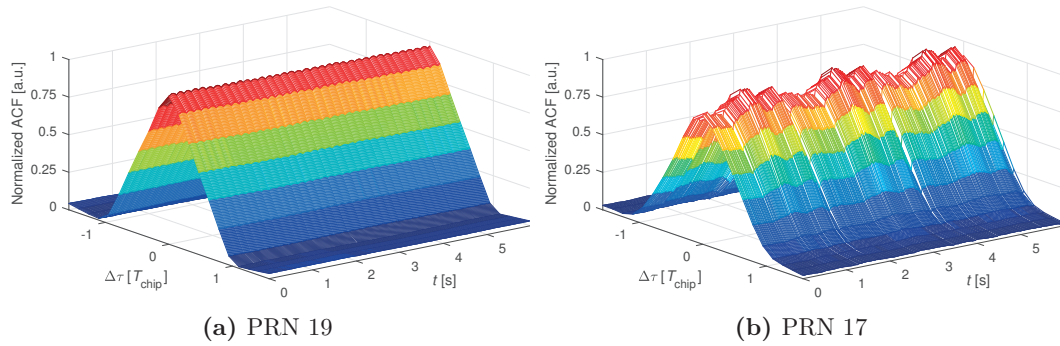
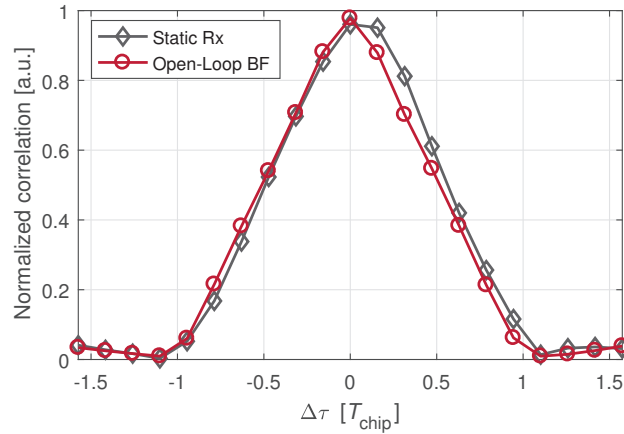


Figure 4.48 – Normalized ACF over time, obtained from the beamformed CAF. MC 3rd Floor Terrace scenario.

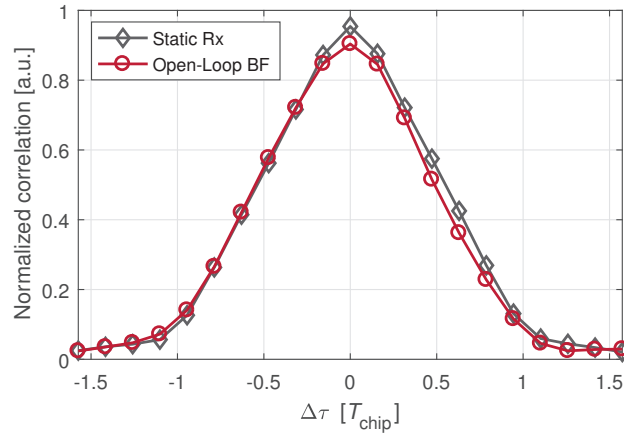
observed over time.

Finally, Figure 4.49 compares the averaged normalized ACFs for the static receiver and the beamformed case for PRN 19 (a) and PRN 17 (b). In both cases, the beamforming appears to reduce the multipath-caused distortion, therefore, it shall reduce the bias in the code delay estimates. We have assumed that the distortion in the normalized ACF shown in Figure 4.49 is caused by the multipath presence, not only because of our a priori knowledge from results in previous Section 4.5.1, but because the distortion mostly happens for positive delays. Intuitively, this makes sense because multipath signals travel longer distances than the LOS signal. Moreover, the likely source of the specular reflection, i.e. the metal covered wall in the East direction (see Figure 4.34), is only a few meters away, thus, the delay difference should be quite small.





(a) PRN 19



(b) PRN 17

Figure 4.49 – Average ACFs over 6 s for signals recorded in MC 3rd Floor Terrace Scenario.

## 4.6 Chapter Conclusion

In this chapter we studied the SA processing of GNSS signals, mainly focusing on quasi-uniform circular motions. In Section 4.2, we obtained a DOA estimation bound for known arbitrary trajectories by deriving the CRB. Under the assumption of a stationary channel, fully characterized by its known covariance matrix, our CRB derivation considered the joint estimation of the amplitudes, DOAs and synchronization parameters of  $M$  coherent GNSS signal components. We forewent the narrowband signal and array assumptions to adapt the received signal model to any deterministic receiver motion. Also, we modeled the effect of the antenna complex gain, which –even for the omnidirectional case– will depend on the antenna’s orientation and the signal’s DOA, through the polarization mismatch coefficient. We put our CRB expressions to the test in two simulation scenarios with two different kinds of motion. The results obtained confirmed the suitability of SA techniques for precise DOA estimation and demonstrated that precision on the order  $1^\circ$  is possible by changing the antenna orientation only –in a spinning motion–. We have assumed an accurately known antenna gain pattern. If this is not the case, one should expect significant biases in the DOA estimation. Even though we used GPS L1 C/A in our simulations, the CRB computed can be particularized for any GNSS signal in a straightforward manner.

In the remaining sections of this chapter, we proposed a development framework to integrate SA techniques into the receiver's signal tracking. Besides, we also proposed a new tracking architecture, compatible with closed-loop and open-loop tracking schemes, to support continuously updated DOA estimation and beamforming with classical and adaptive algorithms. A new SA open-loop tracking scheme was proposed in Section 4.3.3, which is inherently more robust than closed-loop tracking approaches. Moreover, it can be used directly after the acquisition stage, without any previous knowledge about the signal's actual DOA, even when tracking the signal without any SA processing is not possible. In Section 4.3.4, we described two different EKF-based methods, EKF1 and EKF2, to perform the reference carrier frequency estimation necessary to compensate the input of any SA processing in this context.

The results obtained using synthetic GPS L1 C/A signal, which were generated our Spirent GSS8000 simulator, and with real signal recorded in two different sites, are extensively described in sections 4.4 and 4.5. These signals were processed off-line using an extensively modified version of Kai-Borre's SDR GPS receiver [2]. A mechanical rotating arm mounting a GNSS antenna was built to collect the real signal along circular trajectories. The results obtained confirmed that SA techniques can be integrated within the receiver tracking architecture to provide precise DOA estimation and beamforming capabilities. Finally, we have measured a significant reduction in the bias observed in the navigation solution computed by the receiver implementing the proposed SA tracking architecture, in an environment with severe multipath interference.

## Chapter 5

# Conclusions

This thesis has examined the estimation of parameters characterizing GNSS multipath from two different perspectives: retrieving useful information from it with GNSS-R techniques; and estimating its DOA –as well as the LOS signal’s– and mitigating its effects using synthetic aperture processing. In both cases, we studied the theoretical estimation bounds for some specific scenarios by resorting to the CRB. The present chapter aims to summarize the main findings and novel contributions described in previous chapters. To end this chapter, we suggest a series of future research directions and possible further developments beyond the work described in this thesis.

### 5.1 Thesis Achievements

In **Chapter 3** we tried to partially answer the following question: How precise can GNSS-R techniques estimate the height of a receiver and the surface’s reflection coefficient, considering observation times of up to several minutes? Our study has focused on static ground-based receivers with a single antenna and a specular reflection from a horizontal, smooth and homogeneous surface. In these kind of scenarios, the phase coherence of the reflected signal is well preserved. Therefore, it can be used to generate more precise estimates than in scenarios dominated by diffuse scattering.

We started by deriving the CRB considering short observation times of up to 1 second. If the receiver’s height ( $h$ ) and reflection coefficient are assumed unknown, the CRB confirms that the phase information cannot be used to improve the precision of the  $h$  estimate. We have identified two different cases: when the propagation path difference between the LOS and the reflected signal ( $\Delta\rho$ ) is longer than the chip distance ( $\rho_{chip}$ ), and otherwise. Only in the first case, we were able to obtain convenient closed-form expressions for the CRB of the different parameters as a function of the receiver and scenario setup. When  $\Delta\rho < \rho_{chip}$  we resorted to numerical evaluation to obtain the CRB for each specific scenario. The CRB results for  $h$  estimation were consistent across the different GPS and Galileo signals considered, i.e., the higher the RF front end bandwidth, the lower the CRB, as long as the front end bandwidth remains lower or equal to the signal’s transmitted bandwidth. The closed-form expressions of the CRB obtained highlight the following trade-off: the higher the observed satellite elevation, the better the attainable precision. However, for high elevation satellites, the coherence of considered reflected signals decreases, requiring a flatter surface for the smooth assumption to still hold. The CRB of  $h$  also showed that, depending on the reflection coefficient of the

surface, meter and decimeter precisions are –depending on the receiver’s bandwidth and the signal considered– theoretically possible for observation times of 1 second.

We extended the computed CRB to use it for long observation times. To do so, we resorted to the FIM parameter transformation method. To the best of our knowledge, at the time of writing this dissertation, the proposed CRB for long observation times was the only reported precision bound applicable to IPT-like techniques. The proposed CRB characterizes the –already expected– dependency of the attainable precision when estimating  $h$  and the surface reflectivity, on the observed satellite elevation change. The CRB exposes a relevant trade-off: large elevation variations are desired for better precision, but elevation changes displace the specular reflection point and modify the size of the track over the surface –reducing the spatial resolution of the estimates–. The CRB results agree with the cm-level precision that has been reported in many works, e.g., [31, 94, 100, 103, 169–171].

In **Chapter 4** we moved away from GNSS-R techniques to study the synthetic aperture (SA) processing of GNSS signals received by a single antenna in motion. In this case, the goal was to estimate the DOA of the signals received and, ultimately, mitigate the multipath error in PVT applications.

The first contribution of this chapter is the derivation of the CRB of the synchronization and DOA parameters in the GNSS SA context. The derived CRB does not make use of the narrowband signal and (equivalent) narrowband array assumptions –commonly taken in the study of physical arrays–, which makes the CRB valid for long trajectories and fast receiver speeds. Another important novelty of the proposed CRB is that explicitly models the effects of the complex antenna gain. The CRB for the DOA parameters showed that changes in the antenna orientation only, can be sufficient –even with omnidirectional antennas– to generate meaningful DOA estimates, and therefore, to apply spatial processing techniques. Conversely, if the phase changes due to that antenna gain, i.e., the so-called phase wrap-up, are not adequately compensated before the spatial processing, the accuracy of the computed DOA estimates will be impacted. However, the proposed CRB has some limitations, which are mostly related to the channel’s spatiotemporal covariance matrix, which: first, it is assumed known, and second, it makes the obtention of the CRB computationally challenging. Hence, for simplicity, we have assumed CWGN and the presence of the LOS signal only, in the two simulated scenarios. These two scenarios implemented different antenna motions (arm-like rotation and tilted spinning), to compute the CRB of the DOA parameters. As in Chapter 3, the computed CRB was validated by deriving the corresponding MLE and verifying that the variance matches the CRB values in the asymptotic region.

Chapter 4 continued by proposing a SA tracking architecture integrating DOA estimation and beamforming techniques. This SA tracking architecture implement an auxiliary tracking channel to each traditional tracking channel –referred to as “primary” channel–. Each auxiliary channel is performs the SA processing resulting to the “beamformed” correlation outputs. The auxiliary channels can potentially accommodate any spatial filtering technique adapted for SA processing. Then, the receiver can use the “beamformed” correlation outputs to compute a new SA-corrected navigation solution.

The proposed SA architecture can also be implemented as an open-loop tracking architecture. Although more computationally intense, open-loop tracking is inherently more robust and eliminates the critical limitation –when there is no a priori information of the DOA of the LOS signal– of closed-loop SA tracking implementations, i.e., that they also need to be capable of acquiring and tracking the signal before applying any SA processing, thus, limiting their robustness. Indeed, SA open-loop tracking enables the use of SA processing directly

on the acquisition of the signals, which can be of interest in harsh reception environments.

The final part of Chapter 4 summarizes the most relevant results obtained when trying to validate the tracking architecture and the SA techniques proposed earlier in the chapter. This validation was carried out first with synthetic GPS L1 C/A signals generated with a Spirent GSS8000 simulator, and then with real GPS signals recorded from an antenna mounted on a rotating mechanical arm. This arm was built in-house to implement uniform circular motions, with adjustable angular speeds and radii of up to 1 m. Open-loop tracking with SA was capable of reducing the distortion on the measured signal correlation function, both with synthetic and real received signal. One of the sites chosen for the recording of GPS signal with the rotating arm, namely the MC 3rd Floor Terrace site, had particularly limited satellite visibility and strong multipath interference was expected. The DOA estimation results in this site showed that there was an additional signal component present. This signal component was received with approximately the same observed elevation and an azimuth difference of  $180^\circ$ , which agrees with the behavior of a coherent multipath component reflected from the east-side wall.

EKF1 and EKF2 algorithms showed poor performance in the MC 3rd Floor Terrace scenario. This behavior was expected given the fact that these algorithms assume only one received coherent signal component, i.e., the LOS signal. When strong coherent signal reflections are present, the model does not match the actual measurements anymore, therefore the performance degradation (DOA estimation biases and even loss-of-lock with EKF2).

We placed a static antenna next to the rotating arm only in both experimental scenarios. In MC 3rd Floor Terrace scenario, the signal recorded with the static antenna was used to compensate the reference carrier frequency and the navigation data from the signal received by the moving antenna. Finally, we compared the navigation solution obtained by processing the signal from the static antenna, with the one generated by the SA tracking architecture with the signal from the rotating antenna. We observed how the bias due to the multipath interference in the 2-D navigation solution was significantly mitigated.

## 5.2 Directions for Future Research

At the conclusion of this thesis, there remain some research directions which might be worth exploring. First, some envisioned extensions of the work related to GNSS-R described in Chapter 3 can consider:

- Developing an open-source software based on the code developed for this thesis to compute CRB in specular reflection scenarios. This software tool could be used by the GNSS-R research community when testing new techniques or receivers, to have a preliminary expectation of the estimation precision achievable depending on the considered scenario.
- Defining meaningful and standardized GNSS-R scenario and compute its corresponding CRB. This scenario and the CRB could be used to benchmark and compare new and existing estimation techniques for ground-based receivers.
- Validating the proposed SML algorithm with experimental measurements and compare its performance to other estimation algorithms described in the literature.

- Computing the CRB for different models of the surface reflection coefficient (other than the Z-L model), with a different number of parameters. With the proposed FIM transformation method, it should be straightforward to consider a different model, e.g., a multilayer-medium model.
- Modifying the signal model to characterize the effects of receiver's processing on the CRB. If instead of considering the output of the RF front end, we consider the correlation output –after coherent, non-coherent, and interferometric integration techniques [6, 33, 49]– as measurements, the CRB obtained will quantify the precision degradation –if there is any– caused by the specific receiver architecture. We recall that many GNSS-R techniques use the quantized SNR or  $C/N_0$  estimates as measurements. In this case, the CRB could consider the probability density function of these measurements to obtain a tighter bound for those techniques.
- Studying the effect of the receiver clock error on the achievable estimation precision by explicitly taking this error into account within the signal model.
- Exploring more sophisticated signal models describing scenarios with coherent and diffuse multipath simultaneously present. These models would allow defining the estimation precision theoretically possible for rough reflecting surfaces.

Similarly, in the context of SA processing with GNSS signal discussed in Chapter 4, extensions of the work described in this thesis might include:

- Further experimenting with the derived CRB of the DOA and synchronization parameters: in the presence of multiple correlated and uncorrelated signals present (e.g., LOS + jamming signals, spoofing signals, or coherent multipath), different antenna motions, and different antenna gain patterns.
- Generalizing the derived CRB for moving antenna arrays.
- Testing the proposed SA tracking architecture to perform spatial filtering with antenna orientation change only.
- Characterizing the impact of the two main systematic errors in DOA estimation with a synthetic aperture: an inaccurate assumption of the antenna position over time, and an erroneous carrier frequency compensation.
- Improving the mechanical rotating arm by installing sensors to track the antenna motion accurately when using the mechanical rotating arm, and allowing to have a north azimuth reference.
- Implementing adaptive spatial filtering techniques with the proposed open-loop version of SA tracking architecture.
- Deriving the CRB again considering the channel spatiotemporal covariance matrix as unknown.
- Exploring techniques to estimate the channel's spatiotemporal covariance matrix beyond the sample covariance matrix method.
- Computing some Bayesian estimation bounds instead of the classic CRB, for example, by assuming the amplitudes of the received signals as random nuisance parameters.

## 5.2. Directions for Future Research

---

- Studying the adaptation of the proposed SA tracking architecture to be implemented in receivers on board of cars and possibly UAVs for robust navigation in urban environments and jamming and spoofing signals location.

The previous lists were ordered roughly according to the estimated research effort building up from the work described in this thesis: from the lower to higher required effort.

“The future belongs to those  
who believe in the beauty  
their dreams.”

— Eleanor Roosevelt





## Appendix A

# Transformation Matrices and CRB Expressions for Short Observation Times

This appendix provides more detail on how the Jacobian transformation matrices,  $\mathbf{G}$  and  $\mathbf{T}_{long}$ , introduced in Sections 3.2.3 and Section 3.4, are computed. Besides, it shows how to obtain the CRB expressions for short observation times, discussed in Section 3.3.

The invariance principle for the ML states that it is possible to construct the ML estimate for  $\Psi = g(\xi)$  as  $\hat{\Psi}_{ML} = g(\hat{\xi}_{ML})$ . If the function  $g$  defines a linear transformation, estimation efficiency is maintained. Otherwise,  $g$  will only be asymptotically efficient with the number of measurements.

The CRB of  $\Psi$  can be constructed in a similar way. To do so, we shall assume that the transformation function is continuous, non-singular mapping  $g : \mathbb{R}^p \rightarrow \mathbb{R}^p$ , which implies that  $\xi \in \mathbb{R}^p$  and  $\Psi \in \mathbb{R}^p$ . This results extends to maps  $g : \mathbb{R}^p \rightarrow \mathbb{R}^m$ , with  $m \leq p$ , if the likelihood function of  $\Psi$  –given the vector of random measurements  $\mathbf{x}$ – defines a continuous, bounded mapping [143]. Under such assumption, we can obtain the FIM of  $\Psi$ , i.e.,  $\mathbf{J}(\Psi)$ , from the FIM of  $\xi$ , i.e.,  $\mathbf{J}(\xi)$ , as:

$$\mathbf{J}(\Psi) = \mathbf{T}\mathbf{J}(\xi)\mathbf{T}^T, \quad (\text{A.1})$$

where  $\mathbf{T} \in \mathbb{R}^{m \times p}$  is the transformation matrix defined as

$$\mathbf{T} = \frac{\partial \xi}{\partial \Psi} = \begin{pmatrix} \frac{\partial \xi_1}{\partial \Psi_1} & \frac{\partial \xi_2}{\partial \Psi_1} & \cdots & \frac{\partial \xi_p}{\partial \Psi_1} \\ \frac{\partial \xi_1}{\partial \Psi_2} & \frac{\partial \xi_2}{\partial \Psi_2} & \cdots & \frac{\partial \xi_p}{\partial \Psi_2} \\ \vdots & \vdots & \ddots & \vdots \\ \frac{\partial \xi_1}{\partial \Psi_m} & \frac{\partial \xi_2}{\partial \Psi_m} & \cdots & \frac{\partial \xi_p}{\partial \Psi_m} \end{pmatrix}, \quad (\text{A.2})$$

which is just the transpose of the Jacobian matrix [43]. Let us make use now of this transformation property of the CRB for our particular cases of interest.

As discussed in Section 3.3.1, the FIM  $\mathbf{J}(\xi)$ , which is expressed using (3.23) and (3.22),

## Appendix A. Transformation Matrices and CRB Expressions for Short Observation Times

---

becomes a diagonal matrix when  $\Delta\rho > \rho_{chip}$ , i.e.:

$$\mathbf{J}(\boldsymbol{\xi}) = \frac{2K}{\sigma_w^2} \text{diag} \left\{ \begin{bmatrix} R(0) \\ u_0^2 R(0) \\ -u_0^2 R''(0) \\ R(0) \\ u_1^2 R(0) \\ -u_1^2 R''(0) \end{bmatrix} \right\}. \quad (\text{A.3})$$

However, we are interested in computing the CRB for the set of unknown parameters  $\boldsymbol{\Psi}$ , already defined in expression (3.26) as:

$$\boldsymbol{\Psi} = \begin{bmatrix} u_0 \\ \phi_0 \\ \rho_0 \\ |\Gamma| \\ \phi_\Gamma \\ h \end{bmatrix}, \quad (\text{A.4})$$

by transforming  $\mathbf{J}(\boldsymbol{\xi})$  into  $\mathbf{J}(\boldsymbol{\Psi})$  –which is not diagonal anymore–, using below’s expression (A.1). As discussed in Section 3.2.3, the transposed Jacobian matrix  $\mathbf{T} \in \mathbb{R}^{6 \times 6}$  for short observation intervals and this specific case with phase coherence between both signal components is expressed as:

$$\mathbf{T} = \frac{\partial \boldsymbol{\xi}}{\partial \boldsymbol{\Psi}} = \begin{pmatrix} 1 & 0 & 0 & |\Gamma| & 0 & 0 \\ 0 & 1 & 0 & 0 & 1 & 0 \\ 0 & 0 & c^{-1} & 0 & 0 & c^{-1} \\ 0 & 0 & 0 & u_0 & 0 & 0 \\ 0 & 0 & 0 & 0 & 1 & 0 \\ 0 & 0 & 0 & 0 & -2k \sin(\theta) & 2 \sin(\theta) c^{-1} \end{pmatrix}. \quad (\text{A.5})$$

With some algebra, the CRB of  $\boldsymbol{\Psi}$  is then obtained as:

$$\text{CRB}(\boldsymbol{\Psi}) = \left[ \mathbf{J}^{-1}(\boldsymbol{\Psi}) \right]_{ii} = \frac{\sigma_w^2}{2K} \begin{bmatrix} \frac{1}{R(0)} \\ \frac{1}{u_0^2 R(0)} \\ -\frac{c^2}{u_0^2 R''(0)} \\ \frac{|\Gamma|^2 + 1}{u_0^2 R(0)} \\ \frac{(R''(0) - R(0)k^2 c^2)(|\Gamma|^2 + 1)}{u_0^2 |\Gamma|^2 R(0) R''(0)} \\ -\frac{c^2 (|\Gamma|^2 + 1)}{4u_0^2 |\Gamma|^2 \sin^2(\theta) R''(0)} \end{bmatrix}. \quad (\text{A.6})$$

$\text{CRB}(h)$ ,  $\text{CRB}(|\Gamma|)$ ,  $\text{CRB}(\phi_\Gamma)$ , defined in expressions (3.32), (3.33) and (3.36), are obtained in a straightforward manner from the 3rd, 4th and 5th elements of expression (A.6), respectively.

The CRB expression presented in (3.38) for the phase altimetry case, described in Section 3.3.1, is obtained by removing the fifth row and column (both related to  $\phi_\Gamma$ ) from  $\mathbf{J}(\boldsymbol{\Psi})$  and then computing the inverse of the matrix that is left. Now, the  $\text{CRB}_{alt}(h)$  is the element related to  $h$  in the main diagonal, i.e., the fifth element. In the same way, the CRB for the

reflection coefficient estimation case, i.e.,  $\text{CRB}_r$ , described in Section 3.3.1 with expressions (3.39) and (3.40), is obtained following the same procedure, but now by removing the last row and the last column (both related to  $h$ ) from  $\mathbf{J}(\Psi)$ .

The transformation matrix  $\mathbf{T}_{long} \in \mathbb{R}^{6N \times P}$  is introduced in Section 3.4, with  $N$  being the number of  $T_{coh}$  intervals considered, and  $P$  the number of parameters in  $\Psi_{long}$ . For a  $\mathbf{s}_\Gamma = [\varepsilon_r, \sigma]^T$  defined as in Section 3.5, we have:

$$\mathbf{T}_{long} = \frac{\partial \Psi_{ext}}{\partial \Psi_{long}} = \begin{pmatrix} \boldsymbol{\delta}_0 & \mathbf{0} & \dots & & \mathbf{0} \\ \mathbf{0} & \boldsymbol{\delta}_0 & \mathbf{0} & \dots & \mathbf{0} \\ \vdots & & & & \vdots \\ \mathbf{0} & & & \mathbf{0} & \boldsymbol{\delta}_0 \\ \boldsymbol{\delta}_1 & \mathbf{0} & \dots & & \mathbf{0} \\ \mathbf{0} & \boldsymbol{\delta}_1 & \mathbf{0} & \dots & \mathbf{0} \\ \vdots & & & & \vdots \\ \mathbf{0} & & & \mathbf{0} & \boldsymbol{\delta}_1 \\ \boldsymbol{\delta}_2 & \mathbf{0} & \dots & & \mathbf{0} \\ \mathbf{0} & \boldsymbol{\delta}_2 & \mathbf{0} & \dots & \mathbf{0} \\ \vdots & & & & \vdots \\ \mathbf{0} & & & \mathbf{0} & \boldsymbol{\delta}_2 \\ \frac{\partial |\Gamma(\theta_0)|}{\partial \varepsilon_r} \boldsymbol{\delta}_3 & \frac{\partial |\Gamma(\theta_1)|}{\partial \varepsilon_r} \boldsymbol{\delta}_3 & \dots & & \frac{\partial |\Gamma(\theta_{N-1})|}{\partial \varepsilon_r} \boldsymbol{\delta}_3 \\ \frac{\partial \phi_\Gamma(\theta_0)}{\partial \sigma} \boldsymbol{\delta}_4 & \frac{\partial \phi_\Gamma(\theta_1)}{\partial \sigma} \boldsymbol{\delta}_4 & \dots & & \frac{\partial \phi_\Gamma(\theta_{N-1})}{\partial \sigma} \boldsymbol{\delta}_4 \\ \boldsymbol{\delta}_5 & \boldsymbol{\delta}_5 & \dots & & \boldsymbol{\delta}_5 \end{pmatrix}, \quad (\text{A.7})$$

where  $\boldsymbol{\delta}_l \in \mathbb{R}^{1 \times 6}$  has been defined as a row-vector with all its elements equal to zero, except for the position indicated by the subindex  $l \in \{0, \dots, 5\}$ , which has a value of one.  $|\Gamma(\theta_n)|$  and  $\phi_\Gamma(\theta_n)$  will change together with  $\theta_n$  in each of the  $N$  intervals of  $T_{coh}$  duration, over the total observation time.



## Appendix B

# Zavorotny–Larson Model for the Surface Reflection Coefficient $\Gamma$

In [62], the authors propose a model for the complex reflection coefficient, i.e.,  $\Gamma = |\Gamma| \exp\{\phi_\Gamma\}$  of the GPS L1 signal for the case of bare soil with a flat surface.  $\Gamma$  is defined like in expression (3.27), i.e., as the amplitude ratio between the reflected and the LOS signals. We refer to this model as the Z-L model, for brevity. It treats the soil as a single-layer dielectric medium with losses. It also takes into account the polarization dependent antenna gain effect over the reflected signal. The main contribution to the amplitude observed corresponding the reflected signal comes from the first Fresnel zone around the specular reflection point.

According to the model, when the antenna boresight is perpendicular to the ground,  $\Gamma$  can be expressed as a function of the satellite elevation  $\theta$  as:

$$\Gamma(\theta) = (V_{RR}G_{\text{RHCP}}(-\theta) + V_{RL}G_{\text{LHCP}}(-\theta)) \exp\{-0.5 k^2 \sigma_{sh}^2 \sin^2(\theta)\}, \quad (\text{B.1})$$

where the effect of the surface roughness is incorporated by the exponential term, the so-called coherence loss factor [64].  $k = 2\pi/\lambda$  is the carrier wavenumber, and  $\sigma_{sh}$  is the standard deviation of the surface height.  $G_{\text{RHCP}}(\theta)$  and  $G_{\text{LHCP}}(\theta)$  represent the antenna complex amplitude gains for RHCP and LHCP at  $\theta$ , respectively; and

$$\begin{aligned} V_{RR} = V_{LL} &= \frac{1}{2} (V_v + V_h), \\ V_{RL} = V_{LR} &= \frac{1}{2} (V_v - V_h), \end{aligned} \quad (\text{B.2})$$

are the polarization-dependent reflection coefficients, where the first subscript stands for the polarization state ( $R$  for RHCP and  $L$  for LHCP) of the incident wave, while the second subscript stands for the polarization state of the reflected wave.  $V_v$  and  $V_h$  are the coefficient

## Appendix B. Zavorotny–Larson Model for the Surface Reflection Coefficient $\Gamma$

---

for the linear vertical and horizontal polarizations, which can be expressed as:

$$\begin{aligned} V_v &= \frac{\varepsilon \sin(\theta) - \sqrt{\varepsilon - \cos^2(\theta)}}{\varepsilon \sin(\theta) + \sqrt{\varepsilon - \cos^2(\theta)}}, \\ V_h &= \frac{\sin(\theta) - \sqrt{\varepsilon - \cos^2(\theta)}}{\sin(\theta) + \sqrt{\varepsilon - \cos^2(\theta)}}, \end{aligned} \tag{B.3}$$

with:

$$\varepsilon \approx \varepsilon_r - j60\lambda\sigma, \tag{B.4}$$

as the complex dielectric permittivity of the material [61, 201]. In (B.4),  $\varepsilon_r$  represents the real-part of the permittivity, and  $\sigma$  is the conductivity of the reflection surface (in S/m units). The model for  $\Gamma$  can be extended for the multiple layer ground case, where  $\Gamma$  will also depend on the thickness of each layer and their relative permittivity [201, 202]. For example in [119, 203], the authors use a three-layer (air + two soil layers) model for GNSS-R applications working with the GPS L1 band signal. For more details on all of the assumptions made to obtain (B.1), we refer the interested reader to [62].

# Bibliography

- [1] J. Sanz-Subirana, J. Juan-Zornoza, and M. Hernandez-Pajares, “Navipedia: GNSS signal entry,” 2011. [Online]. Available: <http://www.navipedia.net/index.php/GNSS{ }signal>
- [2] K. Borre, *A Software-Defined GPS and Galileo Receiver*, 2007.
- [3] ESA, “European GNSS (Galileo) Open Service, Signal In Space Interface Control Document (OS-SIS-ICD) Issue 1.3,” 2015.
- [4] G. Waelchli, “Architecture of a Real-Time Platform Independent GPS L1 Software Receiver,” Ph.D. dissertation, EPFL, 2010.
- [5] F. van Graas, A. Soloviev, M. Uijt de Haag, and S. Gunawardena, “Closed-Loop Sequential Signal Processing and Open-Loop Batch Processing Approaches for GNSS Receiver Design,” *IEEE Journal of Selected Topics in Signal Processing*, vol. 3, no. 4, pp. 571–586, aug 2009. [Online]. Available: <http://ieeexplore.ieee.org/lpdocs/epic03/wrapper.htm?arnumber=5166586>
- [6] V. U. Zavorotny, S. Gleason, E. Cardellach, and A. Camps, “Tutorial on Remote Sensing Using GNSS Bistatic Radar of Opportunity,” *IEEE Geoscience and Remote Sensing Magazine*, vol. 2, no. 4, pp. 8–45, dec 2014. [Online]. Available: <http://ieeexplore.ieee.org/lpdocs/epic03/wrapper.htm?arnumber=6985926>
- [7] MathWorks Inc., “MATLAB and Optimization Toolbox Release 2016b,” Natick, Massachusetts, United States, 2016. [Online]. Available: <https://ch.mathworks.com/help/optim/>
- [8] T. Lin, A. Broumandan, J. Nielsen, C. O. Driscoll, and G. Lachapelle, “Robust Beamforming for GNSS Synthetic Antenna Arrays,” in *Proceedings of the 22nd International Technical Meeting of The Satellite Division of the Institute of Navigation (ION GNSS 2009)*, no. September, Savannah, GA, US, 2009, pp. 387–401.
- [9] US Department of Defense, “Navstar GPS Space/Segment Navigation User Segment Interface, Interface Specification (IS-GPS-200E).”
- [10] —, “Navstar GPS Space Segment—User Segment L5 Interfaces, Interface Specification (IS-GPS-705).” [Online]. Available: <http://www.gps.gov/technical/icwg/>
- [11] S. Jin, E. Cardellach, and F. Xie, *GNSS Remote Sensing*, ser. Remote Sensing and Digital Image Processing. Dordrecht: Springer Netherlands, 2014, vol. 19.
- [12] E. D. Kaplan and C. J. Hegarty, *Understanding GPS: Principles and Applications*, 2nd ed., E. D. Kaplan and C. J. Hegarty, Eds. Artech House, 2006.
- [13] S. Gleason and D. Gebre-Egziabher, Eds., *GNSS Applications and Methods*, 1st ed. Artech House, 2009.

## Bibliography

---

- [14] N. S. Gowdayyanadoddi, A. Broumandan, J. T. Curran, and G. Lachapelle, "Benefits of an Ultra Stable Oscillator for Long Coherent Integration," in *Proceedings of the 27th International Technical Meeting of The Satellite Division of the Institute of Navigation (ION GNSS+ 2014)*, Tampa, Florida, 2014, pp. 1578–1594.
- [15] J. Leclere, C. Botteron, and P.-A. Farine, "Feature article: High sensitivity acquisition of GNSS signals with secondary code on FPGAs," *IEEE Aerospace and Electronic Systems Magazine*, vol. 32, no. 8, pp. 46–63, aug 2017. [Online]. Available: <http://ieeexplore.ieee.org/document/8068038/>
- [16] C. Gioia, S. Gaglione, and A. Angrisano, "Performance assessment of aided Global Navigation Satellite System for land navigation," *IET Radar, Sonar & Navigation*, vol. 7, no. 6, pp. 671–680, jul 2013. [Online]. Available: <http://digital-library.theiet.org/content/journals/10.1049/iet-rsn.2012.0224>
- [17] G. De Angelis, G. Baruffa, and S. Cacopardi, "GNSS/Cellular Hybrid Positioning System for Mobile Users in Urban Scenarios," *IEEE Transactions on Intelligent Transportation Systems*, vol. 14, no. 1, pp. 313–321, mar 2013. [Online]. Available: <http://ieeexplore.ieee.org/document/6307871/>
- [18] L. Wang, P. D. Groves, and M. K. Ziebart, "Multi-Constellation GNSS Performance Evaluation for Urban Canyons Using Large Virtual Reality City Models," *Journal of Navigation*, vol. 65, no. 03, pp. 459–476, jul 2012. [Online]. Available: <http://www.journals.cambridge.org/abstract{ }S0373463312000082>
- [19] P. D. Groves, "Shadow Matching: A New GNSS Positioning Technique for Urban Canyons," *Journal of Navigation*, vol. 64, no. 03, pp. 417–430, jul 2011. [Online]. Available: <http://www.journals.cambridge.org/abstract{ }S0373463311000087>
- [20] V. Capuano, P. Blunt, C. Botteron, and P. A. Farine, "Orbital Filter Aiding of a High Sensitivity GPS Receiver for Lunar Missions," 2017.
- [21] P. Silva, H. Lopes, T. Peres, J. Silva, J. Ospina, F. Cichocki, F. Dovic, L. Musumeci, D. Serant, T. Calmettes, I. Pessina, and J. Perelló, "Weak GNSS Signal Navigation to the Moon," in *Proceedings of the 26th International Technical Meeting of The Satellite Division of the Institute of Navigation (ION GNSS+ 2013)*, sep 2013, pp. 3357–3367. [Online]. Available: <http://www.ion.org/publications/abstract.cfm?jp=p{&}articleID=11438>
- [22] E. S. Lohan, D. Alonso de Diego, J. A. Lopez-Salcedo, G. Seco-Granados, P. Boto, and P. Fernandes, "Unambiguous Techniques Modernized GNSS Signals: Surveying the solutions," *IEEE Signal Processing Magazine*, vol. 34, no. 5, pp. 38–52, sep 2017. [Online]. Available: <http://ieeexplore.ieee.org/document/8026196/>
- [23] A. Jovanovic, Y. Tawk, C. Botteron, and P.-A. Farine, "Multipath mitigation techniques for CBOC, TMBOC and AltBOC signals using advanced correlators architectures," *IEEE/ION Position, Location and Navigation Symposium*, pp. 1127–1136, may 2010. [Online]. Available: <http://ieeexplore.ieee.org/lpdocs/epic03/wrapper.htm?arnumber=5507231>
- [24] C. Ruf, M. Unwin, J. Dickinson, R. Rose, D. Rose, M. Vincent, and A. Lyons, "CYGNSS: Enabling the Future of Hurricane Prediction," *IEEE Geoscience and Remote Sensing Magazine*, vol. 1, no. 2, pp. 52–67, jun 2013. [Online]. Available: <http://ieeexplore.ieee.org/document/6555846/>



- 
- [25] C. Ruf, P. Chang, M. Clarizia, S. Gleason, Z. Jelenak, J. Murray, M. Morris, S. Musko, D. Posselt, D. Provost, D. Starkenburg, and V. Zavorotny, *CYGNSS Handbook*. Michigan Pub., 2016.
- [26] N. Rodriguez-Alvarez, A. Camps, M. Vall-llossera, X. Bosch-Lluis, A. Monerris, I. Ramos-Perez, E. Valencia, J. F. Marchan-Hernandez, J. Martinez-Fernandez, G. Baroncini-Turricchia, C. Perez-Gutierrez, and N. Sanchez, “Land Geophysical Parameters Retrieval Using the Interference Pattern GNSS-R Technique,” *IEEE Transactions on Geoscience and Remote Sensing*, vol. 49, no. 1, pp. 71–84, jan 2011. [Online]. Available: <http://ieeexplore.ieee.org/lpdocs/epic03/wrapper.htm?arnumber=5475216>
- [27] N. Rodriguez-Alvarez, J. F. Marchan-Hernandez, A. Camps, X. Bosch-Lluis, E. Valencia, I. Ramos-Perez, M. Vall-Llossera, A. Monerris, J. Martinez-Fernandez, C. Perez-Gutierrez, G. Baroncini-Turricchia, N. Sanchez-Martinez, and J. M. Nieto, “Topographic profile retrieval using the interference pattern GNSS-R technique,” in *International Geoscience and Remote Sensing Symposium (IGARSS)*, vol. 3, 2009.
- [28] N. Rodriguez-Alvarez, A. Aguasca, E. Valencia, X. Bosch-Lluis, A. Camps, I. Ramos-Perez, H. Park, and M. Vall-llossera, “Snow Thickness Monitoring Using GNSS Measurements,” *IEEE Geoscience and Remote Sensing Letters*, vol. 9, no. 6, pp. 1109–1113, nov 2012. [Online]. Available: <http://ieeexplore.ieee.org/lpdocs/epic03/wrapper.htm?arnumber=6189031>
- [29] F. G. Nievinski and K. M. Larson, “Inverse Modeling of GPS Multipath for Snow Depth Estimation—Part II: Application and Validation,” *IEEE Transactions on Geoscience and Remote Sensing*, vol. 52, no. 10, pp. 6564–6573, oct 2014. [Online]. Available: <http://ieeexplore.ieee.org/lpdocs/epic03/wrapper.htm?arnumber=6722910>
- [30] —, “Inverse Modeling of GPS Multipath for Snow Depth Estimation—Part I: Formulation and Simulations,” *IEEE Transactions on Geoscience and Remote Sensing*, vol. 52, no. 10, pp. 6555–6563, oct 2014. [Online]. Available: <http://ieeexplore.ieee.org/lpdocs/epic03/wrapper.htm?arnumber=6730665>
- [31] —, “Inverse Modeling of GPS Multipath for Snow Depth Estimation—Part II: Application and Validation,” *IEEE Transactions on Geoscience and Remote Sensing*, vol. 52, no. 10, pp. 6564–6573, 2014. [Online]. Available: <http://ieeexplore.ieee.org/lpdocs/epic03/wrapper.htm?arnumber=6722910>
- [32] C. C. Chew, E. E. Small, K. M. Larson, and V. U. Zavorotny, “Vegetation Sensing Using GPS-Interferometric Reflectometry: Theoretical Effects of Canopy Parameters on Signal-to-Noise Ratio Data,” *IEEE Transactions on Geoscience and Remote Sensing*, vol. 53, no. 5, pp. 2755–2764, may 2015. [Online]. Available: <http://ieeexplore.ieee.org/lpdocs/epic03/wrapper.htm?arnumber=6954462>
- [33] M. Martin-Neira, S. D’Addio, C. Buck, N. Floury, and R. Prieto-Cerdeira, “The PARIS Ocean Altimeter In-Orbit Demonstrator,” *IEEE Transactions on Geoscience and Remote Sensing*, vol. 49, no. 6, pp. 2209–2237, jun 2011. [Online]. Available: <http://ieeexplore.ieee.org/lpdocs/epic03/wrapper.htm?arnumber=5682027>
- [34] S. D’Addio, F. Martin, H. Park, A. Camps, and M. Martin-Neira, “Height precision prediction of the PARIS in orbit demonstrator based on Cramer-Rao bound analysis,” in *2012 IEEE International Geoscience and Remote Sensing Symposium*. IEEE, jul 2012, pp. 7063–7066. [Online]. Available: <http://ieeexplore.ieee.org/lpdocs/epic03/wrapper.htm?arnumber=6352036>

## Bibliography

---

- [35] O. Germain and G. Ruffini, "A revisit to the GNSS-R code range precision," in *GNSS-R '06 Workshop*, ESA/ESTEC, Noordwijk, The Netherlands, jun 2006. [Online]. Available: <http://arxiv.org/abs/physics/0606180>
- [36] D. Pascual, A. Camps, F. Martin, H. Park, A. A. Arroyo, and R. Onrubia, "Precision Bounds in GNSS-R Ocean Altimetry," *IEEE Journal of Selected Topics in Applied Earth Observations and Remote Sensing*, pp. 1–1, 2014. [Online]. Available: <http://ieeexplore.ieee.org/lpdocs/epic03/wrapper.htm?arnumber=6742726>
- [37] E. Cardellach, A. Rius, M. Martin-Neira, F. Fabra, O. Nogues-Correig, S. Ribo, J. Kainulainen, A. Camps, and S. D'Addio, "Consolidating the Precision of Interferometric GNSS-R Ocean Altimetry Using Airborne Experimental Data," pp. 1–13, 2013.
- [38] S. D'Addio, C. Buck, and M. Martin-Neira, "Paris Altimetry Precision Prediction with Galileo Signals-in-Space," in *IGARSS 2008 - 2008 IEEE International Geoscience and Remote Sensing Symposium*, vol. 3. IEEE, 2008, pp. III – 63–III – 66. [Online]. Available: <http://ieeexplore.ieee.org/lpdocs/epic03/wrapper.htm?arnumber=4779283>
- [39] J. G. Proakis and M. Salehi, "Communications Systems Engineering," *Communications*, p. 801, 2002.
- [40] P. Closas, "Bayesian Signal Processing Techniques for GNSS Receivers: from multipath mitigation to positioning," Ph.D. dissertation, Universitat Politècnica de Catalunya, 2009.
- [41] European Global Navigation Satellite Systems Agency, "European GNSS Service Centre," 2017. [Online]. Available: <https://www.gsc-europa.eu/galileo-gsc-overview/system>
- [42] K. Aksnes, "Navigation, world mapping and astrometry with Galileo's moons," *Proceedings of the International Astronomical Union*, vol. 6, no. S269, pp. 42–48, 2010.
- [43] S. M. Kay, *Fundamentals of Statistical Signal Processing: Estimation Theory*. Englewood Cliffs, NJ: Prentice-Hall PTR, 1993.
- [44] G. Hein, T. Pany, S. Wallner, and J.-H. Won, "Platforms for a future GNSS Receiver," *Inside GNSS*, vol. 1, no. 2, pp. 56–62, 2006.
- [45] J. Leclere, C. Botteron, and P.-A. Farine, "Comparison Framework of FPGA-Based GNSS Signals Acquisition Architectures," *IEEE Transactions on Aerospace and Electronic Systems*, vol. 49, no. 3, pp. 1497–1518, jul 2013. [Online]. Available: <http://ieeexplore.ieee.org/lpdocs/epic03/wrapper.htm?arnumber=6558001>
- [46] V. Capuano, P. Blunt, C. Botteron, J. Tian, J. Leclère, Y. Wang, F. Basile, and P.-A. Farine, "Standalone GPS L1 C/A Receiver for Lunar Missions," *Sensors*, vol. 16, no. 3, p. 347, mar 2016. [Online]. Available: <http://www.mdpi.com/1424-8220/16/3/347>
- [47] F. Principe, G. Bacci, F. Giannetti, and M. Luise, "Software-Defined Radio Technologies for GNSS Receivers: A Tutorial Approach to a Simple Design and Implementation," *International Journal of Navigation and Observation*, vol. 2011, pp. 1–27, 2011.
- [48] C. Fernandez-Prades, C. Aviles, L. Estove, J. Arribas, and P. Closas, "Design patterns for GNSS software receivers," in *2010 5th ESA Workshop on Satellite Navigation Technologies and European Workshop on GNSS Signals and Signal Processing (NAVITEC)*. IEEE, dec 2010, pp. 1–8. [Online]. Available: <http://ieeexplore.ieee.org/lpdocs/epic03/wrapper.htm?arnumber=5707981>

- 
- [49] L. Lestarquit, M. Peyrezabes, J. Darrozes, E. Motte, N. Roussel, G. Wautelet, F. Frappart, G. Ramillien, R. Biancale, and M. Zribi, "Reflectometry With an Open-Source Software GNSS Receiver: Use Case With Carrier Phase Altimetry," *IEEE Journal of Selected Topics in Applied Earth Observations and Remote Sensing*, pp. 1–11, 2016. [Online]. Available: <http://ieeexplore.ieee.org/lpdocs/epic03/wrapper.htm?arnumber=7501832>
- [50] C. Fernandez-Prades, J. Arribas, P. Closas, C. Aviles, and L. Esteve, "GNSS-SDR: An Open Source Tool for Researchers and Developers," in *Proceedings of the 24th International Technical Meeting of The Satellite Division of the Institute of Navigation (ION GNSS 2011)*, sep 2011, pp. 780–794. [Online]. Available: <http://www.ion.org/publications/abstract.cfm?ip=p{&}articleID=9640>
- [51] F. Dovis, Ed., *GNSS Interference Threats and Countermeasures*. Artech House, 2015.
- [52] C. O'Driscoll, "Performance analysis of the parallel acquisition of weak GPS signals," Ph.D. dissertation, University College Cork, 2007.
- [53] D. Borio, "A Statistical Theory for GNSS Signal Acquisition," Ph.D. dissertation, Politecnico di Torino, 2008.
- [54] H. L. Van Trees, *Detection, Estimation, and Modulation Theory*, ser. Detection, Estimation, and Modulation Theory. Wiley, 2004, no. Part I.
- [55] S.-H. Kong, "High Sensitivity and Fast Acquisition Signal Processing Techniques for GNSS Receivers: From fundamentals to state-of-the-art GNSS acquisition technologies," *IEEE Signal Processing Magazine*, vol. 34, no. 5, pp. 59–71, 2017. [Online]. Available: <http://ieeexplore.ieee.org/document/8026189/>
- [56] F. S. T. Van Diggelen, *A-GPS : assisted GPS, GNSS, and SBAS*. Artech House, 2009.
- [57] F. Dovis and T. Hai, "High Sensitivity Techniques for GNSS Signal Acquisition," in *Global Navigation Satellite Systems: Signal, Theory and Applications*, J. Shuanggen, Ed. InTech, feb 2012. [Online]. Available: <http://www.intechopen.com/books/global-navigation-satellite-systems-signal-theory-and-applications/high-sensitivity-techniques-for-gnss-signal-acquisition>
- [58] J. Betz and K. Kolodziejski, "Generalized Theory of Code Tracking with an Early-Late Discriminator Part I: Lower Bound and Coherent Processing," *IEEE Transactions on Aerospace and Electronic Systems*, vol. 45, no. 4, pp. 1538–1556, oct 2009. [Online]. Available: <http://ieeexplore.ieee.org/lpdocs/epic03/wrapper.htm?arnumber=5310316>
- [59] —, "Generalized Theory of Code Tracking with an Early-Late Discriminator Part II: Noncoherent Processing and Numerical Results," *IEEE Transactions on Aerospace and Electronic Systems*, vol. 45, no. 4, pp. 1557–1564, oct 2009. [Online]. Available: <http://ieeexplore.ieee.org/lpdocs/epic03/wrapper.htm?arnumber=5310317>
- [60] J. A. Lopez-Salcedo, J. A. D. Peral-Rosado, and G. Seco-Granados, "Survey on robust carrier tracking techniques," pp. 670–688, 2014.
- [61] F. G. Nievinski and K. M. Larson, "Forward modeling of GPS multipath for near-surface reflectometry and positioning applications," *GPS Solutions*, jun 2013. [Online]. Available: <http://link.springer.com/10.1007/s10291-013-0331-y>
- [62] V. U. Zavorotny, K. M. Larson, J. J. Braun, E. E. Small, E. D. Gutmann, and A. L. Bilich, "A Physical Model for GPS Multipath Caused by Land Reflections: Toward

## Bibliography

---

- Bare Soil Moisture Retrievals,” *IEEE Journal of Selected Topics in Applied Earth Observations and Remote Sensing*, vol. 3, no. 1, pp. 100–110, mar 2010.
- [63] V. Zavorotny and A. Voronovich, “Scattering of GPS signals from the ocean with wind remote sensing application,” *IEEE Transactions on Geoscience and Remote Sensing*, vol. 38, no. 2, pp. 951–964, mar 2000. [Online]. Available: <http://ieeexplore.ieee.org/lpdocs/epic03/wrapper.htm?arnumber=841977>
- [64] P. Beckmann and A. Spizzichino, *The Scattering of Electromagnetic Waves from Rough Surfaces*, ser. Radar Library. Artech House, 1987. [Online]. Available: <https://books.google.ch/books?id=AzO7QgAACAAJ>
- [65] M. Skolnik, *Introduction to Radar Systems*. Tata McGraw Hill, 2003. [Online]. Available: <https://books.google.ch/books?id=zlZom9QkjCkC>
- [66] C. Hall and R. Cordey, “Multistatic Scatterometry,” in *International Geoscience and Remote Sensing Symposium, 'Remote Sensing: Moving Toward the 21st Century'*, vol. 1. IEEE, 1988, pp. 561–562. [Online]. Available: <http://ieeexplore.ieee.org/lpdocs/epic03/wrapper.htm?arnumber=570200>
- [67] M. Martin-Neira, “A passive reflectometry and interferometry system (PARIS): application to ocean altimetry,” *ESA Journal*, vol. 17, no. 4, pp. 331–355, 1993.
- [68] J.-C. Auber, A. Bibaut, and J.-M. Rigal, “Characterization of Multipath on Land and Sea at GPS Frequencies,” in *Proceedings of the 7th International Technical Meeting of the Satellite Division of The Institute of Navigation (ION GPS 1994)*, Salt Lake City, UT, 1994, pp. 1155 – 1171.
- [69] J. L. Garrison, S. J. Katzberg, and M. I. Hill, “Effect of sea roughness on bistatically scattered range coded signals from the Global Positioning System,” *Geophysical Research Letters*, vol. 25, no. 13, p. 2257, 1998.
- [70] K. D. Anderson, “Determination of water level and tides using interferometric observations of GPS signals,” *Journal of Atmospheric and Oceanic Technology*, vol. 17, no. 8, pp. 1118–1127, 2000.
- [71] A. Kavak, W. Vogel, and G. Xu, “Using GPS to measure ground complex permittivity,” *Electronics Letters*, vol. 34, no. 3, p. 254, 1998. [Online]. Available: <http://digital-library.theiet.org/content/journals/10.1049/el{ }19980180>
- [72] O. Nogués-Correig, E. Cardellach, J. S. Campderrós, and A. Rius, “A GPS-reflections receiver that computes doppler/delay maps in real time,” *IEEE Transactions on Geoscience and Remote Sensing*, vol. 45, no. 1, pp. 156–174, 2007.
- [73] A. Camps, J. F. Marchan-Hernandez, X. Bosch-Lluis, N. Rodriguez-Alvarez, I. Ramos-Perez, E. Valencia, J. M. Tarongi, H. Park, H. Carreno-Luengo, A. Alonso-Arroyo, D. Pascual, R. Onrubia, G. Forte, and J. Querol, “Review of GNSS-R instruments and tools developed at the Universitat Politecnica de Catalunya-Barcelona tech,” in *2014 IEEE Geoscience and Remote Sensing Symposium*. IEEE, jul 2014, pp. 3826–3829. [Online]. Available: <http://ieeexplore.ieee.org/lpdocs/epic03/wrapper.htm?arnumber=6947318>
- [74] S. Gleason, S. Hodgart, C. Gommenginger, S. Mackin, M. Adjrard, and M. Unwin, “Detection and Processing of bistatically reflected GPS signals from low Earth orbit for the purpose of ocean remote sensing,” *IEEE Transactions on Geoscience and Remote Sensing*, vol. 43, no. 6, pp. 1229–1241, jun 2005. [Online]. Available: <http://ieeexplore.ieee.org/lpdocs/epic03/wrapper.htm?arnumber=1433022>

- [75] F. Martin, S. DAddio, A. Camps, and M. Martin-Neira, "Modeling and Analysis of GNSS-R Waveforms Sample-to-Sample Correlation," *IEEE Journal of Selected Topics in Applied Earth Observations and Remote Sensing*, vol. 7, no. 5, pp. 1545–1559, may 2014. [Online]. Available: <http://ieeexplore.ieee.org/lpdocs/epic03/wrapper.htm?arnumber=6782387>
- [76] M. P. Clarizia, C. P. Gommenginger, S. T. Gleason, M. A. Srokosz, C. Galdi, and M. Di Bisceglie, "Analysis of GNSS-R delay-Doppler maps from the UK-DMC satellite over the ocean," *Geophysical Research Letters*, vol. 36, no. 2, pp. n/a–n/a, jan 2009. [Online]. Available: <http://doi.wiley.com/10.1029/2008GL036292>
- [77] N. Pierdicca, L. Pulvirenti, F. Ticconi, and M. Brogioni, "Radar Bistatic Configurations for Soil Moisture Retrieval: A Simulation Study," *IEEE Transactions on Geoscience and Remote Sensing*, vol. 46, no. 10, pp. 3252–3264, oct 2008. [Online]. Available: <http://ieeexplore.ieee.org/lpdocs/epic03/wrapper.htm?arnumber=4637969>
- [78] N. Pierdicca, L. Guerriero, R. Giusto, M. Brogioni, and A. Egido, "SAVERS: A Simulator of GNSS Reflections From Bare and Vegetated Soils," *IEEE Transactions on Geoscience and Remote Sensing*, vol. 52, no. 10, pp. 6542–6554, oct 2014. [Online]. Available: <http://ieeexplore.ieee.org/lpdocs/epic03/wrapper.htm?arnumber=6725659>
- [79] D. Schiavulli, A. Ghavidel, A. Camps, and M. Migliaccio, "A simulator for GNSS-R polarimetric observations over the ocean," in *2014 IEEE Geoscience and Remote Sensing Symposium*. IEEE, jul 2014, pp. 3802–3805. [Online]. Available: <http://ieeexplore.ieee.org/lpdocs/epic03/wrapper.htm?arnumber=6947312>
- [80] S. Jin and A. Komjathy, "GNSS reflectometry and remote sensing: New objectives and results," *Advances in Space Research*, vol. 46, no. 2, pp. 111–117, jul 2010. [Online]. Available: <http://dx.doi.org/10.1016/j.asr.2010.01.014>
- [81] E. Cardellach, F. Fabra, O. Nogués-Correig, S. Oliveras, S. Ribó, and A. Rius, "GNSS-R ground-based and airborne campaigns for ocean, land, ice, and snow techniques: Application to the GOLD-RTR data sets," *Radio Science*, vol. 46, no. 6, pp. n/a–n/a, dec 2011. [Online]. Available: <http://doi.wiley.com/10.1029/2011RS004683>
- [82] C. Ruf, M. Unwin, J. Dickinson, R. Rose, D. Rose, M. Vincent, and A. Lyons, "CYGNSS: Enabling the Future of Hurricane Prediction [Remote Sensing Satellites]," *IEEE Geoscience and Remote Sensing Magazine*, vol. 1, no. 2, pp. 52–67, jun 2013. [Online]. Available: <http://ieeexplore.ieee.org/lpdocs/epic03/wrapper.htm?arnumber=6555846>
- [83] A. Camps, H. Park, A. Ghavidel, J. M. Rius, and I. Sekulic, "GEROS-ISS, a demonstration mission of GNSS remote sensing capabilities to derive geophysical parameters of the earth surfaces: Altimetry performance evaluation," in *2015 IEEE International Geoscience and Remote Sensing Symposium (IGARSS)*, 2015, pp. 3917–3920. [Online]. Available: <http://ieeexplore.ieee.org/lpdocs/epic03/wrapper.htm?arnumber=7326681>
- [84] S. J. Katzberg, O. Torres, M. S. Grant, and D. Masters, "Utilizing calibrated GPS reflected signals to estimate soil reflectivity and dielectric constant: Results from SMEX02," *Remote Sensing of Environment*, vol. 100, no. 1, pp. 17–28, jan 2006. [Online]. Available: <http://linkinghub.elsevier.com/retrieve/pii/S0034425705002932>
- [85] K. M. Larson, E. E. Small, E. D. Gutmann, A. L. Bilich, J. J. Braun, and V. U. Zavorotny, "Use of GPS receivers as a soil moisture network for water cycle studies," *Geophysical Research Letters*, vol. 35, no. 24, p. L24405, dec 2008. [Online]. Available: <http://doi.wiley.com/10.1029/2008GL036013>

## Bibliography

---

- [86] K. M. Larson, J. J. Braun, E. E. Small, V. U. Zavorotny, E. D. Gutmann, and A. L. Bilich, "GPS Multipath and Its Relation to Near-Surface Soil Moisture Content," *IEEE Journal of Selected Topics in Applied Earth Observations and Remote Sensing*, vol. 3, no. 1, pp. 91–99, mar 2010. [Online]. Available: <http://ieeexplore.ieee.org/lpdocs/epic03/wrapper.htm?arnumber=5325890>
- [87] C. Botteron, N. Dawes, J. Leclère, J. Skaloud, S. Weijs, and P.-A. Farine, "Soil Moisture & Snow Properties Determination with GNSS in Alpine Environments: Challenges, Status, and Perspectives," *Remote Sensing*, vol. 5, no. 7, pp. 3516–3543, jul 2013. [Online]. Available: <http://www.mdpi.com/2072-4292/5/7/3516/>
- [88] A. Alonso Arroyo, A. Camps, A. Aguasca, G. Forte, A. Monerris, C. Rudiger, J. Walker, H. Park, D. Pascual, and R. Onrubia, "Dual-Polarization GNSS-R Interference Pattern Technique for Soil Moisture Mapping," *IEEE Journal of Selected Topics in Applied Earth Observations and Remote Sensing*, vol. 7, no. 5, pp. 1533–1544, may 2014. [Online]. Available: <http://ieeexplore.ieee.org/lpdocs/epic03/wrapper.htm?arnumber=6823624>
- [89] C. Chew, E. E. Small, and K. M. Larson, "An algorithm for soil moisture estimation using GPS-interferometric reflectometry for bare and vegetated soil," *GPS Solutions*, may 2015.
- [90] N. Roussel, F. Frappart, G. Ramillien, J. Darrozes, F. Baup, L. Lestarquit, and M. C. Ha, "Detection of Soil Moisture Variations Using GPS and GLONASS SNR Data for Elevation Angles Ranging From 2 deg to 70 deg," *IEEE Journal of Selected Topics in Applied Earth Observations and Remote Sensing*, pp. 1–14, 2016. [Online]. Available: <http://ieeexplore.ieee.org/lpdocs/epic03/wrapper.htm?arnumber=7446285>
- [91] K. M. Larson, E. D. Gutmann, V. U. Zavorotny, J. J. Braun, M. W. Williams, and F. G. Nievinski, "Can we measure snow depth with GPS receivers?" *Geophysical Research Letters*, vol. 36, no. 17, p. L17502, sep 2009. [Online]. Available: <http://doi.wiley.com/10.1029/2009GL039430>
- [92] K. M. Larson and F. G. Nievinski, "GPS snow sensing: results from the EarthScope Plate Boundary Observatory," *GPS Solutions*, vol. 17, no. 1, pp. 41–52, mar 2012. [Online]. Available: <http://link.springer.com/10.1007/s10291-012-0259-7>
- [93] K. M. Larson and E. E. Small, "Estimation of Snow Depth Using L1 GPS Signal-to-Noise Ratio Data," *IEEE Journal of Selected Topics in Applied Earth Observations and Remote Sensing*, pp. 1–7, 2016. [Online]. Available: <http://ieeexplore.ieee.org/lpdocs/epic03/wrapper.htm?arnumber=7373531>
- [94] S. Vey, A. Guntner, J. Wickert, T. Blume, H. Thoss, and M. Ramatschi, "Monitoring Snow Depth by GNSS Reflectometry in Built-up Areas: A Case Study for Wetzell, Germany," *IEEE Journal of Selected Topics in Applied Earth Observations and Remote Sensing*, pp. 1–8, 2016. [Online]. Available: <http://ieeexplore.ieee.org/lpdocs/epic03/wrapper.htm?arnumber=7399701>
- [95] M. Rivas, J. Maslanik, and P. Axelrad, "Bistatic Scattering of GPS Signals Off Arctic Sea Ice," *IEEE Transactions on Geoscience and Remote Sensing*, vol. 48, no. 3, pp. 1548–1553, mar 2010. [Online]. Available: <http://ieeexplore.ieee.org/lpdocs/epic03/wrapper.htm?arnumber=5256254>
- [96] F. Fabra, E. Cardellach, A. Rius, S. Ribó, S. Oliveras, O. Nogués-Correig, M. Belmonte Rivas, M. Semmling, and S. D'Addio, "Phase altimetry with dual polarization GNSS-R over sea ice," *IEEE Transactions on Geoscience and Remote Sensing*, vol. 50, no. 6, pp. 2112–2121, 2012.

- [97] G. Ruffini, F. Soulat, M. Caparrini, O. Germain, and M. Martín-Neira, “The Eddy experiment: Accurate GNSS-R ocean altimetry from low altitude aircraft,” *Geophysical Research Letters*, vol. 31, no. 12, 2004.
- [98] W. Bai, Y. Sun, Y. Fu, G. Zhu, Q. Du, Y. Zhang, Y. Han, and C. Cheng, “GNSS-R open-loop difference phase altimetry: Results from a bridge experiment,” *Advances in Space Research*, vol. 50, no. 8, pp. 1150–1157, oct 2012. [Online]. Available: <http://dx.doi.org/10.1016/j.asr.2011.10.019>
- [99] J. Dampf, T. Pany, N. Falk, B. Riedl, and J. Winkel, “Galileo Altimetry Using AltBOC and RTK Techniques,” *Inside GNSS*, vol. Jan/Feb, 2013.
- [100] J. S. Löfgren and R. Haas, “Sea level measurements using multi-frequency GPS and GLONASS observations,” *EURASIP Journal on Advances in Signal Processing*, vol. 2014, no. 1, p. 50, apr 2014. [Online]. Available: <http://asp.eurasipjournals.com/content/2014/1/50>
- [101] H. Carreno-Luengo and A. Camps, “Empirical Results of a Surface-Level GNSS-R Experiment in a Wave Channel,” *Remote Sensing*, vol. 7, no. 6, pp. 7471–7493, jun 2015. [Online]. Available: <http://www.mdpi.com/2072-4292/7/6/7471/>
- [102] S. Tabibi, F. G. Nievinski, T. Van Dam, and J. F. G. Monico, “Assessment of modernized GPS L5 SNR for ground-based multipath reflectometry applications,” *Advances in Space Research*, vol. 55, no. 4, pp. 1104–1116, 2015.
- [103] A. Alonso-Arroyo, A. Camps, H. Park, D. Pascual, R. Onrubia, and F. Martin, “Retrieval of Significant Wave Height and Mean Sea Surface Level Using the GNSS-R Interference Pattern Technique: Results From a Three-Month Field Campaign,” *IEEE Transactions on Geoscience and Remote Sensing*, vol. 53, no. 6, pp. 3198–3209, jun 2015. [Online]. Available: <http://ieeexplore.ieee.org/lpdocs/epic03/wrapper.htm?arnumber=6990586>
- [104] J. C. Kucwaj, G. Stienne, S. Reboul, J.-B. Choquel, and M. Benjelloun, “Accurate Pseudorange Estimation by Means of Code and Phase Delay Integration: Application to GNSS-R Altimetry,” *IEEE Journal of Selected Topics in Applied Earth Observations and Remote Sensing*, pp. 1–11, 2016. [Online]. Available: <http://ieeexplore.ieee.org/lpdocs/epic03/wrapper.htm?arnumber=7442528>
- [105] P. Ferrazzoli, L. Guerriero, N. Pierdicca, and R. Rahmoune, “Forest biomass monitoring with GNSS-R: Theoretical simulations,” *Advances in Space Research*, vol. 47, no. 10, pp. 1823–1832, 2011.
- [106] H. Carreno-Luengo, A. Amèzaga, D. Vidal, R. Olivé, J. Munoz, and A. Camps, “First Polarimetric GNSS-R Measurements from a Stratospheric Flight over Boreal Forests,” *Remote Sensing*, vol. 7, no. 10, pp. 13120–13138, oct 2015. [Online]. Available: <http://www.mdpi.com/2072-4292/7/10/13120/>
- [107] F. T. Ulaby and D. Long, *Microwave Radar And Radiometric Remote Sensing*. Artech House, 2015.
- [108] H. Carreno-Luengo, A. Camps, I. Ramos-Perez, and A. Rius, “Experimental Evaluation of GNSS-Reflectometry Altimetric Precision Using the P(Y) and C/A Signals,” *IEEE Journal of Selected Topics in Applied Earth Observations and Remote Sensing*, vol. 7, no. 5, pp. 1493–1500, may 2014. [Online]. Available: <http://ieeexplore.ieee.org/lpdocs/epic03/wrapper.htm?arnumber=6817543>

## Bibliography

---

- [109] C. Martin-Puig and G. Ruffini, "SAR altimeter retracker performance bound over water surfaces," in *2009 IEEE International Geoscience and Remote Sensing Symposium*, vol. 5. IEEE, 2009, pp. V-449-V-452. [Online]. Available: <http://ieeexplore.ieee.org/lpdocs/epic03/wrapper.htm?arnumber=5417633>
- [110] S. D'Addio, M. Martin-Neira, F. Martin, H. Park, and A. Camps, "GNSS-R altimeter performance: Analysis of Cramer-Rao lower bounds," in *2012 Workshop on Reflectometry Using GNSS and Other Signals of Opportunity (GNSS+R)*. West Lafayette, IN, USA: IEEE, oct 2012, pp. 1-4. [Online]. Available: <http://ieeexplore.ieee.org/lpdocs/epic03/wrapper.htm?arnumber=6408258>
- [111] A. Camps, H. Park, E. Valencia i Domenech, D. Pascual, F. Martin, A. Rius, S. Ribo, J. Benito, A. Andres-Beivide, P. Saameno, G. Staton, M. Martin-Neira, S. D'Addio, and P. Willemsen, "Optimization and Performance Analysis of Interferometric GNSS-R Altimeters: Application to the PARIS IoD Mission," *IEEE Journal of Selected Topics in Applied Earth Observations and Remote Sensing*, vol. 7, no. 5, pp. 1-16, 2014. [Online]. Available: <http://ieeexplore.ieee.org/lpdocs/epic03/wrapper.htm?arnumber=6817554>
- [112] A. Rius, E. Cardellach, and M. Martin-Neira, "Altimetric Analysis of the Sea-Surface GPS-Reflected Signals," *IEEE Transactions on Geoscience and Remote Sensing*, vol. 48, no. 4, pp. 2119-2127, apr 2010. [Online]. Available: <http://ieeexplore.ieee.org/lpdocs/epic03/wrapper.htm?arnumber=5393092>
- [113] S. Gleason, "Fading statistics of bistatically scattered GPS signals detected from ocean and land in low earth orbit," in *2007 IEEE International Geoscience and Remote Sensing Symposium*. IEEE, 2007, pp. 5097-5100. [Online]. Available: <http://ieeexplore.ieee.org/lpdocs/epic03/wrapper.htm?arnumber=4424008>
- [114] A. Alonso-Arroyo, J. Querol, C. Lopez-Martinez, V. Zavorotny, H. Park, D. Pascual, R. Onrubia, and A. Camps, "SNR and Standard Deviation of cGNSS-R and iGNSS-R Scatterometric Measurements," *Sensors*, vol. 17, no. 1, p. 183, jan 2017. [Online]. Available: <http://www.mdpi.com/1424-8220/17/1/183>
- [115] J. L. Garrison, "A Statistical Model and Simulator for Ocean-Reflected GNSS Signals," in *IEEE Transactions on Geoscience and Remote Sensing*, vol. 54, no. 10, 2016, pp. 6007-6019.
- [116] A. Bilich, K. M. Larson, and P. Axelrad, "Modeling GPS phase multipath with SNR: Case study from the Salar de Uyuni, Bolivia," *Journal of Geophysical Research*, vol. 113, no. B4, p. B04401, apr 2008. [Online]. Available: <http://doi.wiley.com/10.1029/2007JB005194>
- [117] X. Qian and S. Jin, "Estimation of Snow Depth From GLONASS SNR and Phase-Based Multipath Reflectometry," *IEEE Journal of Selected Topics in Applied Earth Observations and Remote Sensing*, pp. 1-7, 2016. [Online]. Available: <http://ieeexplore.ieee.org/lpdocs/epic03/wrapper.htm?arnumber=7471400>
- [118] A. Alonso-Arroyo, A. Camps, A. Monerris, C. Ruudiger, J. P. Walker, G. Forte, D. Pascual, H. Park, and R. Onrubia, "The dual polarization GNSS-R interference pattern technique," in *2014 IEEE Geoscience and Remote Sensing Symposium*. IEEE, jul 2014, pp. 4058-4061. [Online]. Available: <http://ieeexplore.ieee.org/lpdocs/epic03/wrapper.htm?arnumber=6947377>
- [119] N. Rodriguez-Alvarez, X. Bosch-Lluis, A. Camps, M. Vall-llossera, E. Valencia, J. Marchan-Hernandez, and I. Ramos-Perez, "Soil Moisture Retrieval Using GNSS-R



- Techniques: Experimental Results Over a Bare Soil Field,” *IEEE Transactions on Geoscience and Remote Sensing*, vol. 47, no. 11, pp. 3616–3624, nov 2009. [Online]. Available: <http://ieeexplore.ieee.org/lpdocs/epic03/wrapper.htm?arnumber=5282600>
- [120] C. Fernandez-Prades, J. Arribas, and P. Closas, “Robust GNSS Receivers by Array Signal Processing: Theory and Implementation,” *Proceedings of the IEEE*, vol. 104, no. 6, pp. 1207 — 1220, 2016. [Online]. Available: <http://ieeexplore.ieee.org/stamp/stamp.jsp?arnumber=7444116>
- [121] H. Krim and M. Viberg, “Two decades of array signal processing research: the parametric approach,” *IEEE Signal Processing Magazine*, vol. 13, pp. 67–94, 1996.
- [122] B. D. Van Veen and K. M. Buckley, “Beamforming Techniques for Spatial Filtering,” *The Digital Signal Processing Handbook*, vol. 5, no. 2, pp. 1 – 22, 2009. [Online]. Available: <http://dx.doi.org/10.1109/53.6655Cnpapers2://publication/doi/10.1109/53.665>
- [123] H. L. Van Trees, *Detection, Estimation, and Modulation Theory, Optimum Array Processing*, ser. Detection, Estimation, and Modulation Theory. Wiley, 2002. [Online]. Available: <http://books.google.co.in/books?id=0nRGAAAAYAAJ>
- [124] G. Seco-Granados, “Antenna Arrays for Multipath and Interference Mitigation in GNSS Receivers,” Ph.D. dissertation, Universitat Politècnica de Catalunya, 2000.
- [125] C. Fernandez-Prades, “Advanced Signal Processing Techniques for Global Navigation Satellite Systems Receivers,” Ph.D. dissertation, Universitat Politècnica de Catalunya, 2005.
- [126] A. Broumandan, A. Jafarnia-Jahromi, S. Daneshmand, and G. Lachapelle, “Overview of Spatial Processing Approaches for GNSS Structural Interference Detection and Mitigation,” *Proceedings of the IEEE*, vol. 104, no. 6, pp. 1246–1257, jun 2016. [Online]. Available: <http://ieeexplore.ieee.org/document/7444141/>
- [127] J. C. Curlander and R. N. McDonough, *Synthetic aperture radar : systems and signal processing*, 1991.
- [128] A. Broumandan, J. Nielsen, and G. Lachapelle, “Signal detection performance in indoor environments with a synthetic antenna array,” in *2009 13th International Symposium on Antenna Technology and Applied Electromagnetics and the Canadian Radio Science Meeting*. Banff, AB, Canada: IEEE, feb 2009, pp. 1–4. [Online]. Available: <http://ieeexplore.ieee.org/document/4805048/>
- [129] —, “Narrowband signal detection in correlated rayleigh fading with a moving antenna,” in *Proceedings - 2009 13th International Symposium on Antenna Technology and Applied Electromagnetics and the Canadian Radio Sciences Meeting, ANTEM/URSI 2009*, 2009.
- [130] —, “GLRT signal detection performance of a synthetic array,” in *23rd Canadian Conference on Electrical and Computer Engineering, CCECE 2010*. Calgary, AB, Canada: IEEE, may 2010, pp. 1–5.
- [131] —, “Indoor GNSS Signal Acquisition Performance using a Synthetic Antenna Array,” *IEEE Transactions on Aerospace and Electronic Systems*, vol. 47, no. 2, pp. 1337–1350, apr 2011. [Online]. Available: <http://ieeexplore.ieee.org/document/5751262/>
- [132] Y. L. C. De Jong and M. H. A. J. Herben, “High-resolution angle-of-arrival measurement of the mobile radio channel,” *IEEE Transactions on Antennas and Propagation*, vol. 47, no. 11, pp. 1677–1687, 1999.

## Bibliography

---

- [133] A. Broumandan, T. Lin, A. Moghaddam, D. Lu, J. Nielsen, and G. Lachapelle, "Direction of Arrival Estimation of GNSS Signals Based on Synthetic Antenna Array," in *Proceedings of the 20th International Technical Meeting of the Satellite Division of The Institute of Navigation (ION GNSS 2007)*, sep 2007, pp. 728–738. [Online]. Available: <http://www.ion.org/publications/abstract.cfm?jp=p{&}articleID=7573>
- [134] R. Schmidt, "Multiple emitter location and signal parameter estimation," *IEEE Transactions on Antennas and Propagation*, vol. 34, no. 3, pp. 276–280, 1986. [Online]. Available: <http://ieeexplore.ieee.org/document/1143830/>
- [135] A. Broumandan, J. Nielsen, and G. Lachapelle, "TOA Estimation Enhancement based on Blind Calibration of Synthetic Arrays," in *2008 IEEE 68th Vehicular Technology Conference*. Calgary, AB, Canada: IEEE, sep 2008, pp. 1–5. [Online]. Available: <http://ieeexplore.ieee.org/document/4656918/>
- [136] E. Gonen and J. M. Mendel, "Applications of cumulants to array processing - Part III: Blind beamforming for coherent signals," *IEEE Transactions on Signal Processing*, vol. 45, no. 9, pp. 2252–2264, 1997.
- [137] A. Broumandan, J. Nielsen, and G. Lachapelle, "Practical Results of High Resolution AOA Estimation by the Synthetic Array," in *2008 IEEE 68th Vehicular Technology Conference*. Calgary, AB, Canada: IEEE, sep 2008, pp. 1–5. [Online]. Available: <http://ieeexplore.ieee.org/document/4656917/>
- [138] T. Pany and B. Eissfeller, "Demonstration of a Synthetic Phased Array Antenna for Carrier/Code Multipath Mitigation," in *Proceedings of the 21st International Technical Meeting of the Satellite Division of The Institute of Navigation (ION GNSS 2008)*, sep 2008, pp. 663–668. [Online]. Available: <http://www.ion.org/publications/abstract.cfm?jp=p{&}articleID=7986>
- [139] A. Soloviev and F. Van Graas, "Beam Steering in Global Positioning System Receivers using Synthetic Phased Arrays," *IEEE Transactions on Aerospace and Electronic Systems*, vol. 46, no. 3, pp. 1513–1522, jul 2010. [Online]. Available: <http://ieeexplore.ieee.org/document/5545206/>
- [140] M. H. Keshvadi, A. Broumandan, and G. Lachapelle, "Analysis of GNSS beamforming and angle of arrival estimation in multipath environments," in *Institute of Navigation - International Technical Meeting 2011, ITM 2011*, San Diego, CA, United states, 2011, pp. 427–435.
- [141] T. Pany, N. Falk, B. Riedl, C. Stöber, J. Winkel, and H.-P. Ranner, "GNSS Synthetic Aperture Processing with Artificial Antenna Motion," in *Proceedings of the 26th International Technical Meeting of The Satellite Division of the Institute of Navigation (ION GNSS+ 2013)*, sep 2013, pp. 3163–3171. [Online]. Available: <http://www.ion.org/publications/abstract.cfm?jp=p{&}articleID=11431>
- [142] V. Dehghanian, A. Broumandan, M. Zaheri, J. Nielsen, V. Dehghanian, A. Broumandan, M. Zaheri, and J. Nielsen, "Dual-Polarized Synthetic Antenna Array for GNSS Handheld Applications," *ISRN Communications and Networking*, vol. 2013, pp. 1–11, 2013. [Online]. Available: <http://www.hindawi.com/journals/isrn/2013/985401/>
- [143] L. L. Scharf and C. Demeure, *Statistical Signal Processing: Detection, Estimation, and Time Series Analysis*, ser. Addison-Wesley series in electrical and computer engineering. Addison-Wesley Publishing Company, 1991.

- 
- [144] H. L. Van Trees and K. L. Bell, *Bayesian bounds for parameter estimation and nonlinear filtering / tracking*. IEEE Press, 2007. [Online]. Available: <http://ieeexplore.ieee.org/xpl/bkabstractplus.jsp?bkn=5263120>
- [145] K. Bell, Y. Steinberg, Y. Ephraim, and H. Van Trees, "Extended Ziv-Zakai lower bound for vector parameter estimation," *IEEE Transactions on Information Theory*, vol. 43, no. 2, pp. 624–637, mar 1997. [Online]. Available: <http://ieeexplore.ieee.org/document/556118/>
- [146] E. L. Lehmann and G. Casella, *Theory of Point Estimation*, *Second Edition Springer Texts in Statistics*, 1998, vol. 41, no. 3. [Online]. Available: <http://www.amazon.com/dp/0387985026>
- [147] A. N. D'Andrea, U. Mengali, and R. Reggiannini, "The Modified Cramer-Rao Bound and its Application to Synchronization Problems," *IEEE Transactions on Communications*, vol. 42, no. 234, pp. 1391–1399, 1994.
- [148] P. Stoica, E. G. Larsson, and A. B. Gershman, "The stochastic CRB for array processing: A textbook derivation," *IEEE Signal Processing Letters*, vol. 8, no. 5, pp. 148–150, 2001.
- [149] D. Zachariah and P. Stoica, "Cramér-Rao Bound Analog of Bayes' Rule [Lecture Notes]," *IEEE Signal Processing Magazine*, vol. 32, no. 2, pp. 164–168, mar 2015. [Online]. Available: <http://ieeexplore.ieee.org/lpdocs/epic03/wrapper.htm?arnumber=7038246>
- [150] T. Pany, *Navigation Signal Processing for GNSS Software Receivers*. Artech House, 2010. [Online]. Available: <https://books.google.com/books?id=3pMfZCyyvcvC{&}pgis=1>
- [151] P. Closas, C. Fernandez-Prades, and J. Fernandez-Rubio, "Cramér-Rao Bound Analysis of Positioning Approaches in GNSS Receivers," *IEEE Transactions on Signal Processing*, vol. 57, no. 10, pp. 3775–3786, oct 2009. [Online]. Available: <http://ieeexplore.ieee.org/lpdocs/epic03/wrapper.htm?arnumber=5071218>
- [152] S. Reboul, C. Botteron, M. A. Ribot, G. Stienne, and J. Leclère, "Normalized GNSS Interference Pattern Technique," in *URSI Commission F Microwave Signatures 2013 - Specialist Symposium on Microwave Remote Sensing of the Earth, Oceans, and Atmosphere*, Espoo, Finland, 2013, p. 2013.
- [153] M. Ribot, C. Botteron, and P.-A. Farine, "Derivation of the Cramér-Rao Bound in the GNSS-Reflectometry Context for Static, Ground-Based Receivers in Scenarios with Coherent Reflection," *Sensors*, vol. 16, no. 12, p. 2063, dec 2016. [Online]. Available: <http://www.mdpi.com/1424-8220/16/12/2063>
- [154] M. A. Ribot, J. C. Kucwaj, C. Botteron, S. Reboul, G. Stienne, J. Leclère, J. B. Choquel, P. A. Farine, and M. Benjelloun, "Normalized GNSS interference pattern technique for altimetry," *Sensors (Switzerland)*, vol. 14, no. 6, pp. 10 234–10 257, 2014.
- [155] M. A. Ribot Sanfelix, C. Botteron, and P.-A. Farine, "A New Estimation Algorithm for the GNSS-R Interference Pattern Technique: The Segmented Maximum-Likelihood," in *Proceedings of the 28th International Technical Meeting of The Satellite Division of the Institute of Navigation (ION GNSS+ 2015)*, Tampa, USA, 2015.
- [156] M. Foucras, J. Leclère, C. Botteron, O. Julien, C. Macabiau, P.-A. Farine, and B. Ekambi, "Study on the cross-correlation of GNSS signals and typical approximations," *GPS Solutions*, pp. 1–14, aug 2016. [Online]. Available: <http://link.springer.com/10.1007/s10291-016-0556-7>

## Bibliography

---

- [157] Tsui, *Fundamentals of Global Positioning System Receivers: A Software Approach*. John Wiley & Sons, 2005. [Online]. Available: <http://books.google.com/books?id=HQCGPr7pGV8C{&}pgis=1>
- [158] D. Skournetou, A. H. Sayed, and E. S. Lohan, “Performance of Deconvolution Methods in Estimating CBOC-Modulated Signals,” *International Journal of Navigation and Observation*, vol. 2011, pp. 1–15, 2011. [Online]. Available: <http://www.hindawi.com/journals/ijno/2011/356975/>
- [159] J. W. Betz and K. R. Kolodziejcki, “Extended Theory of Early-Late Code Tracking for a Bandlimited GPS Receiver,” *Navigation*, vol. 47, no. 3, pp. 211–226, sep 2000. [Online]. Available: <http://doi.wiley.com/10.1002/j.2161-4296.2000.tb00215.x>
- [160] Leica Geosystems, “AR25 Choke Ring Antenna - White Paper,” 2009. [Online]. Available: <http://www.leica-geosystems.com/downloads123/zz/nrs/AR25/white-tech-paper/AR25{ }White20Paper.pdf>
- [161] F. G. Nievinski and K. M. Larson, “An open source GPS multipath simulator in Matlab/Octave,” *GPS Solutions*, vol. 18, no. 3, pp. 473–481, mar 2014.
- [162] —, “Forward modeling of GPS multipath for near-surface reflectometry and positioning applications,” *GPS Solutions*, vol. 18, no. 2, pp. 309–322, 2014.
- [163] ITU-R, “Electrical Characteristics of the Surface of the Earh. Recommendation P.527-3 (03/92),” 1992.
- [164] M. A. Ribot, J.-C. Kucwaj, C. Botteron, S. Reboul, G. Stienne, J. Leclère, J.-B. Choquel, P.-A. Farine, and M. Benjelloun, “Normalized GNSS interference pattern technique for altimetry.” *Sensors (Basel, Switzerland)*, vol. 14, no. 6, pp. 10 234–57, jan 2014.
- [165] T. Hobiger, R. Haas, and J. Lofgren, “Software-Defined Radio Direct Correlation GNSS Reflectometry by Means of GLONASS,” *IEEE Journal of Selected Topics in Applied Earth Observations and Remote Sensing*, pp. 1–9, 2016. [Online]. Available: <http://ieeexplore.ieee.org/lpdocs/epic03/wrapper.htm?arnumber=7425137>
- [166] Z. Michalewicz and D. B. Fogel, “How to solve it: modern heuristics,” *Books.Google.Com*, p. 467, 2000.
- [167] A. Antoniou and W. S. Lu, *Practical optimization: Algorithms and engineering applications*, 2007.
- [168] B. M. Hannah, “Modelling and simulation of GPS multipath propagation,” Ph.D. dissertation, 2001.
- [169] A. Helm, G. Beyerle, and M. Nitschke, “Detection of coherent reflections with GPS bipath interferometry,” *Canadian Journal of Remote Sensing*, no. 2000, p. 11, 2004. [Online]. Available: <http://arxiv.org/abs/physics/0407091>
- [170] J. S. Löfgren, R. Haas, and H. G. Scherneck, “Sea level time series and ocean tide analysis from multipath signals at five GPS sites in different parts of the world,” *Journal of Geodynamics*, vol. 80, pp. 66–80, 2014.
- [171] A. Helm, “GPS altimetry with the L1 OpenGPS receiver using carrier phase-delay observations of reflected GPS signals,” *Scientific Technical Report STR08/10*, 2008.

- [172] K. M. Larson, J. S. Löfgren, and R. Haas, “Coastal sea level measurements using a single geodetic GPS receiver,” *Advances in Space Research*, vol. 51, no. 8, pp. 1301–1310, apr 2013. [Online]. Available: <http://dx.doi.org/10.1016/j.asr.2012.04.017>
- [173] M. A. Ribot, J. Cabeza, P. Closas, C. Botteron, and P.-A. Farine, “Estimation Bounds for GNSS Synthetic Aperture Techniques,” in *2017 IEEE 7th International Workshop on Computational Advances in Multi-Sensor Adaptive Processing (CAMSAP)*, Curaçao, Dutch Antilles, 2017.
- [174] M. A. Ribot Sanfelix, J. Cabeza de Pablo, C. Botteron, F. Valdés, B. Alorda, and P.-A. Farine, “GNSS Multipath Estimation and Mitigation Using a Rotating Antenna,” in *Proceedings of the European Navigation Conference 2017*, Lasuanne, CH, 2017. [Online]. Available: <https://infoscience.epfl.ch/record/228836?ln=en>
- [175] B. Hofmann-Wellenhof, H. Lichtenegger, and E. Wasle, *GNSS – Global Navigation Satellite Systems - GPS, GLONASS, Galileo, and more*, 2008. [Online]. Available: <https://www.springer.com/earth+sciences+and+geography/geographical+information+systems/book/978-3-211-73012-6>  
<http://www.amazon.com/dp/3211730125>
- [176] T. Pany, *Navigation Signal Processing for GNSS Software Receivers*, ser. GNSS technology and applications series. Norwood, MA, USA: Artech House, 2010.
- [177] M. Zatman, “How narrow is narrowband?” *IEEE Proceedings - Radar, Sonar and Navigation*, vol. 145, no. 2, p. 85, 1998. [Online]. Available: <http://digital-library.theiet.org/content/journals/10.1049/ip-rsn/19981670>
- [178] A. K. Tetewsky and F. E. Mullen, “Carrier Phase Wrap-Up Induced by Rotating GPS Antennas,” pp. 21–28, 1996. [Online]. Available: <https://www.ion.org/publications/abstract.cfm?articleID=1059>
- [179] T. B. Bahder, “Attitude determination from single-antenna carrier-phase measurements,” *Journal of Applied Physics*, vol. 91, no. 7, pp. 4677–4684, apr 2002. [Online]. Available: <http://aip.scitation.org/doi/10.1063/1.1448871>
- [180] H. Keshvadi, A. Broumandan, and G. Lachapelle, “Spatial characterization of GNSS multipath channels,” *International Journal of Antennas and Propagation*, vol. 2012, 2012.
- [181] H. Mott, *Polarization in antennas and radar*, ser. Wiley-Interscience publication. Wiley, 1986. [Online]. Available: <https://books.google.ch/books?id=XAxTAAAMAAJ>
- [182] T. Pany, N. Falk, B. Ried, C. Stöber, J. O. Winkel, and F.-J. Schimpl, “Synthetic-Aperture GNSS Signal Processing,” *GPS World*, 2013. [Online]. Available: <http://gpsworld.com/innovation-under-cover-synthetic-aperture-gnss-signal-processing/>
- [183] J. C. Lagarias, J. A. Reeds, M. H. Wright, and P. E. Wright, “Convergence Properties of the Nelder–Mead Simplex Method in Low Dimensions,” *SIAM Journal on Optimization*, vol. 9, no. 1, pp. 112–147, 1998. [Online]. Available: <http://epubs.siam.org/doi/10.1137/S1052623496303470>
- [184] A. Broumandan, J. Nielsen, and G. Lachapelle, “Coherent integration time limit of a mobile receiver for indoor GNSS applications,” *GPS Solutions*, vol. 16, no. 2, pp. 157–167, 2012.
- [185] M. Petovello, L. L. Presti, and B. Motella, “The math of ambiguity,” *Inside GNSS*, no. June, 2010.

## Bibliography

---

- [186] M. A. Yaqoob, F. Tufvesson, A. Mannesson, and B. Bernhardsson, "Direction of arrival estimation with arbitrary virtual antenna arrays using low cost inertial measurement units," in *2013 IEEE International Conference on Communications Workshops (ICC)*. Yogyakarta, Indonesia: IEEE, jun 2013, pp. 79–83. [Online]. Available: <http://ieeexplore.ieee.org/document/6649205/>
- [187] J. Serra, "Shrinkage corrections of sample linear estimators in the small sample size regime," Ph.D. dissertation, Universitat Politècnica de Catalunya (UPC), 2016.
- [188] X. Mestre and M. Lagunas, "Finite sample size effect on minimum variance beamformers: optimum diagonal loading factor for large arrays," *IEEE Transactions on Signal Processing*, vol. 54, no. 1, pp. 69–82, jan 2006. [Online]. Available: <http://ieeexplore.ieee.org/document/1561576/>
- [189] Y. I. Abramovich, B. A. Johnson, and X. Mestre, *Classical and Modern Direction-of-Arrival Estimation*, 2009. [Online]. Available: <http://www.sciencedirect.com/science/article/pii/B9780123745248000064>
- [190] A. Pousinho, M. Toledo, T. Ferreira, J. A. López-salcedo, S. Locubiche-serra, G. Seco-granados, M. A. Ribot, A. Jovanovic, C. Botteron, and P. Farine, "Adaptive Tracking Techniques in Non-Stationary Environments," in *28th International Technical Meeting of the Satellite Division of the Institute of Navigation, ION GNSS 2015*, vol. 4, 2014.
- [191] M. Susi, M. Andreotti, M. Aquino, and A. Dodson, "Tuning a Kalman filter carrier tracking algorithm in the presence of ionospheric scintillation," pp. 1–12, 2017.
- [192] J. Vila-Valls, P. Closas, and C. Fernandez-Prades, "Advanced KF-based methods for GNSS carrier tracking and ionospheric scintillation mitigation," in *2015 IEEE Aerospace Conference*. IEEE, mar 2015, pp. 1–10. [Online]. Available: <http://ieeexplore.ieee.org/document/7118930/>
- [193] P. D. Groves, "Principles of GNSS, inertial, and multisensor integrated navigation systems, 2nd edition [Book review]," *IEEE Aerospace and Electronic Systems Magazine*, vol. 30, no. 2, pp. 26–27, 2015. [Online]. Available: <http://ieeexplore.ieee.org/lpdocs/epic03/wrapper.htm?arnumber=7063664>
- [194] Spirent, *Spirent GSS8000 GNSS Simulator datasheet*, 2015. [Online]. Available: <http://www.spirentfederal.com/gps/documents/gss8000{ }datasheet.pdf>
- [195] NSL, *NSL Stereo: dual GNSS front-end datasheet*. Nottingham, UK: Nottingham Scientific Ltd (NSL). [Online]. Available: <http://www.nsl.eu.com/datasheets/stereo.pdf>
- [196] Mini-Circuits Inc, "Mini-Circuits ZRL-2400LN+ LNA Datasheet," 2017. [Online]. Available: <https://ww2.minicircuits.com/pdfs/ZRL-2400LN+.pdf>
- [197] Oscilloquartz SA, "Oscilloquartz OCXO 8663 Datasheet," 2004. [Online]. Available: <http://www.sungwhatech.com/product/pdf/aging/8663.pdf>
- [198] ANTCOM, Ed., *Antcom GNSS Antennas catalogue-datasheet*. Torrance, CA, US: ANTCOM Corporation, 2017. [Online]. Available: <http://www.antcom.com/documents/catalogs/GNSSAntennas1.pdf>
- [199] Fairview Microwave, "FMRJ1001 Datasheet," 2015. [Online]. Available: <https://www.fairviewmicrowave.com/images/productPDF/FMRJ1001.pdf>
- [200] u-blox SA, "u-Blox EVK-6 GPS Receiver User Guide," 2012. [Online]. Available: <https://www.u-blox.com/en/product/evk-6>

- [201] J. R. Wang and T. J. Schmugge, “An Empirical Model for the Complex Dielectric Permittivity of Soils as a Function of Water Content,” *IEEE Transactions on Geoscience and Remote Sensing*, vol. GE-18, no. 4, pp. 288–295, oct 1980. [Online]. Available: <http://ieeexplore.ieee.org/lpdocs/epic03/wrapper.htm?arnumber=4157179>
- [202] G. Lerondel and R. Romestain, “Fresnel coefficients of a rough interface,” *Applied Physics Letters*, vol. 74, no. 19, p. 2740, 1999. [Online]. Available: <http://scitation.aip.org/content/aip/journal/apl/74/19/10.1063/1.123999>
- [203] A. Alonso-Arroyo, A. Camps, A. Aguasca, G. Forte, A. Monerris, C. Rudiger, J. Walker, H. Park, D. Pascual, and R. Onrubia, “Improving the Accuracy of Soil Moisture Retrievals Using the Phase Difference of the Dual-Polarization GNSS-R Interference Patterns,” *IEEE Geoscience and Remote Sensing Letters*, vol. 11, no. 12, pp. 1–5, 2014. [Online]. Available: <http://ieeexplore.ieee.org/lpdocs/epic03/wrapper.htm?arnumber=6814795>





Miguel Angel RIBOT SANFÉLIX  
2000 Neuchâtel (Switzerland)  
Email: [miguel.angel.ribot@gmail.com](mailto:miguel.angel.ribot@gmail.com)

Date of birth: 02/06/1985  
Nationality: Spanish  
Marital status: Single

## Education

---

- 2013 – 2017** **ÉCOLE POLYTECHNIQUE FÉDÉRALE LAUSANNE (EPFL)**, Switzerland.  
**PhD in Microsystems and Microelectronics.** Supported by the Swiss National Science Foundation (SNSF) (grants No : 200020-134766/1 and 200020-153052/1). Thesis Title : “*Parameter Estimation with GNSS-Reflectometry and GNSS Synthetic Aperture Techniques*”.
- 2009 – 2011** **UNIVERSITAT POLITÈCNICA DE CATALUNYA (UPC)** - TELECOM BCN, Barcelona, Spain.  
**MSc in Information and Communication Technologies.** Specialization : Communications and Signal Processing. Master Thesis : “*Modification of a FPGA-based GPS Receiver for Reflectometry Applications (GNSS-R)*” (10/10). Advisor : Prof. Adriano Camps.
- 2003 – 2008** **UNIVERSITAT DE LES ILLES BALEARS (UIB)**, Majorca, Spain.  
**BSc in Telecommunications, specializing in Telematics.** Final year project : “*Study and Methodology Proposal for Power Transmission Selection in ZigBee and IEEE 802.15.4 Networks Based on Energy Consumption*” (10/10). Advisor : Dr. Bartomeu Alorda.

## Professional Experience

---

- 2013 – 2017** **ELECTRONICS AND SIGNAL PROCESSING LABORATORY (ESPLAB - EPFL)**, Switzerland.  
(4.5 years)  
**PhD Student & Research Assistant.**  
2014 – **ESA ADAPT Project** : Adaptive Tracking Techniques for Navigation Signals. Study of adaptive bandwidth switching techniques with high order modulations.  
2013-2016 – Derivation of estimation bounds of GNSS-Reflectometry techniques.  
2015-2017 – Study of synthetic aperture techniques for GNSS receivers using a rotating antenna.
- 2011 – 2012** **INDRA SISTEMAS, UK BRANCH**, Whiteley, UK.  
(1 year and 3 months)  
**Systems Engineer.**  
Definition and development of future Air Traffic Management solutions and systems for the United Kingdom airspace.
- 2011** **ERICSSON**, Barcelona, Spain.  
(5 months)  
**Radio Access Network Engineer.**  
Planification, design and supporting tasks in mobile communication network (3G and GSM) roll-out.
- 2010 – 2011** **ERNST & YOUNG**, Barcelona, Spain.  
(5 months)  
**Internship.**  
Internship in the Advance Security Laboratory managing Intrusion Detection System (IDS) software and performing support tasks in security audition projects.
- 2008 – 2009** **ELECTRONIC TECHNOLOGY GROUP - UIB**, Mallorca, Spain.  
(1 year)  
**Internship.**  
Laboratory assistant in research Wireless Sensor Networks projects : energy saving in the network nodes, ant the study and characterization of ZigBee devices. Extensive work with microcontrollers and 802.15.4 MAC layer protocol.

## Complimentary Education

---

- May 2013** **2013 GENIUS PhD WORKSHOP.**  
Seminar on Modern GNSS, Positioning and Timing, Aalborg University, Denmark.
- July 2015** **FRAUNHOFER FHR 7TH INTERNATIONAL SUMMER SCHOOL ON RADAR/SAR.**  
Radar fundamentals over state-of-the-art Radar/SAR systems to sophisticated radar signal processing techniques and their applications in remote sensing. Bonn, Germany.

- 2016 [CTI ENTREPRENEURSHIP TRAINING: BUSINESS CONCEPT.](#)  
14-week federal training program startup founders. Neuchâtel, Switzerland.

## Teaching Experience

---

- 2014 – 2017 [ADVANCED SATELLITE POSITIONING COURSE, EPFL.](#)  
**Teaching Assistant** in charge of laboratory sessions. Course code : ENV-542.
- 2016 [MSC THESIS ADVISOR, EPFL.](#)  
J. Cabeza “*Digital Beamforming with a Synthetic Aperture Rotating Antenna for GNSS Receivers – Signal Processing*”, EPFL student.
- 2015 [MSC THESIS ADVISOR, EPFL.](#)  
F. Degardins “*Digital Beamforming on a Synthetic Aperture Rotating Antenna*”, exchange student in ESPLAB from ENSEEIHT, Toulouse, France.

## Languages

---

- Spanish, Catalan** – Native speaker.  
**English** – Full professional competence.

## Computer Skills

---

- ▷ Programming : Matlab, C, C++, VHDL, R, Python, Java.  
▷ Office Tools : MS Office & Project, MS Visio. Latex. Graphics : HTML + CSS.

## Honors & Awards

---

- 2011 **Indra Future Minds Award** – 1st Edition.  
International project consulting competition for students organized by Indra Sistemas.

## Publications

---

- 2016 **M. A. Ribot**, C. Botteron, P.-A. Farine. “Derivation of the Cramér-Rao Bound in the GNSS-Reflectometry Context for Static, Ground-Based Receivers in Scenarios with Coherent Reflection”. *MDPI Sensors 2016*, 16, 2063.
- 2014 **M. A. Ribot**, J.-C. Kucwaj, C. Botteron, S. Reboul, G. Stienne, J. Leclère, J.-B. Choquel, P.-A. Farine, M. Benjelloun. “Normalized GNSS Interference Pattern Technique for Altimetry”. *MDPI Sensors 2014*, 14, 10234-10257.

## Conferences

---

- 2017 **M. A. Ribot**, J. Cabeza, P. Closas, C. Botteron, P.-A. Farine. “Estimation Bounds for GNSS Synthetic Aperture Techniques,” in *2017 IEEE 7th International Workshop on Computational Advances in Multi-Sensor Adaptive Processing (CAMSAP)*, 2017, Dutch Antilles. **Accepted.**
- 2017 **M. A. Ribot**, J. Cabeza, P. Closas, C. Botteron, F. Valdés, B. Alorda, n P.-A. Farine. “Carrier Tracking using Extended Kalman Filters for GNSS Synthetic Aperture Processing with a Rotating Antenna,” in *30th International Technical Meeting of the Satellite Division of the Institute of Navigation, ION GNSS+ 2017*, Portland, USA .
- 2017 **M. A. Ribot**, J. Cabeza, C. Botteron, F. Valdés, B. Alorda, P.-A. Farine. “GNSS Multipath Estimation and Mitigation Using a Rotating Antenna,” (extended abstract) in *Proceedings of European Navigation Conference 2017*, Lausanne, Switzerland, 2017.
- 2015 A. Pousinho, M. Toledo, T. Ferreira, J. A. López-Salcedo, S. Locubiche-Serra, G. Seco-Granados, **M. A. Ribot**, A. Jovanovic, C. Botteron, and P. Farine, “Adaptive Tracking Techniques in Non-Stationary Environments,” in *28th International Technical Meeting of the Satellite Division of the Institute of Navigation, ION GNSS+ 2015*, 2015, vol. 4. Tampa, FL, USA.

- 2015** M. A. Ribot, C. Botteron, and P.-A. Farine, “A New Estimation Algorithm for the GNSS-R Interference Pattern Technique : The Segmented Maximum-Likelihood,” in *28th International Technical Meeting of the Satellite Division of the Institute of Navigation, ION GNSS+ 2015*, 2015, vol. 4. Tampa, FL, USA.
- 2014** C. Carmona, B. Alorda, and M. A. Ribot, “Energy consumption savings in ZigBee-based WSN adjusting power transmission at application layer”, in *24th International Workshop on Power and Timing Modeling, Optimization and Simulation (PATMOS)*, 2014, pp. 1–6. Palma (Majorca), Spain.
- 2014** J.-C Kucwaj, M.A. Ribot, G. Stienne, C. Botteron, S. Reboul, J.-B Choquel, M. Benjelloun. “Calibration of the GNSS Signal Amplitudes in the Interference Pattern Technique for Altimetry,” in *In Radar’14*. Lille, France.
- 2013** S. Reboul, C. Botteron, M. A. Ribot, G. Stienne, J. Leclère. “Normalized GNSS Interference Pattern Technique,” in *URSI Commission F Microwave Signatures 2013 - Specialist Symposium on Microwave Remote Sensing of the Earth, Oceans, and Atmosphere* (p. 2013). Espoo, Finland.
- 2012** G. Rodriguez-Navas, M. A. Ribot, B. Alorda, “Understanding the Role of Transmission Power in Component-Based Architectures for Adaptive WSN,” in *2012 IEEE 36th Annual Computer Software and Applications Conference Workshops (COMPSACW)*, 2012. Izmir, Turkey.